Tennis Ball Marker and related PGE mineralization in the Eastern Bushveld Complex, South Africa

Student's name: Busisiwe Khoza

A dissertation submitted in fulfillment of the requirements for a Master of Science degree in Geology at the Department of Geosciences, Faculty of Science, University of the Witwatersrand, Johannesburg, South Africa
2021

Declaration

I declare that this dissertation is my unaided work. It is submitted for the Master of Science at the University of the Witwatersrand, Johannesburg. It has not been submitted before for any degree or examination at any other University.

_____
Signature of Candidate

16 of April 2021 at Johannesburg.

Abstract

At the Rustenburg Layered Suite, orthopyroxenite is interlayered with gabbros, gabbronorite, norites, anorthosites, etc. However, the Main Zone margins show a puzzling feature with spherical orthopyroxenite encased in gabbronorite, norite, and anorthosite. This feature is called the Tennis Ball Marker. Lee and Sharper (1979) interpreted it as a result of the spherical aggregation of orthopyroxene crystals suspended in a magma. The study aims to propose a new model to explain the origin of the spherical orthopyroxenite located at the Tennis Ball Marker, based on field observations, bulk chemical data, mineral compositions, and Rb-Sr, Sm-Nd, and Lu-Hf isotope data. Our results show that: (1) the spherical orthopyroxenite and the gabbronorite matrix are composed of the same mineral assemblage made up of plagioclase, orthopyroxene, clinopyroxene, quartz, biotite, oxides, and sulphides; (2) the spherical orthopyroxenite and the gabbronorite matrix are petrographically distinct; (3) the orthopyroxene and plagioclase on the spherical orthopyroxenite have a higher Magnesium number (Mg#) and Anorthite content (An), respectively, compared to those on the gabbronorite matrix; (4) the whole rock Mg# and normative anorthite content on the spherical orthopyroxenite cumulates, is higher than those of the gabbronorite matrix; (5) the feldspar and pyroxene geothermometers show that the cumulates on the spherical orthopyroxenite crystallized at a higher temperature than those on the gabbronorite, (6) The whole-rock trace elements distribution diagram for the spherical orthopyroxenite and the gabbronorite matrix have contrasting Ba and Sr anomalies; (7) The spherical orthopyroxenite show a negative and no Eu anomaly, which contrast the positive Eu anomaly shown by the gabbronorite matrix and host; (8) the REE patterns of the gabbronorite matrix are steeper than those of the spherical orthopyroxenite; (9) the spherical orthopyroxenite cumulates and the gabbronorite matrix have similar Sr_i $(0.706490 - 0.7077254)$; Nd_i $(0.509622 - 0.0509703)$; Hf_i $(0.281139 - 0.281241)$; εNd (-6.7 to -5.1) and εHf (-11.7 to -8) values are also homogenous with height.

The isotopic data shows that the spherical orthopyroxenite and the gabbronorite crystallized from a magma with the same isotopic signature. The bulk composition, REE patterns, and the mineral composition data imply that the gabbronorite crystalized from the residual melt of the spherical orthopyroxenite. The hypothesis envisages an intrusion of an orthopyroxene saturated magma that underwent fractional crystallization to form an orthopyroxenite layer at the base. The fractionation of orthopyroxene crystals caused the residual magma to evolve (at the chamber and feeder) to the eutectic. The magma with the eutectic composition ascended on the feeder to the chamber, and it broke the orthopyroxenite layer at the base as it was opening the magma chamber. The new magma percolated in between the orthopyroxenite fragments, eroded, and transported them to the south. The spherical shapes of the orthopyroxenite were achieved by a chemical dissolution process that eroded the edges and corners faster than the planar surface.

Acknowledgments

I want to express my gratitude to CIMERA for funding this project and my two supervisors Prof. Rais Latypov and Dr. Sofia Chistyakova, for allowing me to conduct this research. I would also like to thank them for helping me pursue my passion, for encouraging, supporting, directing, and criticizing my work at times. I would also like to thank Christina for giving us access to the Middelkraal farm, Margret, for accommodating our fieldwork period. William Kruger for taking drone images of the outcrops of the farm. I would also like to thank Intertek for analyzing our whole-rock composition, the facilitators of the Thin section and ore blocks lab, WIGL, and the MMU at the university of the Witwatersrand. I would also like to thank the facilitators of the multi-collector at the University of Johannesburg. I would also like to thank my best friend for proofreading this dissertation.

Table of Contents

List of Figures

List of Abbreviations

An	Anorthite content
BBM	Bolder Bed Marker
BIC	Bushveld Igneous Complex
Cpx	Clinopyroxene
DFB	Dullstroom Formation Basalt
En	Enstatite
Fo	Forsterite
GMA	Giant Mottled Anorthosite
Hf_i	Initial Hafnium ratio
LILE	Large Ion Lithophiles Elements
Nd_i	Initial Neodymium ratio
Opx	Orthopyroxene
PGEs	Platinum Group Elements
Plg	Plagioclase
RLS	Rustenburg Layered Suite
	MrZ Marginal Zone
	LZ Lower Zone
	CZ Critical Zone
	MZ Main Zone
	UP Upper Zone
Sr_i	Initial Sr ratio
TS	Transvaal Supergroup
WR	Whole Rock
Wt. %	Weight percentage

List of Tables

List of Appendices

Chapter 1: Introduction

1.1. The Rustenburg Layered Suite and the Tennis Ball Marker

The Rustenburg Layered Suite (RLS) is a large mafic-ultramafic intrusion. It is stratigraphically subdivided into five zones known as the (from base to top): Marginal Zone (MrZ), Lower Zone (LZ), Critical Zone (CZ), Main Zone (MZ), and Upper Zone (UZ) (Eales and Cawthorn, 1996; Cawthorn, 2015; Fig. 1.1). In these zones, orthopyroxenite occur as layered cumulates interlayered with chromitite, norite, anorthosite, gabbronorite, etc. (Harmer and Sharpe, 1985; Cameron, 1980, 1978; Cawthorn and Walraven, 1997; Latypov *et al*., 2018).

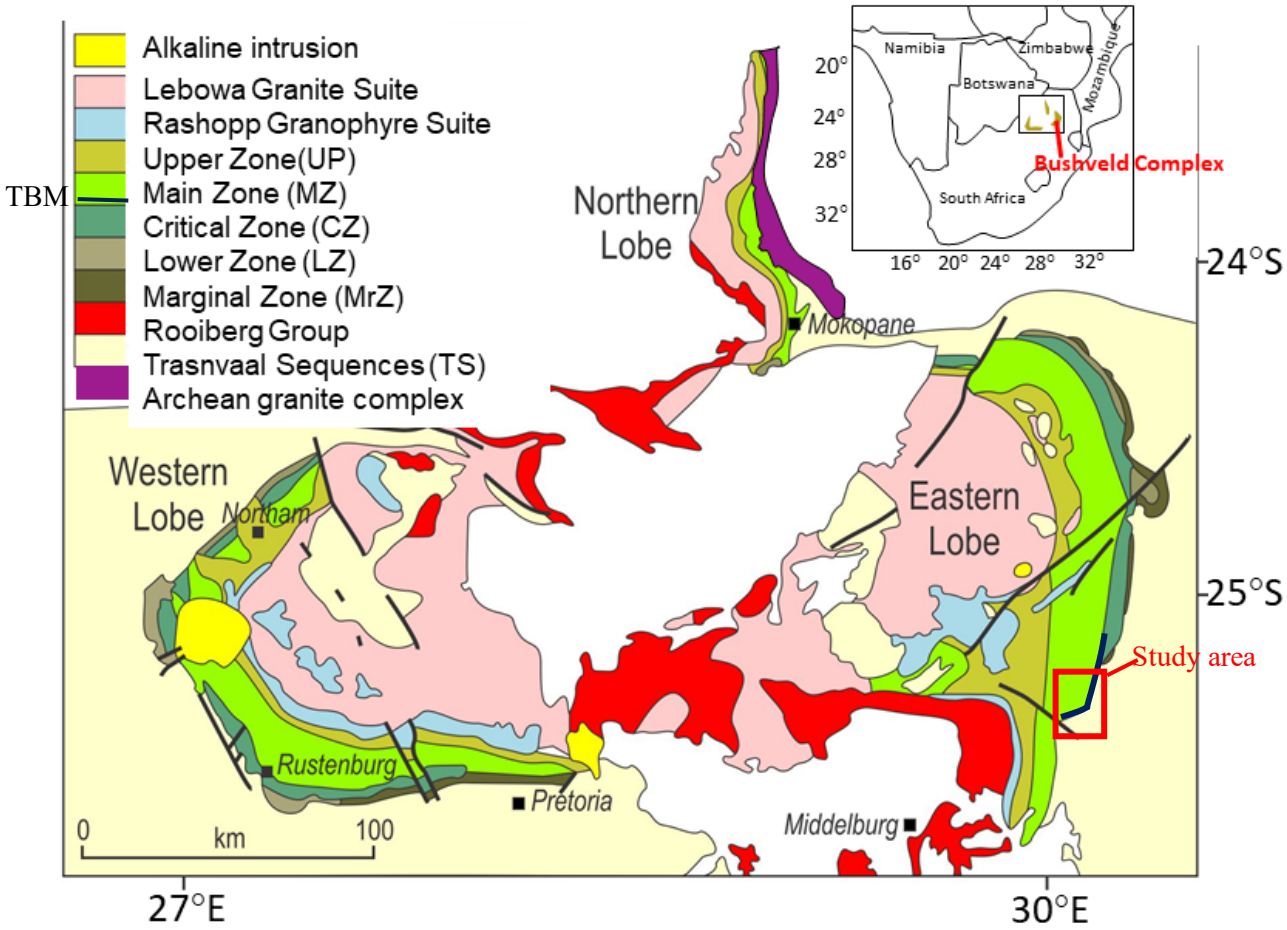

Fig. 1. 1. The schematic geological map of the Bushveld Igneous Complex (BIC) (modified after Latypov, 2015; Lee and Sharpe, 1979) showing three suites known as (from base to top) the Rustenburg Layered Suite (RLS), the Rashoop Granophyre Suite, and the Lebowa Granite Suite. Blue line= Tennis Ball Marker (TBM).

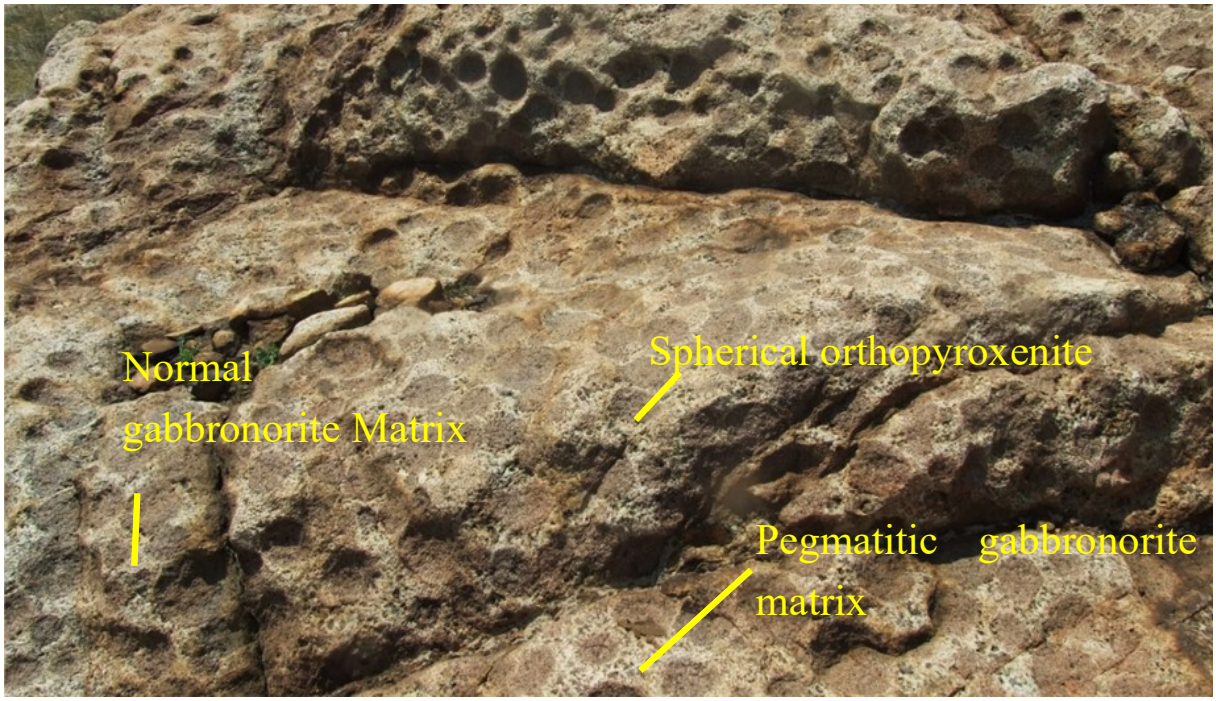

Fig. 1. 2. Field photograph of the TBM layer showing spherical orthopyroxenite encased in a matrix of varying grain sizes

However, the Main Zone margins have a fascinating horizon with orthopyroxenite possessing a spherical shape instead of a layer/plane (Fig. 1.2). This horizon is known as the Tennis Ball Marker (TBM), and it has spherical orthopyroxenite enclosed in gabbronorite, norite, and anorthosite (Fig. 1.2). It occurs as multiple layers that are concordant with the MZ layering (Fig. 1.1). It is also located at the MZ base and outcrops at the Eastern Lobe's southern parts (Fig. 1.1) and shows a transgressive nature like the one exhibited by the MZ (Fig. 1.1). It occurs above the GMA, where the MZ overlies the CZ and overlays the Transvaal Supergroup (TS), where the CZ is absent (Fig. 1.1).

1.2. Proposed hypotheses for the TBM

Lee and Sharpe (1979) proposed that the spherical orthopyroxenite results from pyroxene's physical aggregation from the MZ magma (Fig. 1.3). They suggested the introduction of an immiscible liquid into the MZ magma that was crystalizing plagioclase, orthopyroxene, and clinopyroxene. They further indicated that this immiscible liquid was repulsive to plagioclase crystals but attracted to pyroxenes. Therefore, it favorably coated the pyroxene crystals and excluded the plagioclase. The liquid drops

coalesced with other liquid drops carrying pyroxenes to form aggregates bonded by this liquid until big orthopyroxenite clusters formed (Fig. 1.6d).

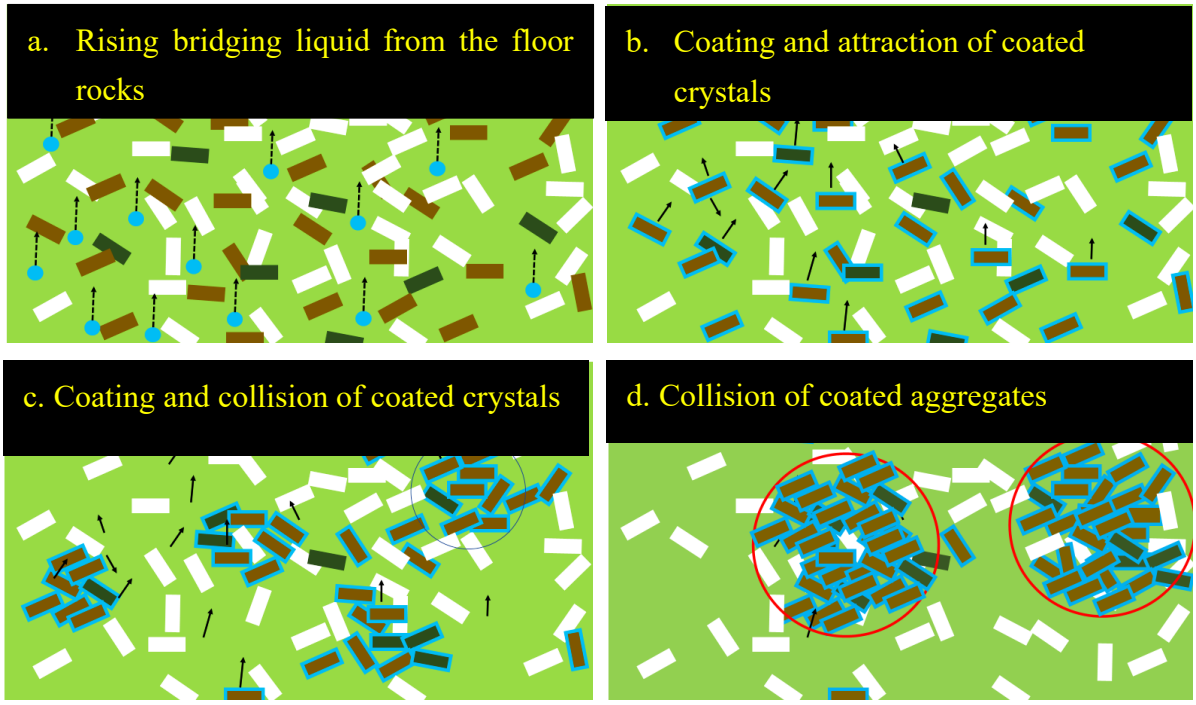

Fig. 1. 3. (a) The crystallization of plagioclase, orthopyroxene, and clinopyroxene in magma and the immiscible introduction. (b) Coating of the pyroxene crystals by the immiscible. (c) The collision of the coated pyroxene. (d) The collision of the pyroxene aggregates to form larger spherical orthopyroxenite.

1.3. Problem statement

The spherical shape exhibited by the orthopyroxenite at the TBM is unique and puzzling. At the RLS, these cumulates occur as layers (planar) that extend for several kilometers. They form layers because orthopyroxene is known to be denser than basaltic melts. Hence, they will most likely settle to the chamber floor as soon as they crystallize to form a continuous layer of orthopyroxenite slurries, which will solidify to form orthopyroxenite layers. The spherical shape of the orthopyroxenite at the TBM do not conform to the origin of such a differentiation process. Therefore, this indicates that there must have been more than one process in the magma chamber during the TBM formations. Additionally, the TBM is one of the least studied horizons at the Bushveld Complex. It lacks a detailed study of petrology, geochemistry, mineralogy, and isotope data; hence it is still not well understood.

1.4. Aim

To produce detailed TBM documentation and provide an alternative model to explain the TBM's origin at the Eastern Bushveld.

1.5. Objective

- Investigate the source of the spherical orthopyroxenite and associated shapes.
- Compare and contrast the mineralogical and textural properties of all orthopyroxenite in the TBM
- Investigate whether the spherical orthopyroxenite and the gabbronorite crystallized from the same magma
- Investigate the signs of melting, dissolution, and alterations on the spherical orthopyroxenite.
- Investigate the origin of the radial matrix around the spherical orthopyroxenite
- Investigate the concentrations of the PGE in both the spherical orthopyroxenite and the matrix

Chapter 2: Method and material

2.1. The geological mapping of the area of the Middelkraal farm

Thirty-nine samples were collected along the red traverse line, which runs from the Dullstroom Formation Basalt (DFB), through the TBM, to the gabbronorite (Fig. 2.1). The samples include twenty-seven gabbronorite (host and matrix), six spherical orthopyroxenite, one local pyroxenite layer, two basalt, and single samples pegmatitic gabbronorite, felsic dyke, and the anorthosite.

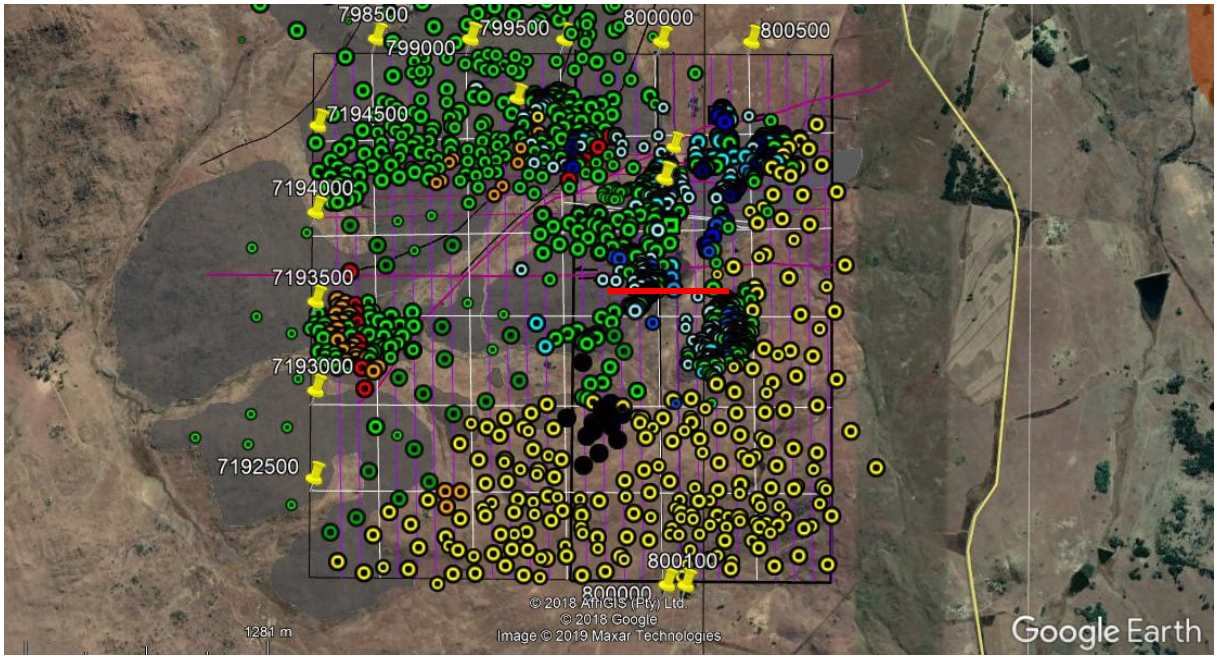

Fig. 2. 1. The light grey shaded areas show the locations with nice outcrop, and the areas with no shading either have soil or float. The colored points show the area visited during the mapping. Yellow-DFB, green-gabbronorite, blue-TBM, orange-anorthosite, and the red-dykes-cross cutting. The red line shows the sampled traversed that starts at the DFB to the gabbronorite.

2.2. Calculating the true thicknesses of the layers

The cross-section along the red line is presented in Fig. 2.2. The calculations for the true thicknesses of the layers at TBM-32 as shown below.

Step 1: Calculation of the horizontal distance between the sampled location and TBM-32 (reference point).

Step 2: Superimposed a right-angled triangle for the hypotonus to be along. Here the dipping layer (Fig. 2.4) and the angle of the triangle was the dip of that layer.

Step 3: Calculated the vertical changes of the height from where the sample location to the position of TBM-32. The vertical change calculation with the equations below: The results for the other layers calculation are in column 5 of Table 2.1

TBM-6: $\tan\theta = \frac{y}{x} \rightarrow y = x\tan\theta \rightarrow y = 730\tan 10 \rightarrow y = 128{,}71,$

TBM-8: $\tan\theta = \frac{y}{x} \rightarrow y = x\tan\theta \rightarrow y = 727\tan 10 \rightarrow y = 128{,}19$

Step 4: Calculated the heights of the layers at location TBM-32 by subtracting the calculated vertical change from the sampled height.

Step 5: The final step was calculating the true thickness of the layers. To draw a second right-angled triangle (Fig. 2.4), with its opposite side in touch with the layer. The actual thickness is the adjacent side to the right-angled triangle.

The results for the other samples are in column 7:

TBM-6: $\mathrm{Cos}\,\theta = \frac{x}{h} \rightarrow x = h\cos\theta \rightarrow y = 142.19\cos 10 \rightarrow y = 143{,}5$

TBM-8: $\mathrm{Cos}\,\theta = \frac{x}{h} \rightarrow x = h\cos\theta \rightarrow y = 145.72\cos 10 \rightarrow y = 140$

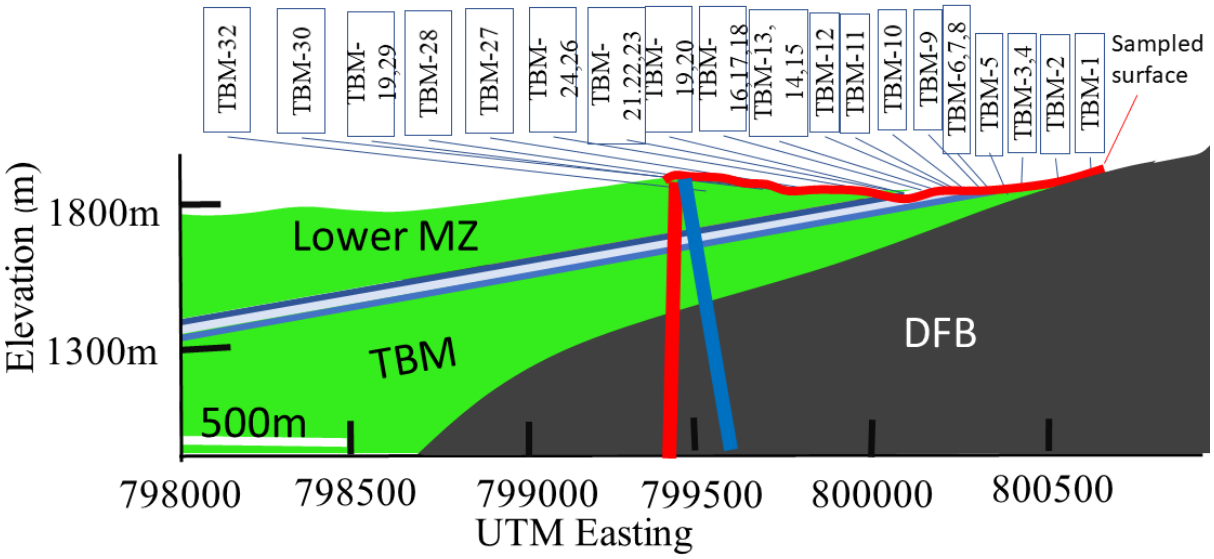

Fig. 2. 2. The cross-section along the sample traverse. It also shows the locations of where the samples were collected and their sample numbers.

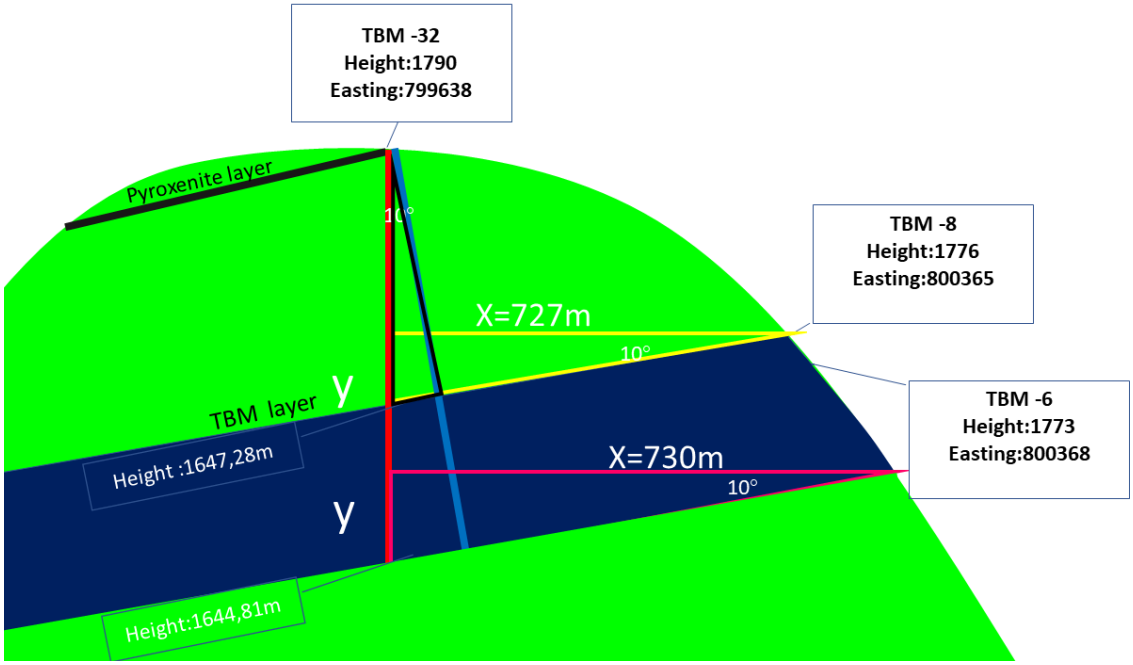

Fig. 2. 3. The simplified cross-section (Not drawn to scale) of the sampled area shows only the first TBM layer location, which occurs between the TBM-6 and TBM 8. It also shows the pyroxenite layer, which is the highest sampled layer. The vertical red line shows the column used to calculate the apparent depth, and the blue line was used to calculate the true depth of the layer

$$\tan\theta = \frac{y}{h} \qquad\qquad h = y\tan(10°)$$

Table 2. 1. Column 1 shows the samples' names, column 2 shows the UTM easting coordinate of where the pieces are collected, and column 3 shows the sampled points' topographical height. The samples' extrapolated height at the Easting of 799638 (location of the TBM-32) is calculated using a bit of trigonometry.

	UTM Easting	Height	The horizontal distance from TBM-32	Vertical change to TBM-32	Depth of layer at TBM-32	Vertical height from TBM-32	True distance from
TBM-1	800441	1770	803	141,6	1628,4	161,6	159,1
TBM-2	800421	1770	783	138,1	1631,9	158,1	155,7
TBM-3	800410	1770	772	136,1	1633,9	156,1	153,8
TBM-4	800410	1771	772	136,1	1634,9	155,1	152,8
TBM-5	800375	1772	737	130,0	1642,0	148,0	145,7
TBM-6m	800368	1773	730	128,7	1644,3	145,7	143,5
TBM-8m	800365	1776	727	128,2	1647,8	142,2	140,0
TBM-7b-1	800363	1774	725	127,8	1646,2	143,8	141,7
TBM-7b-2	800363	1774	725	127,8	1646,2	143,8	141,7
TBM-7m	800363	1774	725	127,8	1646,2	143,8	141,7
TBM-9	800341	1778	703	124,0	1654,0	136,0	133,9
TBM-10	800290	1780	652	115,0	1665,0	125,0	123,1
TBM-11	800247	1776	609	107,4	1668,6	121,4	119,5
TBM-12	800195	1776	557	98,2	1677,8	112,2	110,5
TBM-14	800165	1772	527	92,9	1679,1	110,9	109,2
TBM-13	800164	1772	526	92,7	1679,3	110,7	109,1
TBM-16	800121	1773	483	85,2	1687,8	102,2	100,6
TBM-17	800121	1773	483	85,2	1687,8	102,2	100,6
TBM-18	800102	1781	464	81,8	1699,2	90,8	89,4
TBM-19	800068	1782	430	75,8	1706,2	83,8	82,5
TBM-21	800026	1786	388	68,4	1717,6	72,4	71,3
TBM-20b	800023	1783	385	67,9	1715,1	74,9	73,7
TBM-20m	800023	1783	385	67,9	1715,1	74,9	73,7
TBM-22	800017	1786	379	66,8	1719,2	70,8	69,8
TBM-23	800016	1786	378	66,7	1719,3	70,7	69,6
TBM-24b	800005	1787	367	64,7	1722,3	67,7	66,7
TBM-24m	800005	1787	367	64,7	1722,3	67,7	66,7

TBM-25	799984	1788	346	61,0	1727,0	63,0	62,1
TBM-26	799916	1788	278	49,0	1739,0	51,0	50,2
TBM-27	799844	1776	206	36,3	1739,7	50,3	49,6
TBM-28	799770	1763	132	23,3	1739,7	50,3	49,5
TBM-29	799699	1769	61	10,8	1758,2	31,8	31,3
TBM-30	799638	1763	0	0,0	1763,0	27,0	26,6
TBM-31b	800007	1787	369	65,1	1721,9	68,1	67,0
TBM-31m	800007	1787	369	65,1	1721,9	68,1	67,0
TBM-32	799638	1790	0	0,0	1790,0	0,0	0,0
TBM-33	800072	1790	434	76,5	1713,5	76,5	75,4

2.3. Petrography and thin section preparation

Polished thin sections for petrography were prepared at the Thin Section Preparation Labs, School of Geosciences, University of the Witwatersrand, South Africa. The petrographic features were studied under the transmitted light microscopy at the Petrographic Lab, School of Geosciences, University of the Witwatersrand, South Africa. These microphotographs were captured with the Microscopy and Microanalysis Unit (MMU) Olympus BX 63, University of the Witwatersrand, South Africa.

2.4. Lithogeochemistry

The representative samples were sliced into 3cm by 3cm blocks and sent to Intertek for major, trace, and rare earth elements (REE) analysis. The modal abundances of the minerals in each sample were calculated using the CIPW norm from the whole rock major oxide data.

2.5. Mineral composition by scanning XRF and EPMA

2.5.1. Scanning XRF

Two TBM samples with the spherical orthopyroxenite and the gabbronorite matrix were polished and analyzed for Ca, Si, Al, Cr, and Fe variations.

2.5.2. EPMA

The mineral chemistry of plagioclase and orthopyroxene were analyzed with the Electron Probe Microanalyzer (EPMA) (SX5-FE) at the Microscopy and Microanalysis Unit (MMU) at the University of the Witwatersrand, Johannesburg, South Africa. The analyses are performed under conditions of 15 kV voltage and a current of 10 nA for all the minerals. A total of 50 crystals were analyzed from each thin section, and a standard was measured after analyzing four thin sections. The anorthite content of Plagioclase is calculated with the formula An= (Ca/(Ca+Na+K) *100 and the Mg#= (Mg/(Mg+Fe)) *100. The results of these analyses are given in Appendix 5.

2.6. Whole-rock Rb-Sr, Sm-Nd, and Lu-Hf ratio isotope

The whole-rock Rb-Sr, Sm-Nd, and Lu-Hf isotopic systematics analyses were carried out at the University of the Witwatersrand and the University of Johannesburg. These analyses were conducted on seven representative samples of spherical orthopyroxenite-matrix pairs from three TBM layers and one MZ.

2.6.1. Samples preparations

The samples were crushed into a fine powder, and 220-300mg was measured out of each sample. They later then mixed with 100-150 mg of spikes and added with concentrated $HF - HNO_3$. The solution was placed on a heated plate at 100℃. The summary of the measurements is given in Table 2.

Table 2. 2. The summary of the sample weight and spikes added for Sr (Strontium), Nd (neodymium), and Hf (Hafnium)

Sample ID	sample weight mg	Sr spike mg	Nd spike mg	Hf spike mg
TBM-7b	299,84	120,79	156,68	57,18
TBM-7m	220,48	346,22	276,05	80,21
TBM-blank	10	blank	blank	blank
TBM-20b	250,13	126,05	179,17	70,54
TBM-20m	249,8	334,781	324,65	93,82
TBM-24b	249,28	133,79	242,25	102,81

TBM-24m	249,99	332,28	270	70,38
TBM-32	300,36	152,99	260,5	81,71

2.6.2. Rb-Sr isotope

The samples were added and rinsed by adding 1ml 1.5M HCl three times. The matrix was collected by adding 4ml of 1.5M HCl. The Rb collection was done by adding 4ml of 1.5M HCl. This was followed by rinsing with 10ml of 1.5M HCl before collecting Sr. The Sr was collected by adding 15ml of 1.5M HCl, and the LREEs were collected by adding 7ml 6M HCl. The present-day $(^{87}Sr/^{86}Sr)_p$ was measured by the mass spectrometry-multicollection at the University of Johannesburg, Johannesburg, South Africa. The $(^{87}Rb/^{86}Sr)_p$ was calculated from the Rb/Sr weight ratio. Sr_i were calculated using decay constants of $1.42x10^{-11}$ for the age of 2060 (Dickin, 2005).

2.6.3. Sm-Nd isotope

The raisins were calibrated by adding 2ml M HCl three times before adding the LREE samples. The samples were added and rinsed with 0.4 ml of 0.2M HCl three times. The Nd was collected by adding 10ml of 0.2 M HCl, and this was followed by adding 3ml to discard. The Sm was collected by adding 6ml of 0.2M HCl. The present isotopic ratios were analyzed by the MC-ICPMS, located at the University of Johannesburg. The initial $^{143}Nd/^{144}Nd$ values were calculated using the present day $^{147}Sm/^{144}Nd$ and $^{143}Nd/^{144}Nd$ ratios, the $\lambda^{176}Sm$ decay constant of $6.54x^{-12}$ from Lungmair and Mart (1978). The initial εNd (εNd(2060)) values were calculated using $^{147}Sm/^{144}Nd$ (CHUR)= 0.1967 from Jacobsen and Wasserburg (1980) and $^{143}Nd/^{144}Nd$ (CHUR)=0.512638 from Hamilton *et al*. (1983).

2.6.4. Hf-Lu isotope

The present $^{176}Hf/^{177}Hf$ and $^{176}Lu/^{177}Hf$ was measured and calculated at the MC-ICPMS facility located at the University of Johannesburg. The initial $^{176}Hf/^{177}Hf$ ratios were calculated using the present $-$ day $^{176}Hf/^{177}Hf$ and $^{176}Lu/^{177}Hf$ ratios, the $\lambda^{176}Lu$ decay constant value of $1.865x10^{-11}year^{-1}$ from Scherer *et al*., (2001). The initial (2060) values were calculated using $^{176}Hf/^{177}Hf$ (CHUR)=0.282772 and$^{176}Lu/^{177}Hf$ (CHUR)=0.0332 from Blichert-Toft and Albarede (1997).

2.7. PGE point analysis and sulfides imaging

PGMs associated with the TBM were searched and studied by reflected light microscopy, and polished thin sections were examined by reflected light and analyzed by EPMA. The sulfides' images were captured under reflected light using the Olympus BX-63, and they were scanned for PGE (= Os, Ir, Ru, Rh, Pt, and Pd) to produce chemical maps. The chemical maps of PGE were analyzed using CAMECA EPMA at the MMU facility, University of the Witwatersrand, South Africa. Analytical conditions for quantitative analyses were 20 kV accelerating voltage, 20 nA probe current, and a beam diameter of 1 μm. Pure metals are standards for PGE, Ni, and Cu, arsenopyrite for As, and pyrite for Fe.

Chapter 3: Regional Geology

3.1. Bushveld Igneous Complex (BIC)

The Paleoproterozoic Bushveld Igneous Complex (BIC), in South Africa, is a large igneous province composed of a variety of igneous rocks starting with a layered mafic-ultramafic suite at the base, overlain by younger acidic and granitic suites at the top (Hammerbeck, 1970; Molyneux and Klinkert, 1978). These suites are known as (from the base to top) the RLS, the Rashoop Granophyre Suite, and the Lebowa Granite Suite (Fig. 1.1). The Bushveld Igneous Complex rests above the Transvaal Supergroup and the Rooiberg felsite overlies it. This study is at the Tondeldoos town on a farm called the Middelkraal farm. This farm has good exposure of the MZ and the TBM. Hence, it was the perfect location for the study of TBM.

2.1.1 The Rustenburg Layered Suite

The RLS is the world's largest, known layered mafic-ultramafic intrusion on earth. It encompasses a volume of ~500 000 km3, an area of 60 000-65 000 km2, and a total thickness of 7-9 km (Eales and Cawthorn, 1996; Latypov *et al*., 2017). It hosts world-class Platinum Group Elements (PGEs) deposits that are known as the Merensky Reef, the UG-2 chromitite layer, and the Platreef (Button, 1976; Eales and Costin, 2012; Hall, 1932; Hunter, 1976; Latypov *et al*., 2017; Wagner and Brown, 1968). The RLS magmas ascended to the upper continental crust and intruded into the TS, which now forms the RLS floor rocks (Eales and Cawthorn, 1996; Cawthorn and Walraven, 1998).

The RLS magmas ascended to the upper continental crust and intruded into the TS, which now forms the RLS floor rocks (Eales and Cawthorn, 1996; Cawthorn and Walraven, 1998). They were emplaced as multiple, horizontal sheets that are now preserved as a layered sill-like body that outcrops on the surface as four lobes known as the Eastern, Western, Northern, and the far Western Lobes (Letts *et al*., 2009; Kruger, 1994;

The Eastern Lobe

Marginal Zone (MrZ)

The MrZ occurs as the skin of the RLS (Fig. 3.2). It is sub-divided into two fundamental groups known as the pyroxenite group (B1) and gabbroic group (B2 and B3) (Harmer and Sharpe, 1985; Fig. 3.2). The B1 group occurs at the contact between the TS with the LZ and Lower CZ (Fig. 3.2). It consists of pyroxenites, peridotite, and norite. The gabbroic group is further sub-divided into two sub-groups known as the B2 and B3 subgroups (Fig. 3.2). The B2 sub-group occurs at the contact between the TS and Upper CZ, and it is composed of gabbronorite. The B3 group appears at the connection between the TS and MZ, and it consists of a three-pyroxene gabbro (B3) (Harmer and Sharpe, 1985).

Lower Zone (LZ)

The LZ is the first layered zone of the RLS (Fig. 3.2). It occurs at the base of the RLS and outcrops at the north of the Steelpoort fault. It is the most primitive RLS zone and comprises ultramafic rocks sub-divided into four subzones known as (from base to top) subzone A, B, C, and D (Cameron, 1980; Fig. 3.2). Subzone A comprises feldspathic pyroxenites. Subzone B and D are composed of monotonous orthopyroxenite. Subzone C is composed of cyclic units of dunite, harzburgite, and orthopyroxenite (Cameron, 1978).

It has a mineral assemblage made up of cumulus orthopyroxene with an enstatite content (En) that increases variably between En_{75-86} throughout the zone and cumulus olivine that only occurs at subzone C with forsterite content Fo_{85-87} (Cawthorn and Walraven, 1997; Fig. 1.2). The whole rock initial strontium ratio (Sr_i) of this zone ranges between 0.7050- 0.7075 (Kruger, 1994; Fig. 3.2).

Critical Zone (CZ)

The CZ overlays the LZ and transgresses to the TS towards the south (Fig. 3.2). It is subdivided into the Lower CZ and Upper CZ based on cumulus plagioclase's appearance on the Upper CZ (Cameron, 1980; Eales and Cawthorn, 1996). The Lower CZ has layers of orthopyroxenite, chromitite, and minor harzburgite. The Upper CZ has cyclic units of chromitite, pyroxenite, norite, and anorthosite (Cawthorn and Walraven, 1998; Cameron, 1980; Cawthorn, 1996). The uppermost cyclic units are known as the

Merensky cyclic unit and the Bastard cyclic unit. The Bastard cyclic unit ends with a 50 m thick anorthosite layer known as the Giant Mottled Anorthosite (GMA), which marks the CZ's end (Van Merwe, 2007; Vermaak, 1976; Fig. 1.2).

The rocks in this zone are comprised of a mineral assemblage made up of cumulus orthopyroxene with En_{79-86} and chromite that occurs throughout (Fig. 1.2). They are joined by cumulus olivine with Fo_{81-77} and plagioclase with an anorthite content (An) of An_{87-80} at the Upper CZ (Cawthorn and Walraven, 1998; Fig.1.2). The Lower CZ has a whole rock Sr_i of 0.7055, and it abruptly increases to 0.7065 at the Upper CZ (Kruger, 1994; Fig. 1.2).

Main Zone (MZ)

The MZ overlies the CZ at the north and the TS at the south (Fig. 3.1). It is marked by cumulus clinopyroxene's appearance in the stratigraphy (Von Gruenewaldt, 1973; Fig. 3.2). It is also characterized by the absence of cumulus chromite and olivine. It is sub-divided into three subzones known as (from base to top), subzone A, B, and C. The subdivision bases on the inter-substitution of orthopyroxene and inverted pigeonite (Von Gruenewaldt, 1973).

Subzone A is composed of norite and gabbronorite that interlayers a few pyroxenites, and it hosts the Tennis Ball Marker (TBM) at the base (Fig. 1.2). Subzone B is composed of gabbroic rocks with inverted pigeonite replacing orthopyroxene. Subzone C is similar to Subzone A, and it is composed of gabbronorite with orthopyroxene (Von Gruenewaldt, 1973). The boundary between subzone B and subzone C has a thick pyroxenite layer known as the Pyroxenite Marker (Von Gruenewaldt, 1973).

It is comprised of cumulus plagioclase with An_{85-55}, cumulus orthopyroxenes at subzone A and B with En_{75-60} and cumulus clinopyroxene (Von Gruenewaldt, 1973; Cawthorn and Walraven, 1997; Fig. 1.2). The whole rock Sr_i of the MZ increases variably at the base from 0.7650 to 0.7086 and becomes constant with Sr_i of 0.7086 upwards in stratigraphy (Kruger, 1994; Fig. 1.2).

Upper Zone (UZ)

The UZ overlies the MZ, and it is sub-divided into subzone A, B, and C.Subzone A is composed of two-pyroxene magnetite gabbros. Subzone B comprises similar rocks with olivine bearing cumulates at the base. Subzone C consists of cumulus olivine (and apatite) (Von Gruenewaldt, 1973). The zone is characterized by the occurrence of cumulus magnetite and magnetite layers. The rocks on this zone have a mineral assemblage made up of cumulus olivine withFo_{43-5}, plagioclase with An_{40-7} and orthopyroxenite with En_{60-30} (Cawthorn and Walraven, 1997). The UZ possesses a constant whole-rock Sr_i of 0.7076 (Kruger, 1994; Fig. 3.2).

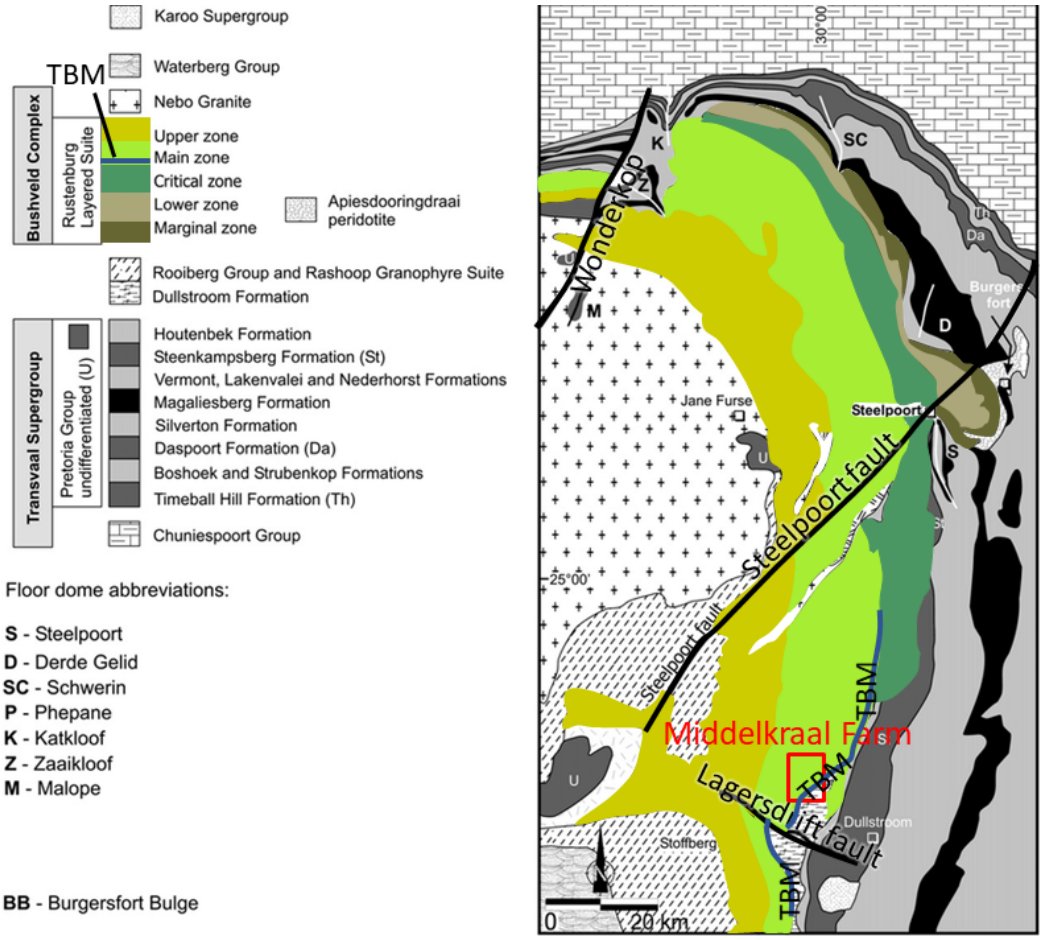

Fig. 3. 1. The Eastern Lobe's geological map shows the LZ and CZ's disappearance and the transgressing MZ towards the south. It also shows the LZ and CZ towards the south approximate locations of the Tennis Ball Marker (Modified after Lee and Sharpe, 1979; Van De Merwe, 2003). The red square indicates the approximate location of the Middelkraal farm.

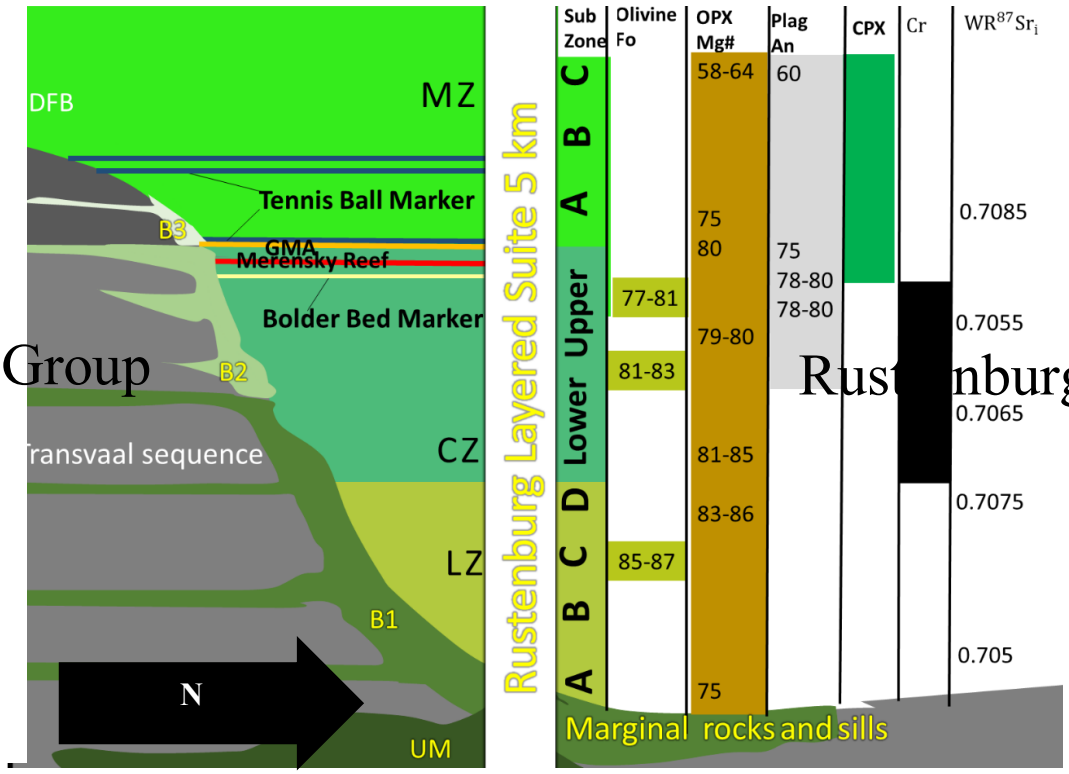

Pretoria Group Rust nburg Layered S

Fig. 3. 2. The cross-section of the contact between the Transvaal Supergroup and the RLS in the south of the Eastern Lobe. It shows its stratigraphic subdivision known as MrZ, LZ, CZ, and MZ, with the Tennis Ball Marker's stratigraphic positions (TBM). The shaded areas on the right show the cumulus phases present in each zone or subzone and their mineral compositions. Fo-Forsterite, En-Enstatite, An-Anorthite content for cumulus olivine, orthopyroxene, and plagioclase, respectively. The last row shows the whole-rock initial Sr ratio for each zone. the

Chapter 4: The geology of the Tennis Ball Marker at the Middelkraal farm

The Middelkraal farm hosts the southern parts of the Eastern Lobe (Fig. 2.1). In this area, the MZ directly contacts the DFB and their contact curves in the NNE direction (Fig. 4.1a). The TBM occurs at 2m above the DFB. It is extensive for more than 2.5 km and strikes in the NNE direction. It outcrops as two shallow dippings (0-10° west) layers that abut into the DFB at the southern contact (Fig. 4.1b). The stratigraphy consists of eight layers named as (from base to the top): DFB, Contact gabbronorite, Lower TBM, spherical orthopyroxenite poor gabbronorite, Upper TBM 1, sandwiched gabbronorite, Upper TBM 2, and the Normal gabbronorite (Fig. 4.1).

4.1. The Dullstroom Formation Basalts

The DFB is the oldest layer at the Middelkraal farm, and it belongs to the TS (Fig. 4.1c). It is composed of basalt that outcrops on the east and the south of the farm (Fig. 4.1a). It is generally fine-grained, grey, and occasionally has voids that could be a primary feature or devolatilization vesicles (Fig. 4.2).

4.2. The Contact gabbronorite

The Contact gabbronorite unconformably overlies the DFB (Fig. 4.1). It is 5-10 m thick and shows an increase in grain size from the base to the top (Fig. 4.3a). The gabbronorite closer to the DFB is grey and fine-grained (Fig.4.3a). It occasionally hosts thin pyroxene-rich stringers parallel to the general layering of the MZ (Fig. 4.3b). The grain size increase upwards to a medium-grained texture that is occasionally pegmatitic (Fig. 4.3c; Fig. 4.3d). The Contact gabbronorite also has roots that percolate into the DFB (Fig. 4.3c)

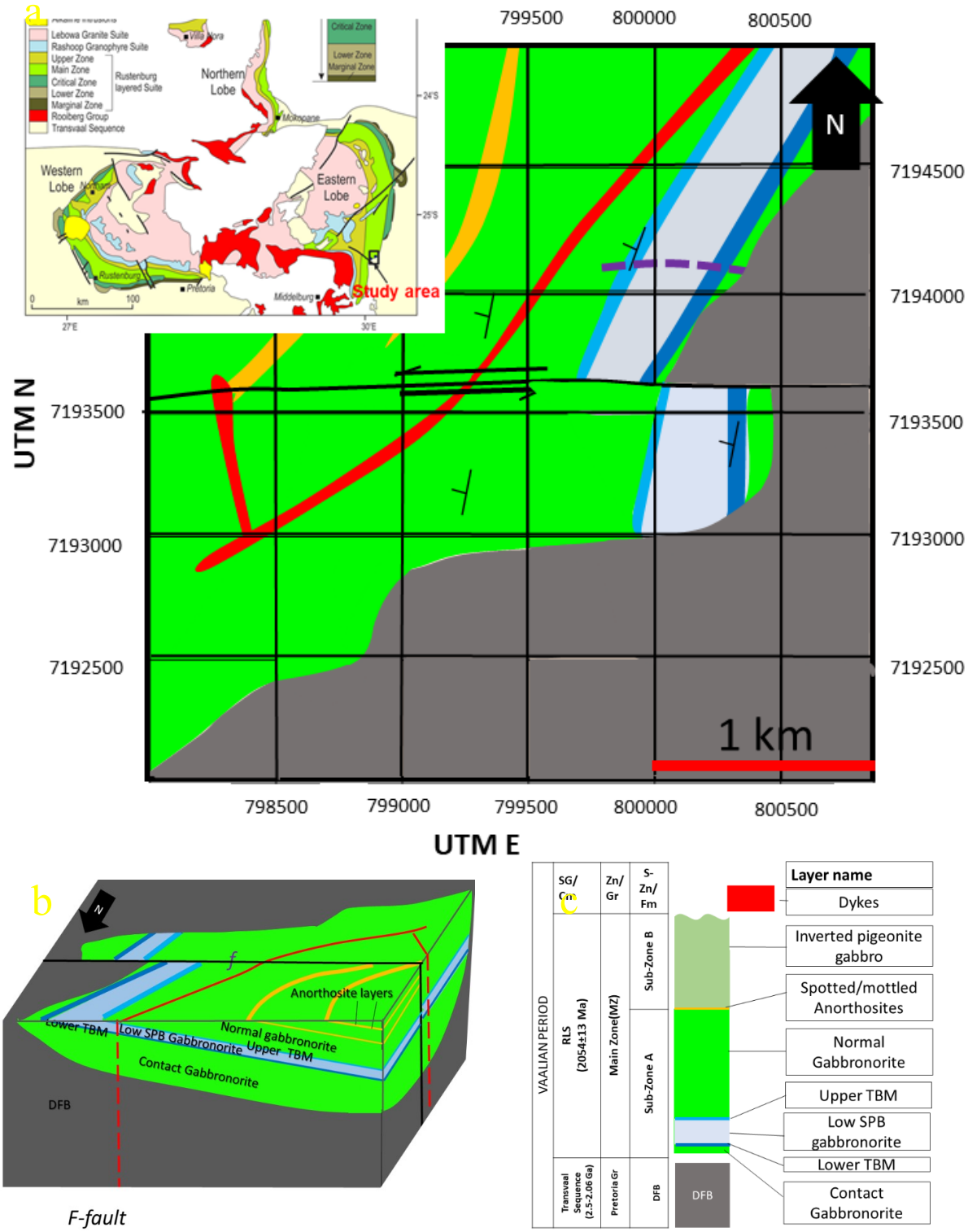

Fig. 4. 1. (a) The geological map of the Middelkraal Farm showing (from base to top): DFB (grey), Contact gabbronorite (green), Lower TBM (dark blue), spherical orthopyroxenite poor gabbronorite (light blue), Upper TBM (medium shaded blue), Normal gabbronorite (green), Spotted/mottled anorthosite (yellow), and dykes (red). (b) The 3-D schematic diagram showing the relationship between the TBM layers, MZ gabbronorite, and the DFB. (c) The stratigraphic column of the rocks hosted by the Middelkraal farm.

Fig. 4. 2. Field photograph of basalt from the DFB showing the circular voids.

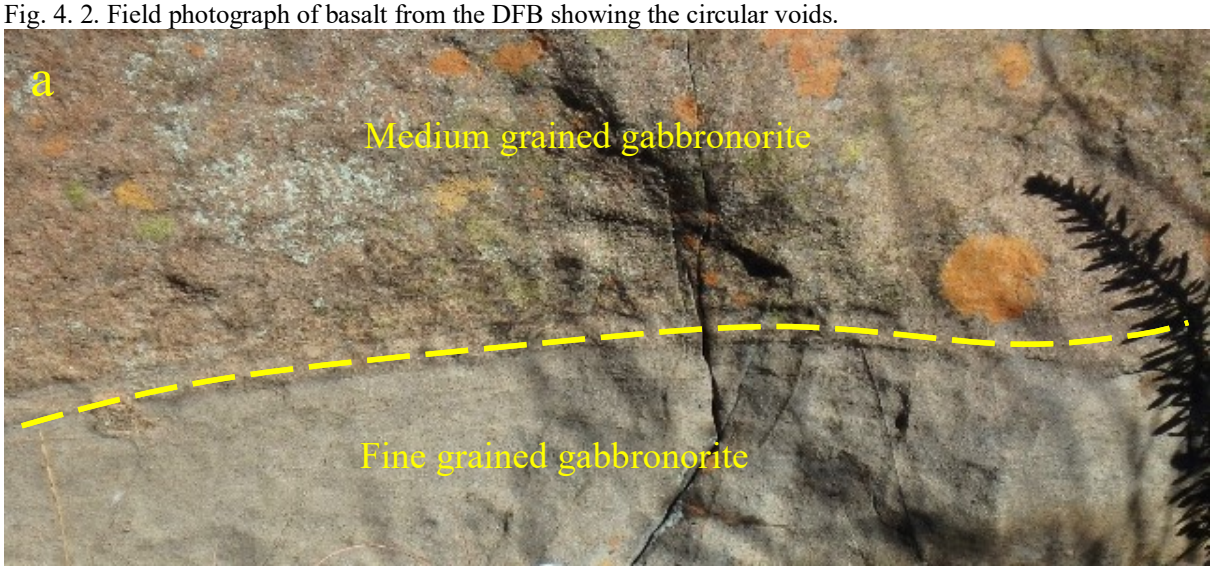

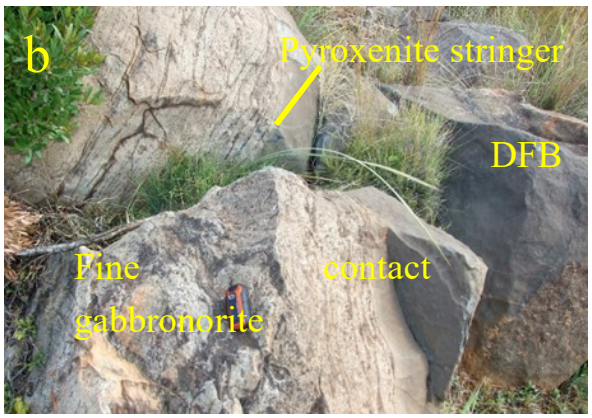

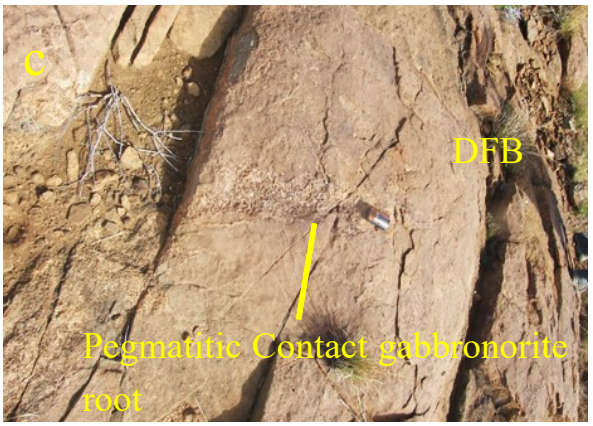

Fig. 4. 3. Field photographs of the Contact gabbronorite. (a) The increase in the grain size of the Contact gabbronorite. (b) The sharp and straight contact between the DFB and the fine-grained Contact gabbronorite with thin pyroxenite stringers. (c) The pegmatitic Contact gabbronorite rooting into the DFB. (d) The Contact gabbronorite layer consisting of a mixture of medium-grained and pegmatitic texture.

4.3. Lower TBM

The Lower TBM starts at the appearance of 5-10% of spherical orthopyroxenite, and their concentration increases to 40-50% towards the top. This layer has a thickness that varies unevenly between 0.2 m to 5 m (Fig.4.4). The spherical orthopyroxenite is also disseminated at the base and closely packed towards the top (Fig. 4.4).

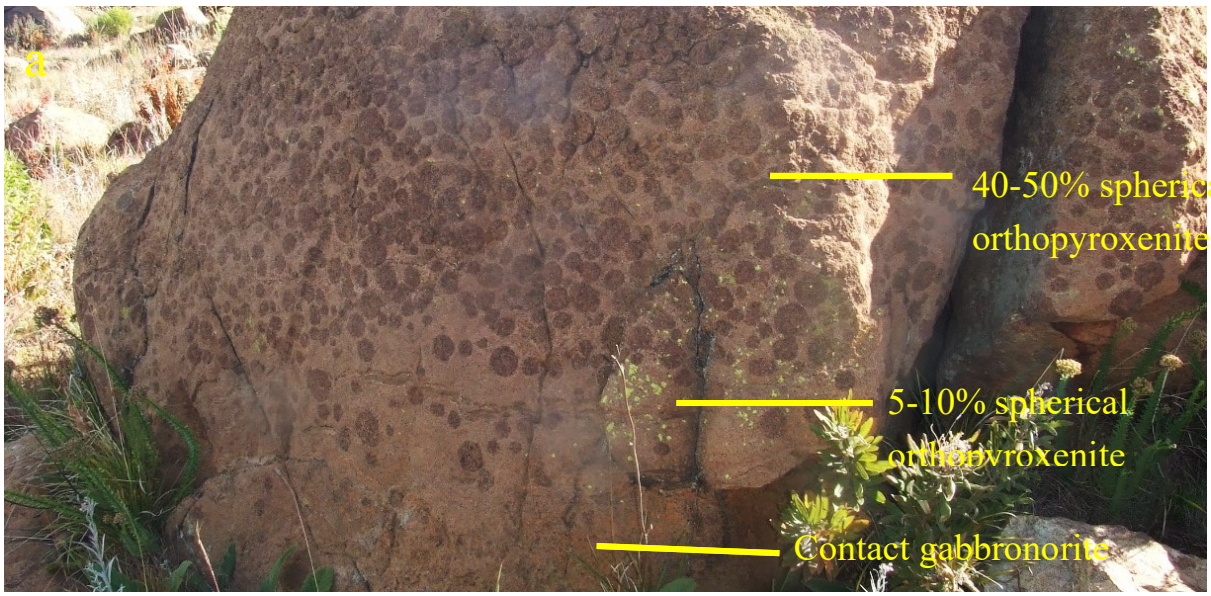

Fig. 4. 4. Field photographs of the Lower TBM. (a) The 2 m thick Lower TBM, with a gradational lower contact with the Contact gabbronorite. (b) The 25 cm thick Lower TBM layer shows the gradational lower connection with the Contact gabbronorite. The sharp upper contact with the spherical orthopyroxenite poor gabbronorite.

4.4. Spherical orthopyroxenite poor gabbronorite

The Lower TBM is truncated by a spherical orthopyroxenite poor gabbronorite, with a thickness of 62 m (Fig. 4.5). It is petrographically similar to the Contact gabbronorite and hosts less than 5% spherical orthopyroxenite (Fig. 4.5). It has pegmatitic pockets with sizes that range from a few millimeters to tens of centimeters (Fig. 4.5d). These pockets are composed of plagioclase, amphiboles, quartz, and minor biotite (4.5c). The amphiboles have a dendritic texture that occasionally radiates from the pockets' walls (Fig. 4.5d).

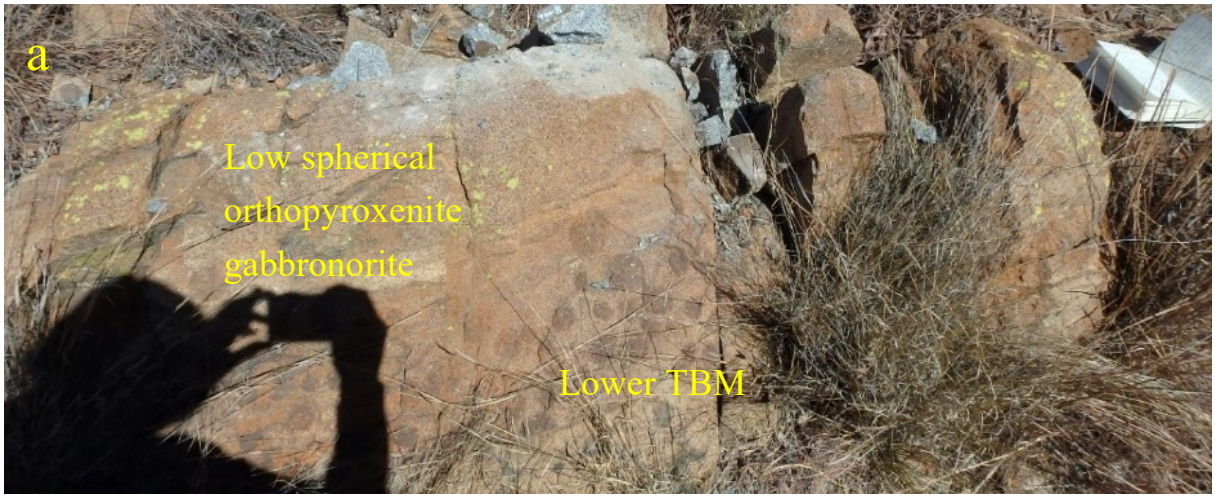

Fig. 4. 5. Field photographs of the spherical orthopyroxenite poor gabbronorite. (a) The upper contact between the Lower TBM and the spherical orthopyroxenite poor gabbronorite. (b) The dispersed spherical orthopyroxenite in a matrix of gabbronorite. (c) The large pocket of the pegmatitic gabbronorite.

4.5. Upper TBM

The Upper TBM overlies the spherical orthopyroxenite poor gabbronorite. It comprises two TBM sub-layers named the Upper TBM 1 and the Upper TBM 2 (Fig. 4.6). These two sub-layers are separated by the sandwiched gabbronorite, with a thin layer of mottled anorthosite matrix (Fig. 4.6b). The Upper TBM 1 starts at the abrupt appearance of 30-40% of densely packed spherical orthopyroxenite (Fig. 4.6a). The concentration of the spherical orthopyroxenite decreases to 1-10% spherical orthopyroxenite

upwards, which marks the beginning of the sandwiched gabbronorite matrix (Fig. 4.6b). The Upper TBM 2 has a gradual increase of spherical orthopyroxenite to a 30-40% up section (Fig. 4.6b). This layer ends with a horizontal and abrupt disappearance of spherical orthopyroxenite (Fig. 4.6b).

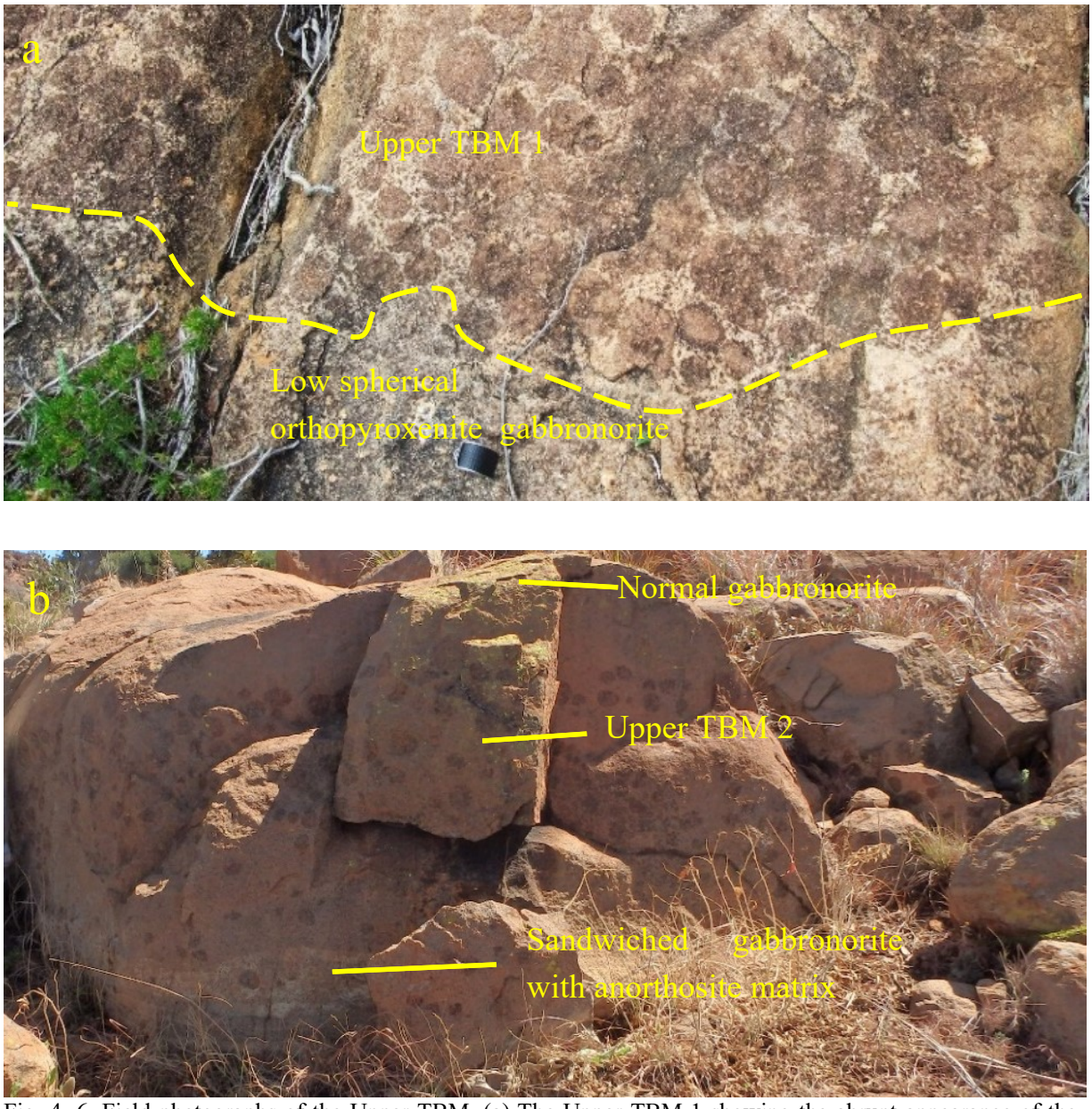

Fig. 4. 6. Field photographs of the Upper TBM. (a) The Upper TBM 1 showing the abrupt appearance of the spherical orthopyroxenite, forming a sharp and almost straight lower contact. (b) The sandwiched gabbronorite with a thin mottled anorthosite matrix encasing 1-10% of spherical orthopyroxenite. This image also shows the gradual increase in the concentrations of spherical orthopyroxenite up section to the Upper TBM 2.

4.6. Normal Gabbronorite and mottled anorthosite

The disappearance of spherical orthopyroxenite marks the beginning of the Normal gabbronorite (Fig. 4.6b). The Normal gabbronorite is massive, with a medium-grained texture (Fig. 4.7). It is interlayered with a few anorthosite layers that are concordant with the MZ layering (Fig. 4.1; Fig. 4.7b). It also hosts pyroxenite layers that are 5-25 cm thick. These pyroxenite layers have sharp lower contact and a gradational upper contact (Fig. 4.8).

Fig. 4. 7. (a) Field photographs of the Normal gabbronorite layer. (b) The contact between the Normal gabbronorite and the mottled anorthosite layers.

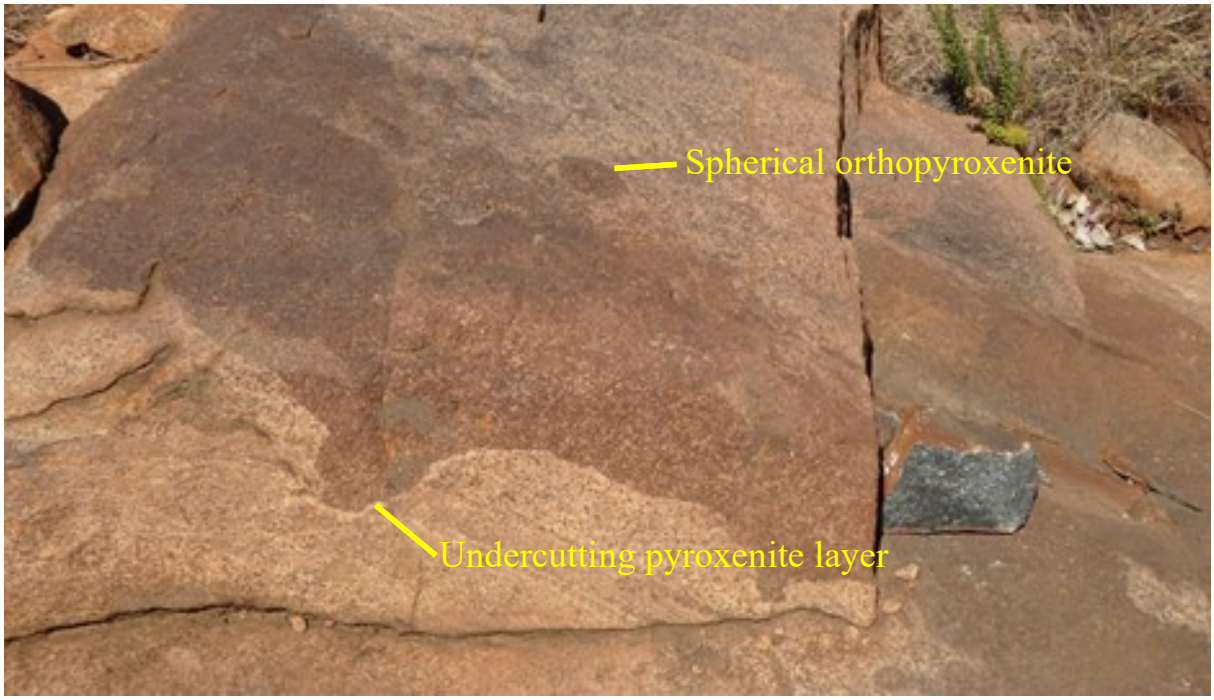

Fig. 4. 8. Field photograph of a Pyroxenite layer with a sharp and straight lower contact and a grading upper contact

4.7. Mafic and felsic dykes

There are two main dykes cutting through the TBM package (Fig. 4.1). The northeast-trending dyke is mafic and has a very fine-grained texture (Fig. 4.9a). It has sharp and straight contacts with the neighboring rocks, with a 2 cm chill margin (Fig. 4.9a). The northwest-trending dyke is relatively more leucocratic and hosts enclaves of the gabbronorite and fragments of mafic dykes (Fig. 4.9b).

Fig. 4. 9. (a) Field photographs of the mafic dyke with a sharp and straight contact. (b) Field photographs of the west-east trending dyke with a sub-surrounded enclave of the mafic dykes.

Chapter 5: Field observations at the Middelkraal farm

5.1. Shapes of the orthopyroxenite at the TBM

The TBM is dominantly composed of perfect spherical orthopyroxenite (Fig. 1.2; Fig. 5.1). Hence, many geologists who have visited this marker assume it entirely consists of perfect spherical pyroxenite. In this study, other cohabiting shapes such as semi-circular, lath-like, rectangular, and oval are documented (Fig. 5.1; Fig. 5.2; Fig. 5.3). Additionally, all these orthopyroxenite have the same mineral assemblage and texture (Fig. 5.1; Fig. 5.2; Fig. 5.3).

5.1.1. The spherical orthopyroxenite

The spherical orthopyroxenite is the most dominant form at the TBM (Fig. 1.2). Hence, it tends to camouflage the other existing shapes, and they are all encased in a matrix of normal or pegmatitic gabbronorite (Fig. 5.1). The pegmatitic gabbronorite occasionally forms a radial texture around the spherical orthopyroxenite. This texture has amphibole crystals that radiate out of the spherical orthopyroxenite (Fig. 5.1).

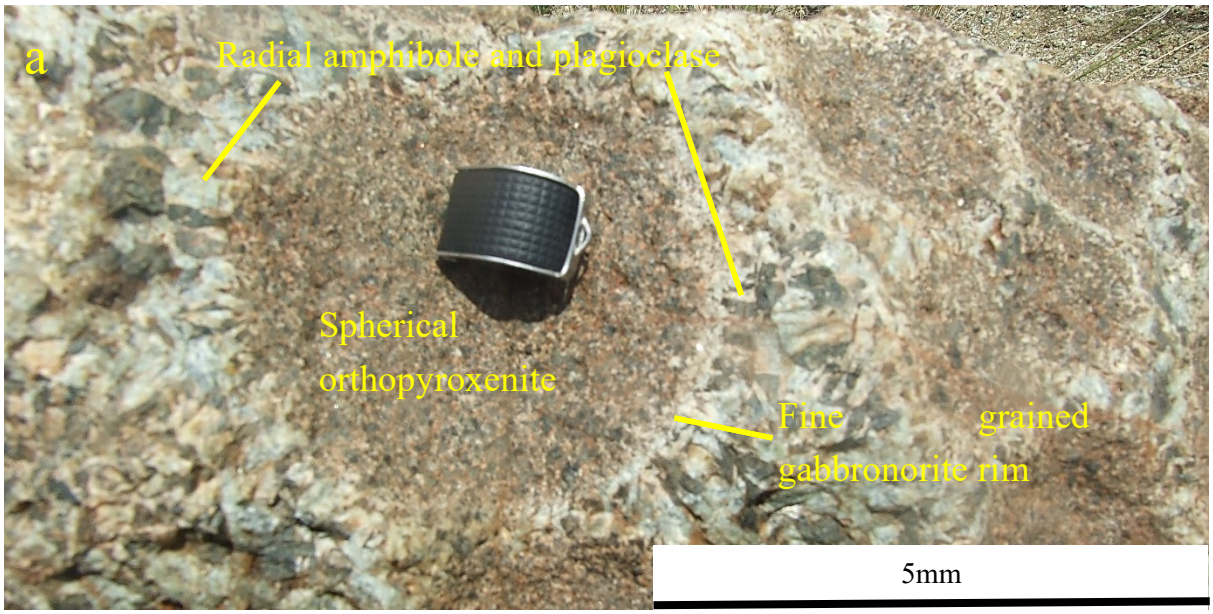

Fig. 5. 1. Field photographs of the perfectly spherical orthopyroxenite at the Lower TBM. (a) Perfectly spherical orthopyroxenite in a pegmatitic matrix, with radial amphiboles around it. (b) Perfect spherical orthopyroxenite in a matrix of a fine to medium-grained gabbronorite.

5.1.2. Small semi-circular, arch-shaped, and rectangular pyroxenites bodies

The semi-circular and lath-like orthopyroxenite are petrographically like the spherical orthopyroxenite (Fig. 5.2). These are generally smaller than the spherical orthopyroxenite, but their cord length and length, respectively, are equal to the diameters of some spherical orthopyroxenite (Fig. 5.2c). These shapes are common in the northern parts of the Upper TBM.

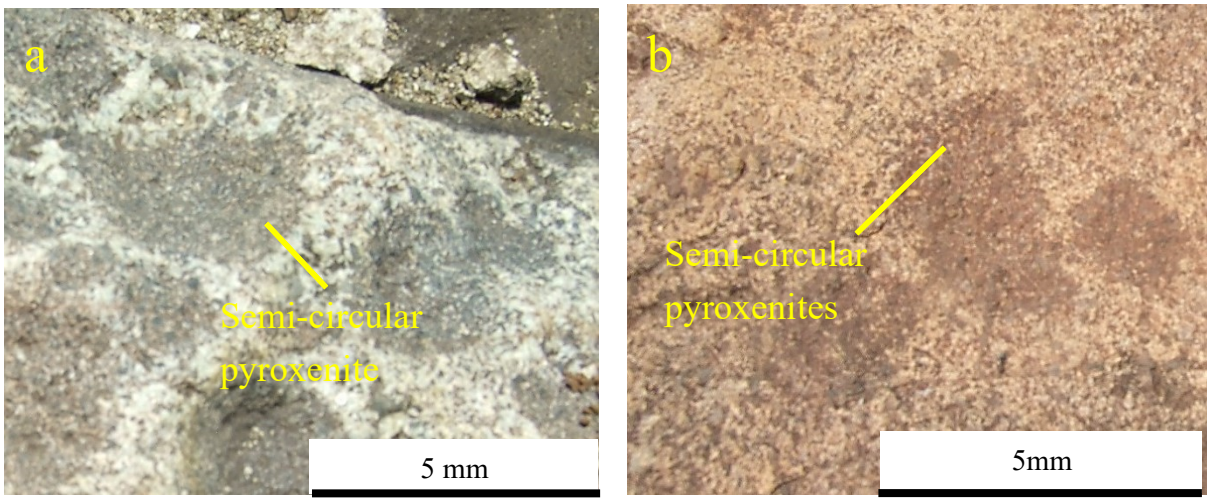

Fig. 5. 2. Field photographs of other shapes possessed by the orthopyroxenite. (a) Semi-circular orthopyroxenite pyroxenite in a matrix of medium-grained gabbronorite. (b) Semi-circular pyroxenite in a matrix of medium-grained gabbronorite. (c) A lath and arch orthopyroxenite coexisting with spherical orthopyroxenite.

5.1.3. Larger angular, sub-rounded, and oval-shaped pyroxenite bodies

The TBM also possesses shapes that are larger than the spherical orthopyroxenite (Fig. 5.3). These shapes range from rectangles with angular edges and straight sides (Fig. 5.3a); rectangles or diamonds with curvy edges and straight sides (Fig. 5.3b; Fig. 5.3c); ovals and boulder-like shapes with undulating margins (Fig. 5.3e; Fig. 5.3f).

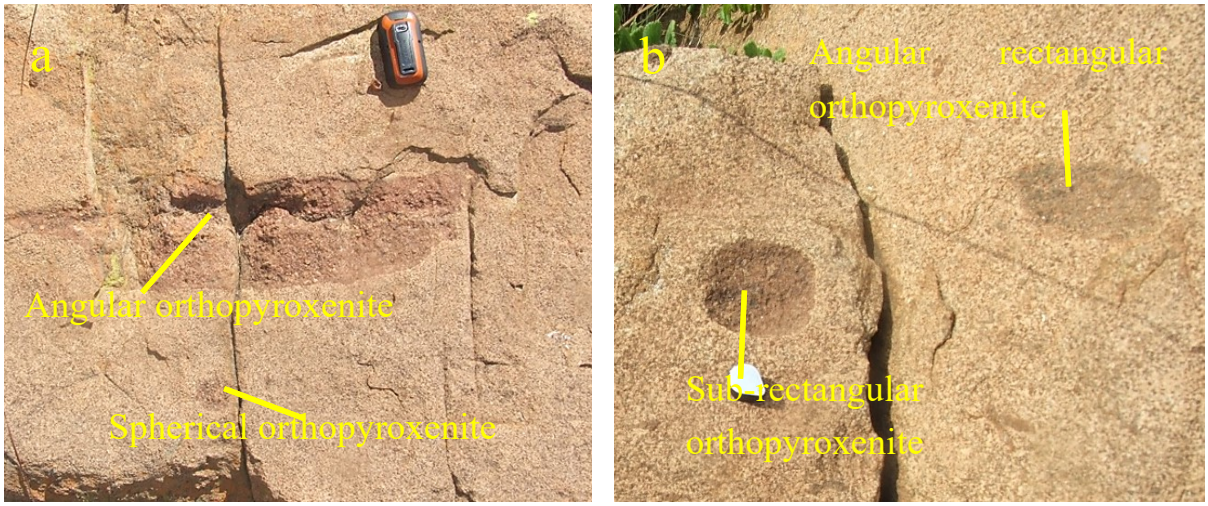

Fig. 5. 3. Field photographs of pyroxenite shapes. (a) Rectangular orthopyroxenite spherical orthopyroxenite (b) Curved-rectangular orthopyroxenite body with curved edges. (c) Curved diamond-shaped orthopyroxenite with curved edges (d) Oval orthopyroxenite encased with two perfect spherical orthopyroxenite in a matrix of gabbronorite. (e-f) Spherical orthopyroxenite with undulating margins.

5.2. Spherical orthopyroxenite chains and bands

The spherical orthopyroxenite forms sub-parallel chains parallel to the layering of the MZ (Fig. 5.4). These chains cluster to form a band with a high concentration of spherical orthopyroxenite (Fig. 5.4). The TBM layers also exhibit a layering characterized by bands with a high concentration of spherical orthopyroxenite interlayered with bands with a low concentration of spherical orthopyroxenite (Fig. 5.5).

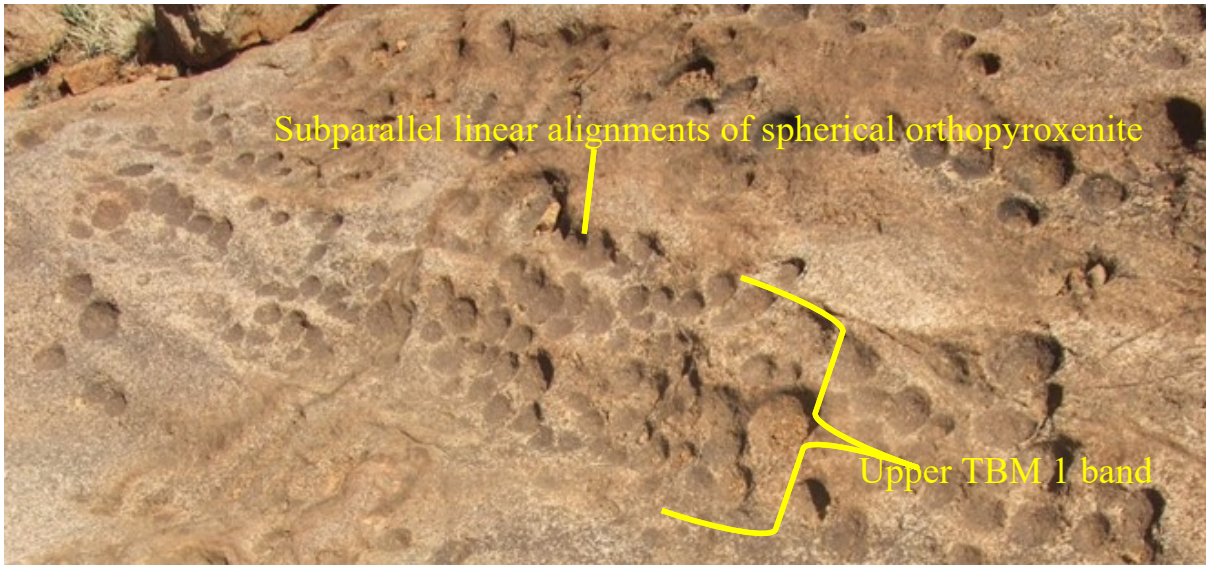

Fig. 5. 4. Field photograph of the UTBM 1 showing spherical orthopyroxenite linear arrays that are subparallel to one another.

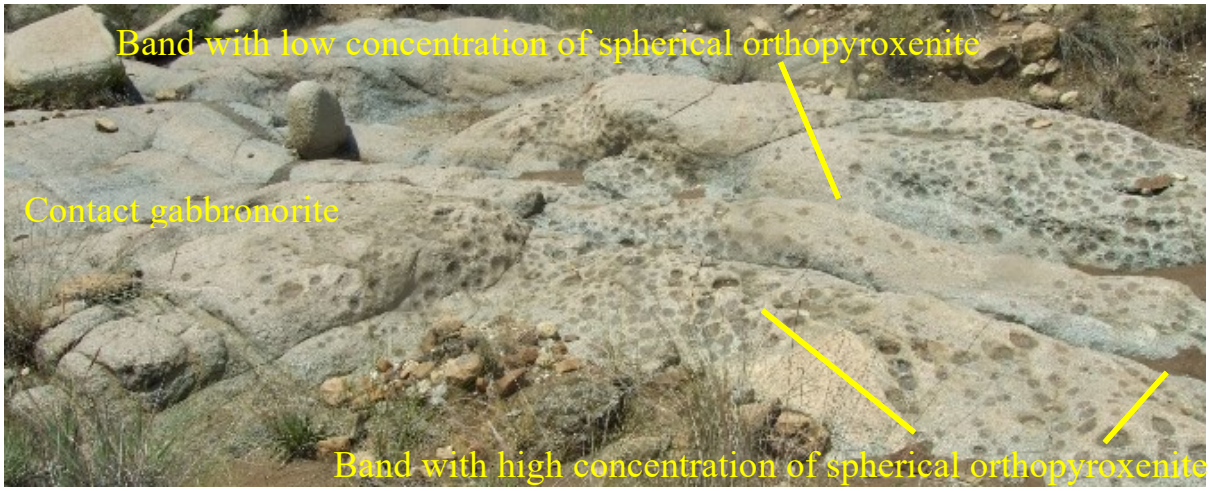

Fig. 5. 5. Field photograph of the UTBM 1 showing spherical orthopyroxenite linear arrays that are subparallel to one another.

5.3. Lateral termination of TBM bands along strike

The bands with a high concentration of spherical orthopyroxenite tend to thin or terminate towards the south along strike (Fig. 5.6a). The Lower TBM occasionally decreases the concentration of spherical orthopyroxenite from 40% to 0% towards the south (Fig. 5.6a). These type of terminations is also characterized by the occurrence of a group of spherical orthopyroxenite clustering in gabbronorite (Fig. 5.6b).

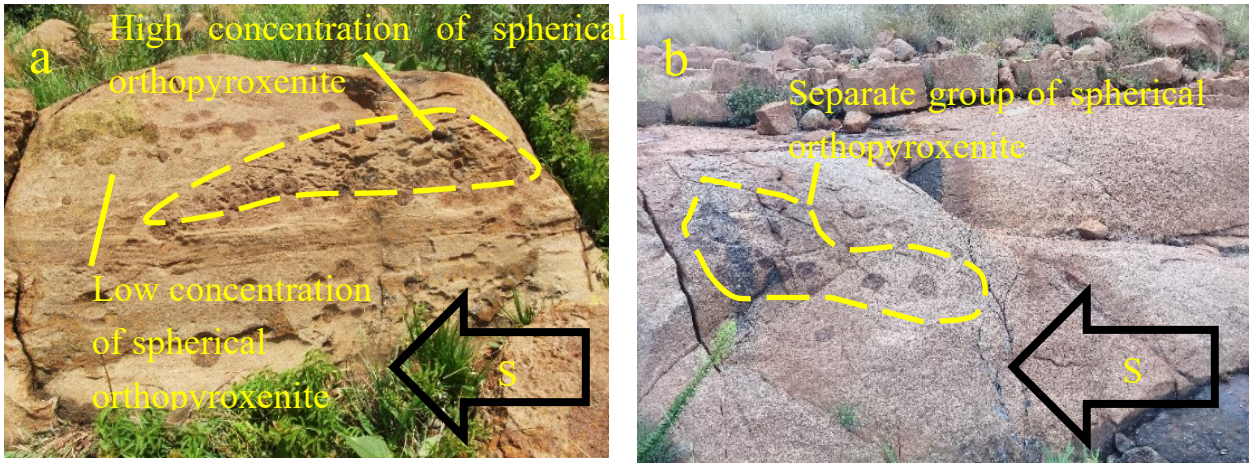

Fig. 5. 6. (a) A TBM band thinning towards the south. (b) A small cluster of spherical orthopyroxenite encased in a massive gabbronorite matrix.

5.4. Sorting of the spherical orthopyroxenite

The sizes of the spherical orthopyroxenite are sorted differently in the Lower TBM and the Upper TBM. The Lower TBM layer shows an increase in size from 1 cm at the base to 4 cm at the top (Fig. 5.7). Conversely, the Upper TBM layer shows a decreased size, starting with 4cm at the bottom to 1cm at the top (Fig. 5.7b).

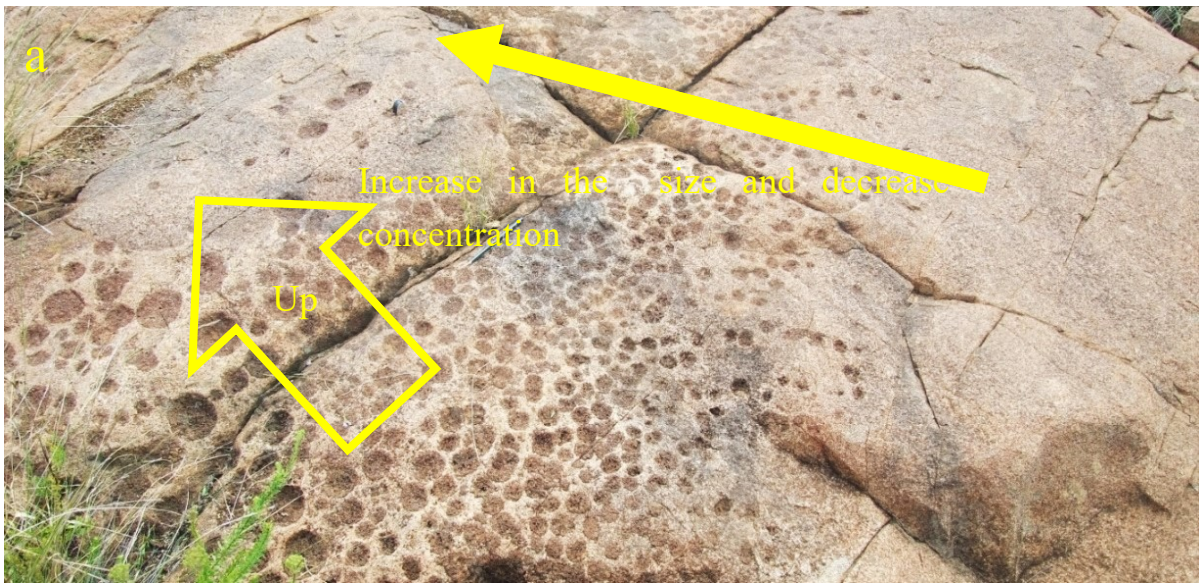

Fig. 5. 7. (a) Field photograph of the Lower TBM shows an increase in the spherical orthopyroxenite sizes from the base to the top. (b) A field photograph of the Upper TBM shows decreased spherical orthopyroxenite sizes from the bottom to the top.

5.6. Sub-spherical anorthosites

The spherical orthopyroxenite occasionally coexists with xenoliths of anorthosites that possess various shapes ranging from sub-rounded to angular. The subrounded anorthosites can either be mutually connected (Fig. 5.8a and Fig. 5.8b) or separated by a gabbronorite (Fig. 5.8c). In other areas, the anorthosite bodies have a rectangular shape with straight sides with angular corners (Fig.5.8d).

Fig. 5. 8. Field photographs of the anorthosite bodies in the Low spherical orthopyroxenite gabbronorite. (a) and (b). The sub-rounded anorthosite bodies at mutual contact with one another. (c) The sub-rounded anorthosite bodies at encased and separated by a medium-grained gabbronorite. (d) The rectangular anorthosite bodies in a medium-grained gabbronorite.

5.7. Bulging layers

5.7.1. Bulging graded gabbronorite and anorthosite rims

The orthopyroxenite occasionally bulge or curves their underlying matrix (Fig. 5.9). In cases where it is encased by a graded gabbronorite, the matrix beneath bulges or curves around it (Fig. 5.9). In some cases, the overlaying top drapes into the oval orthopyroxenite (Fig. 5.9).

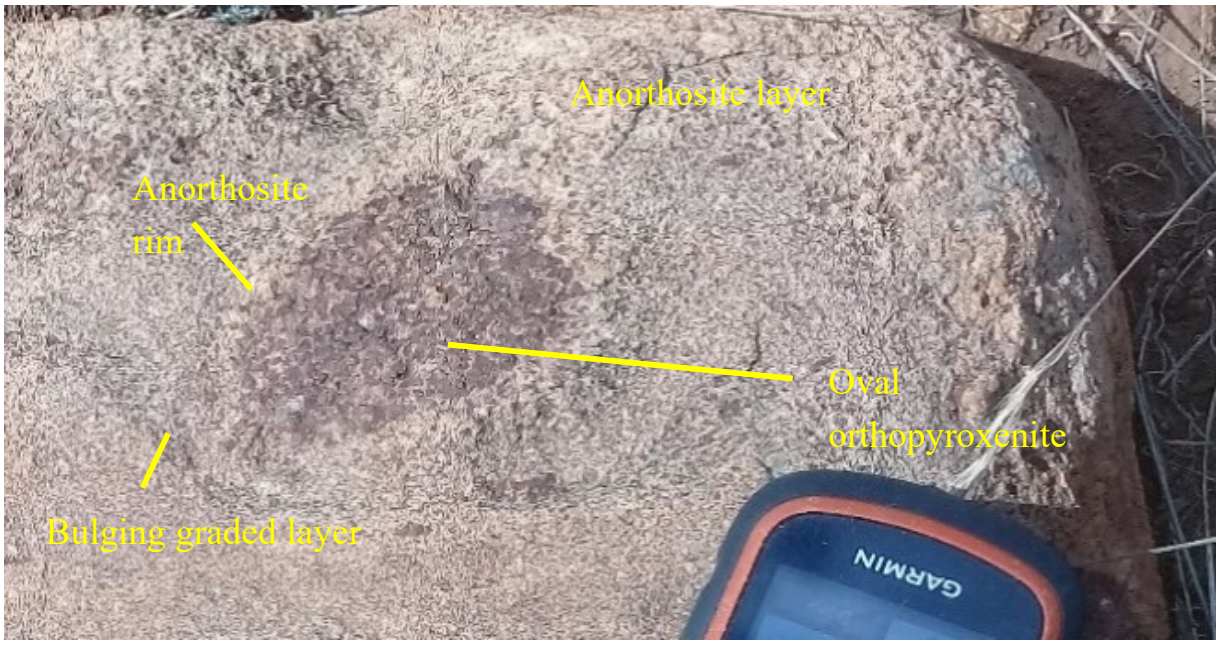

Fig. 5. 9. Field photograph of anorthosite rim around the oval orthopyroxenite, which is encased in a gabbronorite.

5.7.2. Graded gabbronorite matrix across spherical orthopyroxenite

Some of the grading bands at the base of the spherical orthopyroxenite and terminates within their vicinity (Fig. 5.10). This is demonstrated at the spherical orthopyroxenite poor gabbronorite, which shows a 10cm thick pyroxene rich band overlain by a graded gabbronorite band (Fig. 5.10). The graded bar hosts three spherical orthopyroxenite at the base, and it is characterized by impoverishing of Plagioclase up-section (Fig. 5.10). It has a thickness that is half the diameter of the spherical orthopyroxenite (Fig. 5.10). Additionally, some of the orthopyroxenite have a Plagioclase enriched top (Fig. 5.10). The contact between the pyroxene-rich band and the graded gabbronorite band is generally sharp and straight and bulges beneath the spherical orthopyroxenite (Fig. 5.10).

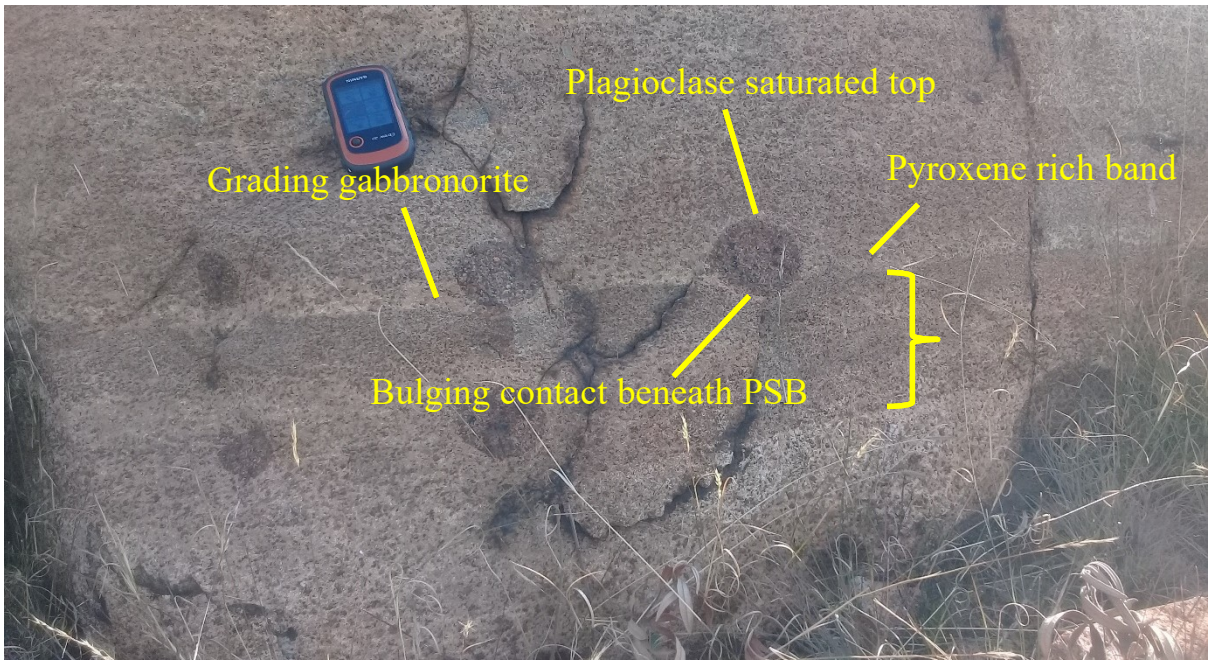

Fig. 5. 10. Field photograph of the spherical orthopyroxenite poor gabbronorite showing the pyroxene rich band overlain by a gabbronorite grading band with spherical orthopyroxenite. It also shows the bulging of these contacts beneath the spherical orthopyroxenite.

5.7.3. Bulging mafic schlieren and grading bands around the spherical orthopyroxenite

In some areas, the mafic bands form schlieren bands composed of pyroxenes, amphiboles, quartz, and minor biotite (Fig. 5.11). These layers are extensive for a few meters along strike, and they are straight in areas with no spherical orthopyroxenite (Fig. 5.11). However, they curve downwards beneath them and bend upwards above the spherical orthopyroxenite (Fig. 5.11).

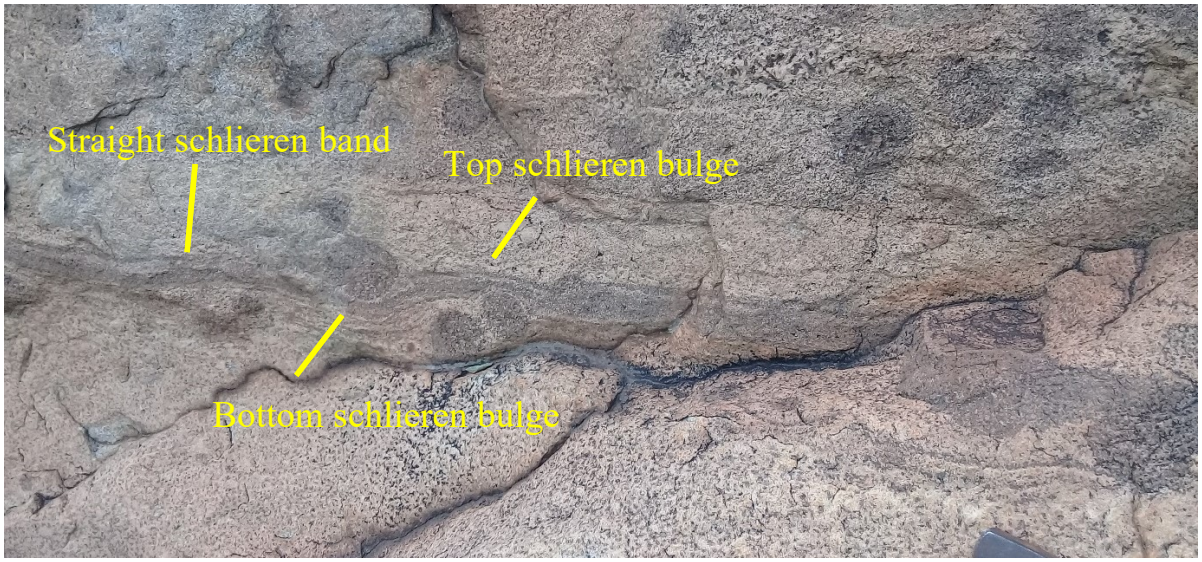

Fig. 5. 11. Field photograph of the pyroxene-rich horizons within the gabbronorite matrix, showing the bulging schlieren layer at the bottom and the top of the spherical orthopyroxenite.

Chapter 6: Petrography

6.1.1. The Dullstroom Formation Basalts

The Dullstroom Formation Basalt has a porphyritic texture. It has 1−5 modal% of plagioclase phenocrysts in a fine-grained groundmass (Fig. 6.1). It has a mineral assemblage of plagioclase (54 modal%), orthopyroxene (21 modal%), clinopyroxene (21 modal %), quartz (1 modal %), and minor biotite (Fig. 5.3). The phenocrysts have a crystal size that ranges between 2-3 mm, and the groundmass has crystal sizes below 200 μm (Fig. 6.1). The groundmass also has an annealing texture, with the pyroxenes and the plagioclase forming a 120º junction where they meet.

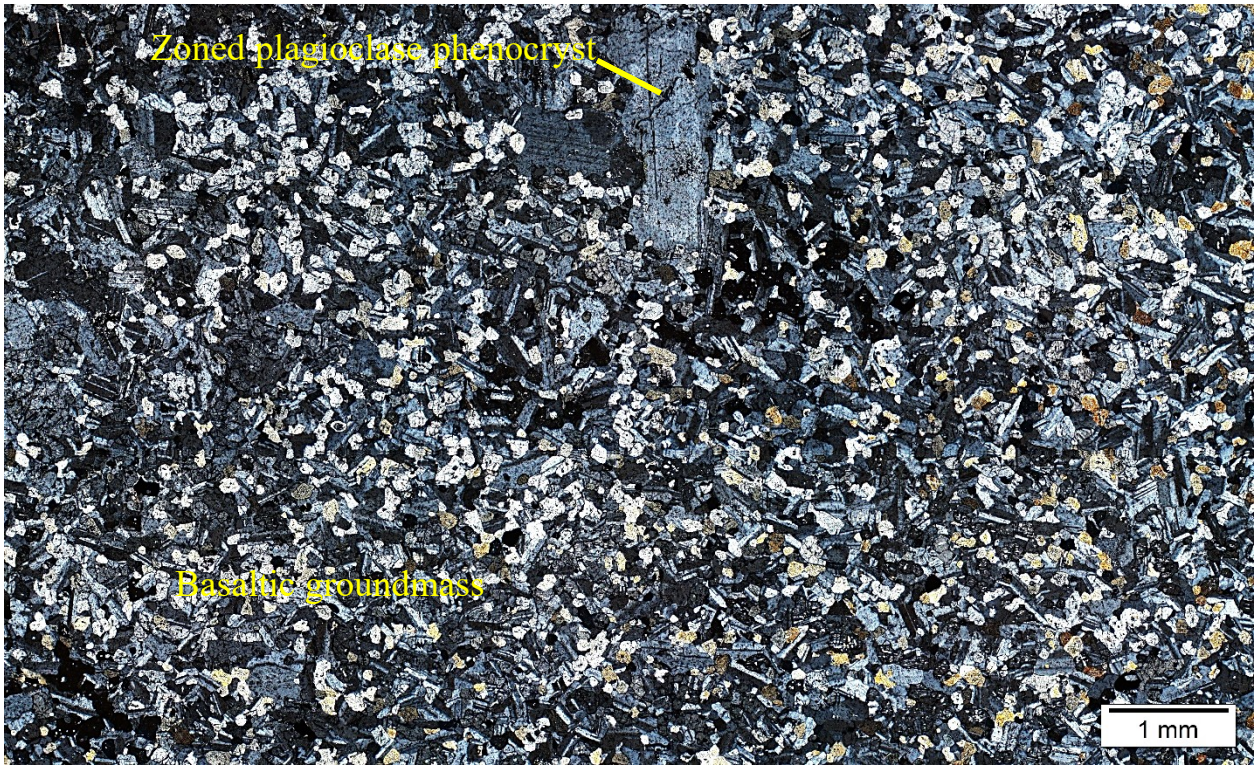

Fig. 6. 1.The photomicrograph of the DFB shows the porphyritic texture, with zoned plagioclase phenocrysts surrounded by a basaltic groundmass.

6.1.2. Contact gabbronorite

The fine-grained gabbronorite at the Contact gabbronorite (Fig. 4.3a) has a spectacular ophitic texture (Fig. 6.2). Plagioclase chadacrysts (0.5−1mm) are subparallel, and larger pyroxene oikocrysts optically enclose them (2−4mm) (Fig. 6.2). They form a 2-D plagioclase chain that could also be continuous in

3-D (Fig. 6.2). This gabbronorite consists of plagioclase (52−54 modal%), orthopyroxene (19−24 modal%), clinopyroxene (17−20 modal%), quartz (1−-2 modal%), and minor biotite.

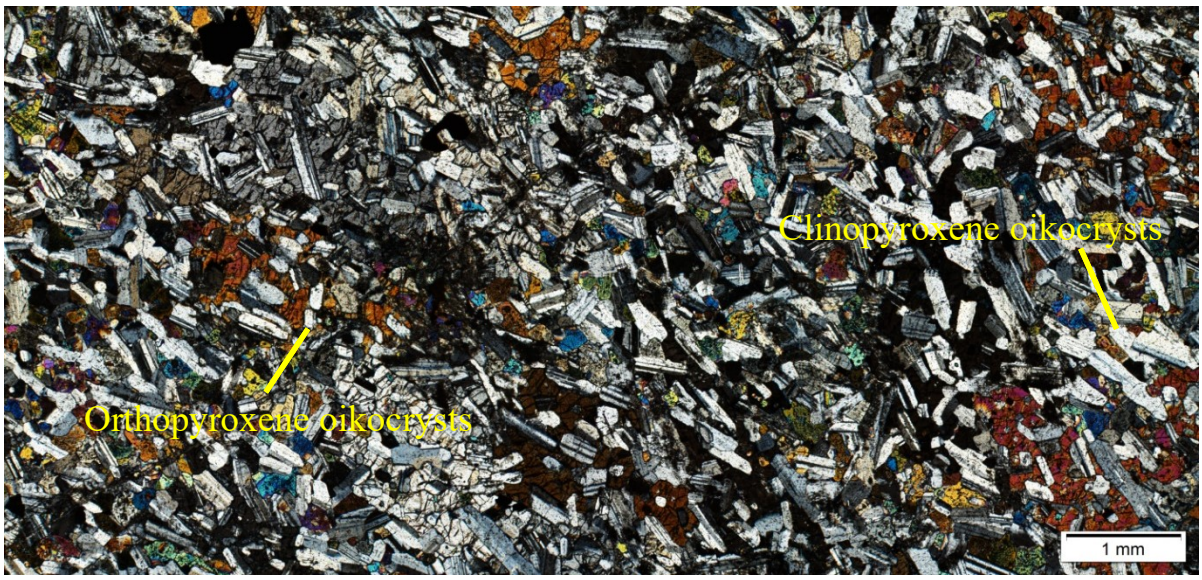

Fig. 6. 2.Microphotograph of the spectacular ophitic texture of the fine-grained Contact gabbronorite. It shows the plagioclase chadacrysts aligned subparallel. The orthopyroxene and clinopyroxene oikocryst optically encloses plagioclase chadacrysts.

6.1.3. Gabbronorite matrix and host

The gabbronorite matrix and host (Fig. 4.3a) have similar ophitic and intergranular textures (Fig. 6.3). The ophitic texture has plagioclase chadacrysts (100μm-1mm) that are ophitically enclosed by pyroxene oikocrysts (1-2 mm) (Fig. 6.3). The intergranular texture is constructed by plagioclase cumulates (1-3mm) that are subparallel (Fig. 6.3). The plagioclase crystals also form a 2-D plagioclase network chain that could also be continuous in 3-D (Fig. 6.3).

The gabbronorite also shows some unique features that only occur in some of the sections. The pyroxene crystals on the gabbronorite matrix with 5-10 % occur in two forms. (1) They occur as circular inclusions on the cumulus plagioclase and (2) intercumulus phases between the plagioclase crystals (Fig. 6.3). The gabbronorite at a few centimeters above the Lower TBM has small circular pyroxene inclusions in larger plagioclase and orthopyroxene crystals (Fig. 6.3e). At 17 m above the Upper TBM, the orthopyroxene is replaced by an inverted pigeonite marking the start of the Subzone B of the MZ (Fig. 6.3f). The inverted pigeonite occurs as an intercumulus phase in between plagioclase cumulates (Fig. 6.3f).

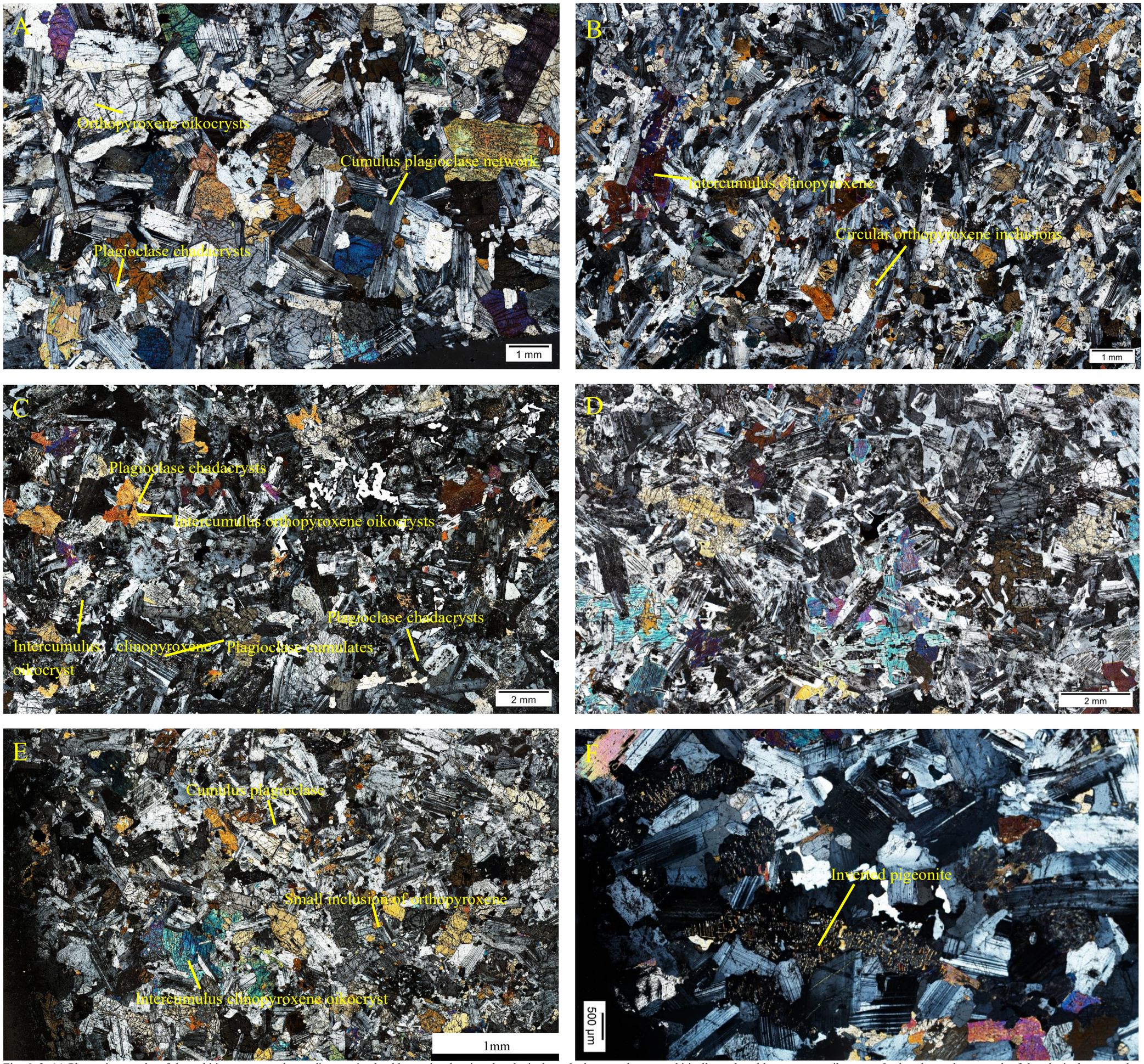

Fig. 6. 3. (a) Photomicrographs of the ophitic texture on the medium-grained gabbronorite showing the plagioclase chadacrysts that are ophitically enclosed by pyroxene oikocrysts. It also shows the network of the plagioclase cumulates between the pyroxenes. (b) Photomicrograph of the gabbronorite matrix with 5-10 modal% spherical orthopyroxenite at the lower TBM layer. It shows the sub-parallel plagioclase cumulates, with intercumulus orthopyroxene and clinopyroxene oikocrysts. It also shows the plagioclase chain made of plagioclase cumulates that are at mutual contact with one another. (c) Photomicrograph of the gabbronorite matrix encasing 40-50 modal% spherical orthopyroxenite, showing an ophitic and intergranular texture, with 1 mm plagioclase chadacrysts that are ophitically enclosed by pyroxene oikocryst. (d) Photomicrographs of the sandwiched gabbronorite. It shows the plagioclase chadacrysts ophitically enclosed in pyroxene oikocrysts. (e) The gabbronorite matrix in contact with the Lower TBM layer, showing an ophitic texture with thin plagioclase chadacrysts that are ophitically enclosed by orthopyroxene oikocryst. It also shows the small pyroxene inclusions in the cumulus plagioclase. (f) A microphotograph of the gabbronorite from the Normal gabbronorite shows the intercumulus inverted pigeonite grains between the plagioclase crystals.

6.1.4. The spherical orthopyroxenite

The spherical orthopyroxenite has an adcumulus texture. It has cumulus orthopyroxene (2−3 mm) and clinopyroxene at mutual contact (Fig. 6.4). It also has intercumulus plagioclase, quartz, biotite, and hornblende (Fig. 6.4a). Some orthopyroxene margins have talc alterations, and the degree of alterations varies from one crystal to the other (Fig. 6.4b). It has orthopyroxene (57-58 modal%), clinopyroxene (8-11 modal%), intercumulus Plagioclase (23-25 modal%), quartz (5 modal%), biotite, and hornblende.

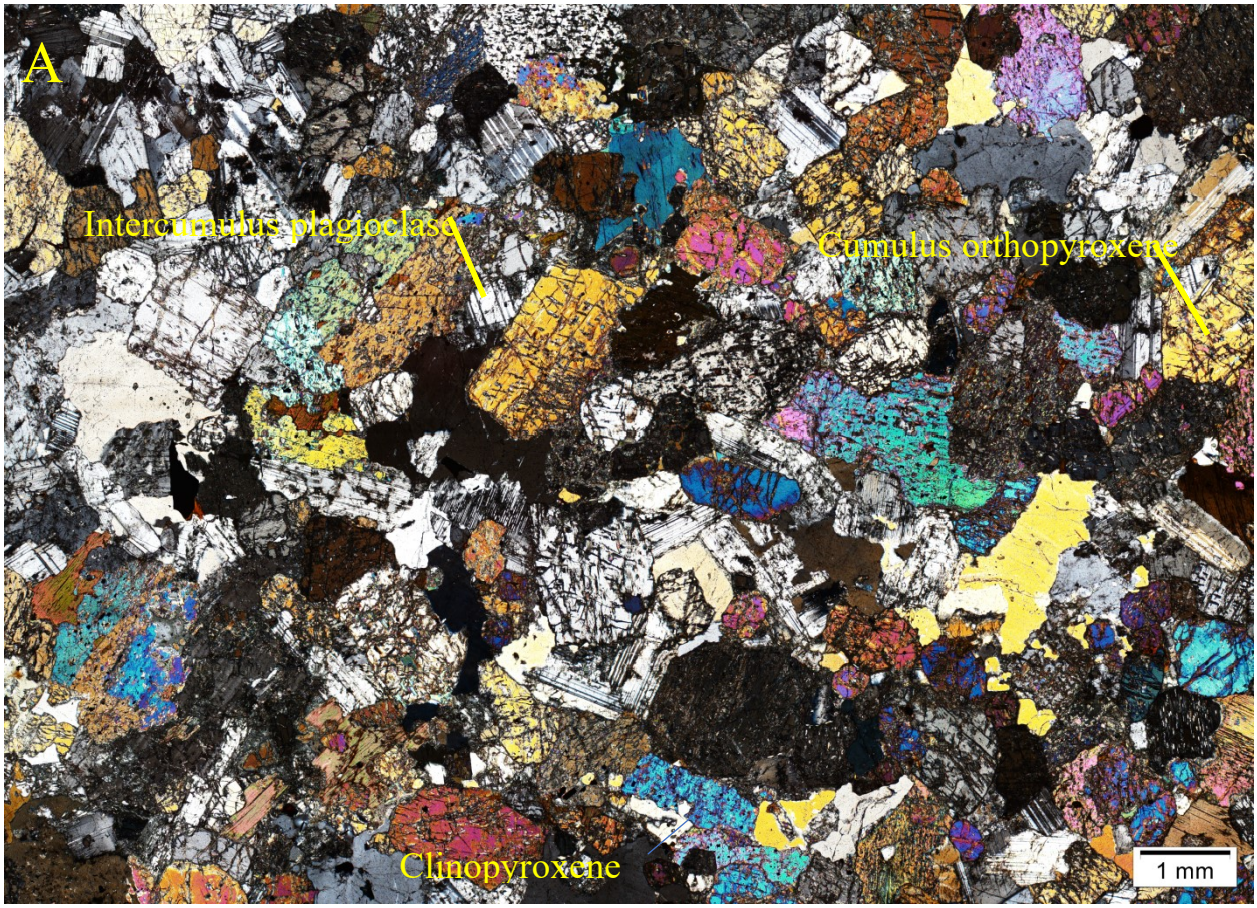

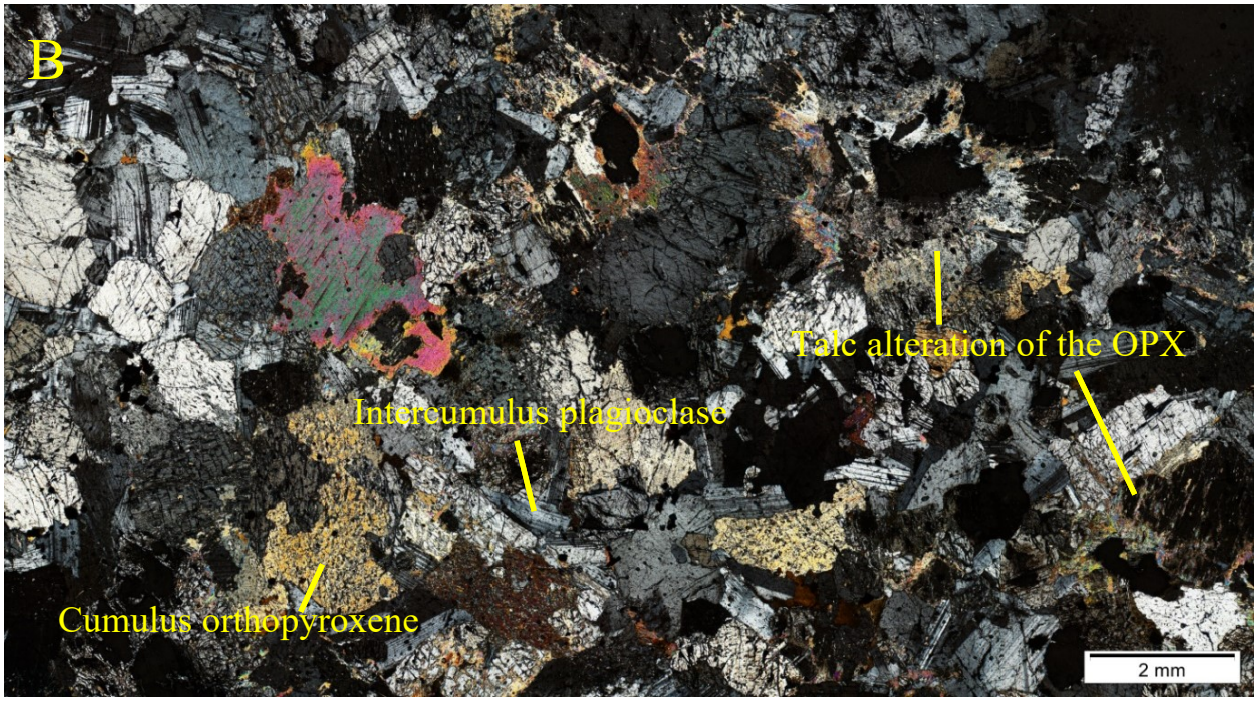

Fig. 6. 4. (a) Photomicrograph of the spherical orthopyroxenite occurring at the Upper TBM, with a mesocumulus texture. (b) Photomicrograph of the spherical orthopyroxenite at the Lower TBM. It shows an adcumulus texture with cumulus orthopyroxene and clinopyroxene. The intercumulus phases consist of plagioclase, quartz, biotite, and hornblende.

6.1.5. Anorthosite matrix

The anorthosite matrix has an ophitic and an intergranular texture (Fig. 6.5). The ophitic texture has plagioclase chadacrysts (1 mm) that are ophitically enclosed by clinopyroxene and orthopyroxene oikocrysts (2-3 mm) (Fig. 6.5). The altered cumulus plagioclase crystals from the intergranular texture with intercumulus pyroxene oikocrysts (Fig. 6.5). The cumulus plagioclase forms a 2-D Plagioclase network chain with crystals that are mutual. The plagioclase crystal has altered into a fine and opaque secondary mineral (Fig. 6.5). The pyroxene intercumulus has also changed into a fine-grained matter that was difficult to conclude (Fig. 6.5). The anorthosite has plagioclase (77 modal%), orthopyroxene (6 modal%), clinopyroxene (6 modal%), quartz (5 modal%), and biotite (5 modal%).

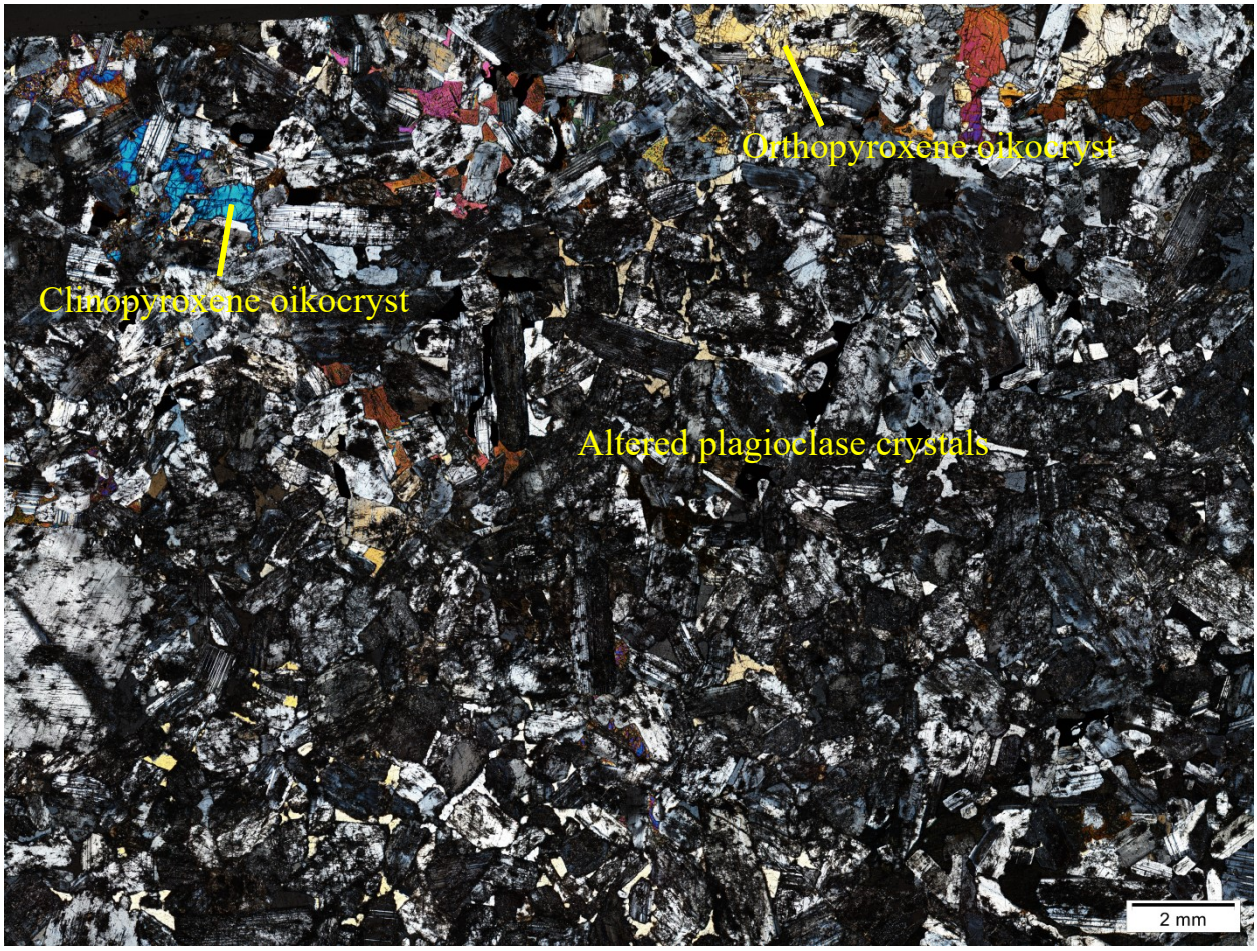

Fig. 6. 5. The microphotograph of the anorthosite matrix from the Upper TBM has an ophitic texture.

6.1.6. Pyroxenite layer

The pyroxenite layer (Fig. 4.8) has a poikilitic texture. It has sub-rounded orthopyroxene chadacrysts (1mm) in plagioclase oikocryst (2-3mm) (Fig. 6.6). It consists of 26 modal% plagioclase, 47 modal% orthopyroxene and 18 modal% clinopyroxene, 5% quartz and 2% biotite.

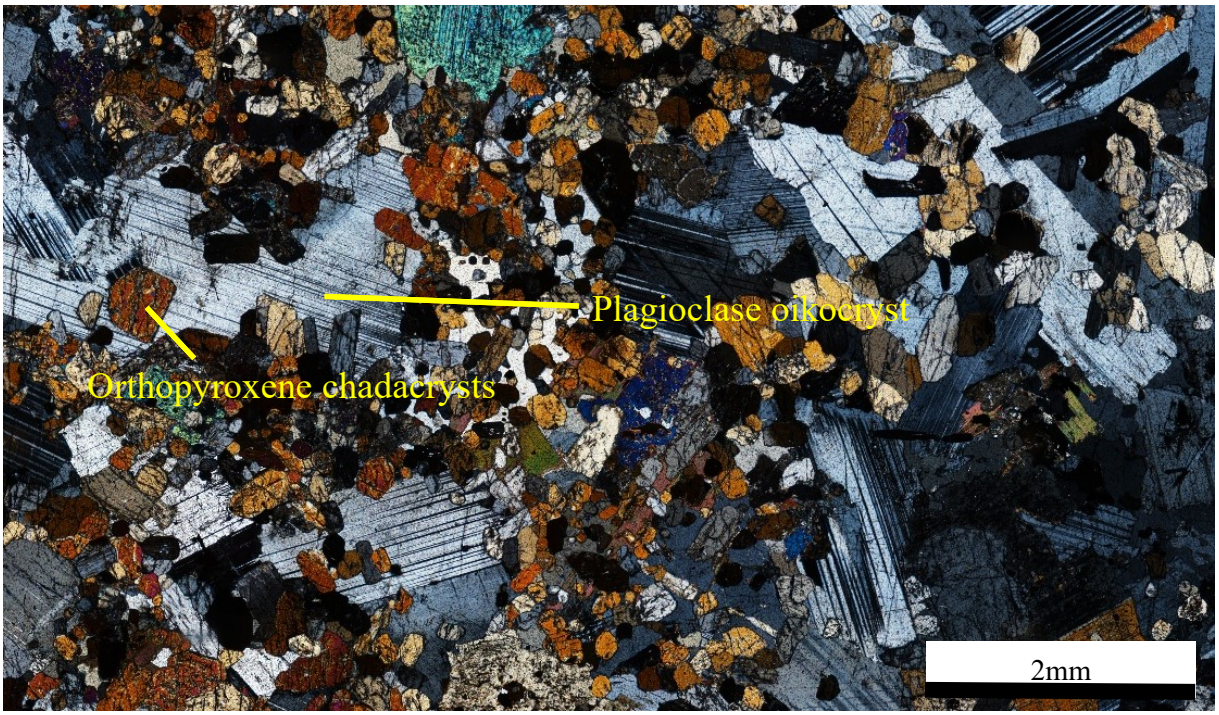

Fig. 6. 6.Microphotograph of the poikilitic pyroxenite, showing the subrounded orthopyroxene, enclosed by plagioclase oikocrysts.

6.2. Differences between the spherical orthopyroxenite and the gabbronorite matrix

The spherical orthopyroxenite and the gabbronorite (matrix and host) are composed of the same mineral assemblage. They are composed of plagioclase, orthopyroxene, clinopyroxene, quartz, biotite, hornblende, oxides, and minor sulfides (Fig. 6.1). These cumulate rocks appear to be petrographically distinct from one another (Fig. 6.1a). However, the gabbronorite matrix and host are petrographically similar to one another.

6.2.1. Petrography of the spherical orthopyroxenite

The spherical orthopyroxenite has orthopyroxenes (62-68 modal%), which dominates over plagioclase (23-26 modal%). They possess an adcumulus-mesocumulate texture that is relatively coarser than their respective gabbronorite matrix (Fig. 6.1). The cumulus orthopyroxene (2-4 mm) are at mutual contact with one another (Fig. 6.1a). They either possess a 120˚ junction or interstitial plagioclase where three orthopyroxenite meets (Fig. 6.1b).

6.2.2. Petrography of the gabbronorite matrix

Oppositely, the gabbronorite matrix has plagioclase (52-68 modal %), which dominates over orthopyroxene (6-30 modal%). It possesses an ophitic and an intergranular texture (Fig. 6.1; Fig. 6.7). The ophitic shows plagioclase chadacrysts that are optically enclosed by orthopyroxene oikocrysts (Fig. 6.1). Plagioclase cumulates construct the intergranular texture with intercumulus pyroxene oikocrysts (Fig. 6.1). The plagioclase cumulates also form a 2-D network. The sketch demonstrates this feature in Fig. 6.2b that shows the traced-out plagioclase crystals in the gabbronorite matrix (Fig. 6.2).

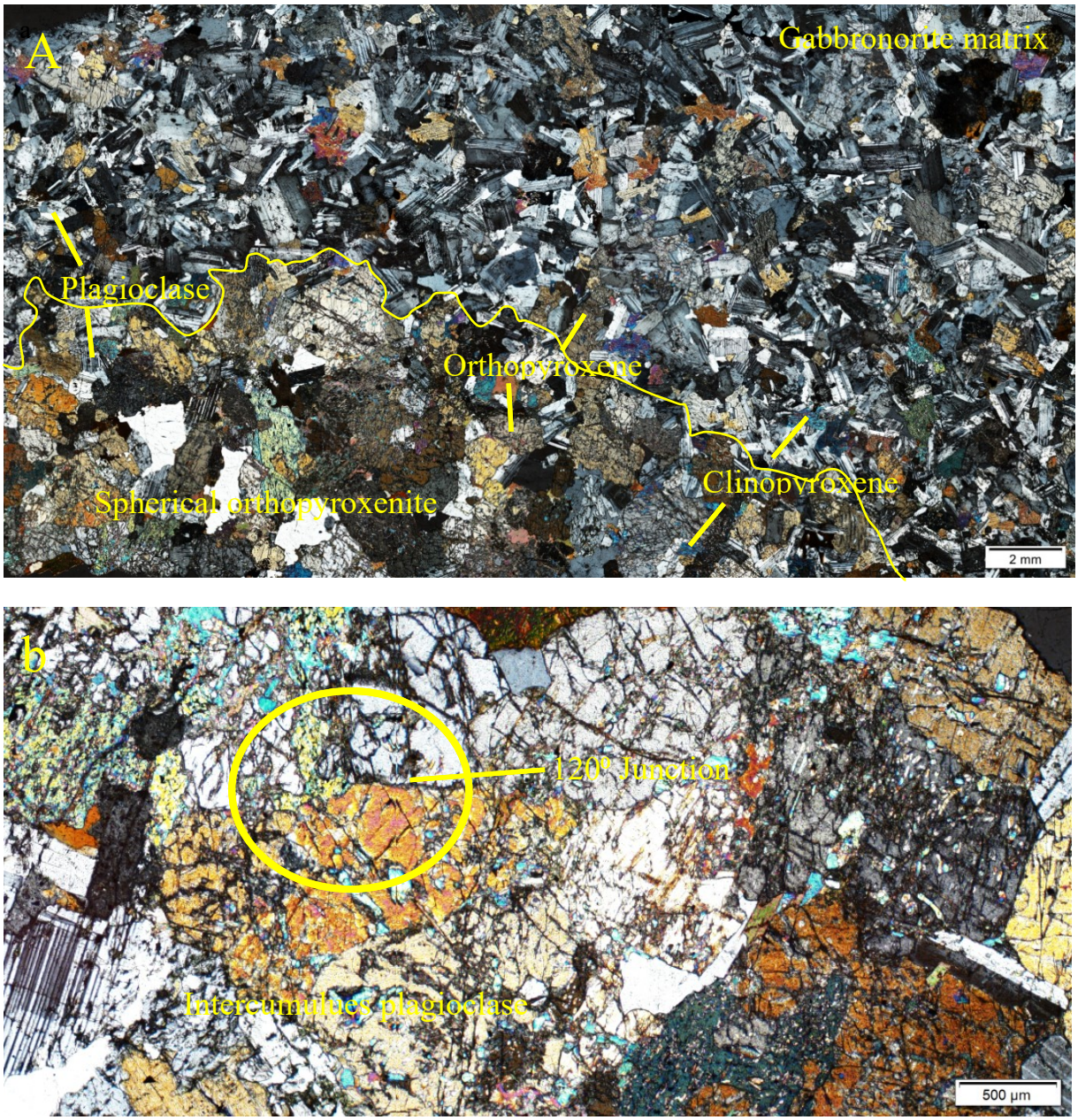

Fig. 6. 7. (a) Photomicrograph of the spherical orthopyroxenite and gabbronorite matrix. The mineral assemblages on the spherical orthopyroxenite and the gabbronorite matrix. (b) The 120° junction and the intercumulus plagioclase the spherical orthopyroxenite.

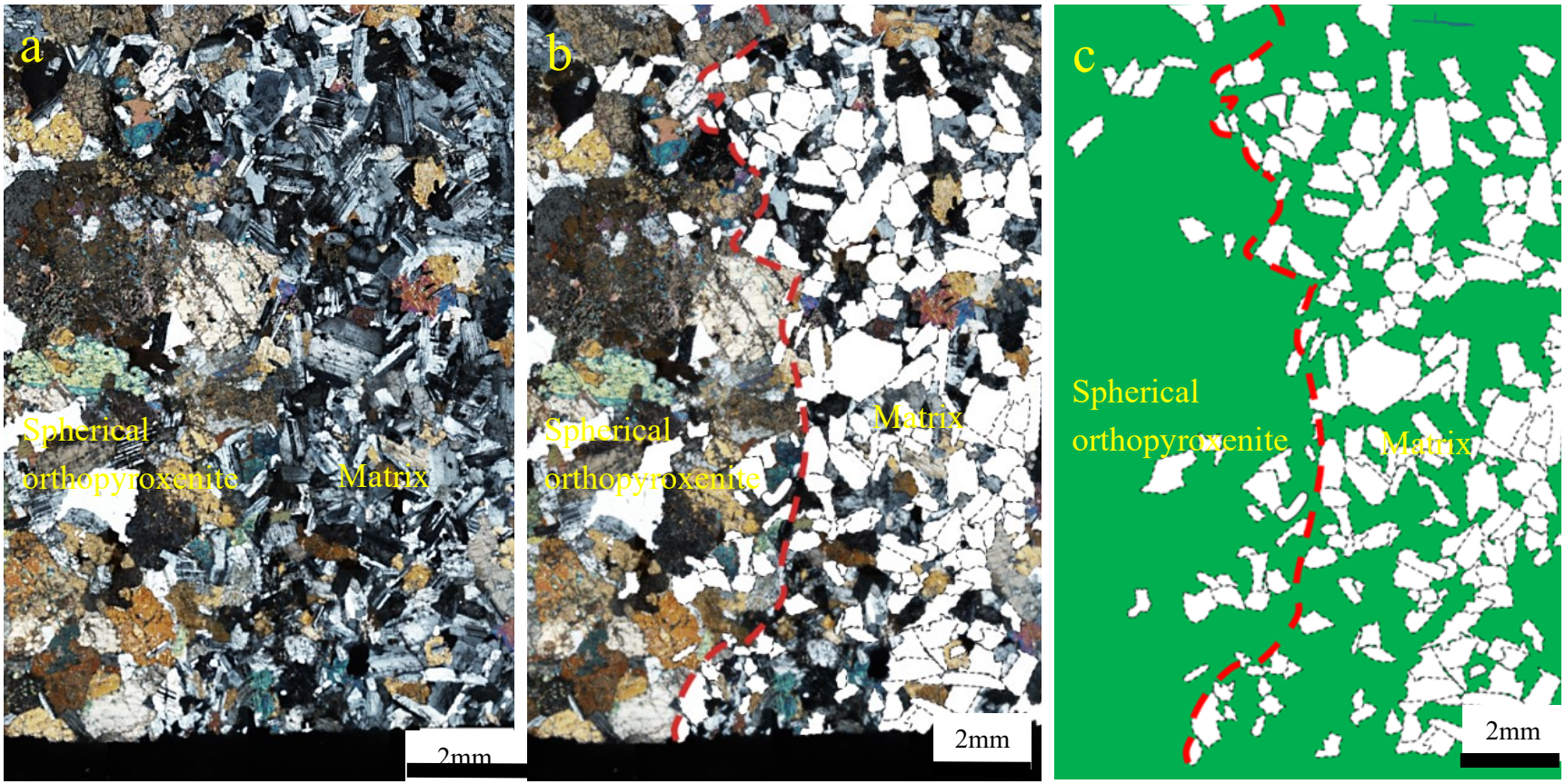

Fig. 6. 8.Photomicrograph of the Upper TBM 1 showing the transaction from the spherical orthopyroxenite to the gabbronorite matrix. (a) The differences in the textures, crystal sizes, and modal abundances. (b) The sketch of the plagioclase crystal network chain over the photomicrograph on the gabbronorite matrix. (c) The illustration of the plagioclase crystal network without the photomicrograph.

Chapter 7: Mineral compositions

This chapter explores the distribution of various elements and phases in the spherical orthopyroxenite and the gabbronorite matrix. It also documents the variations in mineral chemistry upwards in the stratigraphy.

7.1. The in-situ XRF chemical images of the TBM layer

The Ca, Si, and Al are uniformly in all phases(Fig. 7.1b), and a similar relationship occurs Cr, Fe, and Ca chemical image (Fig. 7.1c). However, Cr shows remarkable compositional zoning on the orthopyroxene in the spherical orthopyroxenite, medium, and the pegmatitic gabbronorite matrix (Fig. 7.1c-e).

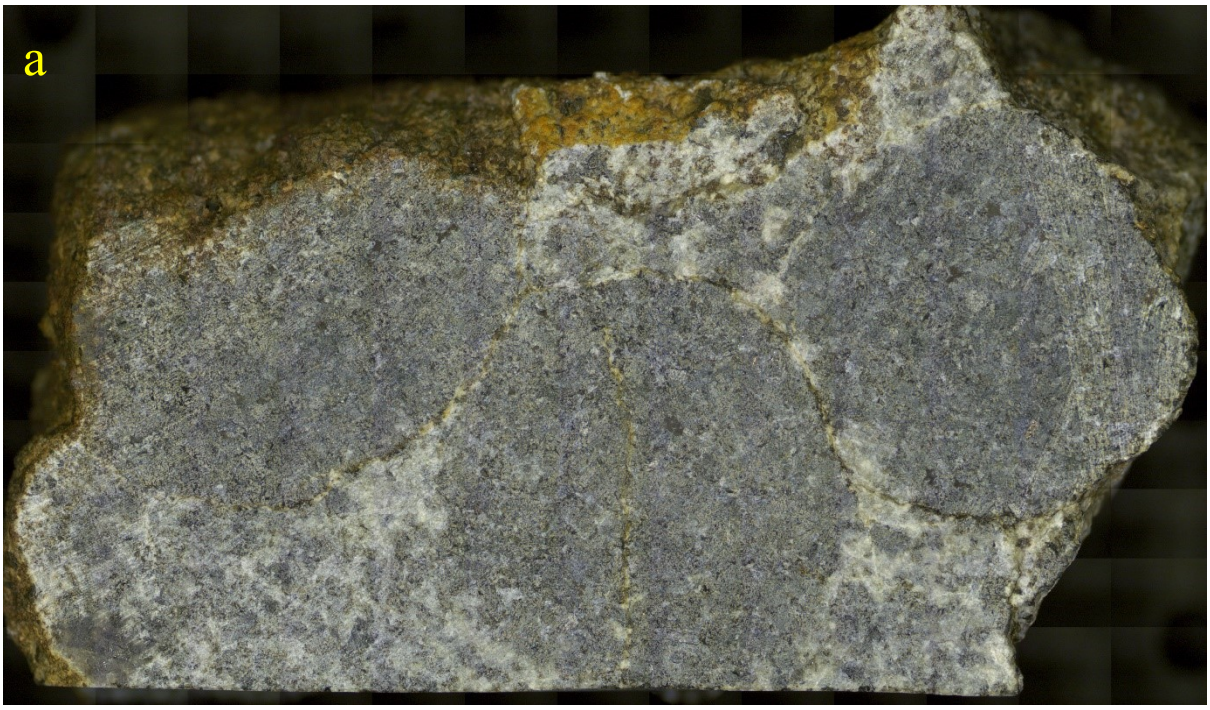

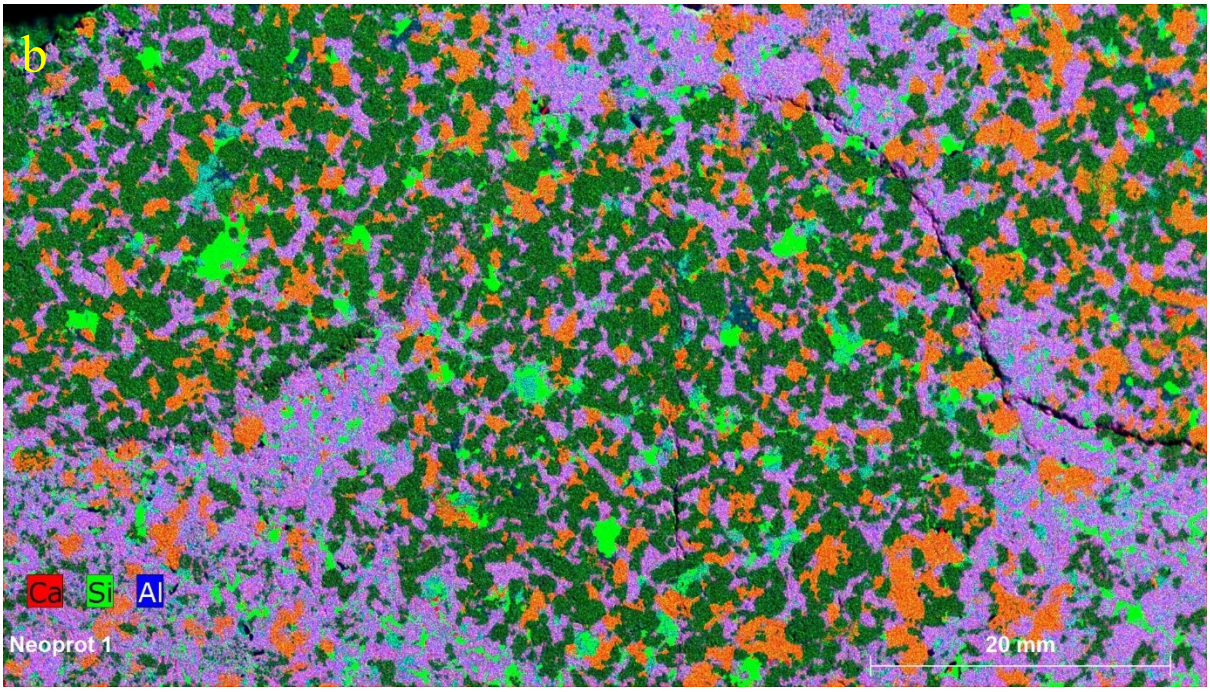
b
Ca
Si
Al
Neoprot 1
20 mm

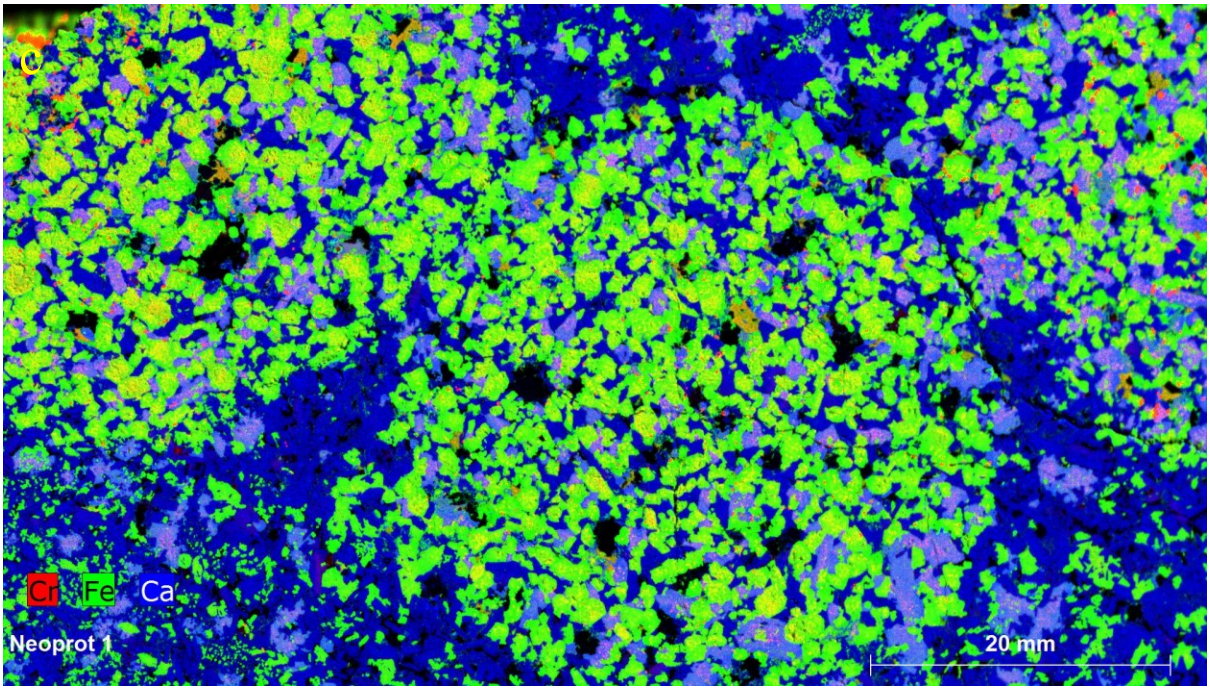
c
Cr
Fe
Ca
Neoprot 1
20 mm

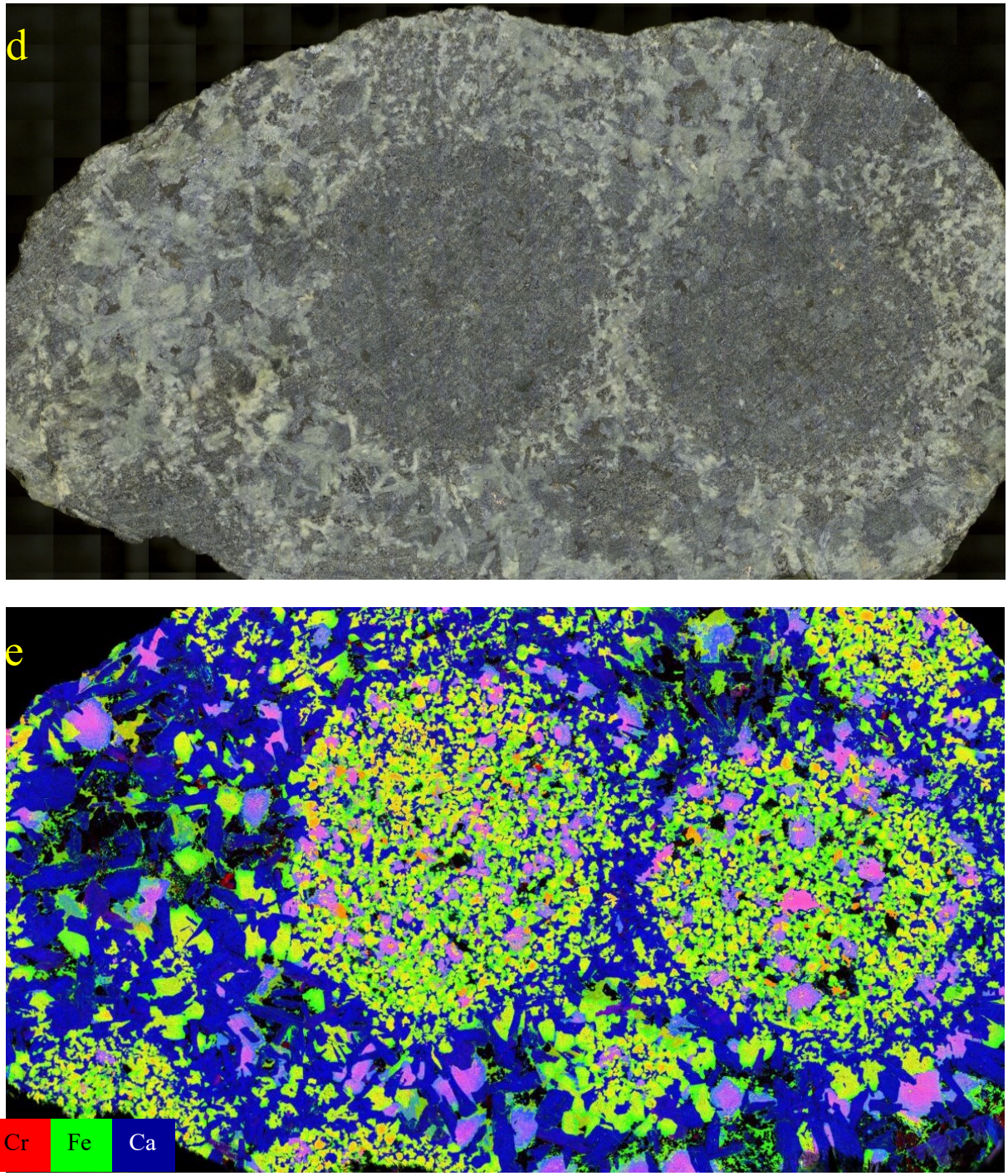

Fig. 7. 1. XRF images of the TBM slab (a) The TBM with a medium-grained gabbronorite matrix. (b) The Ca, Si, and Al XRF image of the TBM layer with a medium-grained gabbronorite matrix, showing the uniform distribution of the Ca, Si, and Al on the plagioclase (purple), orthopyroxene (green), and clinopyroxene (orange). (c) The Cr, Fe, and Ca XRF image of the TBM layer slab with a medium-grained gabbronorite, showing the uniform distribution of Ca and Fe; and Cr zoning on the orthopyroxenes. (d) The slab of the TBM layer with spherical in a matrix of pegmatitic gabbronorite. (e) The Cr, Fe, and Ca XRF image of the TBM layer with a pegmatitic gabbronorite. It shows the uniform distribution of Ca and Fe; and Cr zoning on the orthopyroxenes.

7.2. Chemical compositions of plagioclase and orthopyroxene

7.2.1. The anorthite content (An) of the plagioclase feldspar

The plagioclase on the gabbronorites has An ($= 100 \times CaO/(CaO + 2 * Na_2O)$) that ranges between An_{65} to An_{78} (Fig. 7.2a). It decreases unevenly upwards, from the Contact gabbronorite (An_{76}) to the Normal gabbronorite (An_{66}) (Fig. 7.2a). The plagioclase on the spherical orthopyroxenite has An that ranges between An_{74} to An_{76} (Fig. 7.2a). Additionally, the An on the spherical orthopyroxenite is always higher than the An of their respective matrixes (Fig. 7.2a).

7.2.2. The Mg# of the orthopyroxenes

The Mg# (=100*(MgO/(MgO+FeO))) of the orthopyroxene in the gabbronorite shows a trend that correlates with the An (Fig. 7.2b). It ranges from Mg_{73} to Mg_{51} and it generally decreases with an increase upwards (Fig. 7.2b). The Mg# of the orthopyroxene on the spherical orthopyroxenite gradually decreases upwards from the Lower TBM to the Upper TBM (Fig. 7.2b). Additionally, the Mg# of the orthopyroxene in the spherical orthopyroxenite is higher than those in the gabbronorite (Fig. 7.2b).

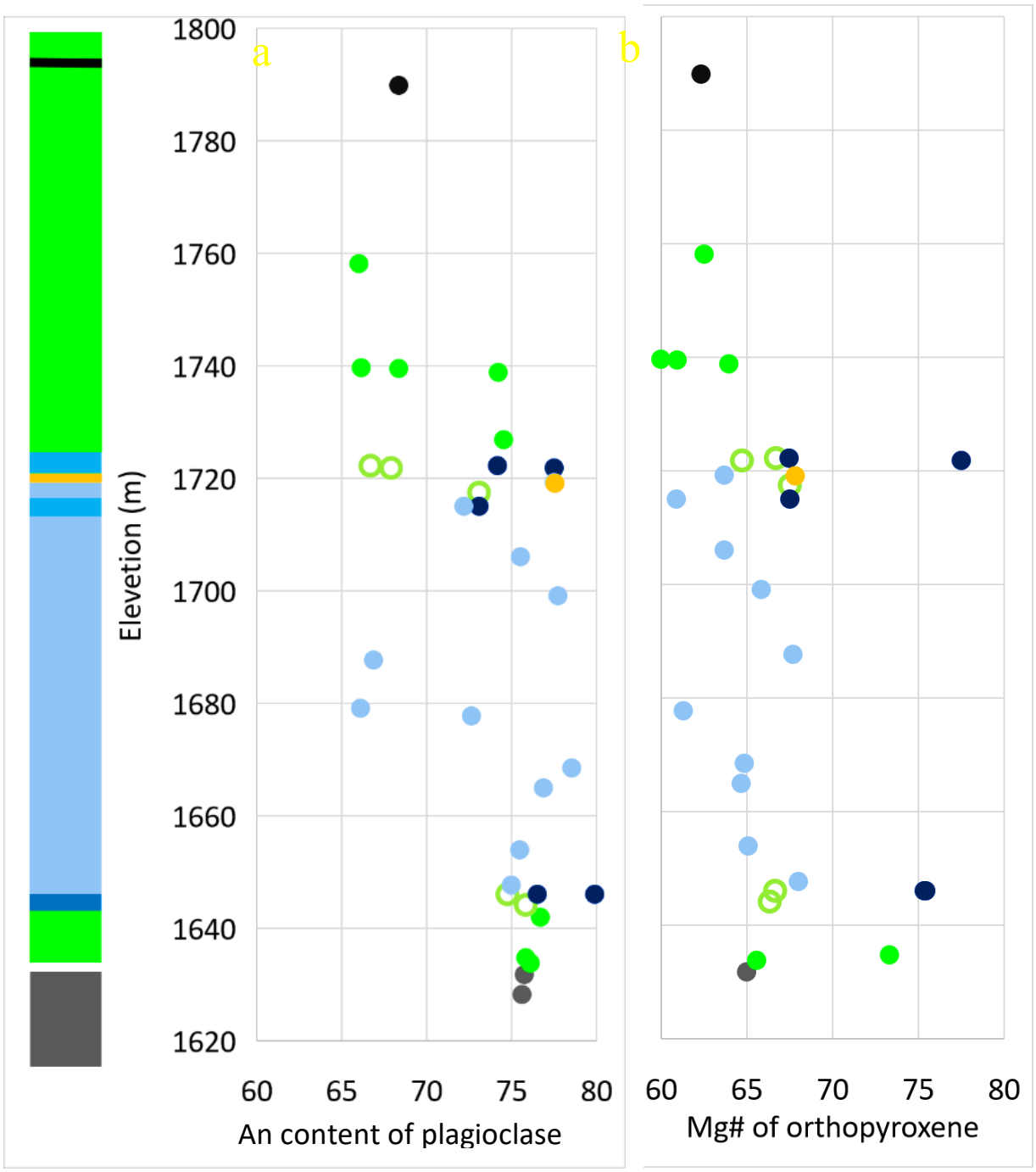

Fig. 7. 2. Chemical profiles through the TBM. (a) The decrease in the An of plagioclase upwards. (b) The decrease in the Mg# of the orthopyroxene upwards. Grey circle-DFB; green closed circles- Contact gabbronorite and Normal gabbronorite; olive green open circles-gabbronorite matrix, navy blue closed circles-spherical orthopyroxenite, light blue filled circle-spherical orthopyroxenite poor gabbronorite, and the orange filled circle- anorthosite matrix.

Chapter 8: Whole-rock geochemistry of the TBM

8.1. Stratigraphic changes in major elements

8.1.1. Geochemical profiles of the whole rock MgO and Mg#

The MgO wt. % and the Mg# (=100*(MgO/(MgO+FeO))) show trends that are similar to the orthopyroxene and clinopyroxene modal proportions (Fig. 8.1a, c, d). The Mg# of the gabbronorite gradually decreases with an increase in height (Fig. 8.1d). It abruptly increases at the top of the Lower TBM layer and the midpoint of the spherical orthopyroxenite poor gabbronorite matrix.

8.1.2. Geochemical profiles of the whole rock NaO, CaO and Al_2O_3

The NaO, CaO and Al_2O_3 on the gabbronorite vary slightly with an increase in height. They also show an inverse relationship to the trend exhibited by the MgO and Mg#. The spherical orthopyroxenite also indicates a smaller content of NaO, CaO and Al_2O_3 and constant with an increase in height (Fig. 8.2).

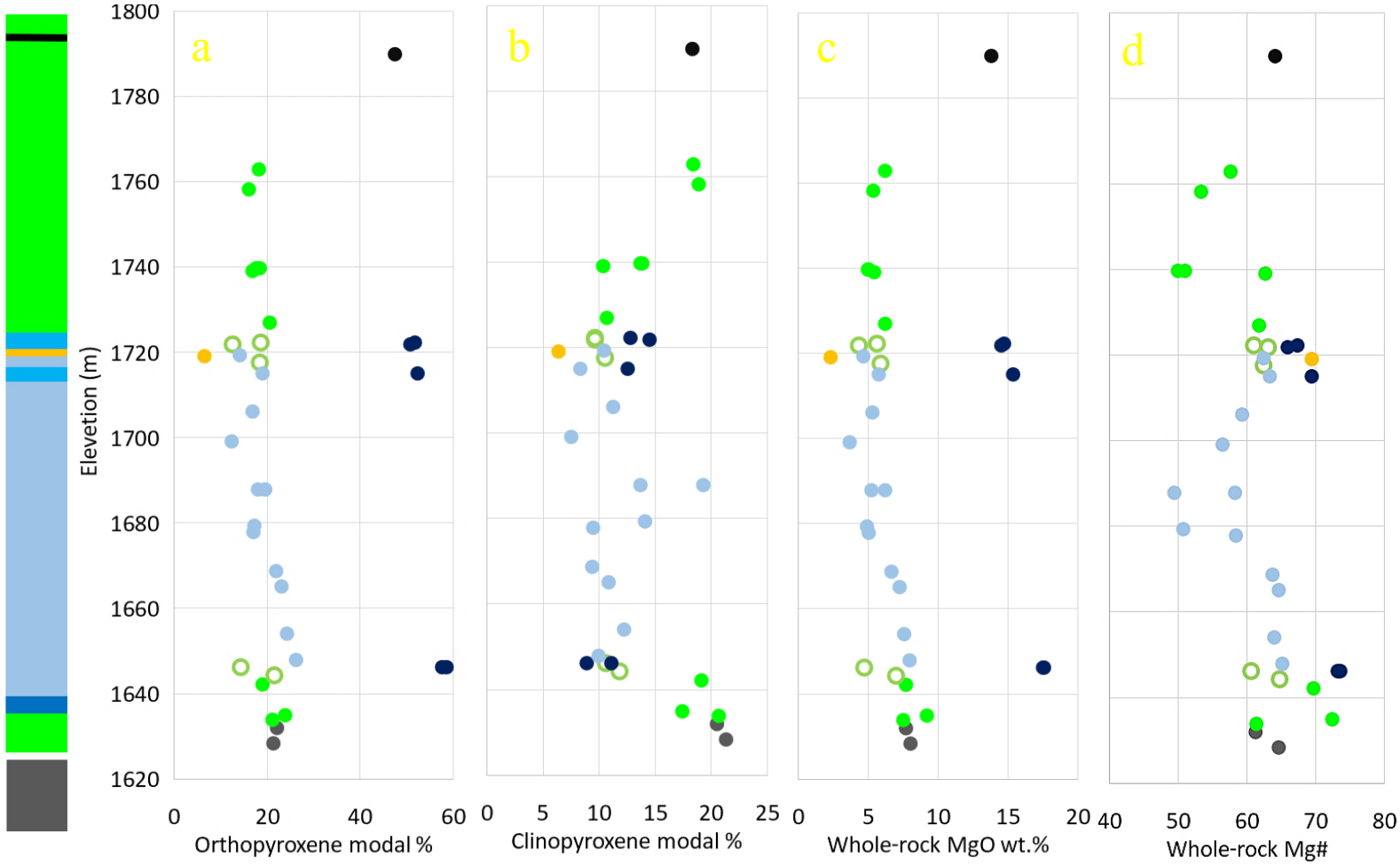

Fig. 8. 1. Generalized stratigraphic columns through the TBM package showing the variations orthopyroxene, clinopyroxene, MgO Wt.%, and the Mg#. It shows the basal cycles below 1680m and their gradual increase in these components above. Colour scheme: grey circle-DFB; green closed circles- Contact gabbronorite and Normal gabbronorite; olive green open circles-gabbronorite matrix, navy blue closed circles-spherical orthopyroxenite, light blue filled circle-spherical orthopyroxenite poor gabbronorite, and the orange filled circle- anorthosite matrix.

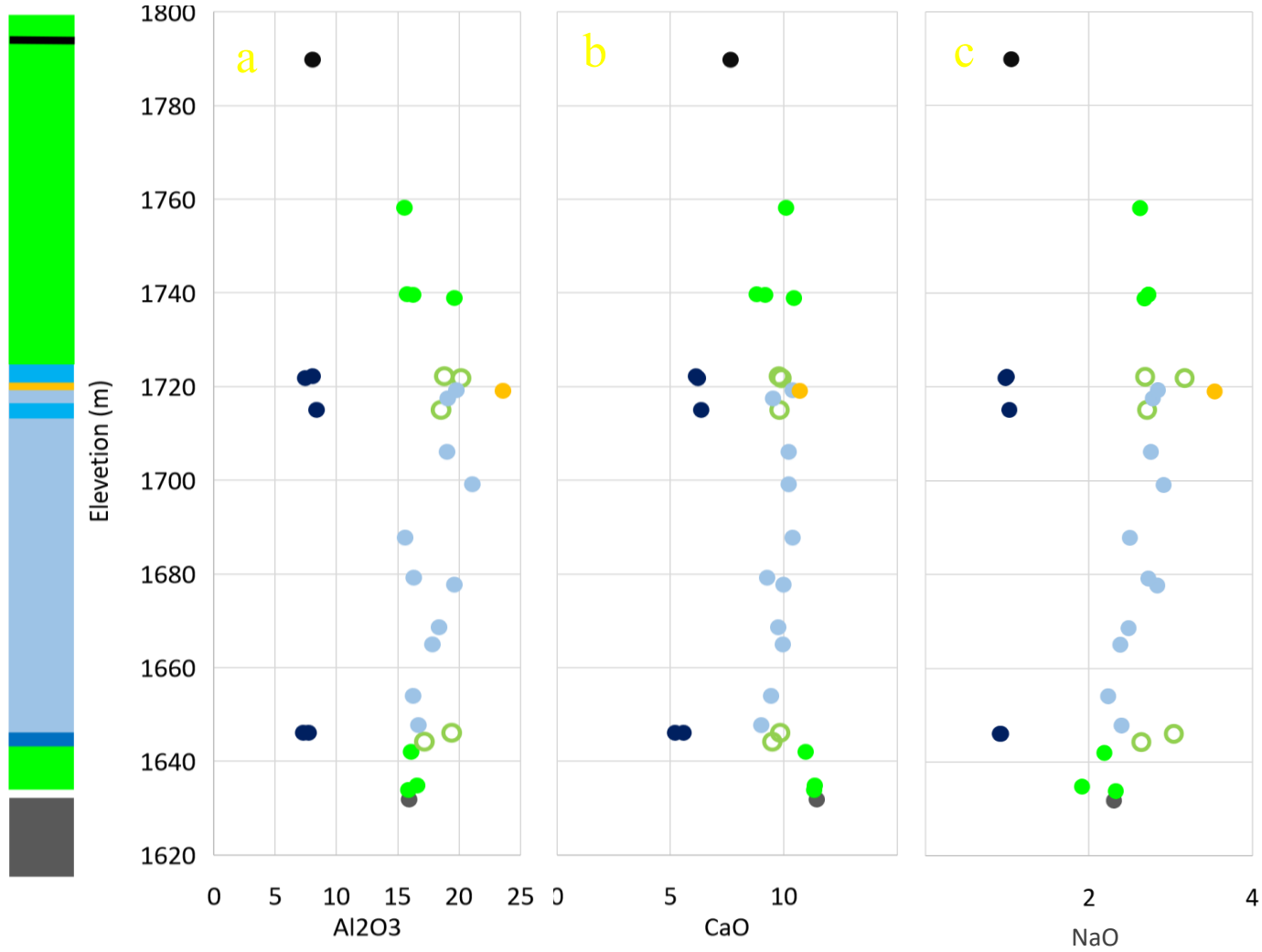

Fig. 8. 2. The changes in the concentrations of felsic components in the TBM profile. Colour scheme: grey circle-DFB; green closed circles- Contact gabbronorite and Normal gabbronorite; olive green open circles-gabbronorite matrix, navy blue closed circles-spherical orthopyroxenite, light blue filled circle-spherical orthopyroxenite poor gabbronorite, and the orange filled circle- anorthosite matrix.

8.2. Harker diagram of the spherical orthopyroxenite, gabbronorite (matrix and host)

8.2.1. For MgO and other major oxides

The Na_2O, Al_2O_3FeO, CaO, MnO content are plotted against MgO for the gabbronorites and the spherical orthopyroxenite (Fig. 8.3). The FeO, MnO and Fe_2O_3 show a positive correlation with MgO. Whereas, the Na_2O, Al_2O_3, CaO and K_2O shows a negative correlation (Fig. 8.3). There is also a MgO gap at 9-13 Wt. % that occurs between the spherical orthopyroxenite and the gabbronorite (Fig. 8.3). The spherical orthopyroxenite have a narrow SiO_2 compositional range (52.87-53.27 wt.%) compared to the gabbronorite matrix (52.16-56.21 wt.%). Hence, MgO and SiO_2 does not show any correlation relationship (Fig. 8.3).

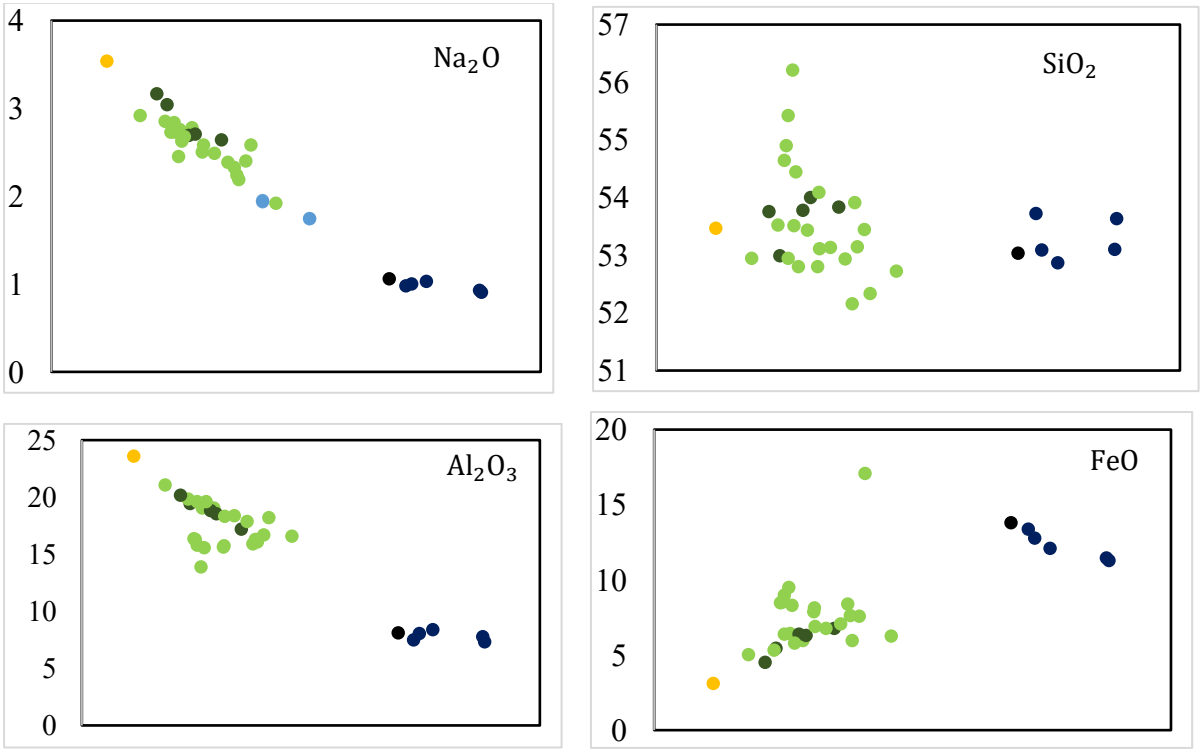

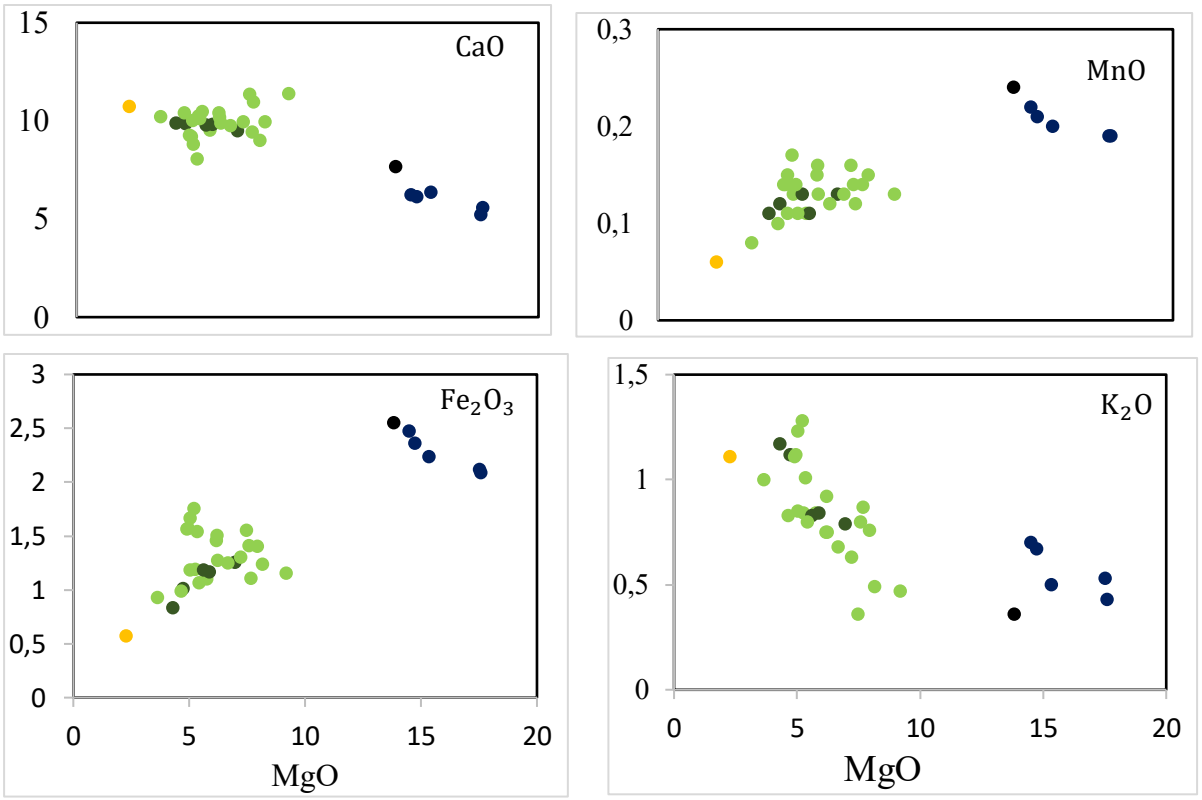

Fig. 8. 3. Harker diagram of whole-rock major elements oxides plotted against MgO for the TBM.

8.3. Trace elements distribution

The trace element distribution diagram normalized to the MORB (Pearce and Parkinson,1993) shows a general negative slope with strong enrichment in Large Ion Lithophiles Elements (LILE) and negative Nb, Ta, and Ti anomalies (Fig. 8.4). The spherical orthopyroxenite and the gabbronorite have contrasting Ba and Sr content (Fig. 8.4)

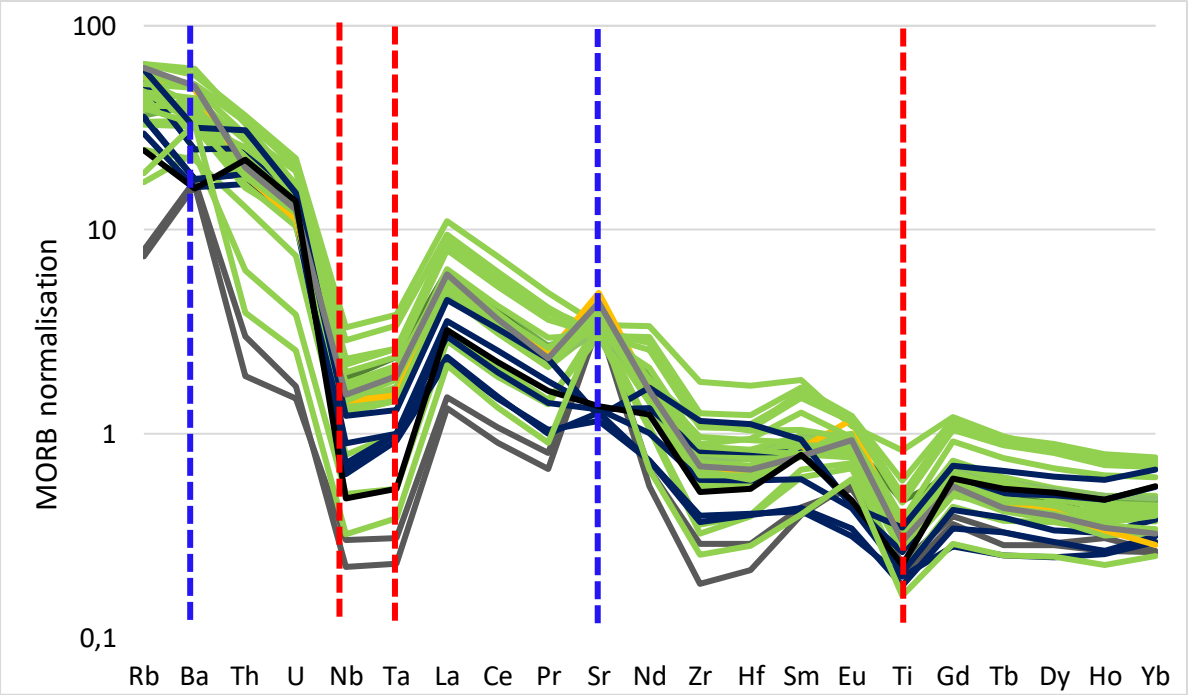

Fig. 8. 4. Multi-element diagram of the TBM showing the negative slope with an enriched LILE and depletion of HFSE. It also indicates Nd, Ta, Ti's negative anomalies in the red dotted line and Ba and Sr's contrasting anomalies indicated by the blue lines. Blue-spherical orthopyroxenite; green solid- gabbronorite; yellow-anorthosite matrix; grey-DFB; green dash-gabbronorite matrix.

8.4. Rare Earth Elements (REE) Pattern

The rare earth element (REE) patterns of the TBM, normalized to the chondrite values (Sun and McDonough, 1995), show a steep REE pattern that is characterized by enrichment in the LREE relative to the HREE (Fig. 8.5).

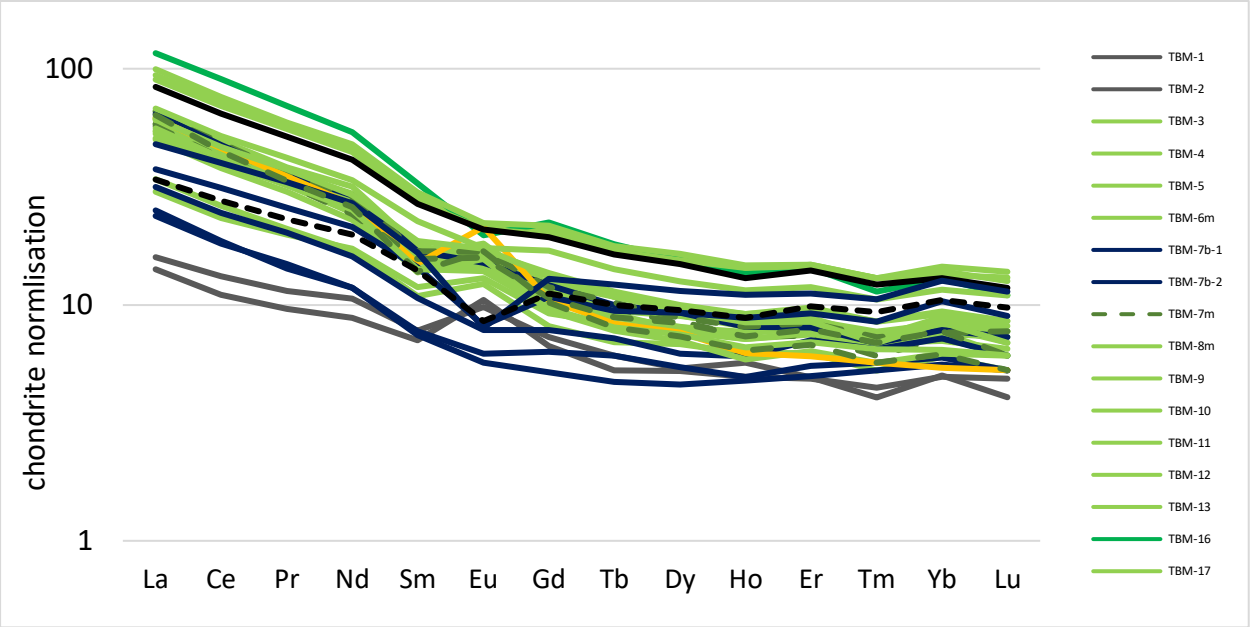

Fig. 8. 5. The REE pattern of the TBM rocks, showing a negative slope characterized by an enriched LREE and depleted HREE. Blue-spherical orthopyroxenite; green solid- gabbronorite; yellow-anorthosite matrix; grey-DFB; green dash-gabbronorite matrix.

The Contact gabbronorite shows enrichment and steepening in the REE up section (Fig. 8.5a). The Contact gabbronorite (Fig. 6.4c) shows the disappearance of positive Eu anomaly, up to section (Fig. 6.5; Fig. 8.6c). The spherical orthopyroxenite and the gabbronorite matrix at the Lower TBM have slightly different REE patterns. The gabbronorite matrix is enriched in LREE, and it has a steeper REE pattern compared to the spherical orthopyroxenite (Fig. 8.6b). The spherical orthopyroxenite has a flat REE pattern that lacks an Eu anomaly, whiles the gabbronorite matrix shows a slight positive anomaly (Fig. 8.6b).

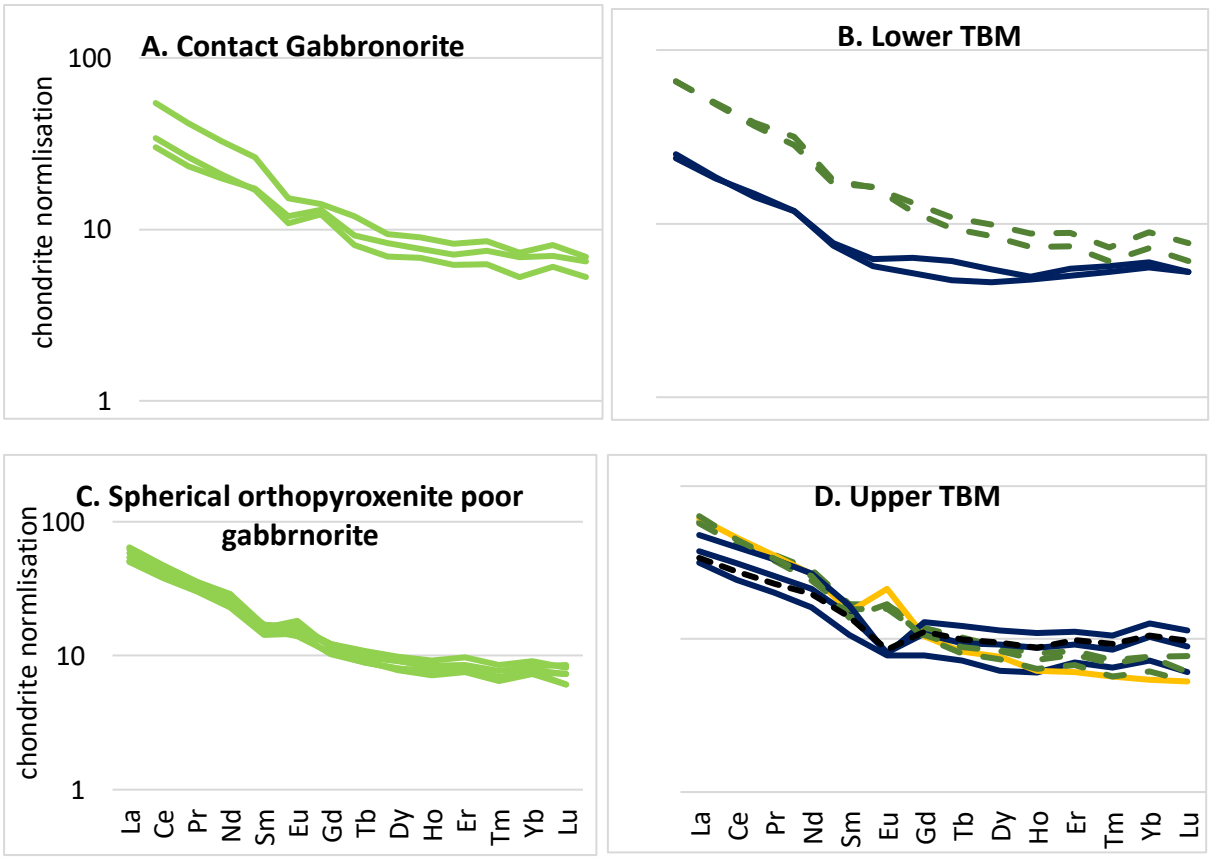

Fig. 8. 6. The REE patterns of (a). Contact gabbronorite. (b) Lower TBM. (c) Spherical orthopyroxenite gabbronorite. (d) Upper TBM.

The spherical orthopyroxenite poor gabbronorite has an REE pattern similar to the Lower TBM matrix because they have identical slopes and slight positive Eu anomaly (Fig. 8.6c; Fig. 8. 6a). The spherical orthopyroxenite, gabbronorite matrix, and the anorthosite matrix show enrichments in the REE upsection (Fig. 8.6d).

The spherical orthopyroxenite at the Upper TBM have REE patterns that progressively become more enriched and steeper up section (Fig. 8.6d). Also, the REE pattern of the spherical orthopyroxenite at the Upper TBM 2 is relatively flat and similar to the REE pattern of the spherical orthopyroxenite at the Lower TBM (Fig. 8.6b; Fig. 8.6d). However, the spherical orthopyroxenite at the Upper TBM 2 are more enriched in REE; their REE pattern is steeper and has a negative Eu anomaly.

The pyroxenite layer in Fig. 4.8 has an REE pattern similar to those of the spherical orthopyroxenite at the Upper TBM 2. The gabbronorite and anorthosite matrix have a steep REE pattern. It is characterized by enrichment on the LREE and a depletion of the HREE relative to those on the spherical orthopyroxenite. Also, they possess a stronger Eu anomaly compared to the poor gabbronorite.

Chapter 9: Rb-Sr, Sm-Nd, and Lu-Hf isotopic composition of the TBM layers

9.1. Rb-Sr isotope

The spherical orthopyroxenite, gabbronorite matrix and the pyroxenite layer yield similar calculated Sr_i that ranges between 0.706490 to 0.7077254 (Table. 9.1; Fig. 9.1). These values are consistent in all TBM layers and fall within each other's errors (Fig. 9.1), except for the spherical orthopyroxenite at the Lower TBM that yields the lowest calculated Sr_i of 0.705251 (Table. 9.1; Fig. 9.1).

The Rb-Sr isotope data of the spherical orthopyroxenite and the gabbronorite matrix are plotted on an Rb-Sr isochron plot (Fig. 9.2a). The gabbronorite matrix data falls within the isochron line, and those of the spherical orthopyroxenite do not fall along the isochron line (Fig. 9.2a). Also, this isochron yields a crystallization age of 1947.20 ± 3.76 Ma and Sr_i of 0.0707387±0.000021 (Fig. 9.2a).

The Rb-Sr isotope data for spherical orthopyroxenite and the gabbronorite matrix are also plotted on separate isochron plots. They yield discordant ages of 2253.08 ± 9.27 Ma and 2301.37.01± 37 Ma, respectively (Fig. 9.2b and Fig. 9.2c). The isochron plots for the spherical orthopyroxenite show an Sr_i of 0.704842±0.000073, whereas the isochron plot of the gabbronorite matrix yields a higher Sr_i of 0.70645±0.00011 (Fig. 9.2b; Fig. 9.2c).

Table. 9. 1. Rb-Sr isotopic data for the spherical orthopyroxenite, gabbronorite matrix, and the Pyroxenite layer from the TBM.

Sample occurrence	**Rb**	**Sr**	$(^{87}Rb/^{86}Sr)_p$	**1SD**	$(^{87}Sr/^{86}Sr)_p$	**1SD**	$(^{87}Sr/^{86}Sr)_i$
Spherical orthopyroxenite							
LTBM	16.59	104.33	0.461340	0.000250	0.718878	0.000003	0.705184
LUTBM	19.82	118.88	0.484643	0.000350	0.721241	0.000004	0.706855
UUTBM	29.09	118.13	0.743557	0.000530	0.728453	0.000004	0.706382
Gabbronorite matrix							
LTBM	33.38	383.55	0.250956	0.000220	0.714667	0.000024	0.707217
LUTBM	23.13	327.83	0.200596	0.000130	0.712931	0.000022	0.706977
UUTBM	22.73	328.3	0.193429	0.000110	0.712832	0.000020	0.707090
Upper pyroxenite layer (UPL)							
Pyroxenite	13.74	122.83	0.328438	0.00015	0.716918	0.000004	0.707169

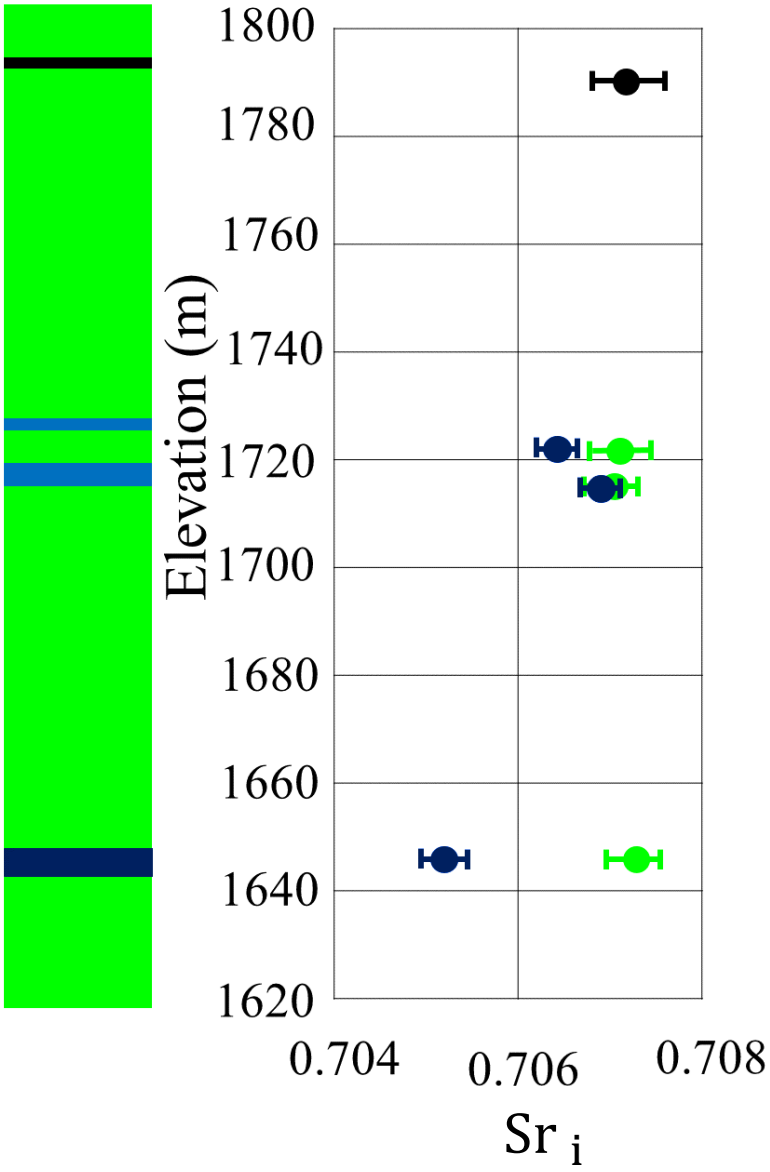

Fig. 9. 1. The Sr isotopic profile of the TBM layers, showing the changes in the Sr_i of the spherical orthopyroxenite and the gabbronorite matrix. The blue closed circles - spherical orthopyroxenite and the green closed circles - gabbronorite matrix

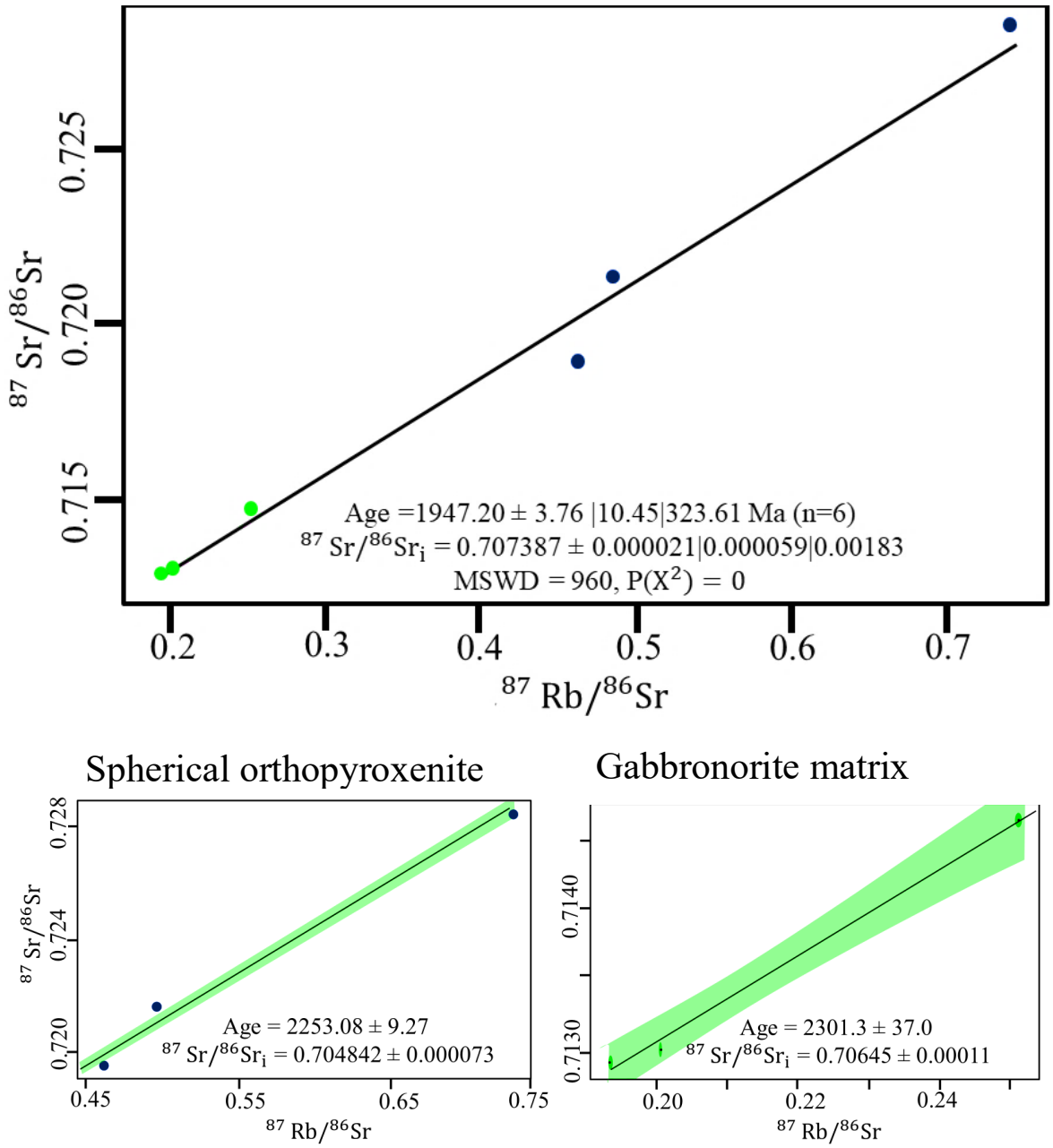

Fig. 9. 2. The isochron plots of the TBM layers and the gabbronorite matrix. (a) Isochron plots of the spherical orthopyroxenite and the gabbronorite matrix, showing the Rb-Sr ages and their Sr_i. (b) Isochron plot of the spherical orthopyroxenite, showing their age and Sr_i. (c) Isochron plot of the gabbronorite matrix, showing its age and Sr_i.

9.2. Sm-Nd isotope

The spherical orthopyroxenite, gabbronorite matrix, and the pyroxenite layers yield similar calculated Nd_i and ε_{Nd}that range from 0.509622 to 0.509703 and -5.1 to -6.7, respectively (Table. 9.2; Fig. 9.3). These values have minor variations with height but fall within their errors (Fig. 9.3). The ε_{Nd} The spherical orthopyroxenite and the gabbronorite matrix plot below the CHUR line consistent with an increase in height (Fig. 9.3).

The Sm-Nd isotope data for the spherical orthopyroxenite and the gabbronorite matrix from the TBM layers are plotted on an isochron diagram (Fig. 9.4a). These values form a linear array with all the points falling on the isochron line and within its errors (Fig. 9.4a). The age yield by this linear array is 2220 ± 186 Ma with an Nd_i of 0.50953 ± 0.000015 (Fig. 9.4a).

The spherical orthopyroxenite and the gabbronorite matrix are also plotted on different isochron plots and yields Sm-Nd age of 3275 ± 1142 Ma and 1281± 593 Ma, respectively (Fig. 9.4b; Fig. 9.4c). Also, the isochron diagrams of the gabbronorite yield a higher Nd_i of 0.51026±0.00047, compared to the spherical orthopyroxenite that yields an Nd_i of 0.50863±0.00098 (Fig. 9.4)

Table. 9. 2. Sm-Nd isotopic data for the spherical orthopyroxenite, gabbronorite matrix, and the Pyroxenite layer from the TBM package.

Sample location	Sm (ppm)	Nd (ppm)	$^{147}Sm/^{144}Nd$	1SD	$^{143}Nd/^{144}Nd$	2SD	Constant	$^{143}Nd/^{144}Nd_i$	εNd
The spherical orthopyroxenite									
LTBM	1.14	5.4	0.130309	0.000040	0.511475	0.000030	6.54E-12	0.509703	-5.1
UTBM-1	1.58	7.34	0.127076	0.000040	0.511386	0.000017	6.54E-12	0.509658	-6
UTBM-2	2.13	9.78	0.130144	0.000040	0.511442	0.000020	6.54E-12	0.509673	-5.7
Gabbronorite matrix									
LTBM	2.51	12.99	0.115077	0.000040	0.511227	0.000021	6.54E-12	0.509662	-5.9
UTBM-1	2.49	13.02	0.122821	0.000050	0.511292	0.000015	6.54E-12	0.509622	-6.7
UTBM-2	2.31	11.08	0.119512	0.000030	0.511266	0.000022	6.54E-12	0.509641	-6.3
Pyroxenite layer									
Pyroxenite	2.07	9.05	0.138348	0.000060	0.511523	0.000031	6.54E-12	0.509642	-6.3

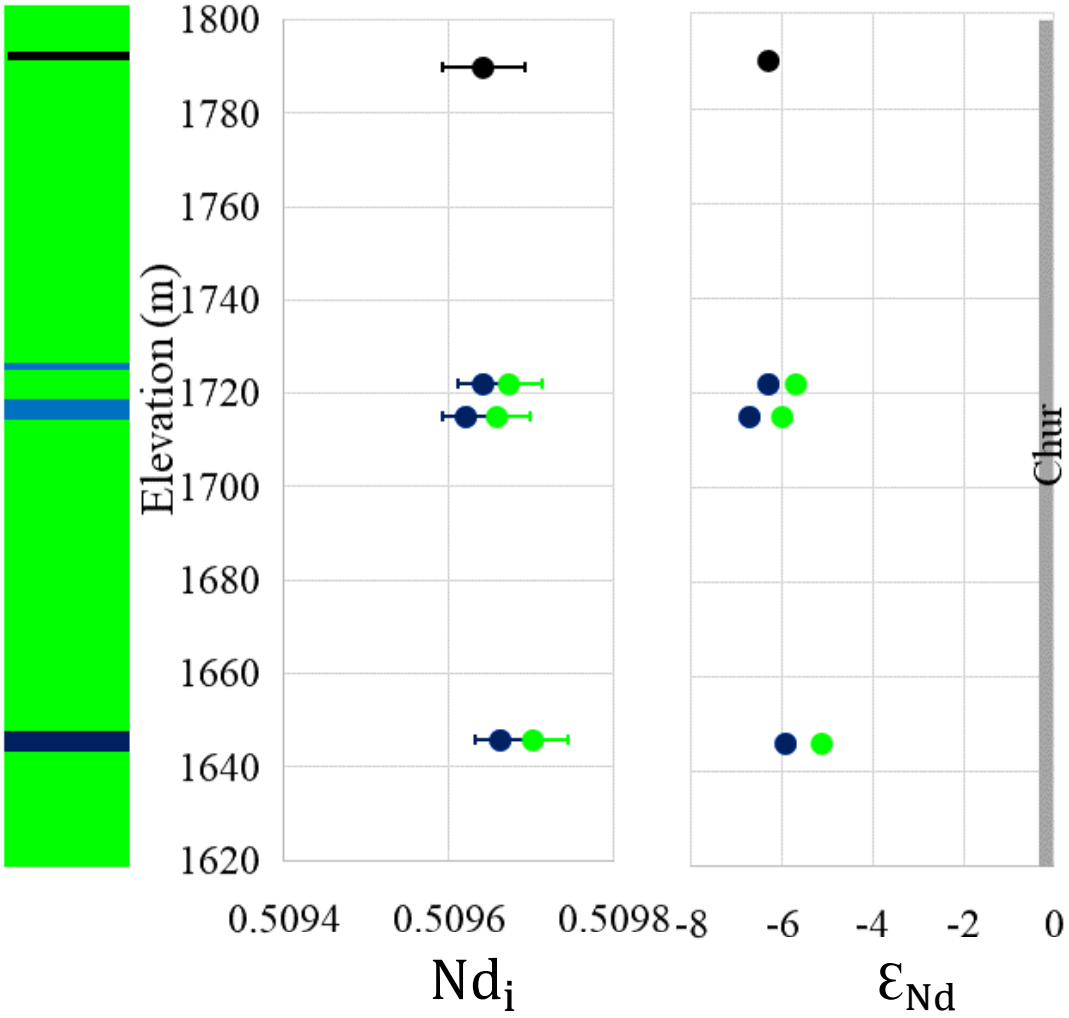

Fig. 9. 3. The Sr isotopic profile of the TBM layers, showing the approximate locations of the TBM layers and the changes in the Nd_i and the ε_{Nd} of the spherical orthopyroxenite and the gabbronorite matrix. The blue closed circles -spherical orthopyroxenite and the green closed circles-gabbronorite matrix.

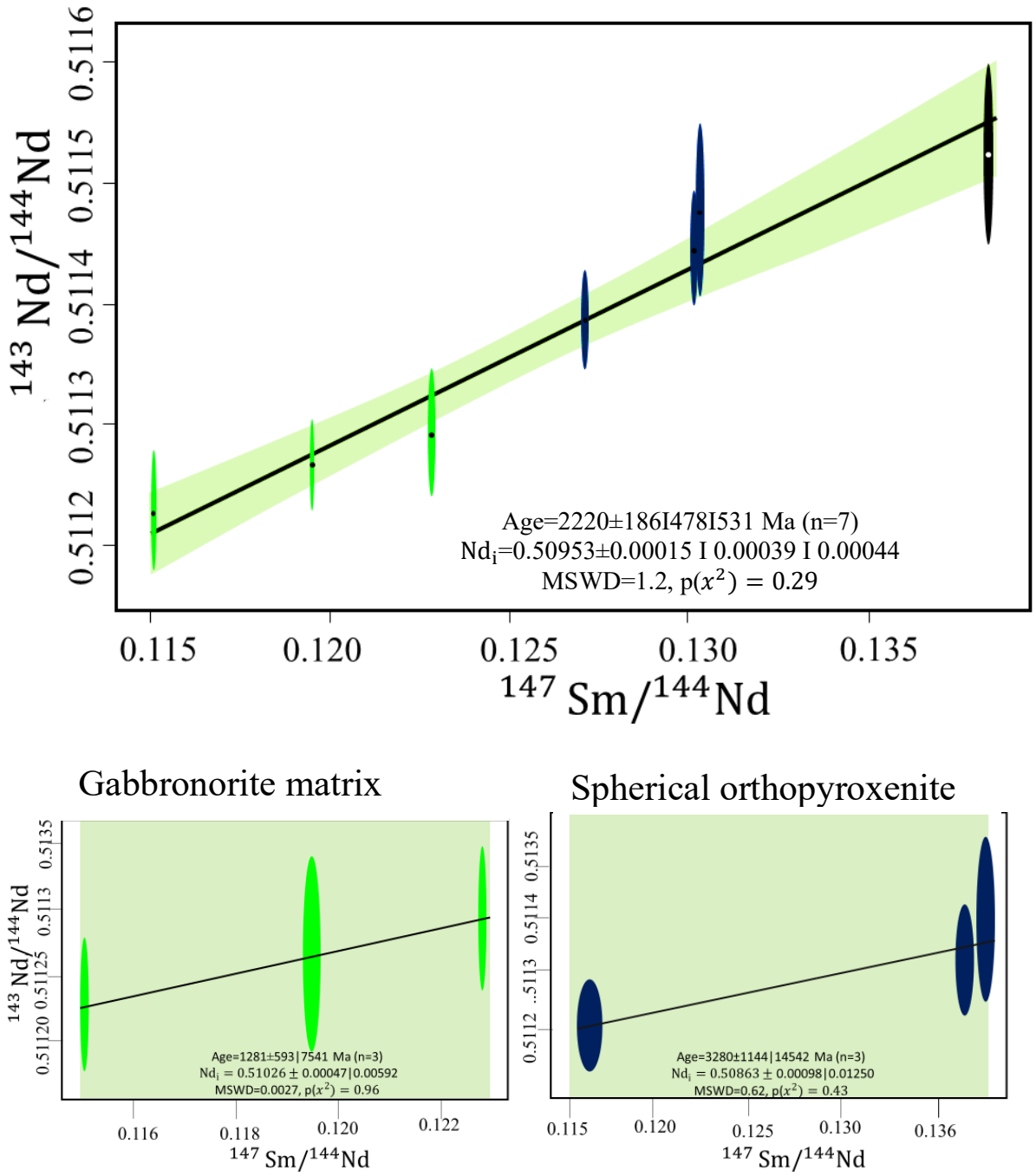

Fig. 9. 4. The isochron plots of the TBM layers. (a) Isochron plots of the spherical orthopyroxenite and the gabbronorite matrix, showing the Rb-Sr calculates ages and their Nd_i. (b) Isochron plot of the spherical orthopyroxenite, showing its age and the Nd_i (c) Isochron plot of the gabbronorite matrix, showing its age and the Nd_i.

9.3. Lu-Hf isotope

The spherical orthopyroxenite, gabbronorite matrix, and the pyroxenite layer yield similar Hf_i that ranges between 0.281139 to 0.281241 (Fig. 9.5). These values are constant with height and fall within their errors (Fig. 9.5). The ε_{Hf} plots below the CHUR-line with values ranging from -8.0 to -11.7 and show a slight decrease with an increase in height (Table.9.3; Fig. 9.5).

The Lu-Hf isotope data for the spherical orthopyroxenite and the gabbronorite matrix from the TBM layer are plotted on an isochron diagram (Fig. 9.6). The data forms a linear array with all the data points falling along the isochron line and within its errors (Fig.9.6). The age yield by this linear array is 1861 ± 338 Ma with an Hf_i of 0.28125 ± 0.000011 (Fig. 9.6). The Lu-Hf data for the spherical orthopyroxenite and the gabbronorite matrix are also plotted on different isochrons, and they yield Lu-Hf ages of 2119 ± 948 Ma and 779 ± 696 Ma, respectively (Fig. 9.6). Also, isochron diagrams of the spherical orthopyroxenite yield a higher Nd_i of 0.28117±0.00033, compared to the gabbronorite matrix that yields an Nd_i of 0.28154±0.00019 (Fig. 8.4)

Table. 9. 3. Lu-Hf isotopic data for the spherical orthopyroxenite, gabbronorite matrix, and the Pyroxenite layer from the TBM.

Sample location	Lu (ppm)	Hf (ppm)	$^{176}Lu/^{177}Hf$	2SE	$^{176}Hf/^{177}Hf$	2SE	Constant	$^{176}Hf/^{177}Hf_i$	εHf
Spherical orthopyroxenite									
LTBM	0,13	0,82	0.019424	0.000124	0.281931	0.000039	1.867E-11	0.281168	-10.6
UTBM-1	0,15	1,66	0.018428	0.000054	0.281949	0.000040	1.867E-11	0.281225	-8.6
UTBM-2	0,22		0.016334	0.000066	0.281817	0.000042	1.867E-11	0.281175	-10.4
Gabbronorite matrix									
LTBM	0,15	1,61	0.013172	0.000034	0.281759	0.000032	1.867E-11	0.281241	-8.0
UTBM-1	0,19	1,21	0.013974	0.000030	0.281701	0.000032	1.867E-11	0.281152	-11.2
UTBM-2	0,15	1,28	0.016516	0.000090	0.281788	0.000033	1.867E-11	0.281139	-11.7
Pyroxenite layer									
Pyroxenite	0,24	1,1	0.029155	0.000012	0.282324	0.000036	1.867E-11	0.281178	-10.3

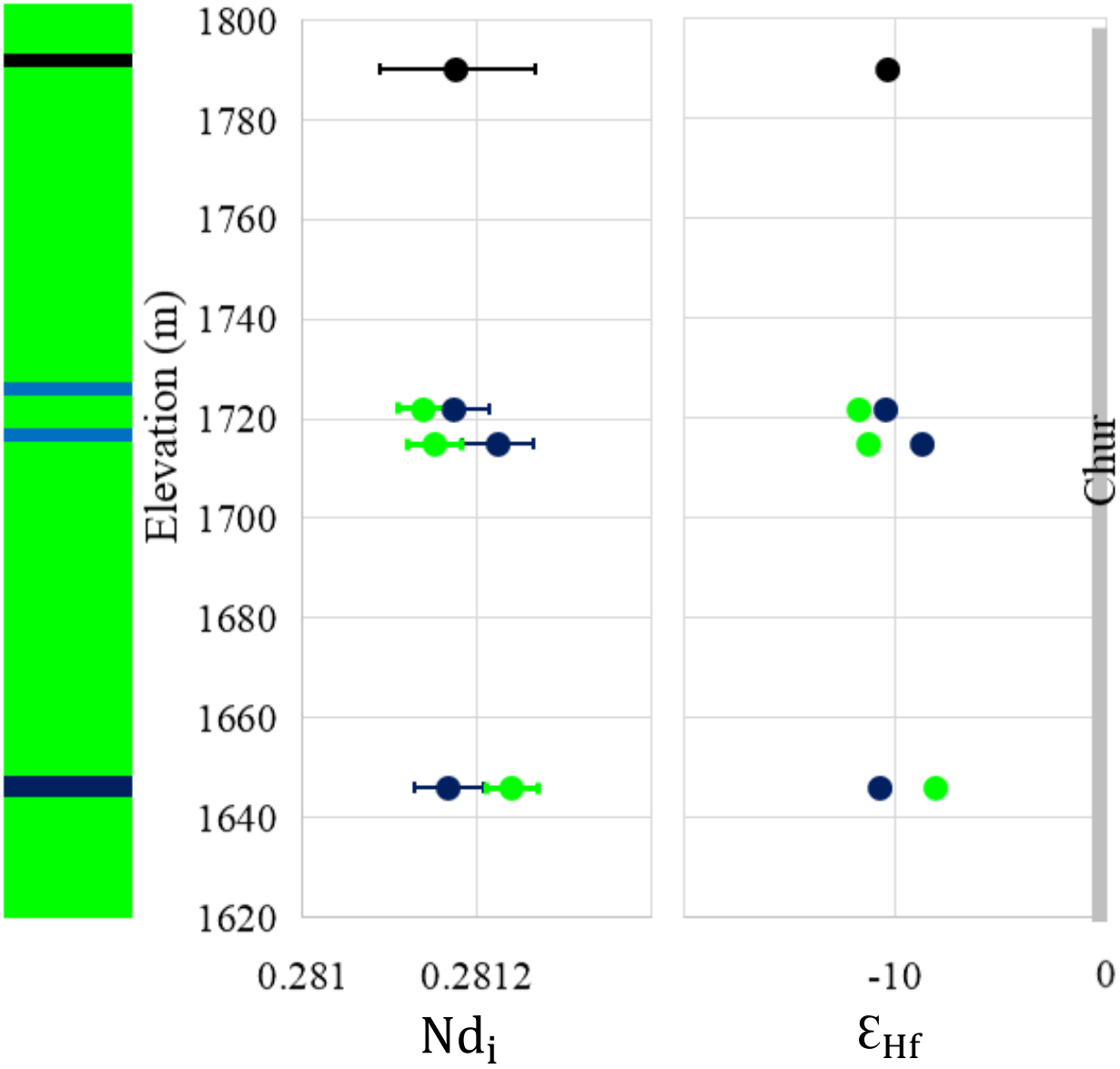

Fig. 9. 5. The stratigraphic columns of the TBM package, showing the approximate locations of the TBM layers and the changes in the Hf_i and the ε_{Hf} Hf of the spherical orthopyroxenite and the gabbronorite matrix. The blue closed circles represent the spherical orthopyroxenite, and the green closed circles represent the gabbronorite matrix.

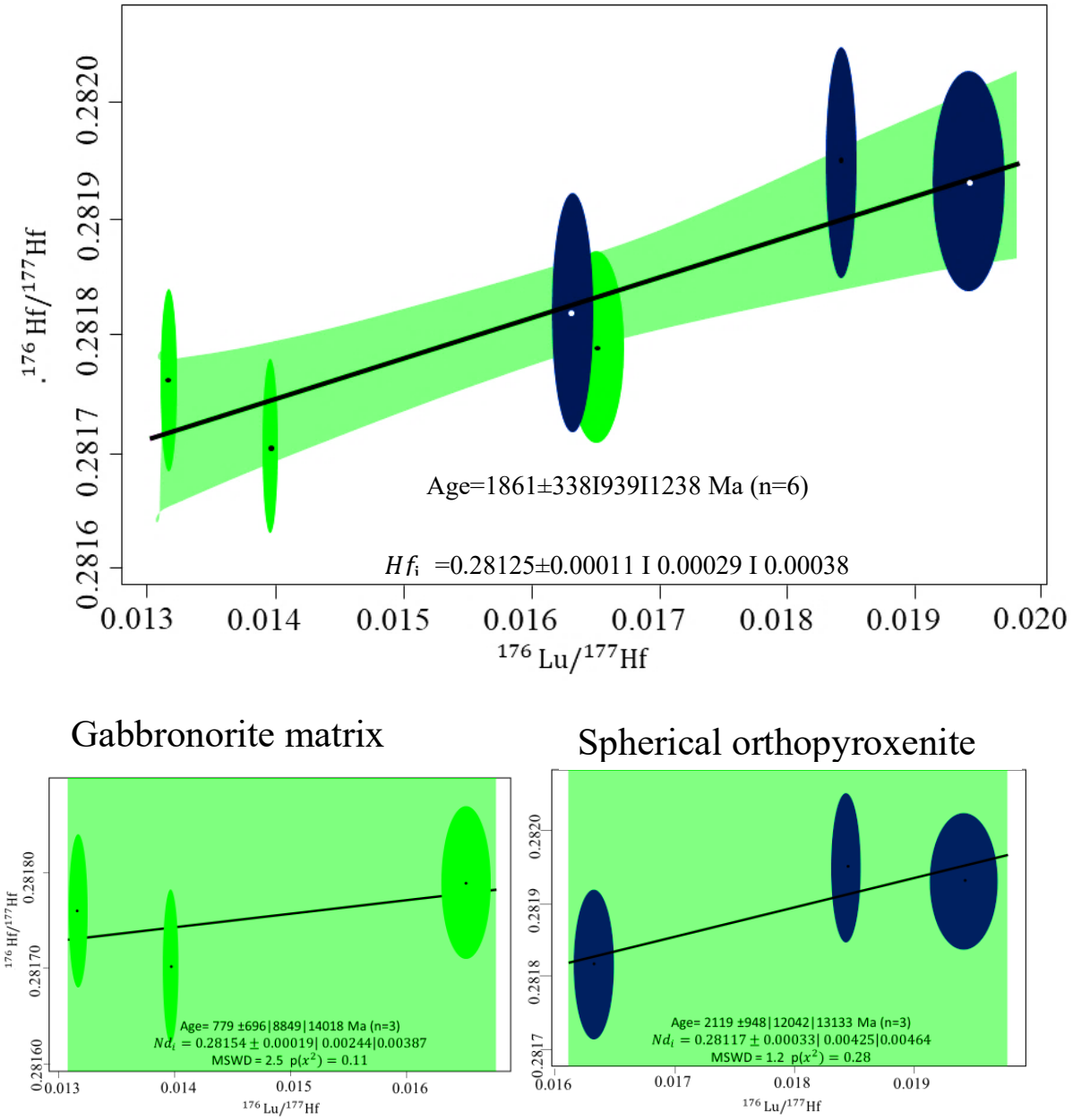

Fig. 9. 6. The isochron plots of the TBM layers (a) Isochron plots of the spherical orthopyroxenite and the gabbronorite matrix, showing the Lu-Hf calculates ages and the Hf_i . (b) Isochron plot of the spherical orthopyroxenite, showing its age and the Hf_i (c) Isochron plot of the gabbronorite matrix, showing its age and the Hf_i .

Chapter 10: Sulphides and PGE mineralization

TBM layers were intercepted several times during a drilling exploration project that a mining company conducted at the Western Lobe of the RLS. The boreholes' core logging confirmed a strong correlation between the TBM layers and BMS (Appendix 1). This sparked an interest in investigating the possible occurrence of BMS and PGEs (osmium (Os), iridium (Ir), ruthenium (Ru), rhodium (Rh), platinum (Pt), and palladium (Pd)) at the TBM layers on the Eastern Lobe. In nature, PGEs occur as alloys with other elements such as antimony (Sb), tin (Sn), mercury (Hg), bismuth (Bi), tellurium (Te), sulfur (S), and lead (Pb) to form platinum-group minerals (PGM). Also, PGMs are usually associated with magmatic bodies with nickel-copper-iron (Ni-Cu-Fe) sulfide and chromite deposits like those at the RLS (Uysal *et al*., 2009).

10.1. Stratigraphic variations of chalcophile elements

S, Cu, Ni, and Co are common elements in PGE ores. Hence, they are considered good indicators of BMS occurrences in a rock (Latypov *et al*., 2017, Seabrook, 2003). The concentrations of these elements have been plotted against height to study their distribution within the TBM layers (Fig. 10.1).

The S concentrations at the TBM vary unstably between 0.004 Wt.% to 0.056 Wt.% (Fig. 10.1a). It does not show preference to occur in either the spherical orthopyroxenite or the gabbronorite or TBM layers. However, the spherical orthopyroxenite in the Upper TBM 2 possesses the highest sulfur content concentrations (0.056 Wt.%) relative to the other rocks in this area. This amount of sulfur corresponds to 0.1 vol% of disseminated sulfides in the spherical orthopyroxenite.

The spherical orthopyroxenite has a higher Ni concentration on the spherical orthopyroxenite relative to the gabbronorites (Fig. 10.1b). Additionally, it slightly decreases upwards in both the spherical orthopyroxenite and the gabbronorites (Fig. 10.1b). The Ni concentrations on the gabbronorites exhibit a pattern like the one possessed by orthopyroxene modal % (Fig. 8.1a).

The Cu concentrations show an increase from the Contact gabbronorite to the Lower TBM and become constant from the spherical orthopyroxenite poor gabbronorite to the Normal gabbronorite (Fig. 10.1c). Some spherical orthopyroxenite have a higher concentration in Cu than their respective matrixes (Fig. 10.1c). The spherical orthopyroxenite with the highest Cu concentration on the Upper TBM 2 is the same sample that had the highest sulfur content.

10.2. Correlation diagram of chalcophiles with sulfur

The gabbronorite matrix, host, and spherical orthopyroxenite do not show any correlations between S with Co and Cu (Fig. 10.2). The gabbronorites show a fragile correlation relationship between the S and Cu. However, spherical orthopyroxenite shows a positive S and Cu correlation with only one point falling out of the lineation (Fig. 10.2a). The Co and S variation diagram shows a horizontal correlation trend which implies that the amount of Co remains constant with an increase in S for both the spherical orthopyroxenite and the gabbronorites (Fig. 10.2a).

10.3. Sulphide minerals in the TBM

A total of 17 sulfide grains were found on the gabbronorites and the spherical orthopyroxenite. They occur as intercumulus phases between plagioclase, orthopyroxene, and clinopyroxene cumulates (Fig. 10.3). They have crystal sizes that range between 50-100 microns, and they are not easily distinguishable on the SEM images. Hence, some were analyzed to identify their mineral compositions. The TBM's sulfides are assembled by pyrrhotite, chalcopyrite, pentlandite, and pyrite (Table. 10.1).

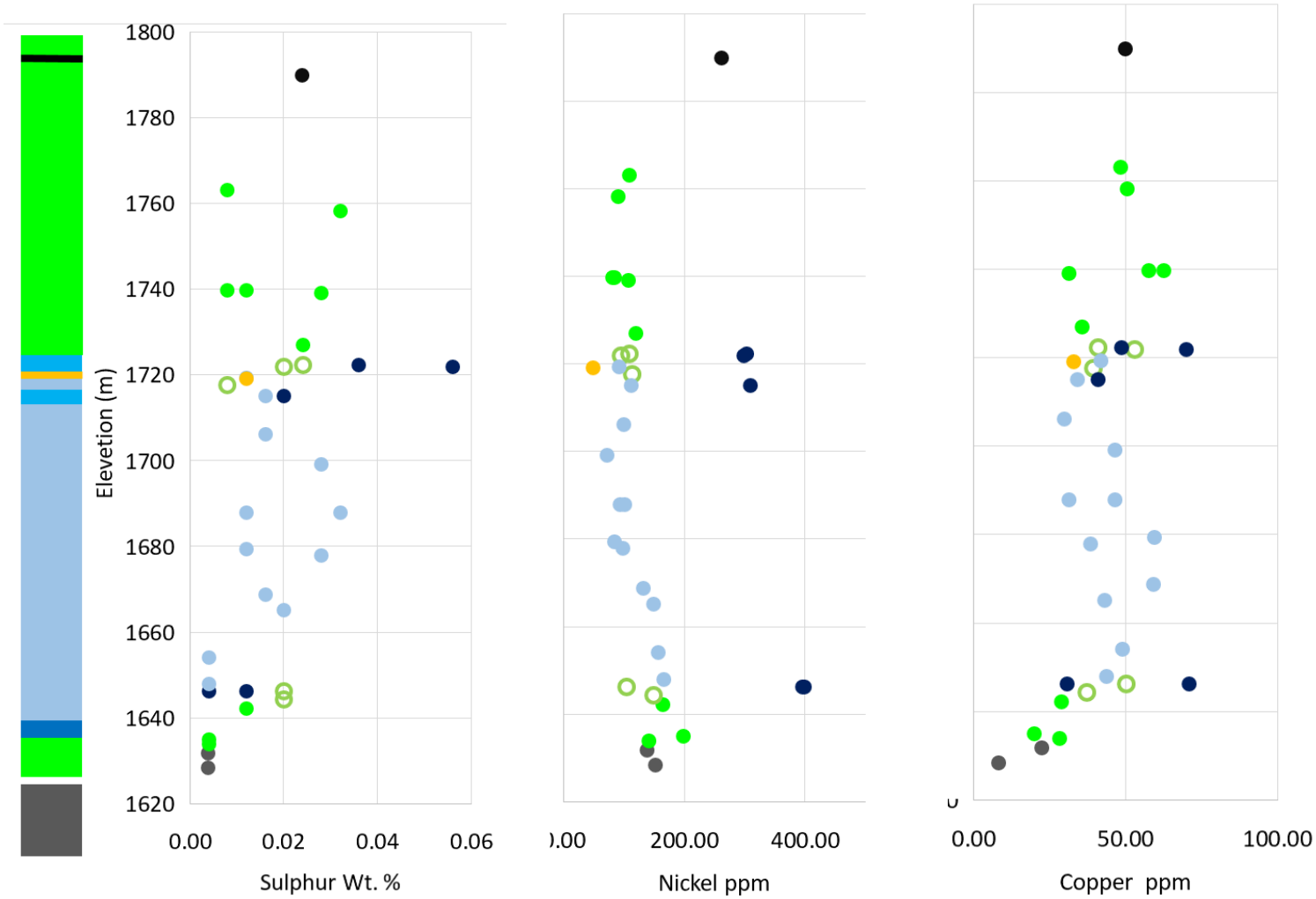

Fig. 10. 1. Profile of chalcophile elements through the TBM showing the variation of S, Cu, and Co upwards. (a) The S profile shows the unstable variation of S. Its highest concentration of the spherical orthopyroxenite at the Upper TBM 2 (b) Ni profile shows a higher concentration of Ni on the spherical orthopyroxenite in all the TBM layers, which also decreases slightly upwards. (c) Co profiles showing the increase in the Cu concentrations at the Contact gabbronorite, which becomes constant at the Lower TBM to the Normal gabbronorite.

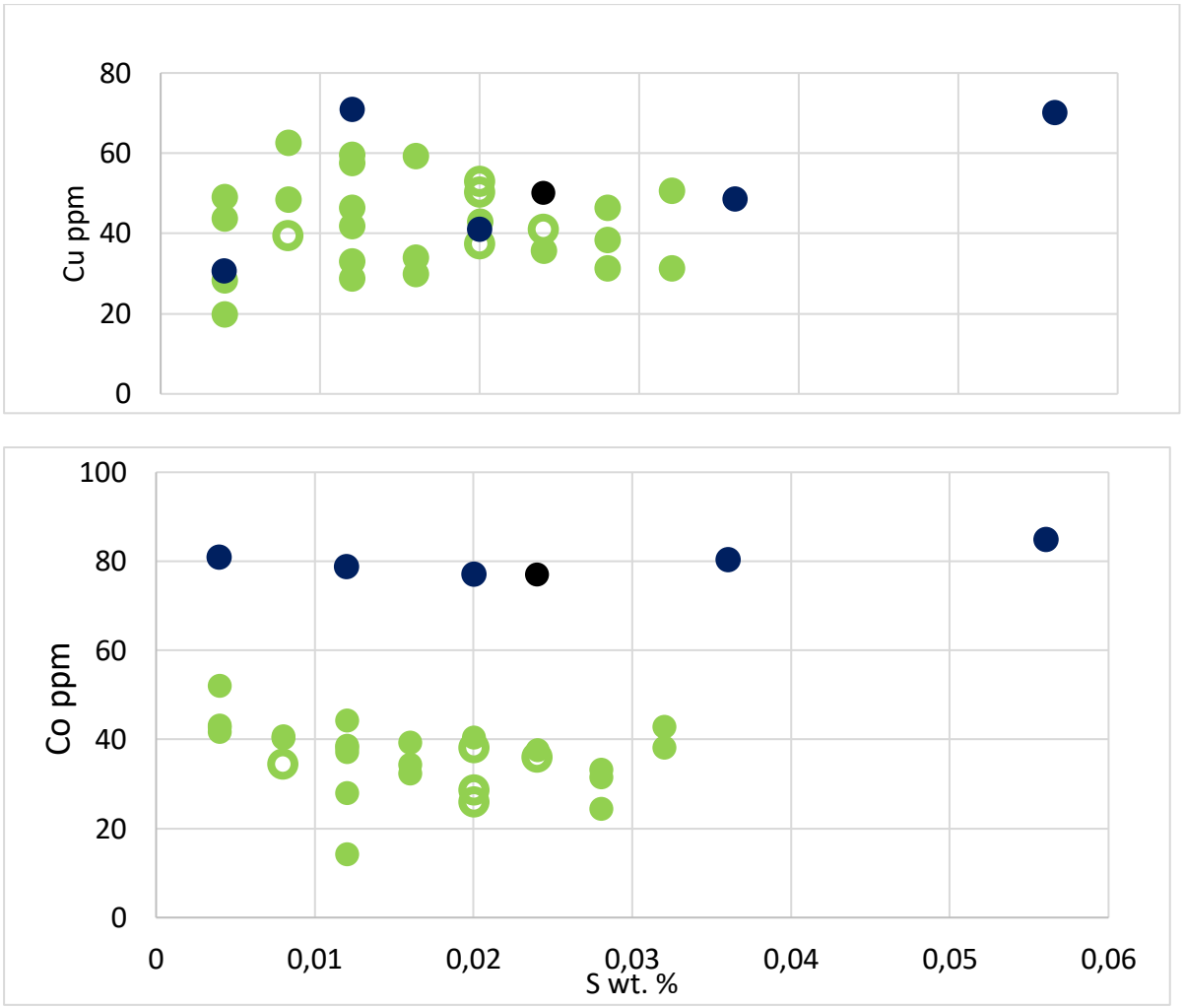

Fig. 10. 2. The correlation trends between S with Co and Cu. (a) The different correlations trends between the spherical orthopyroxenite and the gabbronorite matrix and host. The gabbronorite shows no correlation, while the spherical orthopyroxenite show a stronger correlation relationship. (b) The horizontal correlation between S and Co for the spherical orthopyroxenite and the encasing gabbronorite.

Table. 10. 1. Selected electron microprobe analyses on some sulfide minerals at the TBM.

	Major Sulphide forming elements							PGE alloys				PGE			
PGM	S	Fe	Ti	Cr	Co	Ni	Cu	As	Sb	Bi	Te	Rh	Pd	Os	Pt
?	7,11	78,76	1,71	9,92		0,50	0,32		0,39				1,03	0,26	
?	11,14	78,60	0,90	0,59		0,54			0,78	5,13					2,32
?	7,39	78,40	10,67	1,08		0,70	0,18					0,23		0,29	1,05
?	13,45	77,74	5,03	0,78		0,55	0,82								1,63
pyrrhotite	23,27	74,62	0,63	0,00		0,54			0,36	0,52			0,06		
?	5,76	74,30	14,23	2,93	0,10	0,64		1,28			0,07	0,04	0,42	0,24	
pyrrhotite	23,76	72,84	1,00	0,00		0,02	0,33	0,80	0,06					1,20	
?	8,27	72,14	13,53	4,18		0,31				1,04		0,31	0,22		
pyrrhotite	23,69	67,59	0,63	0,50	0,26	0,23	0,26	0,26	0,40	5,33	0,41	0,26		0,18	
pyrrhotite	23,55	66,93	0,40	0,00	0,66	0,97	0,40	0,38	0,70	3,53			0,66	0,07	1,75
chalcopyrite	26,37	65,28	0,07	0,00	0,21	1,65	3,44	1,19		0,00			1,40	0,38	
pyrrhotite	29,60	59,84	1,11	0,43	0,49	0,14	0,53	3,93	1,07	2,16	0,25		0,21		0,23
Pentlandite	27,96	59,17	1,38	0,48	0,86	4,69					0,43		2,38		2,65
pyrrhotite	20,20	56,56	10,75	1,37		1,65	1,43	1,84		5,76		0,27		0,16	
pyrrhotite	47,39	47,76	2,14	0,03	0,15	1,43	0,30	0,08	0,56		0,02			0,13	
pyrrhotite	48,64	47,35	2,23	0,00		0,51	0,32		0,66		0,07	0,13		0,05	0,05
pyrite	52,97	43,39	0,09	0,03	0,22	0,41	1,09	0,28	0,17	0,70			0,13	0,19	0,35

10.3.1. Microphotographs

The TBM has a few pyrrhotite and chalcopyrite grains that occur as inclusion and intercumulus phases, respectively (Fig. 10.3). They have a diameter of 100-600µm and are enclosed by plagioclase cumulates (Fig. 10.3). On some occasions, they are surrounded by both plagioclase and biotite grains (Fig. 10.4, Fig. 10.5a). These minerals were scanned for Au, Ir, Pd, Os, Pt, and Ru. The Os, Au, Ir, and Pt show a slight enrichment in the chalcopyrite's PGEs relative to the silicate minerals (Fig. 10.5a). However, the Pd and Ru do not display any form of enrichment on the chalcopyrite.

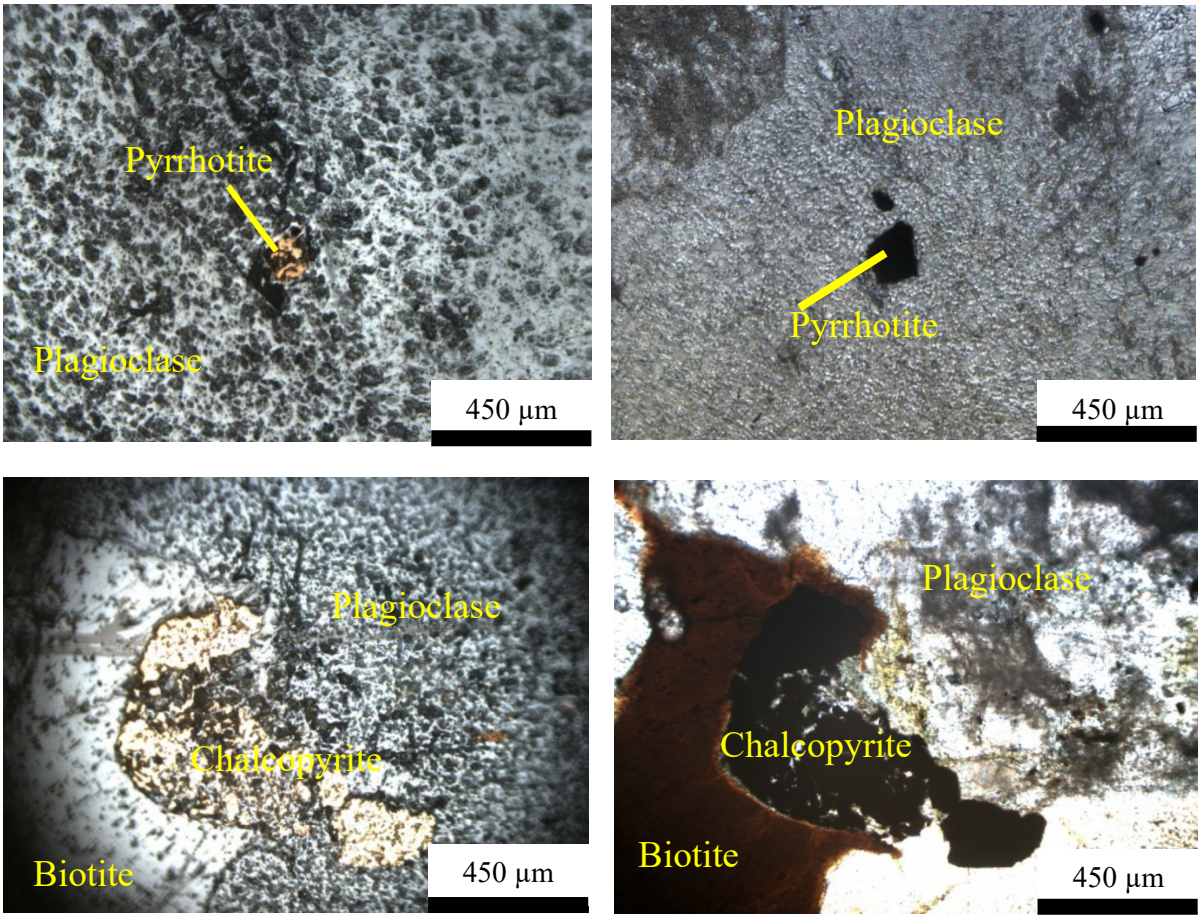

Fig. 10. 3. (a) Photomicrograph of the Contact gabbronorite taken at reflected light, showing the pyrrhotite inclusion of the cumulus plagioclase. (b) Photomicrograph of the Contact gabbronorite, taken under XPL. It shows the pyrrhotite inclusion on the plagioclase crystal. (c) Photomicrograph of the Contact gabbronorite taken at reflected light. It shows the intercumulus chalcopyrite between cumulus plagioclase and intercumulus biotite. (d) Photomicrograph of the Contact gabbronorite taken at XPL. It shows the intercumulus chalcopyrite between cumulus plagioclase and intercumulus biotite.

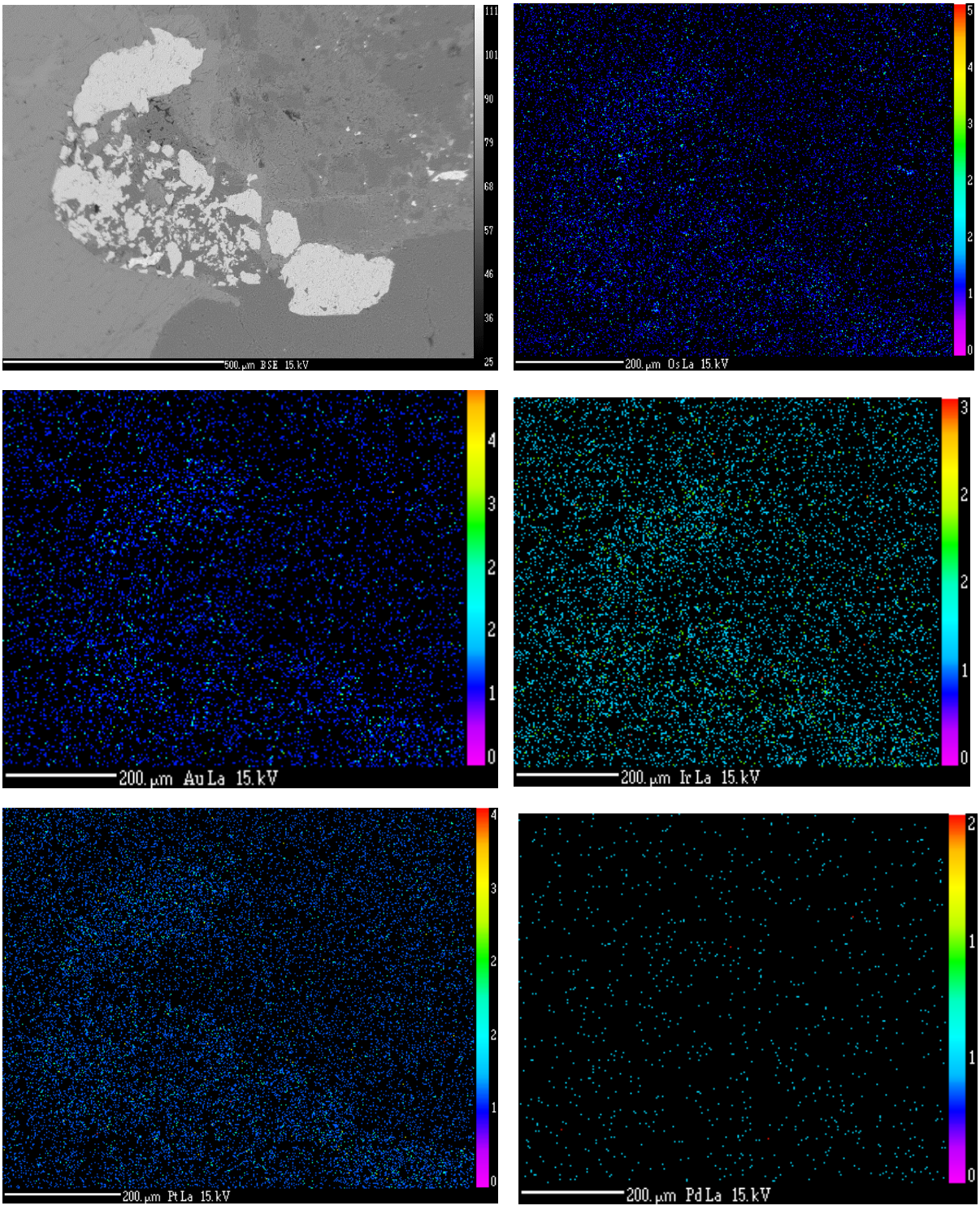

Fig. 10. 4. (a) Backscattered electron images showing the morphology of the chalcopyrite between the plagioclase and the biotite from the Contact gabbronorite. (b-f) Chemical maps of PGE and Au on one of the chalcopyrite grains.

Chapter 11: Interpretation and discussion

The TBM is Ball Marker, its host, the RLS, consists of the same mineral assembles at different propositions. This is proposed to originate from several processes such as fractional crystallization, sorting of crystal mushed in the magma chamber, and two (or more) staging chambers that bring magma simultaneously into the RLS chamber (Bowen, 1915; Cawthorn, 1996; Yao *et al*., 2020). The spherical orthopyroxenite is a unique feature of the RLS. The spherical rocks are rare in the mafic-ultramafic intrusion. However, they are dominant in are common felsic and intermediate intrusion worldwide (Barbarin, 2005; Bateman & Chappel, 1979; Campbell, 1977; Elliston, 1984; Farnand, Smith, & Puddington, 1961). Many hypotheses have been proposed to explain the origin of the spherical shape. These hypotheses include liquid immiscibility, crystal aggregations, superheating, volatile addition, etc.

11.1. The parental magma of the spherical orthopyroxenite and the gabbronorite matrix

11.1.1. The magmatic sources of the orthopyroxenite and the gabbronorite matrix

The basis of the study is to establish the source of rock composition. The primary question is whether these two cumulates are differentiation products or two staging chambers products. This study shows a similar isotopic composition of spherical orthopyroxenite, gabbronorite matrix, and pyroxenite layers (Fig. 9.1; Fig. 9.2; Fig. 9.3; Fig. 9.4; Fig. 9.5 and Fig. 9.6). The diversity of the cumulate composition could be a result of magma differentiation.

11.1.2. Differentiation of the pyroxene rich magma to a gabbroic magma

The pyroxenite layer, which shares the same isotopic composition, shows a critical observation explaining the differentiation process. This layer shows a sharp-undulating lower contact and a grading upper contact (Fig. 4.8). This layer's contacts show that the fundamental processes driving magma composition's evolution are possible fractional crystallization. The undulating, sharp lower contact shows the introduction of a new magma that partially dissolved the footwall. The dissolution is accompanied by cooling and crystal growth and the immediate removal of crystals from the melt, which caused the melt to evolve. This study interprets the orthopyroxene inclusions in plagioclase (Fig. 6.6) as additional evidence for this evolution. Hence it proposed that the inclusion mark when the melt composition shifted from pyroxene saturation to eutectic composition.

11.1.3. Magma fractionation

The evolution of the magma is also supported by the REE patterns of the TBM package. They show more LREE enrichment on the gabbronorite relative to the spherical orthopyroxenite (Fig. 8.5). In contrast, they possess similar HREE abundance (Fig. 8.5). The LREE enrichment in the gabbronorites shows that it crystallized from more fractionated magma than the spherical orthopyroxenite.

11.1.2. Crystallization of the pre-existing orthopyroxenite layer

The similarity between the pyroxenite and spherical orthopyroxenite suggests that they crystallized from a similar magma. Therefore, this study proposed that the spherical orthopyroxenite was once layering like the pyroxenite layer. An introduction of orthopyroxene saturated magma into the chamber cooled through fractional crystallization and evolved to the eutectic (Wager and Brown,1968; Campbell *et al*., 1978; Cawthorn, 2002; Fig.11.1b; Fig. 11.1c). Hence, the magma solidified from the base, with the solidifying front propagating upwards as the orthopyroxene crystals settled to the floor (Fig. 11.1c).

11.2. The break up of the pre-existing orthopyroxenite

The angular orthopyroxenite supports the break up of a pre-existing orthopyroxenite layer during the intrusion of magma. Therefore, the orthopyroxenite layer crystallized (as per section 11.1.2) got fragmented by the incoming magma into the chamber. The Eastern Lobe's transgressive nature suggests lateral chamber growth, with magmas flowing towards the south in our study area (Fig. 1. 2; Fig. 1.3). This study proposes that magma intrusion, fractional crystallization, and chamber extension took place simultaneously. Also, the isotopically homogenous magma intruded as multiple injections into the chamber that subsequently broke pre-existing layers.

The ascending pressure at the feeder increased the pressure on the magma chamber, and it overcame the confining pressure at the sides of the magma chamber. Therefore, the surrounding rocks were fracturing, including the base's orthopyroxenite layer when magma was intruding (Fig. 11.1d). The magma started percolating between the orthopyroxenite fragments as it continues to extend the magma chamber (Fig. 11.1e). The hydraulic force from the percolating magma eventually eroded the angular orthopyroxenite from the chamber floor and moved them further towards the south (Fig. 11.1f).

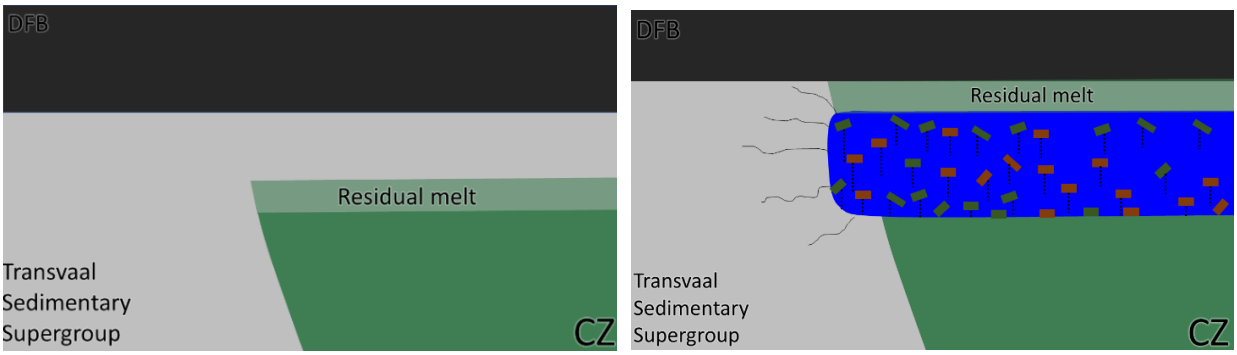

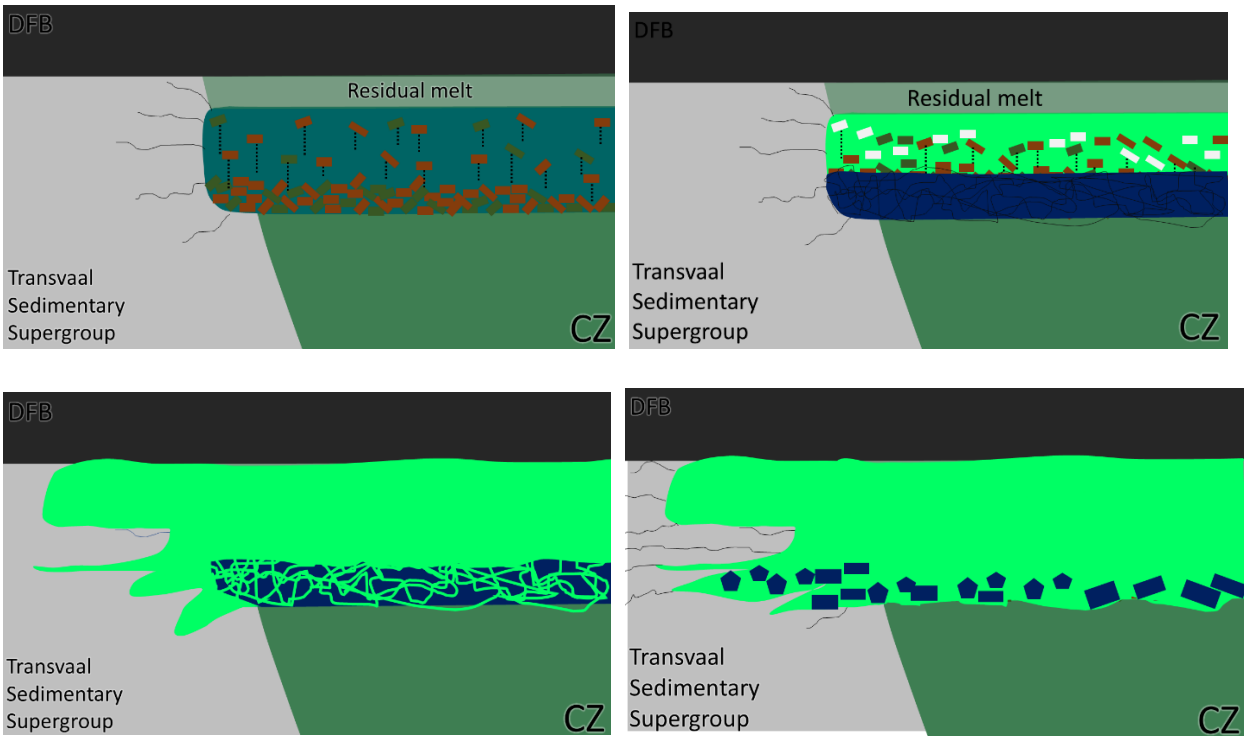

Fig. 11. 1. Model illustrating the crystallization and fragmentation of orthopyroxenite layer. (a)The chamber before the introduction of the MZ magma showing CZ overlain by the residual melt. (b) The influx and fractional crystallization of pyroxene saturated magma. (c) The formation of the orthopyroxene mush is the base of the chamber and changes in the magma composition. (d) The solidification of the orthopyroxene mush, introduction of new magma, and fractional crystallization. (e) Break up the pre-existing orthopyroxenite layer and percolation of the magma between the orthopyroxenite fragments. (f) The hydraulic pressure of the percolating magma overcomes the weight of the orthopyroxenite pieces, and it erodes it and transports it towards the south.

11.3 The origin of the spherical orthopyroxenite

11.3.1. Insight from the different shapes of the orthopyroxenite

At the RLS, orthopyroxenite occur as interlayered layers with gabbronorite, norite, anorthosites, and other lithologies (Eales and Cawthorn, 1996; Mukherjee *et al*., 2017). Conversely, orthopyroxenite at the TBM possess various shapes, ranging from spherical, oval, and sub-rounded to rectangular/angular (Fig. 3.3).

This study interprets the subrounded-square, oval, and sub-trapezium orthopyroxenite (Fig. 5.3a and Fig. 5.3e) as pieces of evidence for the progressive stages that took place during the transformation of angular orthopyroxenite to spherical orthopyroxenite. The orthopyroxenite were angular after the fragmentation,

and they went through dissolution, which produced the spherical orthopyroxenite observed on the TBM. This study referred to this process as the "spherical dissolution," resulting from the thermo/chemical disequilibrium between melts and solids with different chemical compositions (Campbell, 1986; Latypov *et al*., 2015; Latypov *et al*., 2017).

11.3.2. Chemical disequilibrium

Thermal disequilibrium causes bulk or selective melting of the solid and solid and liquid interface (Latypov *et al*., 2015). The orthopyroxenite at the TBM does not show any signs of bulk or selective melting. Therefore, the effects of thermal equilibrium were petite, and those of chemical disequilibrium were more dominant during the spherical dissolution process. There was chemical disequilibrium between the solid angular orthopyroxenite and the gabbronorite melt (Fig. 11.2). Therefore, the chemical disequilibrium caused the orthopyroxenite to dissolve into the gabbronorite melt as the system re-equilibrated.

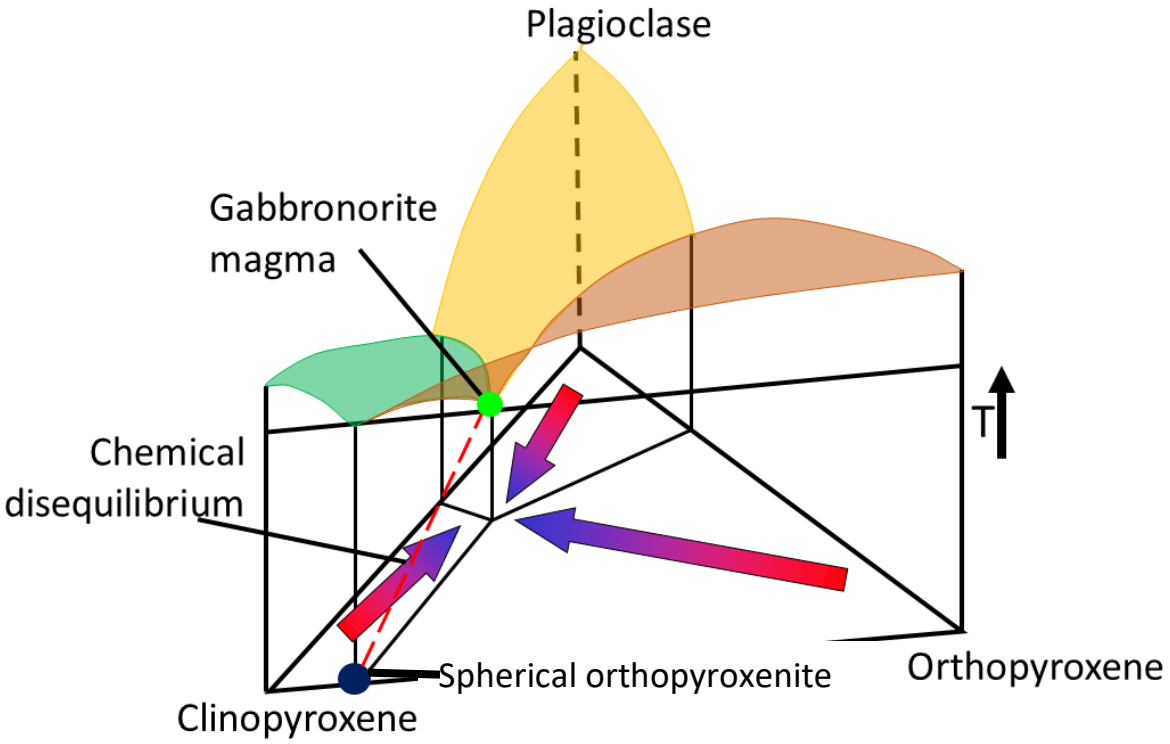

Fig. 11. 2. The ternary diagram showing the position of the gabbronorite melt and the orthopyroxenite. The red line is the chemical disequilibrium between the two bodies.

11.3.3. Spherical dissolution

This study suggested that the dissolution of angular orthopyroxenite was initiated at the solid-liquid interface and propagated towards the orthopyroxenite bodies' centers. The dissolution took place on the surface of the angular orthopyroxenite at a uniform rate in all the planes because they have a uniform composition and texture throughout (Fig. 6.4 and Fig. 6.7). However, the areas where two or three planes meet to form corners and edges experienced dissolution in two or three directions, parallel to the dissolution direction of the joining planes (Fig. 11.3a).

Therefore, the dissolution rate was faster on the edges and corners, which caused them to dissolve more rapidly (Fig. 5.3c, Fig. 5.3d, and Fig. 11.3b). As a result, the edges and the corners of the angular orthopyroxenite dissolved to form sub-angular pyroxenite (Fig. 5.3c, Fig. 5.3d, and Fig. 11.3b). This process continuously dissolved the edges and corners on the orthopyroxenite until they yield a sub-rounded shape (Fig. 11.3c), and eventually, all the borders dissolved to form spherical orthopyroxenite (Fig. 11.3c).

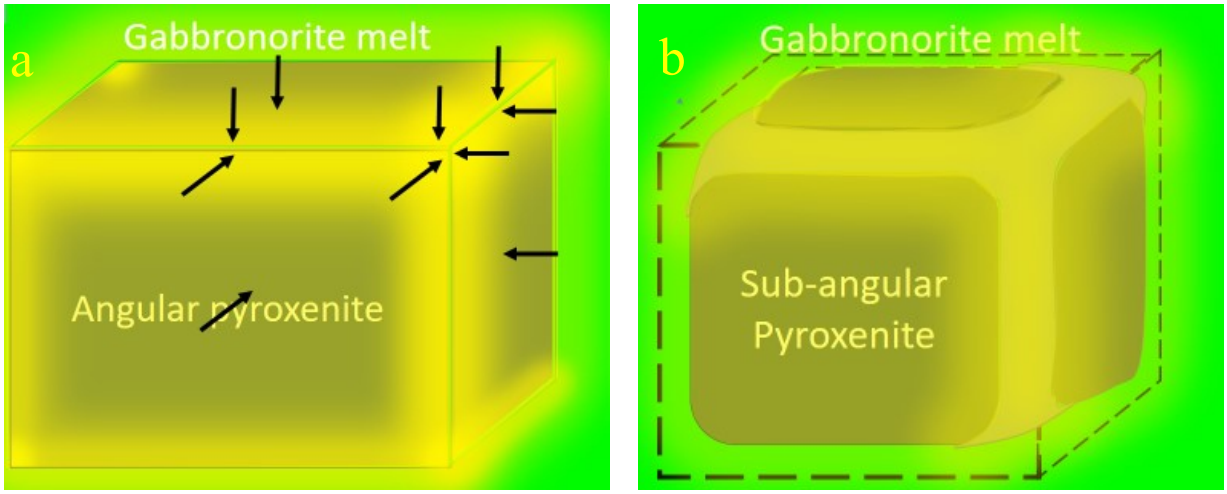

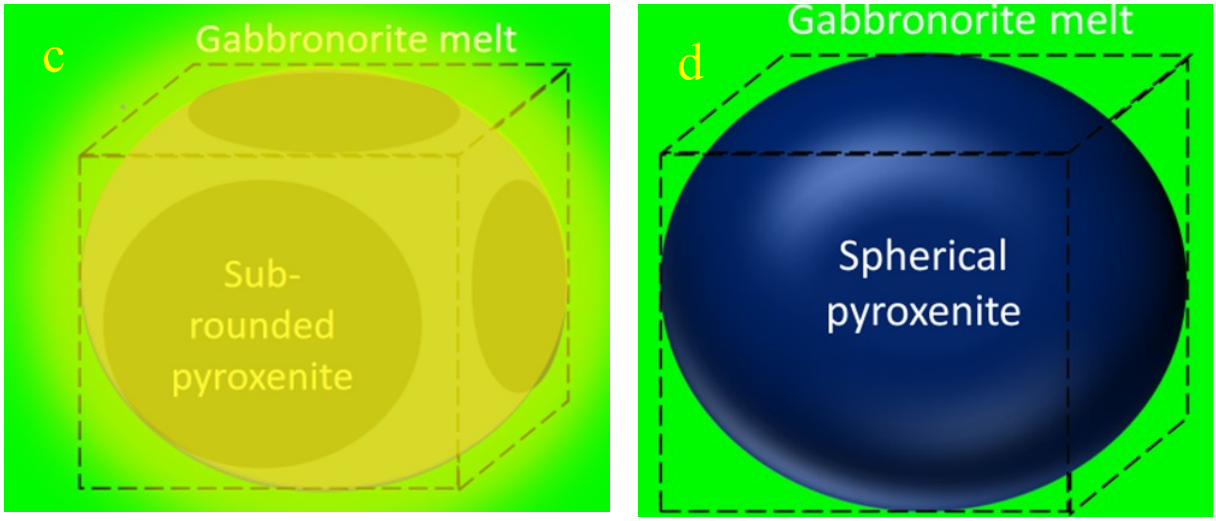

Fig. 11. 3. Schematic annotation of the spherical dissolution process. (a) Intense dissolution on the corners and edges of the angular orthopyroxenite. The black arrows show the direction of dissolution on the planer surfaces, corners, and edges. (b) The partially dissolved angular orthopyroxenite body, with a sub-angular shape. (c) The subrounded orthopyroxenite with a few corners joining curved. (d) The spherical orthopyroxenite bodies in the matrix of gabbronorite.

11.3 Transportation of spherical orthopyroxenite

11.3.1. Attrition spherical orthopyroxenite

The semi-circular, arc-shaped, and thin rectangular orthopyroxenite (Fig. 5.2) are interpreted as broken pieces of spherical orthopyroxenite. As the magma intruded into the floor rocks, its hydraulic force pushed the spherical orthopyroxenite towards the south. As a result, some spherical orthopyroxenite collided together and broke into smaller pieces with these shapes (Fig. 5.2). This piece of evidence shows that the spherical orthopyroxenite are xenoliths at the TBM.

113.2. Lateral opening of the magma chamber

The Contact gabbronorite is fingering into the DFB (Fig. 4.3c). The confinement resulted from the rigid TS and Rooiberg felsite, which are the host rocks of the RLS. Magma moving in an enclosed chamber acts like fluids that obey Pascal's principle in a hydraulic jack (Aragón *et al*., 2019). This principle states that " the pressure experienced by fluid in an enclosed container is equal throughout the container, and any

changes in pressure in one point will be distributed everywhere in that container (Aragón *et al*., 2019). This principle is governed by equations 1.

$$A_{roof}\left(\frac{F_{feeder}}{A_{feeder}}\right) = F_{confining} > F_{conduit} = A_{conduit\ magma}\left(\frac{F_{feeder}}{A_{feeder}}\right) \quad 1$$

In a hydraulic Jack, the pistol represents the magma feeder, the expandable container represents the magma chamber, and the ascending magma represents the input force (Aragón *et al*., 2019). The force exerted at the feeder must overcome the fracture strength and the confining pressure of the floor rocks (Aragón *et al*., 2019). The magnitude of the confining pressure in both directions plays an essential role in influencing expansion.

This magnitude depends on the magma flow direction (Aragón *et al*., 2019). The dotted lines highlight the cross-section areas of the roof, and the cross-section area of the side is highlighted by the red rectangle (Fig. 11.4). The top of the chamber has a larger size compared to the sides of the chamber. Therefore, the upwards confining pressure is larger than the sideways confining pressure. Hence, it will be easier to overcome the sideways confining pressure, and the magma chamber will prefer to expand laterally.

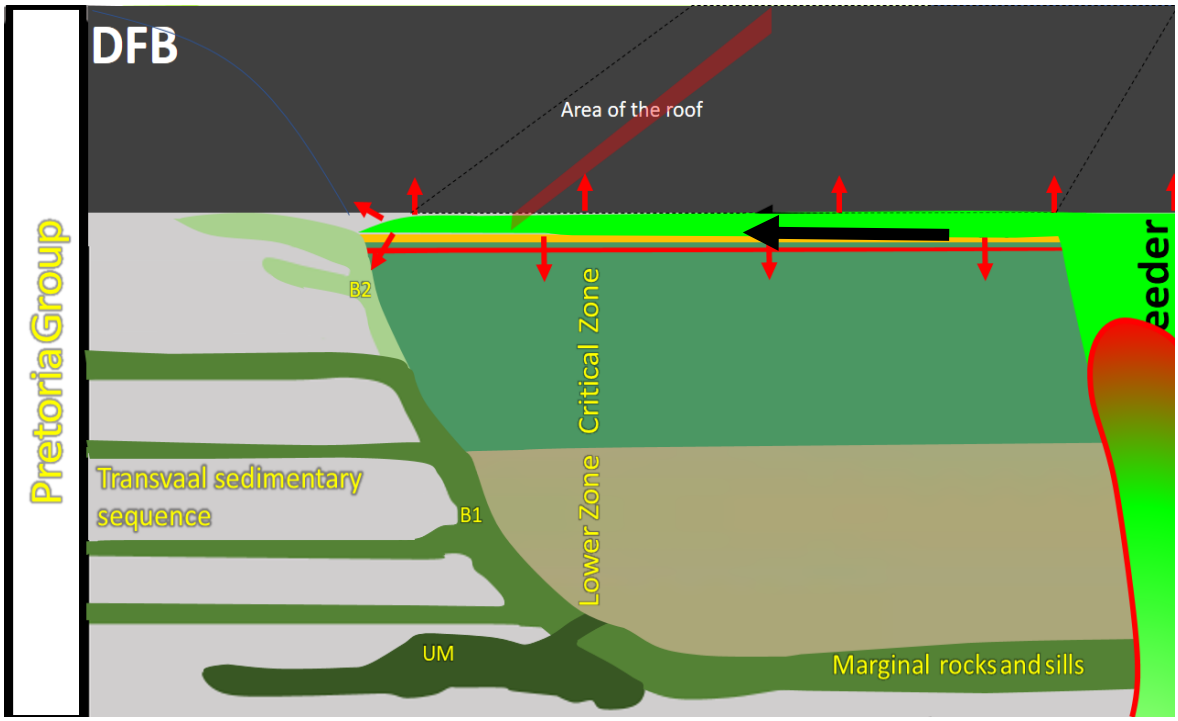

Fig. 11. 4. The cross-sections through the bushveld magma chamber showing the magma feeder and the intrusion of magma.

11.3.3. The missing cotectic cumulates

The Harker diagrams show a space between the chemical compositions of the spherical orthopyroxenite and the gabbronorites (Fig. 8.3). The normal differentiation sequence of an orthopyroxene saturated magma will form orthopyroxenite, norites, and gabbronorites. In some cases, it will form orthopyroxenite, gabbro, and gabbronorite. Therefore, this study suggests a fractional gab crystallization of the magma was taking place at the chamber and the feeder, as the magma was still intruding into the chamber. Hence, it recommends that the missing norite and the gabbro crystallized as the magma was flowing to the final destinations.

11.4 Deposition of the spherical orthopyroxenite

11.4.1. Marginal deposition of the spherical orthopyroxenite

The TBM shows a transgressive relationship with its footwall, and it abuts into the DFB (Fig. 1.1; Fig. 2.1; Fig. 2.2; Fig. 4.1b). This is interpreted as a consequence of magma intruding from the north towards the south. Hence, they were deposited at the margins when the magma stopped flowing.

11.4.2. Sinking spherical orthopyroxenite

The matrix occasionally hosts graded horizons that also seem to be distorted by the spherical orthopyroxenite (Fig. 5.9; Fig. 5.10; Fig. 5.11). These are interpreted as evidence of the depositions of the spherical orthopyroxenite on a crystal mush. There are orthopyroxene enriched horizons with straight and sharp contact with plagioclase enriched bands (Fig. 5.10). Additionally, the contact bend beneath the spherical orthopyroxenite (Fig. 5.10).

It is proposed that there was orthopyroxene enriched crystal mush at the base of the magma chamber (Fig. 11.5a). There was an introduction plagioclase saturated magma carrying the spherical orthopyroxenite (Fig. 11.5b). This magma deposited the spherical orthopyroxenite above the orthopyroxene enriched horizon and started crystallizing plagioclase. It formed a plagioclase horizon that graded to a gabbronorite. Also, some of the spherical orthopyroxenite have plagioclase saturated rims at their tops (Fig. 5.10). Hence, Philpotts and Dickson's (2000) theory was adopted to suggest that plagioclase crystals also settled to the chamber floor (Fig. 11.5c). The forces of gravity pulled the spherical orthopyroxenite downwards, and it caused a bulging of the underlying horizon (Fig. 11.5d).

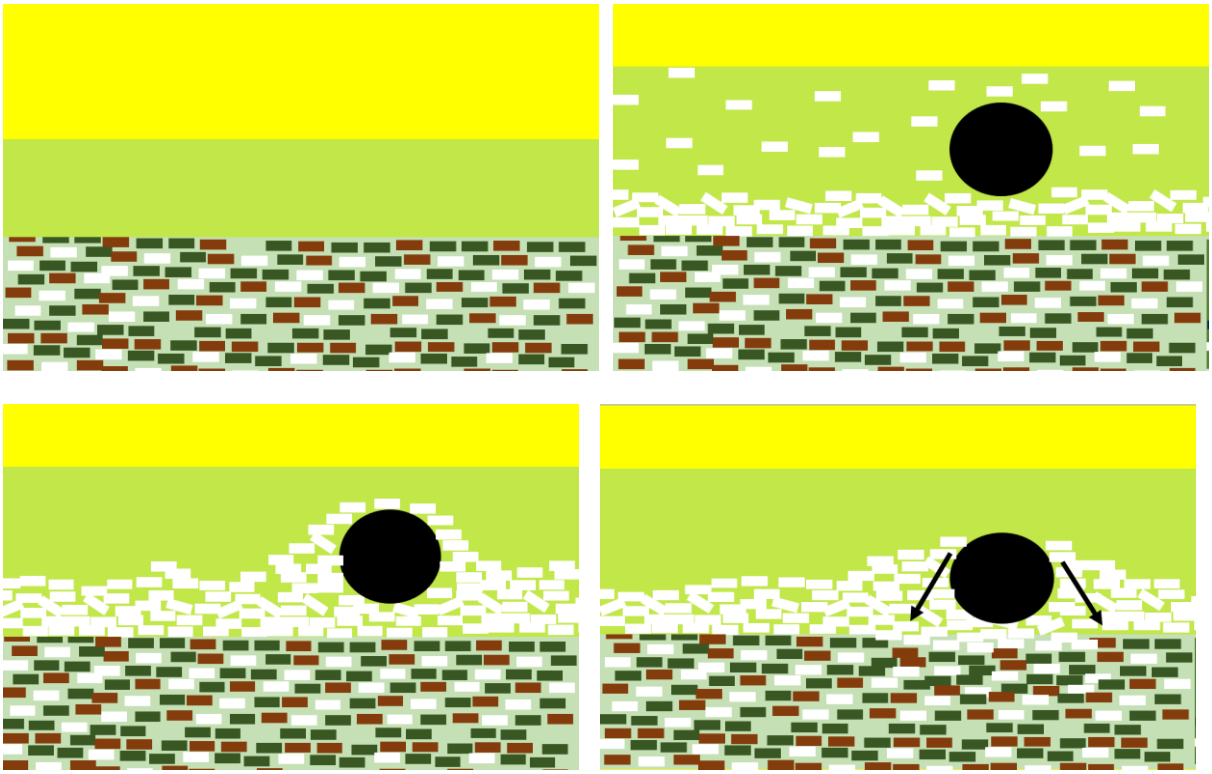

Fig. 11. 5. (a) The orthopyroxene enriched mush at the base of the magma chamber. (b) The intrusion of a plagioclase saturated magma that deposited the spherical orthopyroxenite. The crystallization and gravitational setting of plagioclase.

11.4.3. Insight from the changes in the spherical orthopyroxenite sizes

The spherical orthopyroxenite is sorted differently between the TBM layers. They are either poorly sorted (Fig. 5.6b) or the size increase (Fig. 5.6a) or decrease (Fig. 5.6c) up section. Stokes' law shows that its size and densities control the settling velocity of the sphere. The spherical orthopyroxenite have the same densities; hence sorting would be influenced by their sizes. Therefore, the larger spherical orthopyroxenite are expected to settle faster than the smaller ones. Thus the spherical orthopyroxenite would show an upwards decrease in their sizes. However, this does not explain the sorting in Fig. 5.6a and Fig. 5.6b. The sorting is interpreted as evidence that shows that the spherical orthopyroxenite was not deposited simultaneously.

11.4.4. Episodic deposition of the spherical orthopyroxenite

The decrease in the mafic components in the spherical orthopyroxenite up-section implies that its parental magma was getting more involved with time because of fractional crystallization of the magma (Cawthorn, 1996). The increase in the MgO, Mg# and Ni, indicate that the magma was becoming relatively more primitive at these levels, which is a reverse of average fractionation trends. Therefore, this shows a replenishment of new magma at these levels. This also changes the overall composition of magma before a normal fractionation process resumes.

Moreover, the TBM has spherical orthopyroxenite chains that are subparallel to one another (Fig. 5.4). That sub-parallel chains are interpreted as evidence of episodic deposition of the spherical orthopyroxenite as the magma was replenishing. This study proposes that each chain represents an introduction of magma carrying spherical orthopyroxenite (Fig. 11.7a). This magma deposited the spherical orthopyroxenite as it started to lose its energy (Fig. 11.7b). The spherical orthopyroxenite aligned parallel to the chamber floor to form the chains that were overlain by the magma (Fig. 11.7b). Upon cooling, the magma started crystalizing to form the gabbronorite matrix, which covered the spherical orthopyroxenite chain (Fig. 11.7c). This process took place repeatedly to form bands with high concentrations of the spherical orthopyroxenite.

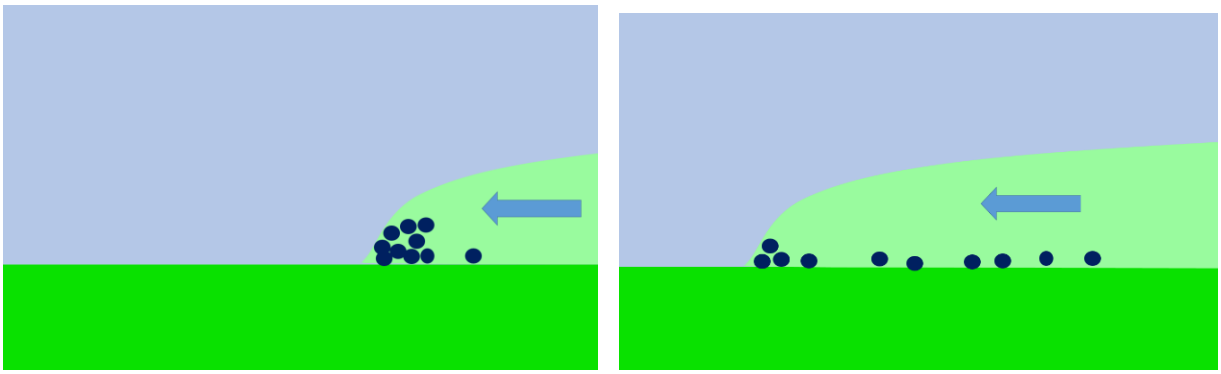

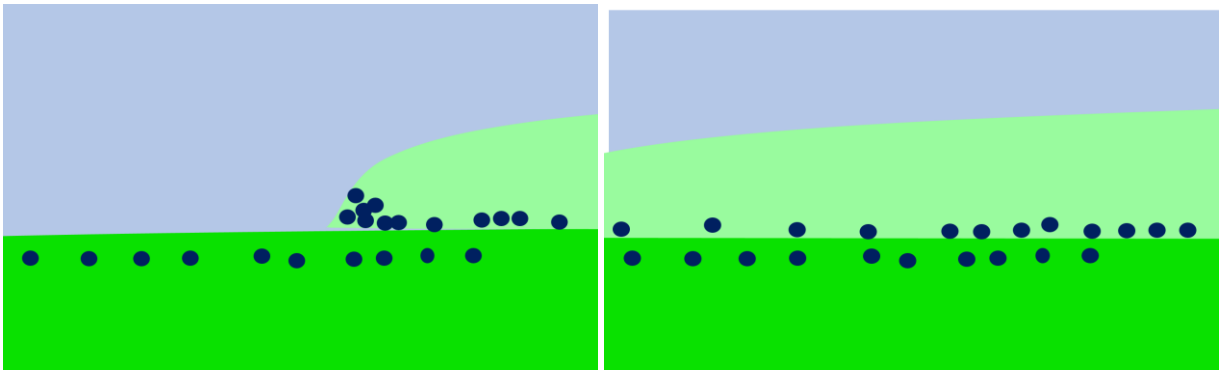

Fig. 11. 6. Schematic diagram showing the formation of spherical orthopyroxenite chains. (a) The intrusion of a magma transporting the spherical orthopyroxenite. (b) The deposition of the spherical orthopyroxenite and the magma loses its energy. (c) The intrusion of the succeeding magma carrying the spherical orthopyroxenite (d) Deposition of the second chain of spherical orthopyroxenite.

Chapter 12: Conclusions

This study documented the TBM's stratigraphy in the eastern Bushveld and coupled it with some field observations, geochemistry as isotopic data. The most significant observations are the occurrences of several orthopyroxenite shapes, spherical orthopyroxenite chains, breaks in the geochemical data, and the similarities in the isotopic composition of the spherical orthopyroxenite and the gabbronorite matrix.

These observations show that several processes simultaneously took place at the magma feeder and chamber during the TBM's origin. These processes include magma intrusion, fractional crystallization, magma chamber extension, the break-up of the orthopyroxenite layer, transportation of the fragments, dissolution of the fragments, deposition. Based on the observations presented in this study, the spherical, oval, subrounded, and angular orthopyroxenite (Fig. 1.2) represent fragments of a pre-existing orthopyroxenite layer that formed on the floor of the Bushveld chamber. The replenishment of magma broke the orthopyroxenite layer at the base as the magma chamber extended laterally. This process also may provide information about the magmas flow along with the sound of the Eastern Bushveld. The abutting nature of the TBM into the DFB in this study suggests that the Main Zone magma intruded southwards from the North.

This study presents a summarized model (a) An intrusion of an orthopyroxene saturated magma (Fig. 12). (b) Fractional crystallization of magma to form an orthopyroxenite layer at the base (Fig. 12). (c) The evolution of the resident magma (at the chamber and feeder). The gabbronorite magma ascended on the feeder and exerted a force to the chamber, which broke the base's orthopyroxenite layer as it was opening the magma chamber (Fig 12). (d) The new magma percolated in between the orthopyroxenite fragments (Fig. 12). (e) The magma-solid ratio increased, and it eroded and transported orthopyroxenite to the south (Fig. 12. (f) The spherical shapes of the orthopyroxenite were achieved by a chemical dissolution process

that eroded the edges and corners at a higher rate than the planar surface (Fig. 12). The magma's force flipped and overturned the orthopyroxenite for the dissection evenly (Fig. 12). (g) Transportation and (h) deposition of the spherical orthopyroxenite

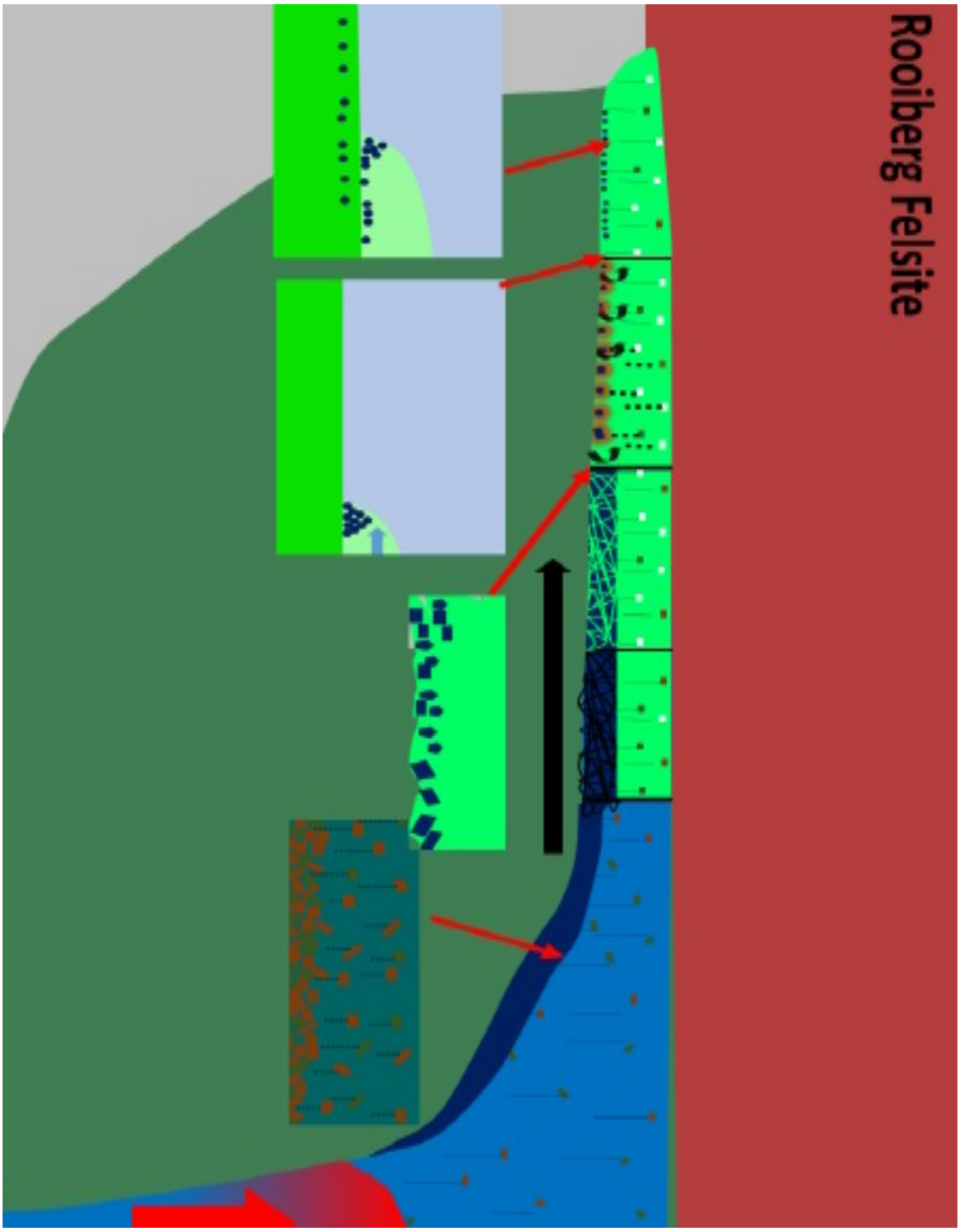

Fig. 12. 1. (a) Introduction of orthopyroxene saturated magma into the Bushveld chamber. (b) Cooling and crystallization of an orthopyroxenite layer at the base of the magma chamber. (c) Change in the magma composition and crystallization of gabbronorite above the orthopyroxenite layer. There was also an introduction of the magma, which extended the chamber and brokered the underlying orthopyroxenite layer. (d) Percolation of magma between orthopyroxenite fragments. (e) Erosion of the orthopyroxenite pieces to the south. (f) Overturning of the orthopyroxenite and even dissolution of the orthopyroxenite. (g) Transportation of spherical orthopyroxenite. (h) Episodic deposition of spherical orthopyroxenite at the chamber floor.

Recommendation

To extend the study to the Bolder Bed Marker, located at 30 below the Merensky Reef and the Western LIMB, to examine the petrographical relations of the two markers

Compare the petrographical and geochemical data of the TBM in the Eastern and Western Limb

Compared to the degree of differentiation between the Spherical orthopyroxenite and the gabbronorite matrix?

Explore the base metal sulfides on the western lobe and explore PGE mineralizations on the borehole logged by the mine.

To examine the texture of the pyroxenite layer from the base to the to track the differentiation process

References

Aragón, E., F. J., Lucio, P., Demartis, M., María, J., F., R., & E., J. (2019). Magma chamber growth models in the upper crust: A review of the hydraulic and inertial constraints. *Geoscience Frontiers*, Vol. 10, pp. 1211-1218.

Ballhaus, C. G., & Stumpfl, E. F. (1974). Occurrence and petrological significance of graphite in the Upper Critical Zone, western Bushveld Complex, South Africa. *Earth and Planetary Science Letters*, vol. 74, pp. 58-68.

Bamisaiye, O., Eriksson, P., Van Rooy, J., Brynard, H., Foya, S., Nxumalo, V., . . . Billay, A. (2014). Three-dimensional geometry of the Rustenburg layered suite, South Africa. *Canadian Journal of Tropical Geography*, Vol. 2. pp.1-14.

Barbarin, B. (2005). Mafic magmatic enclaves and mafic rocks associated with some granitoids of the central Sierra Nevada batholith, California: nature, origin, and relations with the hosts. *Science direct*, pp. 155-177.

Barnes, S. J., & Robertson, J. C. (2019). Time scales and length scales in magma flow pathways and the origin of magmatic NieCuePGE ore deposits. *Geoscience Frontiers*, Vol. 10; pp. 77-87.

Bateman, P. C., & Chappel, B. W. (1979). Crystallization, fractionation, and solidification of the Tuolumne Intrusive Series, Yosemite National Park, California. *Geological Society of America Bulletin*, Vol.90, p.465-482.

Blichert-Toft, J., & Albarède, F. (1997). The Lu-Hf isotope geochemistry of chondrites and the evolution of the mantle-crust system. . *Earth Planet. Sci. Lett.* , Vol. 148, pp. 243–258.

Boudreau, A. E. (1992). Volatile fluid overpressure in layered intrusions and the formation of potholes. *Australian Journal of Earth Sciences*, vol. 39, pp. 277-287.

Bowen, N. L. (1915). Crystallization differentiation in silicate liquids. . *American Journals Science*, Vol. 39, pp. 175-191.

Bowen, N. L. (1928). *The Evolution of the Igneous Rocks.* Princeton: Princeton University Press.

Brigham, R. H. (1983). A fluid dynamic appraisal of a model for the origin of comb layering and orbicular structure. *The Journal of Geology*, Vol. 91, No. 6, pp. 720-724.

Button, A. (1976). Stratigraphy and relations of the bushveld floor in the Eastern Transvaal. *South African Journals of Geology*, pp. 3-12.

Cameron, E. N. (1964). Chromite deposits of the Eastern part of the Bushveld Complex in Haughton: The geology of the ore deposits of Southern Africa. *Geological Society of South Africa*, Vol.2, pp.754-779.

Cameron, E. N. (1978). The Lower zone of the eastern Bushveld Complex in the Olifants River trough. *Journal of Petrology*, Vol. 19, pp. 437–462.

Cameron, E. N. (1980). Evolution of the Lower Critical Zone, Central Sector, Eastern Bushveld Complex, and Its Chromite Deposits. *Economic Geology*, Vol.75, 845-871.

Campbell, G. (2011). Exploration geophysics of the Bushveld Complex in South Africa. *The leading edge*, Vol. 30, pp. 622.

Campbell, I. (1986). Fluid dynamic processes in basaltic magma chambers. In: Cawthorn, R.G. (Ed.), Layered Intrusions. *Elsevier, Amsterdam*, pp. 45–76.

Campbell, I. (1987). Distribution of Orthocumulate Textures in the Jimberlana Intrusion. *The Journal of Geology*, Vol. 95, pp. 35-53.

Campbell, I. H. (1978). Some problems with the cumulustheory. *Lithos*, Vol. 11, pp.311–323.

Campbell, I. H. (1986a). A fluid-dynamic model for the potholes of the Merensky Reef. *Economic Geology*, Vol. 81, pp. 1118–1125.

Campbell, T. H. (1977). A study of macro-rhythmic layering and cumulate processes in the Jimberlana intrusion, western Australia. Part I: The upper layered series. *Journals of Petrology*, Vol. 18, pt. 2, pp. 83-215.

Cawthorn. (1996). Re-evaluation of magma compositions and processes in the uppermost Critical Zone of the Bushveld Complex. *Mineralogical Magazine*, pp. 131-148.

Cawthorn, R. G. (1996). Re-evaluation of magma compositions and processes in the uppermost Critical Zone of the Bushveld Complex. *Mineralogical Magazine*, pp. 131-148.

Cawthorn, R. G., & Walraven, F. (1998). Emplacement and Crystallization Time for the Bushveld Complex. *Journal of Petrology*, Vol. 39, pp. 1669–1687.

Cawthorn, R., Barnes, S., Ballhaus, C., & Malitch, K. (2005). Platinum-group element, chromium, and vanadium deposits in mafic and ultramafic rocks. *Economic geology*, pp. 215-249.

Chappell, B., & A.J.R, W. (2001). Two contrasting granite types: 25 years later. *Australian Journal of Earth Sciences*, Vol. 48, pp. 489–499.

Chappell, B., & D, W. (2010). Cumulate and Cumulative Granites and Associated Rocks. *Resources of Geology*, Vol. 54, pp.227–240.

Chen, T., & Nabelek, P. (2020). Numerical Modeling of Dike Propagation Out of Continuously and Episodically Growing Midcrustal Magma Chambers. *Journal of Geophysical Research: Solid Earth*, Vol. 125.

Chistyakova, S., & Latypov, R. (2015). Adcumulate mafic dykes in layered intrusions: a case study of a late-stage dyke in the Bayantsagaan layered intrusion, Mongolia. *Geological Magazine*, Vol. 152, pp. 621-631.

Chubb, P. T., Peck, D., James, R. S., & Ercit, T. S. (1995). Nature and origin of nodular texture in anorthositic cumulates from the East Bull Lake Intrusion, Ontario, Canada. *Mineralogy and Petrology*, pp. 93-103.

Clarke, B., Uken, R., & Reinhardt, J. (2008). Structural and compositional constraints on the emplacement of the Bushveld Complex, South Africa. *lithos*, Vol. 111, pp. 21-36.

Cousins, C. A. (1959). The structure of the mafic portion of the Bushveld Igneous Complex. *Geological Society of South Africa*, Vol. 62, pp.179-189.

Daly, R., & Molengraaff, G. (1924). Structural relations of the Bushveld Igneous Complex, Transvaal. *Journal of Geology*, Vol. 32, pp. 1–35.

Dickin, A. P. (2005). *Radiogenic Isotope Geology. (Second Edition).* New York: Cambridge University Press.

Donaldson, C. (1977). Laboratory duplication of comb layering in the Rhum pluton. *Mineralogical Magazine*, Vol. 41, pp. 323–336.

Du Plessis, A., & Kleywegt, R. (1987). A dipping sheet model for the mafic lobes of the Bushveld Complex. *South African Journal of Geology*, Vol. 90, pp. 1–6.

E., R. (1951). Low-temperature liquid immiscibility in the system K2O–FeO–Al2O3–SiO2. . *American Mineralogist*, Vol. 36, pp. 292–286.

Eales, H. V., & Costin, G. (2012). Crustally Contaminated Komatiite: Primary Source of the Chromitites and Marginal, Lower, and Critical Zone Magmas in a Staging Chamber Beneath the Bushveld Complex. *Economic Geology*, pp. 645-665.

Eales, H., & Cawthorn, R. (1996). *The Bushveld Complex. In: Cawthorn, R.G. (Ed.), Layered Intrusions.* Amsterdam: Elsevier.

Eales, H., Botha, W., Hattingh, P., de Klerk, W., Maier, W., & Odgers, A. (1993). The mafic rocks of the Bushveld Complex: a review of emplacement and crystallization history, and mineralization, in light of recent data. *Journal of African Earth Sciences*, Vol. 16, pp. 21–42.

Elkins, L., & Grove, T. (1990). Ternary feldspar experiments and thermodynamic models. . *American Mineralogist*, Vol. 75, pp. 544– 559.

Elliston, J. N. (1984). Orbicular: An Indication of the Crystallisation of Hydrosilicates. Es, *arth-Science Review*, Vol. 20, pp. 265-344.

Farnand, J. R., Smith, H. M., & Puddington, I. E. (1961). Spherical agglomeration of solid in liquid suspension. *Journal of chemical engineering*, pp. 94-97.

Flowerdew, M., Millar, I., Vaughan, A., Horstwood, M., & Fanning, C. (2006). The source of granitic gneisses and migmatites in the Antarctic Peninsula: a combined U-Pb SHRIMP and laser ablation Hf isotope study of complex zircons. *Contrib. Miner.Petrol.* , Vol. 151, pp. 751–768.

Foster, D. a. (1990). Magma mixing and mingling between synplutonic mafic dikes and granite in the Idaho-Bitterroot batholith, Chap. 20, in Anderson, J.L., ed., The Nature and Origin of Cordilleran. *Geological Society of America*, pp. 347–358.

Frost, T. P., & Mahood, G. A. (1987). Field, chemical, and physical constraints on mafic-felsic magma interaction in the Lamarck Granodiorite, Sierra Nevada, California. *Geological Society of America Bulletin*, Vol. 99, pp. 272-291.

Gough, D., & van Niekerk, C. (1959). A study of the paleomagnetism of the Bushveld Complex. *Philosophical Magazine*, Vol. 14, pp. 126–134.

Griffin, W. X. (2002). Zircon chemistry and magma mixing, SE China: In-situ analysis of Hf isotopes, Tonglu and Pingtan igneous complexes. . *Lithos*, Vol. 61, pp.237–269.

Hall, A. L. (1932). The Bushveld Igneous Complex. *Geological Survey of South Africa Memoir*, pp. 560.

Hammerbeck, E. (1970). The Steelpoort Granite, the eastern part of the Bushveld Complex, and the magnetite in the gabbroic country rock. *Geological Society of South Africa*, Special Publication, Vol. 1, pp. 299-311.

Harmer, R. E., & Sharpe, M. R. (1985). Field relations and strontium isotope are systematic of the rocks of the Eastern Bushveld Complex. *Economic Geology*, pp. 813-837.

Hattingh, P. (1986). The paleomagnetism of the main zone of the Bushveld Complex. *Tectonophysics*, Vol.1 24, pp. 271–295.

Hong, W. C. (2017). Tourmaline-rich features in the Heemskirk and Pieman Heads granites from western Tasmania, Australia: Characteristics, origins, and implications for tin mineralization. *American Mineralogist*, Vol. 102, pp. 876–899.

Hulbert, L. v. (1985). Textural and compositional features of chromite in the lower and critical zones of the Bushveld Complex South of Potgietersrus. *Economic Geology*, pp. 872–895.

Hunt, E. j., Latypov, R., & Horvath, P. (2018). The Merensky cyclic unit, Bushveld Complex, South Africa: Reality or Myth? *Minerals*, Vol. 8, pp. 144.

Hunter, D. R. (1976). Some Enigmas of the Bushveld Complex. *Economic Geology*, Vol. 71, pp. 229-248.

Ibrahim, U., Zaccarini, B., Heinz-Jürgen, B., Simon, B., & Giorgio, G. (2009). Occurrence of rare Ru-Fe-Os-Ir-oxide and associated Platinum-group minerals (PGM) in the chromitite of Mug˘ la ophiolite, SW-Turkey. *Schweizerbart'sche Verlagsbuchhandlung*, Vol. 185/3, pp. 323–333.

Irvine, T. N., Keith, D. W., & Todd, S. G. (1983). The J-M platinum-palladium reef of the Stillwater Complex, Montana: II. Origin by double-diffusive convective magma mixing and implications for the Bushveld Complex. *Economic Geology*, Vol. 78, pp. 1287–1334.

Jaupart, C. &. (1995). Dynamics of differentiation in magma reservoirs. *Journal of Geophysical Research*, Vol. 100, pp.17617–17636.

Keer, R. C. (1994). Dissolving driven by vigorous compositional convection. *Fluid Mechanisms*, Vol. 280, pp. 255-285.

Kinny, P., & Maas, R. (2003). Lu-Hf and Sm-Nd isotope systems in zircon. In: Hanchar, J.M., Hoskin, P.W.O. (Eds.), Zircon. *Reviews in Mineralogy & Geochemistry*.

Kouchi, A., & Sunagawa, l. (1985). A model for mixing basaltic and dacitic magmas as deduced from experimental data. *Contributions to Mineralogy and Petrology*, Vol. 89: pp. 17-23.

Kruger, F. J. (1994). The Sr-isotopic stratigraphy of the western Bushveld Complex. *South African Journal of Geology*, Vol. 97, pp. 393-398.

Kruger, F. J., & Marsh, J. (1982). Significance of 87Sr/86Sr ratios in the Merensky cyclic unit of the Bushveld Complex. *Nature*, pp. 53-55.

Kruger, F. M. (1985). The mineralogy, petrology, and origin of the Merensky cyclic unit in the western Bushveld Complex. *Economic geology*, Vol. 80, pp. 958-974.

Larsen, L., & Smith, E. (1990). Mafic magmatic enclaves in the Wilson Ridge pluton, northwestern Arizona: Implications for the generation of a calc-alkaline intermediate pluton in an extensional environment. *Journal of Geophysical Research*, Vol. 95, pp. 17693–17716.

Latypov, R. M., & Egorova, V. (2012). Plagioclase compositions give evidence for in situ crystallization under horizontal flow conditions in mafic sills. *Geology*, Vol. 40, pp. 883–16.

Latypov, R., Chistyakova, S., Barnes, S. J., & Hunt, E. J. (2017). Origin of Platinum Deposits in Layered Intrusions by In Situ Crystallization: Evidence from Undercutting Merensky Reef of the Bushveld Complex. *Journal of Petrology*, Vol. 58, No. 44, pp. 715-762.

Latypov, R., Chistyakova, S., Page, A., & Hornsey, R. (2015). Field Evidence for the In Situ Crystallization of the Merensky Reef. *Journals of petrology*, pp. 1-32.

Latypov, R., Costin, G., Chistyakova, S., Hunt, E. J., Mukherjee, R., & Naldrett, T. (2018). Platinum-bearing chromite layers are caused by pressure reduction during magma ascent. *Nature communications*, Vol. 9; pp. 462.

Lee, C. A. (1996). A review of mineralization in the Bushveld Complex and some other layered intrusions. *Developments in Petrology*, Vol. 15, pp. 103-145.

Lee, C. A., & Sharpe, M. R. (1979). Spheroidal aggregations in the Bushveld Complex: A special case of silicate liquid immiscibility. *Earth and Planetary Science Letters*, pp. 295-310.

Leeb Du-Toit, A. (1986). The Impala Platinum mines. In: Anhaeusser, C.R., Maske, S.,(Eds.), Mineral Deposits of Southern Africa, II. *Geological Society of South Africa*, pp. 1091–1106.

Lesher, C. E., & Walker, D. (1988). Cumulate migration and melt migration in a temperature gradient. *Journal of Geophysical Research*, Vol.93, pp.10295–10311.

Letts, S., Torsvik, T., Webb, S., & Ashwal, L. (2009). Palaeomagnetism of the 2054 Ma Bushveld Complex (South Africa): implications for emplacement and cooling. *Geophysical Journal International*, Vol. 179, pp. 850–872.

Lindsley, D. H. (1983). Pyroxene Thermometer . *Americam mineralogist*, Vol. 68; pp. 47-493.

Lugmair, G., & Marti, K. (1978). Lunar initial 143Nd/144Nd: Differential evolution of the lunar crust and mantle. *Earth Planet. Sci. Lett*, Vol. 39, pp. 349–357.

Maas, R., Nicholls, I., & Legg, C. (1997). Igneous and metamorphic enclaves in the S-type Deddick granodiorite, Lachlan Fold Belt, SE Australia: Petrographic, geochemical, and Nd-Sr isotopic evidence for crustal melting and magma mixing. *Journals of Petrology*, Vol. 38, pp.815–841.

Maier, W. D., Barnes, S. J., & Groves, D. I. (2013). The Bushveld Complex, South Africa: formation of platinum–palladium, chrome- and vanadium-rich layers via hydrodynamic sorting of a mobilized cumulate slurry in a large, relatively slowly cooling, subsiding magma chamber. *Mineralium deposita*, Vol. 48, pp. 1–56.

McDonough, W., & Sun, S. (1995). The Composition of the Earth. *Chemical Geology*, Vol. 120, pp. 223-253.

Molyneux, T. G., & Klinkert, P. (1978). A structural interpretation of part of the eastern mafic lobe of the Bushveld Complex and its surroundings. *Transactions of the Geological Society of South Africa*, Vol. 81, pp. 359-368.

Moore, J., & Lockwood, J. (1973). Origin of comb layering and orbicular structure, Sierra Nevada batholith, California. *Geological Society of America Bulletin*, Vol. 104, pp. 1048–1058.

Morse, S. A. (1986.). Convection in aid of adcumulus growth. *Journal of Petrology*, Vol. 27, pp. 183–214.

Morse, S. A. (1988). The motion of crystals, solute, and heat in layered intrusions. *Canadian Mineralogist*, Vol. 26, pp.209–244.

Mukherjee, R., Latypov, R., & Balakrishna. (2017). An intrusive origin of some UG-1 chromitite layers in the Bushveld Igneous Complex, South Africa: Insights from field relationships. *Ore Geology Reviews*, Vol. 90, pp. 94-109.

Naldrett, A., Kinnaird, J., Wilson, A., Yudovskaya, M., & Chunnett, G. (2011). The genesis of the PGE-enriched Merensky Reef and chromitite seams of the Bushveld Complex. In: Li, C., Ripley, E.M. (Eds.), Review in economic geology: magmatic Ni-Cu and PGE deposits. *geology, geochemistry and genesis*, Vol. 17, pp. 235–296.

Naslund, H. R. (1996). Mechanisms of formation of igneous layering. In: Cawthorn, R. G. (ed.).Layered Intrusions. Developments in Petrology 15. Elsevier, .

Nguuri, T., Gore, J., James, D., Webb, S., Wright, C., Zengeni, T., . . . Snoke, J. A. (2001). Crustal structure beneath southern Africa and its implications for the formation and evolution of the Kaapvaal and Zimbabwe cratons. *Geophysical Research Letters*, Vol. 28, pp.2501-2504.

Pandura, K., Ansdella, K. M., Eglingtona, B. M., Harperc, C. T., Hanchard, J., & McFarlanee, C. R. (2020). In situ U-Pb geochronology, Lu-Hf and Sm-Nd isotope systematics of the Hoidas Lake REE deposit, northern Saskatchewan, Canada. *Precambrian Research*, Vol. 339. pp. 105591.

Patchett, P. (1983). Importance of the Lu-Hf isotopic system in studies of planetary chronology and chemical evolution. *Geochim. Cosmochim*, Acta 47, pp. 81–91.

Patchett, P., Kouvo, O., Hedge, C., & Tatsumoto, M. (1981). Evolution of continental crust and mantle heterogeneity: evidence from Hf isotopes. *Contrib. Miner. Petrol.*, Vol. 78, pp. 279–297.

Pearce, J., Kempton, P., Nowell, G., & Noble, S. (1999). Hf–Nd element isotope perspective on the nature and provenance of mantle and subduction components in Western Pacific arc-basin systems. *J. Petrol.* , Vol. 40 (11), pp.1579–1611.

Philpotts. (1990). Principles of Igneous and Metamorphic Petrology. *Prentice-Hall*, pp. 498.

Philpotts, A. R. (1976). Silicate liquid immiscibility: its probable extent and petrogenetic significance. *American Journals of science*, Vol. 276, pp.1147–1177.

Philpotts, A. R., & Dickson, L. D. (2000). The formation of plagioclase chains during convective transfer in basaltic magma. *letters to nature*, Vol. 406.

Puddington, I. E., & Spark, B. D. (1975). Spherical agglomeration process. *Mineral science of engineering*, pp. 282-288.

Reid, J., Evans, O., & Fates, D. (1983). Magma mixing in granitic rocks of the central Sierra Nevada California. *Earth and Planetary Science Letters*, vol. 66, pp. 243-261.

Roberts, M., Reid, D., Miller, J., Basson, I., Roberts, M., & Smith, D. (2007). The Merensky Cyclic Unit and its impact on footwall cumulates below Normal and Regional Pothole reef types in the Western Bushveld Complex. Miner. *Deposita*, Vol. 42, pp. 271–292.

Roelofse, F., & Ashwal, L. D. (2012). The Lower Main Zone in the Northern Limb of the Bushveld Complex: a > 1.3 km thick sequence of intruded and variably contaminated crystal mushes. . *Journal of petrology*, Vol. 7, pp. 1449-1476.

Rollingson, H. (1993). *Using geochemical data: Evaluation, presentation, and interpretation.* Harlow: Longman Group UK.

Schannor, M. V. (2018). Small-scale Sr and O isotope variations through the UG2 in the eastern Bushveld Complex: The role of crustal fluids. *Chemical Geology*, Vol. 485, pp. 100–112.

Scherer, E., Münker, C., & Mezger, K. (2001). Calibration of the Lutetium-Hafnium Clock. . *Science* , Vol. 293, pp. 683–687.

Scoates, J. S. (2008). The precise age of the platiniferous Merensky Reef, Bushveld Complex, South Africa, by the U/Pb zircon chemical abrasion ID-TIMS technique. . *Economic Geology*, Vol. 103, pp. 465-471.

Scoon, R. T. (1994). Platinum-group element mineralization in the critical zone of the Western Bushveld Complex: I. Sulfide poor-chromitites below the UG-2. . *Economic Geology*, Vol. 89, pp. 1094–1121.

Sharpe, M. R. (1980). A model for the emplacement of the eastern compartment~ of the bushveld complex. . *Tectonophysics*, Vol. 65, pp. 85-l 10.

Smith, D., Basson, I., & Reid, D. (2003). Normal reef sub-facies of the Merensky Reef at Northam Platinum Mine, Zwartklip facies, Western Bushveld Complex. *South African Can. Minerals*, Vol. 42, pp. 243-260.

Sparks, R. S., & Marshall, L. A. (1986). Thermal and mechanical constraints on mixing between mafic and silicic magma. *Journal of Volcanology and Geothermal Research*, pp. 99-124.

Stumpfl, E. F. (1962). Some aspects of the genesis of platinum. *Economic Geology*, V. 57, pp. 619-623.

Sylvester, A. G. (2011). Nature and polygenetic origin of orbicular granodiorite in the Lower Castle Creek pluton, northern Sierra Nevada batholith, California. *Geosphere*, Vol. 7; no. 5; pp. 1–9.

Tait, S., & Jaupart, C. (1996.). The production of chemically stratified and adcumulate plutonic igneous rocks. *Mineralogical Magazine*, Vol. 60, pp. 99–114.

Taylor, T., Vogel, T., & Wilband, J. (1980). The Composite Dikes at Mount Desert Island, Maine: An Example of Coexisting Acidic and Basic Magma. *The Journal of Geology*, Vol. 88, pp. 433–444.

Tegner, C., Thy, P., Holness, M. B., & Jakobsen, J. K. (2009). Differentiation and compaction in the Skaergaard intrusion. *Journal of Petrology* , Vol. 50, pp.813–84.

Teigler, B. E. (1996). The Lower and Critical Zones of the western limb of the Bushveld Complex as intersected by the Nooitgedagt borehole. *Geological Survey of South Africa*, pp. 111-126.

Tobisch, O. M. (1997). Microgranitoid enclave swarms in granitic plutons central Sierra Nevada. *Lithos*, Vol. 40, pp. 321–339.

Van Merwe, M. V. (2007). The occurrence of the critical zone along with the exposed southeastern sector of the eastern Bushveld Complex. *Geological Society of South Africa*.

Vermaak, C. F. (1976). The Merensky Reef -Thought on its environment and genesis. *Economic geology*, Vol. 71, pp. 1270-1298.

Vermeesch, P. (2018). IsoplotR: a free and open toolbox for geochronology. *Geoscience Frontiers*, Vol. 9, pp.1479-1493.

Vernon, R. 1. (1985). The possible role of superheated magma in the formation of orbicular granitoids. *Geology*, Vol. 13, pp. 843–845.

Vernon, R. (1983). Restite, xenoliths, and microgranitoid enclaves in granites. *Journal and Proceedings of the Royal Society of New South Wales*, Vol. 116, pp. 77–103.

Vernon, R. (1984). Microgranitoid enclaves in granites–globules of hybrid magma quenched in a plutonic environment. *Nature*, Vol. 309, pp.438– 439.

Vernon, R. S. (2008). Mesoscopic structures resulting from crystal accumulation and melt movement in granites. *Transactions of the Royal Society of Edinburgh. Earth Sciences*, Vol. 97, pp. 369–381.

Von Gruenewaldt, G. (1973). The Main and Upper Zones of the Bushveld Complex in the Roossenekal area, Eastern Transvaal. *Geological Society of South Africa*, pp. 207-227.

Wager, L. R., & Brown, G. M. (1968). *Layered Igneous Rocks.* Oliver & Boyd.

Wager, L. R., & Deer, W. A. (1939). Geological investigations in East Gree~Lland, Pt. lll. The petrology of the Skaergaard Intrusion, Kanger~l|ugssuaq, East Greenland. *Medd. om Greenland*, 105-352.

Webb, S. J., Ashwal, L. D., & Cawthorn, R. G. (2011). Continuity between eastern and western Bushveld Complex, South Africa, confirmed by xenoliths from kimberlite. *Contributions to Mineralogy and Petrology*, Vol. 162, pp. 101-107.

Webb, S. J., Cawthorn, R. G., Nguuri, T., & James, D. (2004). Gravity modeling of Bushveld Complex connectivity supported by Southern African Seismic Experiment results. *South African Journal of Geology*, Vol. 107, pp. 207–218.

White, A., & B.W., C. (1977). Ultrametamorphic and granitoid genesis. *Tectonophysics*, Vol. 43, pp. 7–22.

Wilson, J. R., Esbensen, K. H., & Thy, P. (1981). A new pyroxene fractionation trend from a layered basic intrusion. *Nature*, Vol. 290, pp.325-326.

Woods, A. W. (1992). Melting and dissolving. . *Journal of Fluid Mechanics*, Vol. 239, pp. 429–44.

Wu, Y., Zheng, Y., Zhang, S., Zhao, F., Wu, F., & Liu, X. (2007). Zircon U-Pb ages and Hf isotope compositions of migmatite from the North Dabie terrane in China: constraints on partial melting. *J. Metamorph. Geol.*, Vol. 25, pp. 991–1009.

Yang, J. F. (2004). Multiple sources for the origin of granites: Geochemical and Nd/Sr isotopic evidence from the Gudaoling granite and its mafic enclaves, Northeast China. . *Geochemistry*, Vol. 68, pp. 4469–4483.

Zeh, A. G. (2007). Archean to Proterozoic crustal evolution in the Central Zone of the Limpopo Belt (South Africa/ Botswana): constraints from combined U-Pb and Lu-Hf isotope analyses of zircon. *J. Petrol*, Vol. 48, pp. 1605–1639.

Zheng, Y., Wu, Y., Zhao, Z., Zhang, S., Xu, P., & Wu, F. (2005). Metamorphic effect on zircon Lu-Hf and U-Pb isotope systems in ultrahigh-pressure eclogite-facies metal granite and metabolite. *Earth Planet. Sci. Lett.* , Vol. 240, pp. 378–400.

Zorpi, M. C. (1989). Magma mingling, zoning, and emplacement in calc-alkaline granitoid plutons. *Tectonophysics*, Vol. 157, No. 4, pp. 315–329.

Appendices

Appendix. 1. Core log from a mining company in the western Lobe, showing the correlation between base metal sulfides and the Tennis Ball Marker.

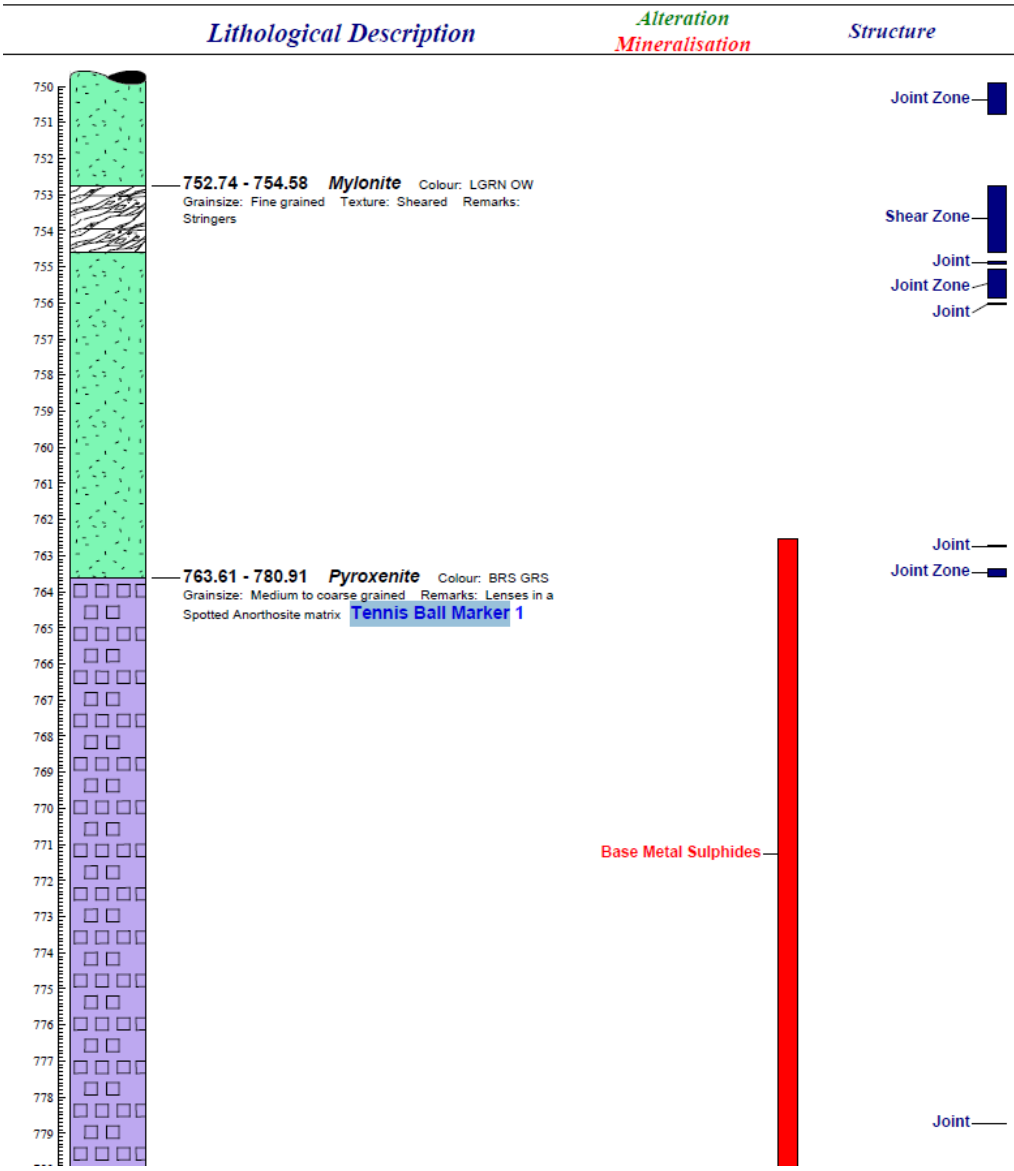
Lithological Description
Alteration
Mineralisation
Structure
RQD %
CBA
(0°)
750
751
752
753
754
755
756
757
758
759
760
761
762
763
764
765
766
767
768
769
770
771
772
773
774
775
776
777
778
779
752.74 - 754.58 Mylonite Colour: LGRN OW
Grainsize: Fine grained Texture: Sheared Remarks:
Stringers
763.61 - 780.91 Pyroxenite Colour: BRS GRS
Grainsize: Medium to coarse grained Remarks: Lenses in a
Spotted Anorthosite matrix Tennis Ball Marker 1
Joint Zone
Shear Zone
Joint
Joint Zone
Joint
Joint
Joint Zone
Base Metal Sulphides
Joint

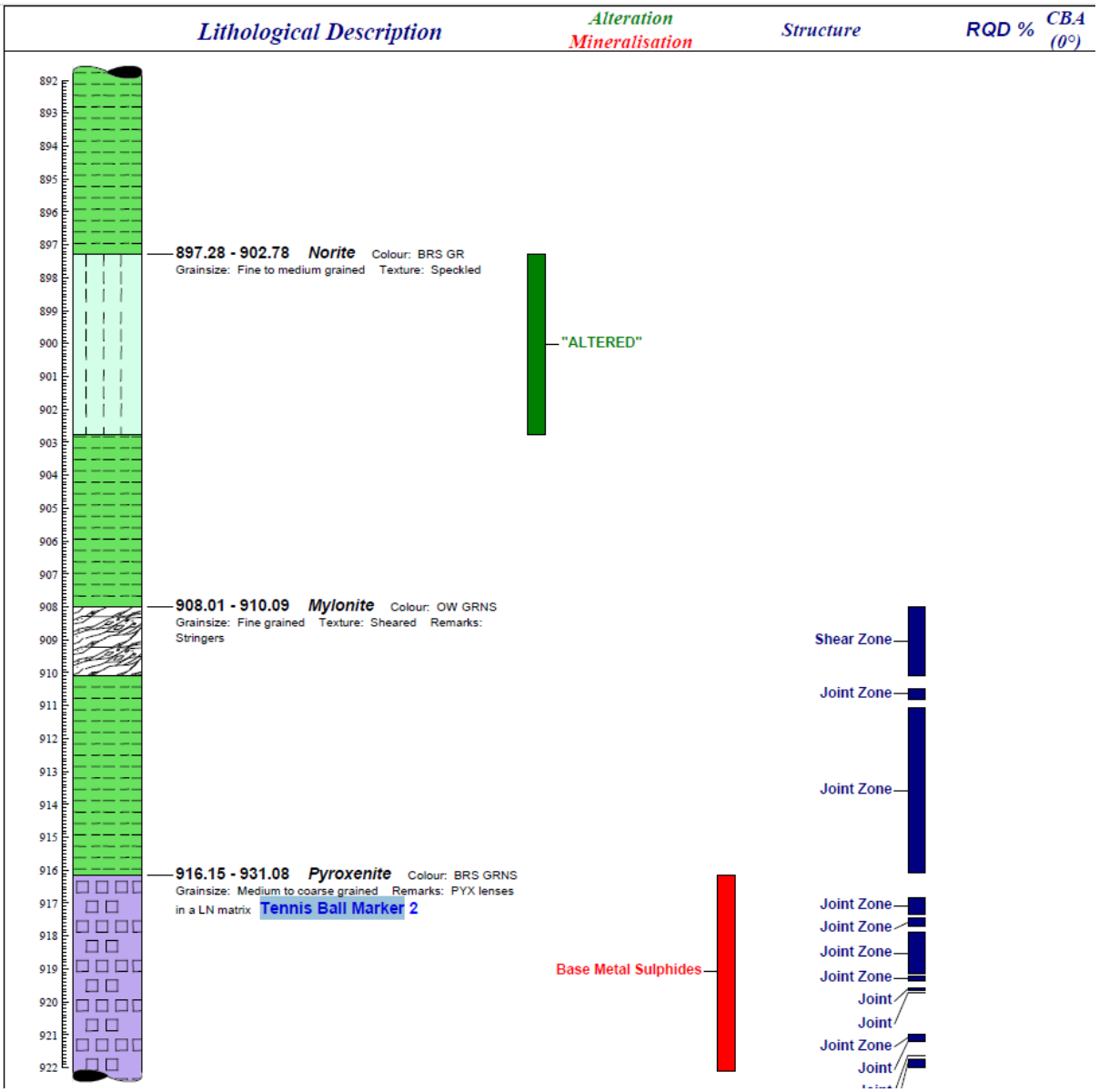
Lithological Description
Alteration
Mineralisation
Structure
RQD %
CBA
(0°)
892
893
894
895
896
897
898
899
900
901
902
903
904
905
906
907
908
909
910
911
912
913
914
915
916
917
918
919
920
921
922
897.28 - 902.78 Norite Colour: BRS GR
Grainsize: Fine to medium grained Texture: Speckled
"ALTERED"
908.01 - 910.09 Mylonite Colour: OW GRNS
Grainsize: Fine grained Texture: Sheared Remarks:
Stringers
916.15 - 931.08 Pyroxenite Colour: BRS GRNS
Grainsize: Medium to coarse grained Remarks: PYX lenses
in a LN matrix Tennis Ball Marker 2
Base Metal Sulphides
Shear Zone
Joint Zone
Joint Zone
Joint Zone
Joint Zone
Joint Zone
Joint Zone
Joint
Joint
Joint Zone
Joint

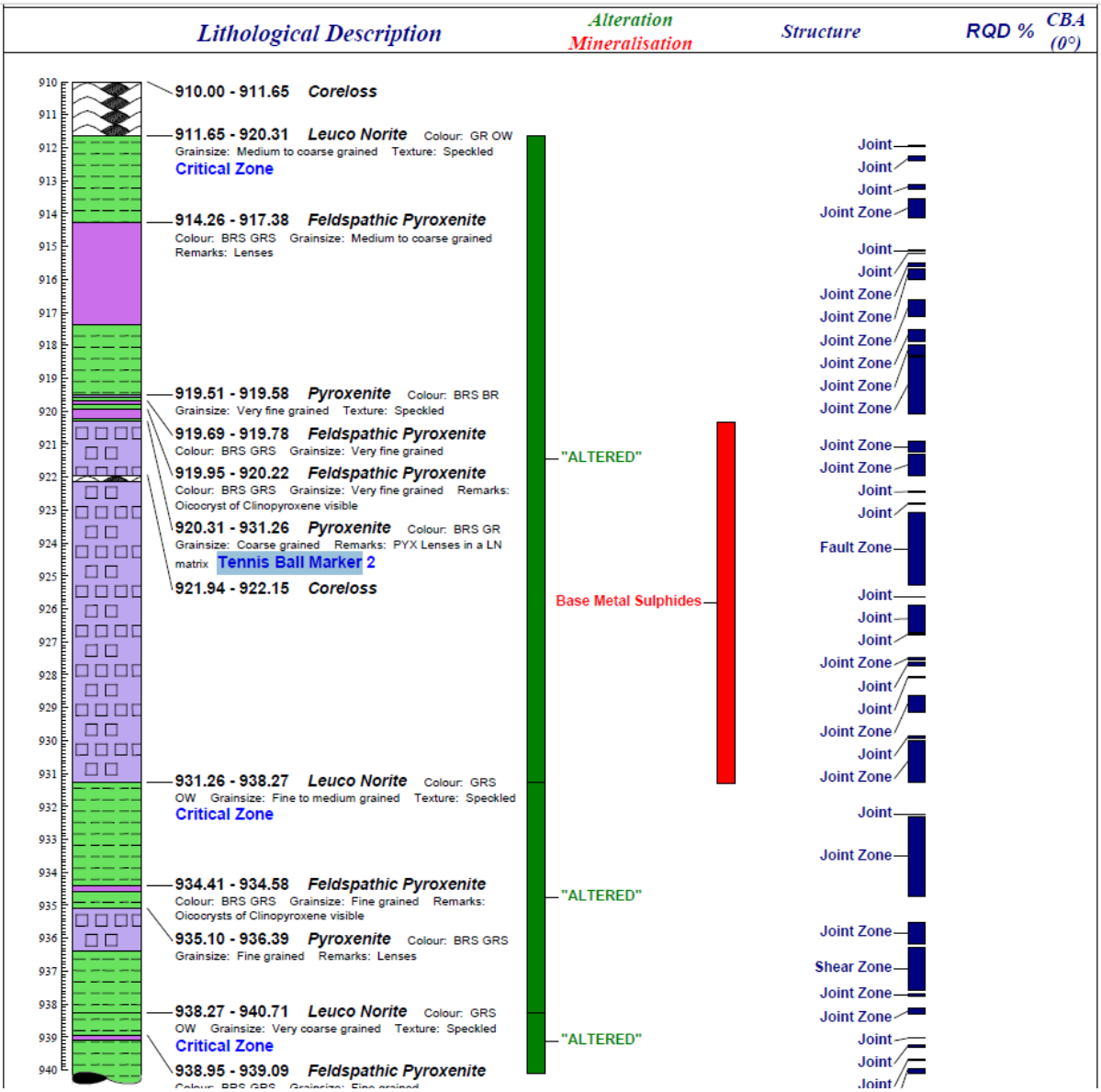
Lithological Description
Alteration
Mineralisation
Structure
RQD %
CBA
(0°)
910
911
912
913
914
915
916
917
918
919
920
921
922
923
924
925
926
927
928
929
930
931
932
933
934
935
936
937
938
939
940
910.00 - 911.65 Coreloss
911.65 - 920.31 Leuco Norite Colour: GR OW
Grainsize: Medium to coarse grained Texture: Speckled
Critical Zone
914.26 - 917.38 Feldspathic Pyroxenite
Colour: BRS GRS Grainsize: Medium to coarse grained
Remarks: Lenses
919.51 - 919.58 Pyroxenite Colour: BRS BR
Grainsize: Very fine grained Texture: Speckled
919.69 - 919.78 Feldspathic Pyroxenite
Colour: BRS GRS Grainsize: Very fine grained
919.95 - 920.22 Feldspathic Pyroxenite
Colour: BRS GRS Grainsize: Very fine grained Remarks:
Oicocryst of Clinopyroxene visible
920.31 - 931.26 Pyroxenite Colour: BRS GR
Grainsize: Coarse grained Remarks: PYX Lenses in a LN
matrix Tennis Ball Marker 2
921.94 - 922.15 Coreloss
931.26 - 938.27 Leuco Norite Colour: GRS
OW Grainsize: Fine to medium grained Texture: Speckled
Critical Zone
934.41 - 934.58 Feldspathic Pyroxenite
Colour: BRS GRS Grainsize: Fine grained Remarks:
Oicocrysts of Clinopyroxene visible
935.10 - 936.39 Pyroxenite Colour: BRS GRS
Grainsize: Fine grained Remarks: Lenses
938.27 - 940.71 Leuco Norite Colour: GRS
OW Grainsize: Very coarse grained Texture: Speckled
Critical Zone
938.95 - 939.09 Feldspathic Pyroxenite
"ALTERED"
Base Metal Sulphides
"ALTERED"
"ALTERED"
Joint
Joint
Joint
Joint Zone
Joint
Joint
Joint Zone
Joint Zone
Joint Zone
Joint Zone
Joint Zone
Joint Zone
Joint Zone
Joint Zone
Joint
Joint
Fault Zone
Joint
Joint
Joint
Joint Zone
Joint
Joint
Joint Zone
Joint
Joint Zone
Joint
Joint Zone
Shear Zone
Joint Zone
Joint Zone
Joint
Joint
Joint

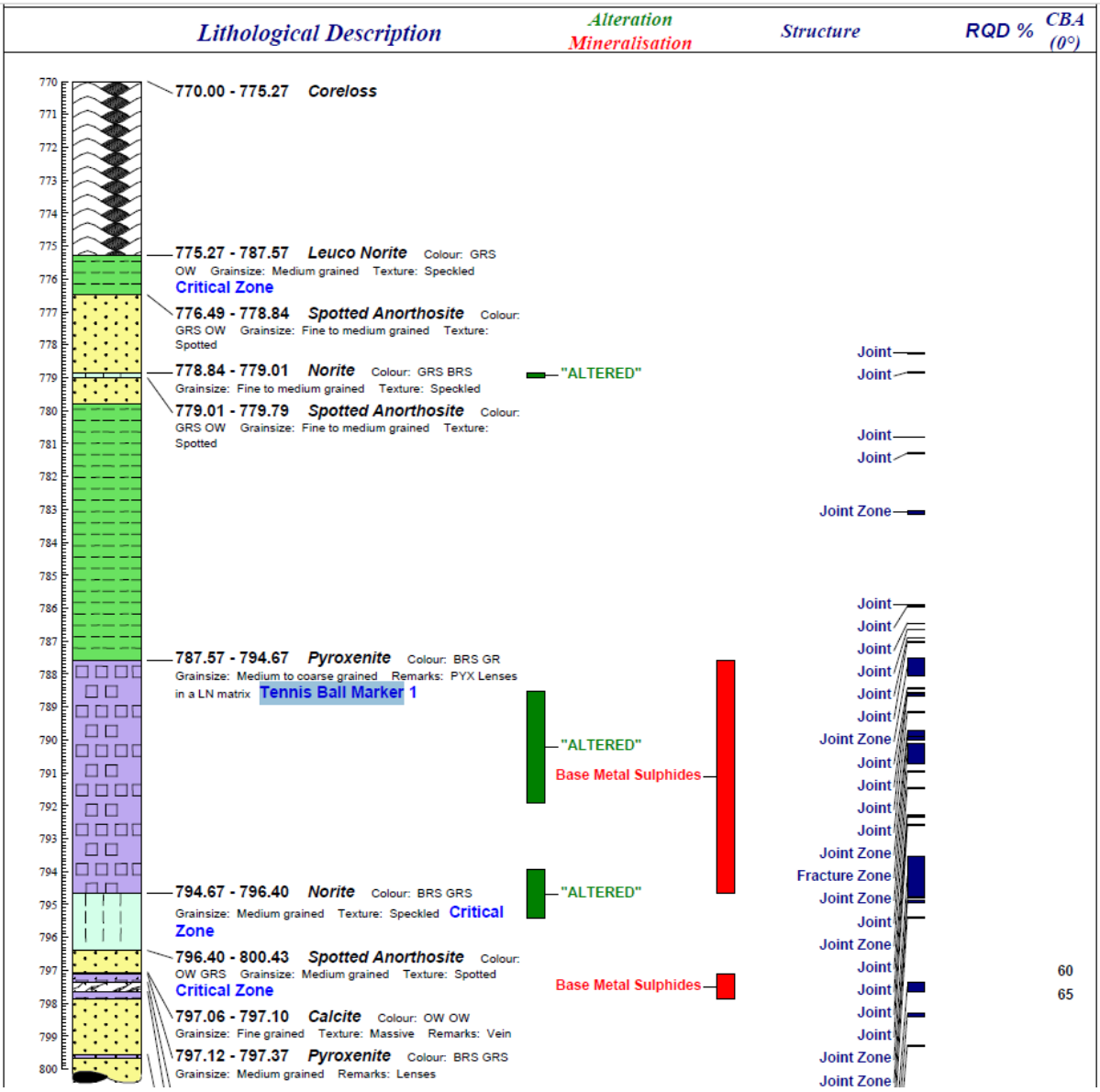
Lithological Description
Alteration
Mineralisation
Structure
RQD %
CBA
(0°)
770
771
772
773
774
775
776
777
778
779
780
781
782
783
784
785
786
787
788
789
790
791
792
793
794
795
796
797
798
799
800
770.00 - 775.27 Coreloss
775.27 - 787.57 Leuco Norite Colour: GRS OW Grainsize: Medium grained Texture: Speckled
Critical Zone
776.49 - 778.84 Spotted Anorthosite Colour: GRS OW Grainsize: Fine to medium grained Texture: Spotted
778.84 - 779.01 Norite Colour: GRS BRS Grainsize: Fine to medium grained Texture: Speckled
779.01 - 779.79 Spotted Anorthosite Colour: GRS OW Grainsize: Fine to medium grained Texture: Spotted
787.57 - 794.67 Pyroxenite Colour: BRS GR Grainsize: Medium to coarse grained Remarks: PYX Lenses in a LN matrix Tennis Ball Marker 1
794.67 - 796.40 Norite Colour: BRS GRS Grainsize: Medium grained Texture: Speckled Critical Zone
796.40 - 800.43 Spotted Anorthosite Colour: OW GRS Grainsize: Medium grained Texture: Spotted
Critical Zone
797.06 - 797.10 Calcite Colour: OW OW Grainsize: Fine grained Texture: Massive Remarks: Vein
797.12 - 797.37 Pyroxenite Colour: BRS GRS Grainsize: Medium grained Remarks: Lenses
"ALTERED"
"ALTERED"
Base Metal Sulphides
"ALTERED"
Base Metal Sulphides
Joint
Joint
Joint
Joint
Joint Zone
Joint
Joint
Joint
Joint
Joint
Joint
Joint Zone
Joint
Joint
Joint
Joint Zone
Fracture Zone
Joint Zone
Joint
Joint Zone
Joint
Joint
Joint
Joint
Joint Zone
Joint Zone
60
65

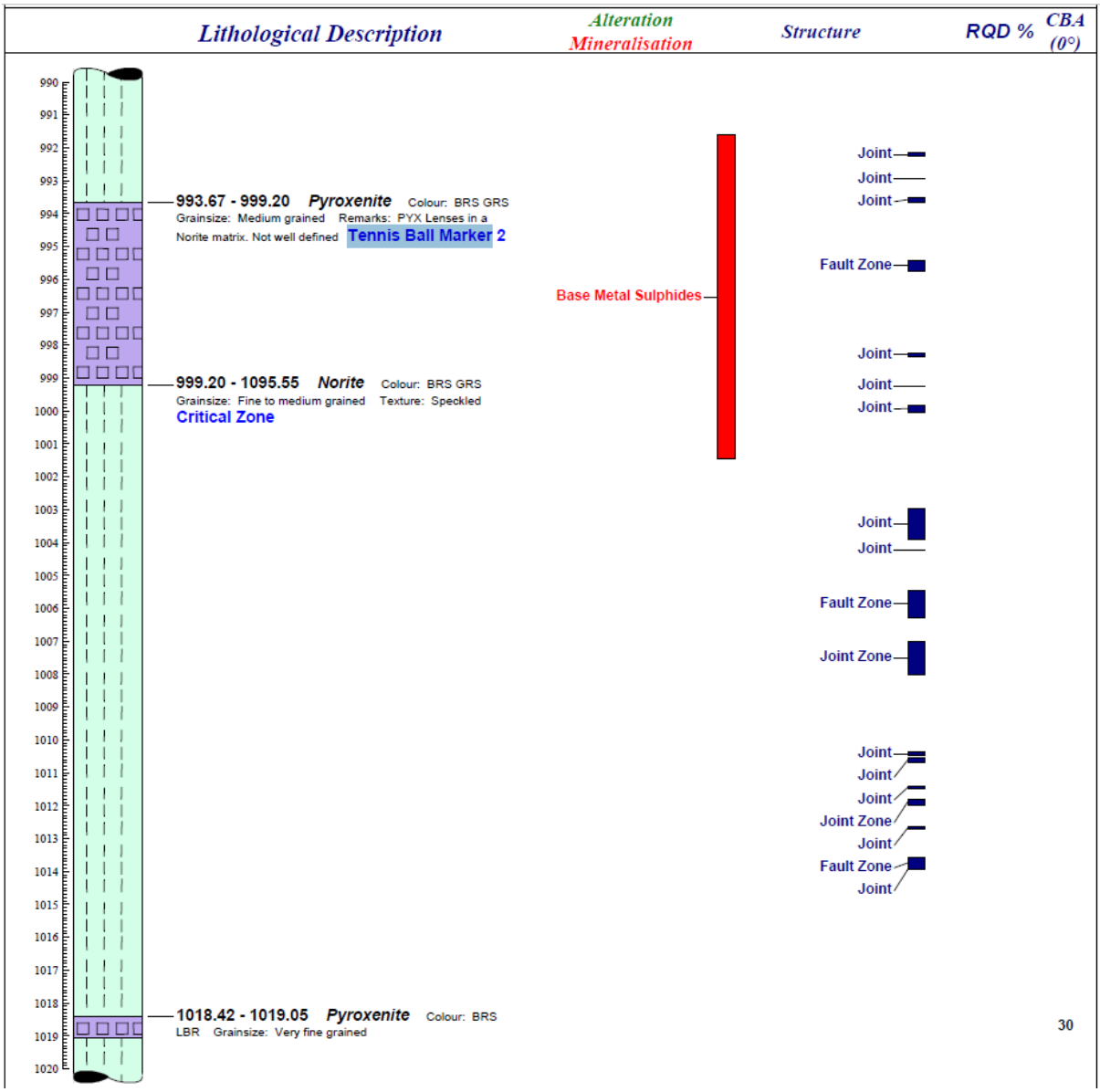
Lithological Description
Alteration
Mineralisation
Structure
RQD %
CBA
(0°)
990
991
992
993
994
995
996
997
998
999
1000
1001
1002
1003
1004
1005
1006
1007
1008
1009
1010
1011
1012
1013
1014
1015
1016
1017
1018
1019
1020
993.67 - 999.20 Pyroxenite Colour: BRS GRS
Grainsize: Medium grained Remarks: PYX Lenses in a
Norite matrix. Not well defined Tennis Ball Marker 2
999.20 - 1095.55 Norite Colour: BRS GRS
Grainsize: Fine to medium grained Texture: Speckled
Critical Zone
1018.42 - 1019.05 Pyroxenite Colour: BRS
LBR Grainsize: Very fine grained
Base Metal Sulphides
Joint
Joint
Joint
Fault Zone
Joint
Joint
Joint
Joint
Joint
Fault Zone
Joint Zone
Joint
Joint
Joint
Joint Zone
Joint
Fault Zone
Joint
30

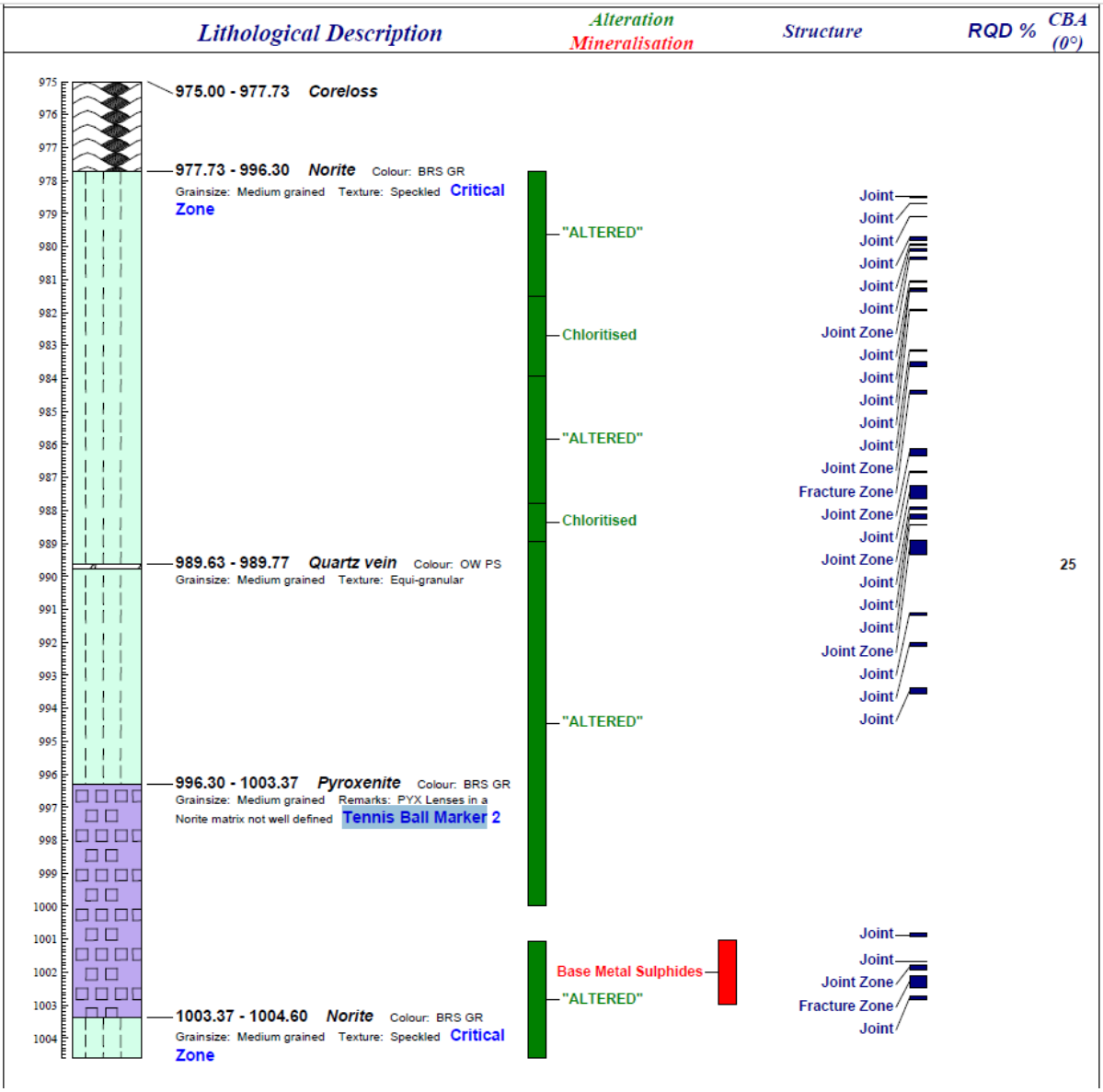
Lithological Description
Alteration
Mineralisation
Structure
RQD %
CBA
(0°)
975.00 - 977.73 Coreloss
977.73 - 996.30 Norite Colour: BRS GR
Grainsize: Medium grained Texture: Speckled Critical Zone
989.63 - 989.77 Quartz vein Colour: OW PS
Grainsize: Medium grained Texture: Equi-granular
996.30 - 1003.37 Pyroxenite Colour: BRS GR
Grainsize: Medium grained Remarks: PYX Lenses in a Norite matrix not well defined Tennis Ball Marker 2
1003.37 - 1004.60 Norite Colour: BRS GR
Grainsize: Medium grained Texture: Speckled Critical Zone
"ALTERED"
Chloritised
"ALTERED"
Chloritised
"ALTERED"
Base Metal Sulphides
"ALTERED"
Joint
Joint Zone
Fracture Zone
25

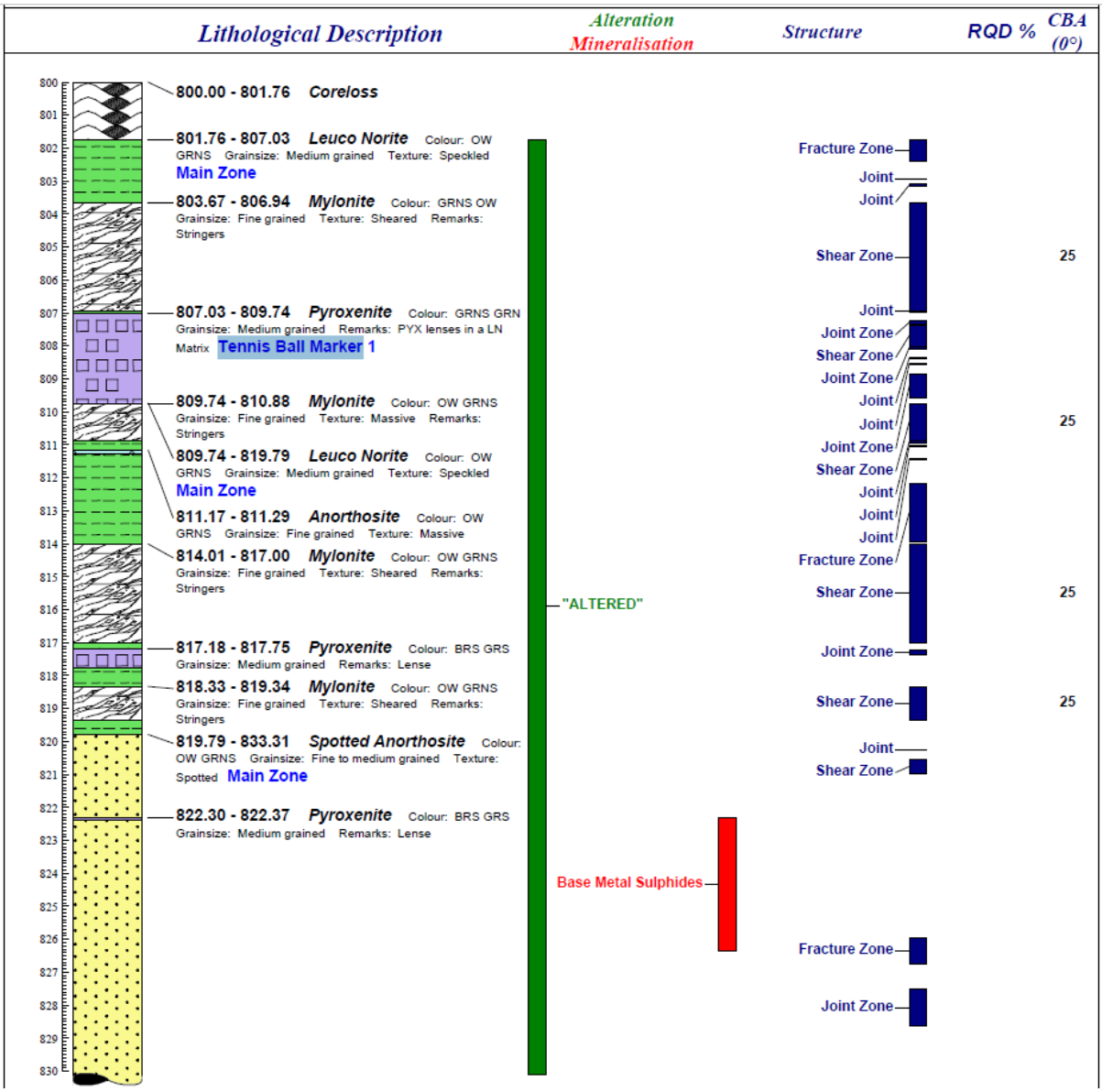
Lithological Description
Alteration
Mineralisation
Structure
RQD %
CBA (0°)
800.00 - 801.76 Coreloss
801.76 - 807.03 Leuco Norite Colour: OW GRNS Grainsize: Medium grained Texture: Speckled
Main Zone
803.67 - 806.94 Mylonite Colour: GRNS OW Grainsize: Fine grained Texture: Sheared Remarks: Stringers
807.03 - 809.74 Pyroxenite Colour: GRNS GRN Grainsize: Medium grained Remarks: PYX lenses in a LN Matrix
Tennis Ball Marker 1
809.74 - 810.88 Mylonite Colour: OW GRNS Grainsize: Fine grained Texture: Massive Remarks: Stringers
809.74 - 819.79 Leuco Norite Colour: OW GRNS Grainsize: Medium grained Texture: Speckled
Main Zone
811.17 - 811.29 Anorthosite Colour: OW GRNS Grainsize: Fine grained Texture: Massive
814.01 - 817.00 Mylonite Colour: OW GRNS Grainsize: Fine grained Texture: Sheared Remarks: Stringers
817.18 - 817.75 Pyroxenite Colour: BRS GRS Grainsize: Medium grained Remarks: Lense
818.33 - 819.34 Mylonite Colour: OW GRNS Grainsize: Fine grained Texture: Sheared Remarks: Stringers
819.79 - 833.31 Spotted Anorthosite Colour: OW GRNS Grainsize: Fine to medium grained Texture: Spotted
Main Zone
822.30 - 822.37 Pyroxenite Colour: BRS GRS Grainsize: Medium grained Remarks: Lense
"ALTERED"
Base Metal Sulphides
Fracture Zone
Joint
Joint
Shear Zone
25
Joint
Joint Zone
Shear Zone
Joint Zone
Joint
Joint
25
Joint Zone
Shear Zone
Joint
Joint
Joint
Fracture Zone
Shear Zone
25
Joint Zone
Shear Zone
25
Joint
Shear Zone
Fracture Zone
Joint Zone

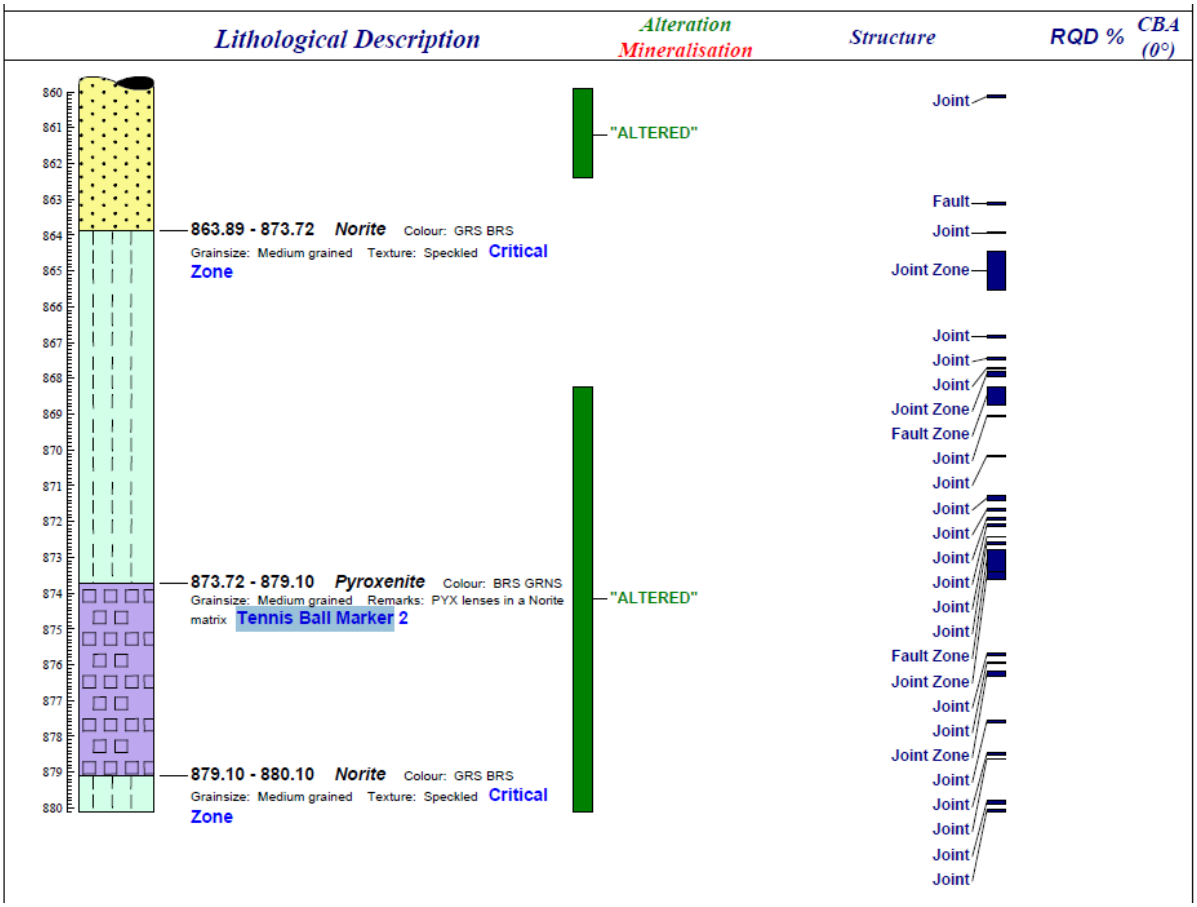

Appendix. 2. The field images of the most important features found at the TBM package

1. DFB




1. Contacts gabbronorite

1. Lower TBM

1. Upper TBM

2. Normal gabbronorite

3. Perfectly spherical pyroxenite bodies

4. Semi-circular SPB

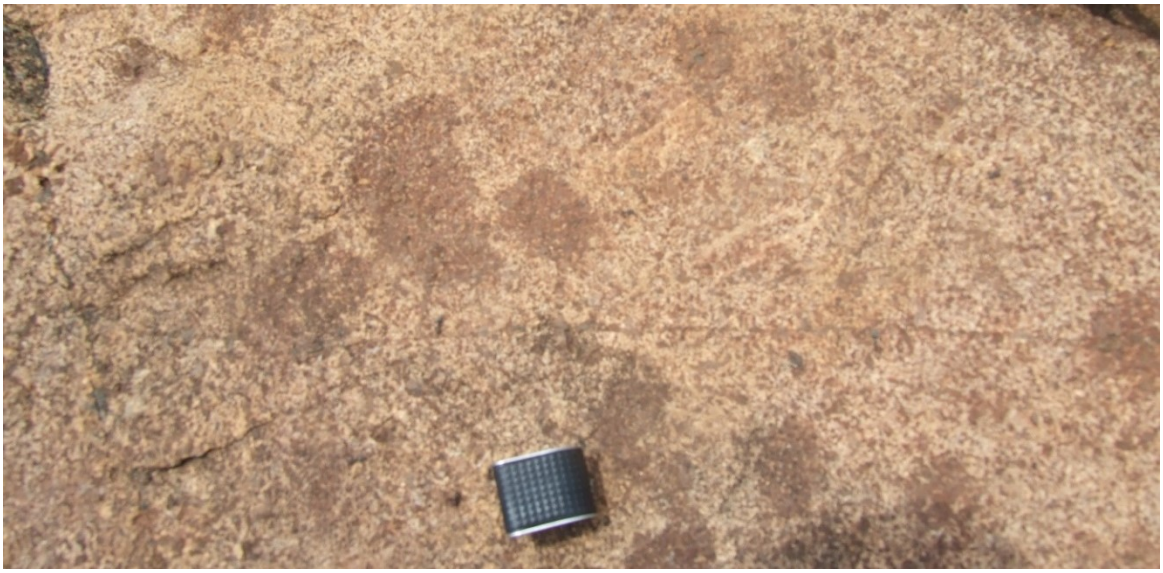

5. Broken SPB




1. Angular pyroxenite


2. Angular pyroxenites with curvy edges

3. Oval shaped pyroxenite bodies






1. The undulating boundary of the SPB

2. Spherical and Anorthosite xenoliths

3. The white rim around the SPB

4. Sorting of the SPB

5. Dispersed SPB

6. A small group of SPB

7. The gradational lower contact of the LTBM

8. SPB linear alignment

9. Gabbronorite roots into the lower pyroxenite layer

1. Thin layers of the TBM layers

2. Anorthosite matrix

3. Layered SPB concentration

4. Bending of the pyroxene rich layers around SPB






5. Pegmatitic gabbronorite matrix

6. Abrupt TBM layer upper contact




7. Pegmatoidal gabbronorite



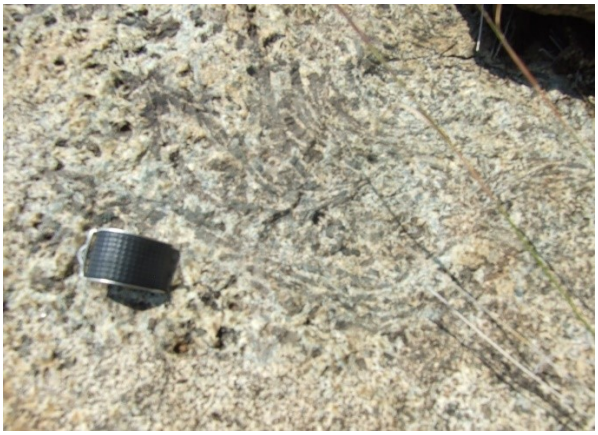


28. Pyroxenite layers






1. Dark rims around SPB

2. Discontinuous SPB layers

3. Sheared SPB

4. Anorthosite layers




5. Dykes
6.

Appendix. 3. Plate of the collected samples for this study showing field images of the collected samples, the images of the samples, and their images under PPL and XPL.

Sample No.	Location (UTM)	Sample image	Section outline	Thin section PPL	T
TBM-1	800441E 7194036S			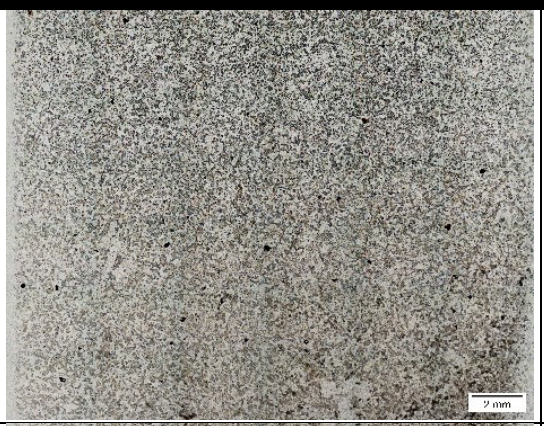	
TBM-2	800421E 7194032S				
TBM-3	800410E 7194031S				

TBM-4	800410E 7194034S			
TBM-5	800375E 7194036			
TBM-6m	800368E 7194053			
TBM-7b-1	800363E 7194037S			

TBM-7b-2					
TBM-7m	800367E 7194033S				
TBM-7bm				The thin section could be made	T
TBM-8m	800365E 7194048S				
TBM-9	800341E 7194057S				

TBM-11	800247E 7194060S			
TBM-12	800195E 7194069			
TBM-13	800164E 7194044S			
TBM-14	800165E 7194043S			

TBM-15	800167E 7194044S		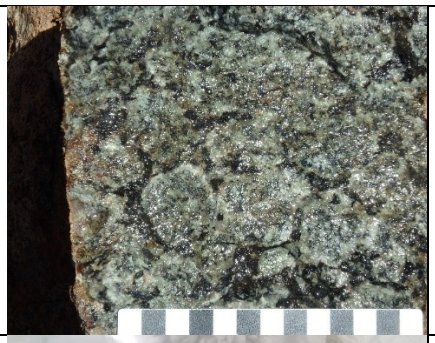	The thin section could not be made	T
TBM-16	800121E 7194048S			The thin section could not be made	T
TBM-17	800121E 7194047		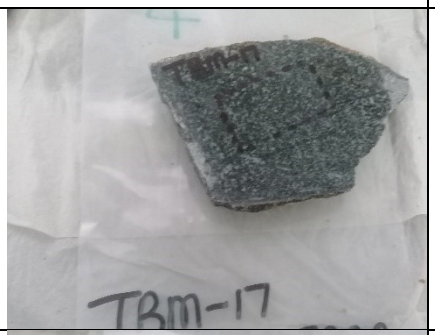	The thin section could not be made	T
TBM-18	800102E 7194098S		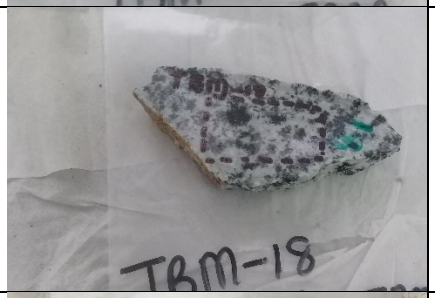		
TBM-19	800068E 7194096S		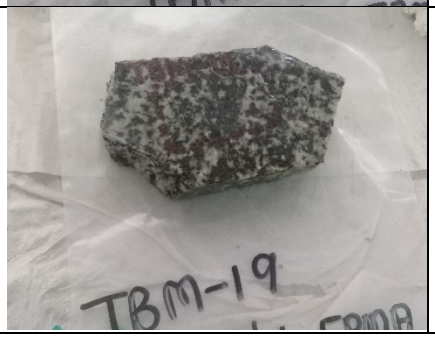		

TBM-20b	800023E 7194071	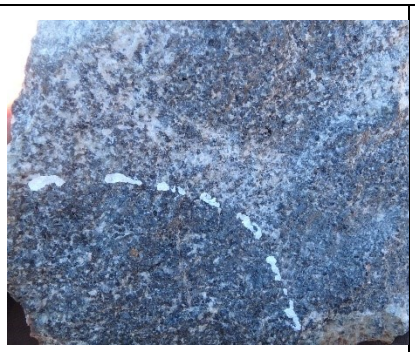			
TBM-20m	800024E 7194071S		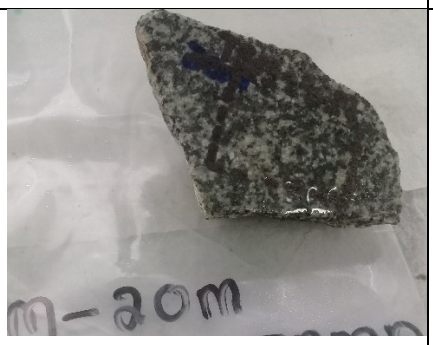		
TBM-20bm			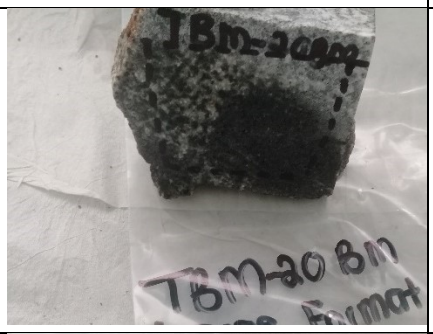	The thin section could not be made	
TBM-21	800026E 7194105S		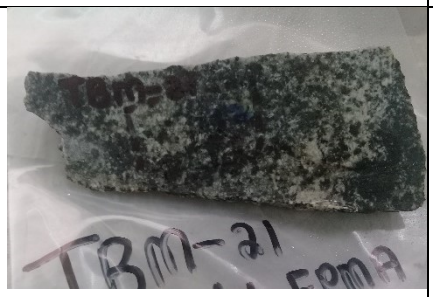		

TBM-22	800017E 7194101S		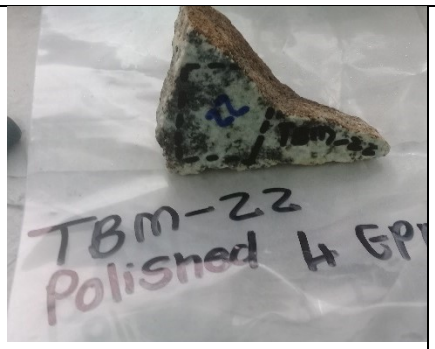	
TBM-23	800016E 7194099S			
TBM-24b	800005E 7194103S		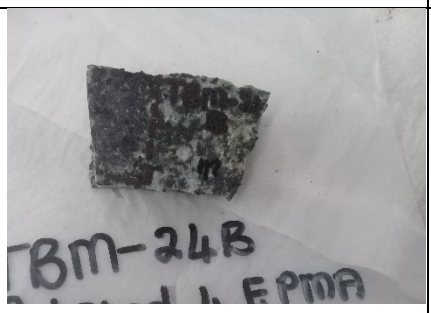	The thin section could not be made
TBM-24m	800005E 7194103S		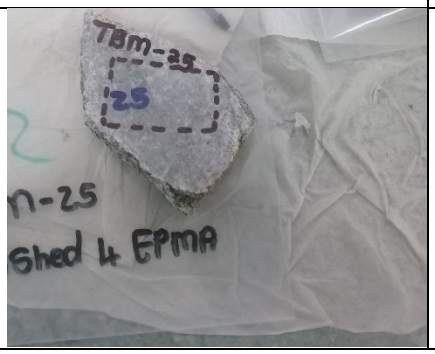	The thin section could be made

TBM-25	TBM-26	TBM-27	TBM-28
799984E 7194109S	799916E 7194108S	799844E 7194135S	799770E 7194134S

TBM-30	799638E 7194088S			
TBM-32	799638E 7194088S			
TBM-33	800072E 7194245S			

Appendix. 4. Raw data of the analyzed samples showing the Major oxide, trace elements, and rare earth elements.

4.1 Major oxide

0,18	Height (m)	SiO2	TiO2	Al2O3	Fe2O3	FeO	MnO	MgO	CaO	Na2O	K2O	P2O5	Cr2O
		%	%	%	%	%	%	%	%	%	%	%	%
TBM-1	1628,41	52,04	0,31	16,16	1,46	6,58	0,15	8,08	11,74	2,35	0,26	0,02	0,05
TBM-2	1631,94	51,97	0,28	15,97	1,61	7,24	0,17	7,71	11,47	2,31	0,23	0,02	0,05
TBM-3	1633,88	52,16	0,36	15,90	1,55	6,99	0,16	7,48	11,35	2,33	0,36	0,04	0,05
TBM-4	1634,88	52,73	0,30	16,61	1,16	5,22	0,13	9,18	11,39	1,92	0,47	0,04	0,11
TBM-5	1642,05	53,15	0,38	16,09	1,11	4,98	0,12	7,67	10,97	2,19	0,87	0,06	0,09
TBM-6m	1644,28	53,84	0,52	17,19	1,26	5,65	0,13	6,96	9,51	2,64	0,79	0,09	0,11

TBM-8m	1646,16	53,63	0,26	7,31	2,09	9,41	0,19	17,59	5,58	0,91	0,43	0,03	0,46
TBM-7b-1	1646,16	53,10	0,29	7,76	2,12	9,54	0,19	17,51	5,23	0,93	0,53	0,03	0,68
TBM-7b-2	1646,16	52,99	0,63	19,43	1,01	4,56	0,12	4,72	9,86	3,04	1,12	0,10	0,04
TBM-7m	1647,81	53,45	0,47	16,69	1,41	6,33	0,14	7,94	9,02	2,40	0,76	0,08	0,10
TBM-9	1654,04	53,91	0,49	16,28	1,41	6,34	0,14	7,59	9,44	2,24	0,80	0,08	0,07
TBM-10	1665,03	52,94	0,42	17,87	1,31	5,89	0,13	7,21	9,96	2,39	0,63	0,07	0,06
TBM-11	1668,62	53,13	0,41	18,40	1,25	5,65	0,12	6,66	9,76	2,49	0,68	0,06	0,06
TBM-12	1677,79	52,95	0,47	19,62	1,18	5,33	0,11	5,03	10,01	2,84	0,85	0,06	0,04
TBM-13	1679,25	54,65	0,68	16,34	1,57	7,05	0,14	4,89	9,27	2,73	1,11	0,13	0,02
TBM-16	1687,83	56,21	1,10	13,87	1,76	7,92	0,17	5,21	8,07	2,45	1,28	0,25	0,01
TBM-17	1687,83	52,80	0,43	15,63	1,46	6,57	0,15	6,17	10,41	2,50	0,75	0,05	0,02
TBM-18	1699,18	52,95	0,53	21,10	0,93	4,18	0,08	3,64	10,22	2,92	1,00	0,08	0,03
TBM-19	1706,18	53,51	0,45	19,05	1,19	5,36	0,13	5,26	10,24	2,76	0,84	0,08	0,03
TBM-21	1715,11	52,87	0,28	8,40	2,24	10,07	0,20	15,33	6,36	1,03	0,50	0,03	0,22
TBM-20b	1715,11	54,00	0,50	18,53	1,17	5,27	0,11	5,88	9,82	2,71	0,84	0,06	0,05
TBM-20m	1717,59	53,43	0,37	19,08	1,10	4,96	0,11	5,76	9,54	2,78	0,84	0,08	0,05
TBM-22	1719,17	53,47	0,42	23,60	0,58	2,59	0,06	2,28	10,72	3,54	1,11	0,07	0,02
TBM-23	1719,35	53,52	0,47	19,81	0,99	4,45	0,10	4,65	10,40	2,85	0,83	0,08	0,04
TBM-24b	1722,29	53,09	0,36	8,07	2,36	10,64	0,21	14,73	6,15	1,00	0,67	0,05	0,19
TBM-24m	1722,29	53,78	0,39	18,81	1,19	5,34	0,13	5,61	9,78	2,69	0,83	0,07	0,04
TBM-25	1726,99	53,11	0,39	18,33	1,28	5,74	0,13	6,23	9,90	2,58	0,75	0,07	0,04
TBM-26	1738,98	52,80	0,42	19,64	1,07	4,81	0,11	5,43	10,46	2,68	0,80	0,08	0,05
TBM-27	1739,68	54,90	0,64	16,30	1,57	7,09	0,14	4,96	9,20	2,73	1,12	0,12	0,02
TBM-28	1739,72	55,42	0,79	15,78	1,67	7,51	0,15	5,04	8,81	2,73	1,23	0,13	0,02
TBM-29	1758,24	54,45	0,63	15,56	1,54	6,94	0,14	5,34	10,11	2,63	1,01	0,12	0,04
TBM-30	1763,00	54,09	0,53	15,75	1,51	6,79	0,16	6,20	10,17	2,60	0,92	0,08	0,03
TBM-31b	1721,94	53,72	0,45	7,48	2,48	11,15	0,22	14,49	6,22	0,98	0,70	0,05	0,17
TBM-31m	1721,94	53,76	0,40	20,19	0,83	3,75	0,11	4,30	9,90	3,17	1,17	0,07	0,04
TBM-32	1790,00	53,04	0,33	8,11	2,55	11,50	0,24	13,81	7,68	1,06	0,36	0,09	0,13

	BaO	Ag	Al	As	Ba	Be	Bi	Ca	Cd	Ce	Co	Cr	Cs	Cu	Fe
	%	ppm	ppm	ppm	ppm	ppm	ppm	ppm	ppm	ppm	ppm	ppm	ppm	ppm	%
TBM-1	0,02	X	83305	X	103,8	0,31	X	82070	0,11	8,09	52	288	0,32	8,4	6
TBM-2	0,02	X	83075	X	109,7	0,34	0,03	80062	0,06	6,76	53,3	246	0,25	22,4	6,
TBM-3	0,03	X	84240	X	149,2	0,5	0,01	81809	0,05	14,26	52,1	264	0,56	28,3	6,
TBM-4	0,03	X	85382	0,6	138,7	0,42	0,02	79574	0,03	16,08	41,8	516	0,56	19,8	4,

TBM-5	0,04	X	84815	1,3	223,2	0,65	0,03	77846	0,04	25,42	37,2	519	1,2	28,8	4
TBM-6m	0,04	X	85726	0,8	258,1	0,68	0,02	65043	0,02	30,35	38,1	629	0,68	37,3	5
TBM-7b-1	0,01	X	38424	0,6	101,6	0,25	0,02	38864	0,06	11,13	78,8	2455	0,69	70,8	8
TBM-7b-2	0,02	X	41013	0,5	112,1	0,25	0,02	36335	0,05	11,38	80,9	3971	0,78	30,6	8
TBM-7m	0,05	0,49	102807	1,3	309,4	0,76	0,08	70692	0,17	29,76	28,7	261	1,45	50,2	4
TBM-8m	0,03	X	88525	0,8	232,6	0,65	0,02	64112	0,04	25,1	43,2	569	0,99	43,6	5
TBM-9	0,04	X	84434	1,5	235,3	0,68	0,04	65157	0,09	28,89	42,8	413	0,87	49	5
TBM-10	0,03	0,17	94423	0,9	202,8	0,58	0,02	70354	0,05	23,33	40,5	328	0,78	42,9	5
TBM-11	0,04	0,05	96281	0,9	215,9	0,66	0,04	69138	0,08	25,09	39,3	317	0,68	59,2	5
TBM-12	0,04	X	105245	0,8	247,1	0,71	0,03	72552	0,05	26,69	33,2	158	1,11	38,3	4
TBM-13	0,05	X	85388	1,3	326,5	0,93	0,03	65838	0,07	44,32	38,6	96	0,85	59,5	6
TBM-16	0,05	0,07	71451	1,4	361	0,89	0,06	55865	0,14	55,35	44,3	60	1,25	46,4	7
TBM-17	0,04	X	81068	1	251	0,68	0,03	72980	0,08	24,28	42,9	87	1,14	31,2	5
TBM-18	0,04	X	111093	0,9	257,1	0,72	0,02	73039	0,05	28,63	24,5	130	1,51	46,3	3
TBM-19	0,04	X	98004	1,1	248,9	0,71	0,04	72512	0,05	29,11	34,4	175	0,77	29,9	4
TBM-20b	0,02	X	43787	1,4	110,7	0,32	0,02	43758	0,07	14,98	77,1	1213	0,85	40,9	9
TBM-20m	0,04	X	96327	0,9	265,6	0,75	0,02	68592	0,04	27,42	34,5	282	0,87	39,4	4
TBM-21	0,04	X	99942	0,7	247,2	0,75	0,03	68152	0,07	26,83	32,4	276	0,96	34	4
TBM-22	0,05	X	125422	0,8	307,3	0,86	0,02	77155	0,03	28,2	14,3	101	1,32	33	2
TBM-23	0,04	X	105052	0,7	246,4	0,73	0,02	74595	0,04	28,61	28	206	0,95	41,8	4
TBM-24b	0,02	X	42784	1,8	156,1	0,34	0,07	43023	0,13	19,21	80,4	1055	1,2	48,5	9
TBM-24m	0,04	X	99027	0,8	254	0,72	0,02	69183	0,07	25,73	36	215	1,11	41	4
TBM-25	0,04	X	95307	0,9	207,5	0,62	0,03	69652	0,06	24,51	37,7	228	1,04	35,7	5
TBM-26	0,04	X	103552	1,3	209,8	0,63	0,03	75185	0,04	25,69	31,6	245	1,04	31,3	4
TBM-27	0,04	X	84030	1,2	321,9	0,99	0,03	64957	0,07	42,52	38,2	98	0,89	57,5	6
TBM-28	0,05	X	83511	1,2	387	0,95	0,03	62815	0,09	46,55	40,4	99	0,75	62,5	6
TBM-29	0,04	X	82435	1,2	311,1	0,88	0,02	70716	0,06	39,63	38,2	195	0,78	50,6	6
TBM-30	0,04	X	81270	1,3	278,3	0,79	0,03	71305	0,06	31,77	40,8	168	0,85	48,4	6
TBM-31b	0,03	0,07	40099	2,5	199,7	0,37	0,07	43103	0,09	24,49	84,9	962	1,48	70	1
TBM-31m	0,05	0,08	107759	1,3	318,9	0,8	0,06	71828	0,18	27,38	25,9	188	1,74	52,8	3
TBM-32	0,02	X	41601	0,9	100,4	0,31	0,02	51940	0,04	16,89	77	683	0,41	50	1

4.3 Rare Earth Elements

ELEMENTS	La	Ce	Pr	Nd	Sm	Eu	Gd	Tb	Dy	Ho	Er	Tm
UNITS	ppm	ppm	ppm	ppm	ppm	ppm	ppm	ppm	ppm	ppm	ppm	ppm

DETECTION	0,01	0,01	0,01	0,01	0,01	0,01	0,01	0,01	0,01	0,01	0,01	0,01
METHOD	4A/MS	4A/MS	4A/MS	4A/MS	4A/MS	4A/MS	4A/MS	4A/MS	4A/MS	4A/MS	4A/MS	4A/
	0,237	0,613	0,093	0,457	0,148	0,056	0,199	0,036	0,246	0,0546	0,16	0,02
TBM-1	3,77	8,09	1,06	4,86	1,15	0,55	1,45	0,22	1,32	0,31	0,79	0,1
TBM-2	3,35	6,76	0,89	4,03	1,05	0,59	1,33	0,19	1,29	0,27	0,78	0,11
TBM-3	7,14	14,26	1,84	7,91	1,76	0,73	1,83	0,3	1,89	0,39	1,2	0,17
TBM-4	8,07	16,08	1,94	7,75	1,61	0,69	1,61	0,25	1,68	0,34	1	0,13
TBM-5	12,93	25,42	3,02	12,01	2,24	0,79	2,38	0,34	2,21	0,45	1,37	0,18
TBM-6m	15,58	30,35	3,55	14,45	2,62	0,91	2,63	0,39	2,43	0,48	1,41	0,18
TBM-7b-1	5,64	11,13	1,38	5,4	1,14	0,35	1,26	0,22	1,34	0,27	0,88	0,14
TBM-7b-2	5,95	11,38	1,32	5,4	1,1	0,32	1,03	0,17	1,13	0,26	0,8	0,13
TBM-7m	15,67	29,76	3,38	12,99	2,51	0,92	2,32	0,34	2,08	0,4	1,18	0,15
TBM-10	11,88	23,33	2,8	10,44	2,11	0,82	2,05	0,32	1,97	0,42	1,26	0,17
TBM-11	12,81	25,09	2,98	11,35	2,3	0,79	2,1	0,32	1,99	0,41	1,3	0,17
TBM-12	13,82	26,69	3,13	12,38	2,5	0,91	2,44	0,35	2,25	0,46	1,37	0,19
TBM-13	22,25	44,32	5,35	20,72	4,22	1,22	4,12	0,64	3,88	0,77	2,37	0,32
TBM-17	12,03	24,28	2,99	12,15	2,51	0,93	2,45	0,39	2,41	0,5	1,56	0,21
TBM-18	14,79	28,63	3,32	12,72	2,38	1,02	2,28	0,33	1,92	0,39	1,21	0,16
TBM-19	15,26	29,11	3,32	13,22	2,49	0,85	2,41	0,36	2,27	0,44	1,28	0,17
TBM-20b	7,48	14,98	1,87	7,34	1,58	0,44	1,56	0,26	1,53	0,33	1,13	0,16
TBM-20m	13,82	27,42	3,29	13,02	2,49	0,94	2,36	0,37	2,17	0,44	1,34	0,18
TBM-21	14,35	26,83	2,99	11,21	2,03	0,88	1,88	0,28	1,73	0,32	1,02	0,14
TBM-22	14,63	28,2	3,25	12,17	2,22	1,2	2,08	0,3	1,88	0,34	0,97	0,14
TBM-23	14,53	28,61	3,47	13,37	2,75	0,97	2,64	0,39	2,32	0,46	1,36	0,17
TBM-24b	8,89	19,21	2,39	9,78	2,13	0,46	2,15	0,34	2,27	0,48	1,47	0,21
TBM-24m	13,53	25,73	3,02	11,08	2,31	0,89	2,12	0,32	2,06	0,4	1,26	0,17
TBM-25	12,65	24,51	2,91	11,26	2,1	0,91	1,95	0,31	2,09	0,37	1,23	0,17
TBM-26	13,24	25,69	3	11,58	2,09	0,78	1,92	0,29	1,84	0,36	1,11	0,16
TBM-27	21,32	42,52	5,15	20,32	4,07	1,17	3,98	0,61	3,79	0,78	2,33	0,32
TBM-28	23,59	46,55	5,48	21,82	4,44	1,25	4,31	0,64	4,04	0,8	2,36	0,32
TBM-29	19,85	39,63	4,78	18,82	3,95	1,17	3,84	0,59	3,67	0,71	2,23	0,3
TBM-30	16,07	31,77	3,9	15,42	3,35	0,98	3,38	0,51	3,09	0,63	1,9	0,26
TBM-31b	11,35	24,49	3,07	12,3	2,46	0,45	2,56	0,44	2,81	0,6	1,79	0,26
TBM-31m	15,08	27,38	3,1	11,84	2,04	0,95	2,04	0,29	1,81	0,35	1,08	0,14
TBM-32	8,04	16,89	2,14	9,05	2,07	0,48	2,22	0,36	2,34	0,48	1,58	0,23
TBM-33	5,4	10,1	1,19	4,87	1,06	0,61	1,06	0,17	1,14	0,23	0,71	0,11

The tables below show the Raw data oxide data as it was calculated from the EPMA and results are given in the table bounded by the bold lines. The values that gave a total that fell out of the 99-101% range were filtered out of the data. In the case where the standard was being measured, the true compositional values are shown in the blocks highlighted in yellow and the error is calculated under column Error. It is important to note the $\mathbf{SiO_2}$ measurements are quite variable within each sample; this also affected the total values of the oxides. Sample TBM 12, TBM 13, TBM 17, TBM 18, and TBM 25 was not responding properly to the analyses and gave totals that are less than 60%

Standards before TBM 3, 4, 5 and 6

Filename: Standard before TBM 3 4 5 6. qtiDat13.qtiDat
Signal(s) Used: Na Ka, Mg Ka, Al Ka, Si Ka, K Ka, Ca Ka, Fe Ka
Spectrometers Conditions: Sp4 TAP, Sp4 TAP, Sp2 TAP, Sp1 TAP, Sp5 LPET, Sp5 LPET, Sp3 LLIF
Full Spectromers Conditions : Sp4 TAP(2d= 25.745,K= 0.00218), Sp4 TAP(2d= 25.745,K= 0.00218), Sp2 TAP(2d= TAP(2d= 25.745,K= 0.00218), Sp5 LPET(2d= 8.75,K= 0.000144), Sp5 LPET(2d= 8.75,K= 0.000144), Sp3 LLIF(2d= 4
Column Conditions: Cond 1: 15keV -0.001nA
Date: 9-July 2020
Username: SX
Setup Name: Plagioclase quantification method 15. qtiSet
Dataset Comment:
Comment:
Analysis Date: 12/9/2019 9:34:34 AM
Project Name: Default Project
Sample Name: Default Sample
Analysis Parameters:

Sp	Elements	Xtal	Position	Bg+	Bg-	Slope	Bias	Gain	Dtime	Blin	Wind	Mode
Sp4	Na Ka		TAP	46357		-500	500		1278	2516	3	560
Sp4	Mg Ka		TAP	39181		-500	500		1278	2516	3	560
Sp2	Al Ka		TAP	32457		-500	500		1296	2927	3	560
Sp1	Si Ka		TAP	27745		-500	500		1330	4095	3	560
Sp5	K Ka		LPET	42777		-500	500		1820	617	3	560
Sp5	Ca Ka		LPET	38392		-500	500		1820	617	3	560
Sp3	Fe Ka		LLIF	48122		-500	500		1865	494	3	560

Peak Position : Sp4 46357 (-500, 500), Sp4 39181 (-500, 500), Sp2 32457 (-500, 500), Sp1 27745 (-500, 500), Sp5 427 (-500, 500), Sp3 48122 (-500, 500)

Current Sample Position: X = 12825 Y = -28349 Z = 4

Standard Name:

Na, Mg, Al, Si, K, Ca, Fe On Plagioclase

Standard composition:

Plagioclase = O: 46.79%, Na: 3.24%, Mg: 0.06%, Al: 15.54%, Si: 24.83%, K: 0.2%, Ca: 8.53%, Fe: 0.27%

Calibration file name (Element intensity cps/nA):

Na, K: Plagioclase_NaSp4_K Sp5_001.calDat (Na: 21.2 cps/nA, K: 5.9 cps/nA)

Mg: Plagioclase_MgSp4_001.calDat (Mg: 3.8 cps/nA)
Al, Si: Plagioclase_AlSp2_SiSp1_001.calDat (Al: 322.1 cps/nA, Si: 377.5 cps/nA)
Ca, Fe: Plagioclase_CaSp5_FeSp3_001.calDat (Ca: 217.2 cps/nA, Fe: 1.3 cps/nA)
Beam Size: 0 µm

Dataset/Point	Na2O	MgO	Al2O3	SiO2	K2O	CaO	FeO
Standards before TBM 3 4 5 6	4,313	0,1018	28,98	52,1316	0,24	11,96	0,334
Standards before TBM 3 4 5 6	4,297	0,1011	29,47	53,0633	0,24	11,94	0,37
Standards before TBM 3 4 5 6	4,29	0,1021	29,5	53,1247	0,24	11,88	0,334
Standards before TBM 3 4 5 6	4,298	0,1008	29,39	53,2175	0,24	11,93	0,364
Standards before TBM 3 4 5 6	4,539	0,0955	29,53	53,1849	0,26	11,88	0,345
Standards before TBM 3 4 5 6	4,444	0,1069	29,17	53,0299	0,24	12,1	0,417
Standards before TBM 3 4 5 6	4,337	0,0985	29,57	53,2721	0,22	12	0,323
Standards before TBM 3 4 5 6	4,391	0,0981	29,46	53,6647	0,24	11,91	0,295
Standards before TBM 3 4 5 6	4,331	0,1005	29,13	53,1102	0,24	11,92	0,299
Standards before TBM 3 4 5 6	4,36	0,0945	29,31	53,4012	0,23	11,78	0,319
True Value	4,36	0,1	29,35	53,12	0,24	11,93	0,34

Sample TBM 3, 4, 5 and 6

File Name: TBM 3 4 5 6. qtiDat
Signal(s) Used: Na Ka, Mg Ka, Al Ka, Si Ka, K Ka, Ca Ka, Fe Ka
Spectromers Conditions: Sp4 TAP, Sp4 TAP, Sp2 TAP, Sp1 TAP, Sp5 LPET, Sp5 LPET, Sp3 LLIF
Full Spectromers Conditions : Sp4 TAP(2d= 25.745,K= 0.00218), Sp4 TAP(2d= 25.745,K= 0.00218), Sp2 TAP(2d= 25.745,K 25.745,K= 0.00218), Sp5 LPET(2d= 8.75,K= 0.000144), Sp5 LPET(2d= 8.75,K= 0.000144), Sp3 LLIF(2d= 4.0267,K= 0.0000

Column Conditions: Cond 1: 15keV -0.001nA

Date: 9-July-2020

Username: SX

Setup Name: Plagioclase quantification method 15. qtiSet

Data Set Comment:

Comment:

Analysis Date: 12/9/2019 10:22:26 AM

Project Name: Default Project

Sample Name: Default Sample

Analysis Parameters:

Sp	Elements	Xtal	Position	Bg+	Bg-	Slope	Bias	Gain	Dtime	Blin	Wind	Mode
Sp4	Na Ka		TAP	46357		-500	500		1278	2516	3	560
Sp4	Mg Ka		TAP	39181		-500	500		1278	2516	3	560
Sp2	Al Ka		TAP	32457		-500	500		1296	2927	3	560
Sp1	Si Ka		TAP	27745		-500	500		1330	4095	3	560
Sp5	K Ka		LPET	42777		-500	500		1820	617	3	560
Sp5	Ca Ka		LPET	38392		-500	500		1820	617	3	560
Sp3	Fe Ka		LLIF	48122		-500	500		1865	494	3	560

Peak Position : Sp4 46357 (-500, 500), Sp4 39181 (-500, 500), Sp2 32457 (-500, 500), Sp1 27745 (-500, 500), Sp5 4277

(-500, 500), Sp3 48122 (-500, 500)

Current Sample Position: X = -12780 Y = 38424 Z = 125

Standard Name:

Na, Mg, Al, Si, K, Ca, Fe On Plagioclase
Standard composition:
Plagioclase = O: 46.79%, Na: 3.24%, Mg: 0.06%, Al: 15.54%, Si: 24.83%, K: 0.2%, Ca: 8.53%, Fe: 0.27%
Calibration file name (Element intensity cps/nA):
Na, K: Plagioclase_NaSp4_K Sp5_001.calDat (Na: 21.2 cps/nA, K: 5.9 cps/nA)
Mg: Plagioclase_MgSp4_001.calDat (Mg: 3.8 cps/nA)
Al, Si: Plagioclase_AlSp2_SiSp1_001.calDat (Al: 322.1 cps/nA, Si: 377.5 cps/nA)
Ca, Fe: Plagioclase_CaSp5_FeSp3_001.calDat (Ca: 217.2 cps/nA, Fe: 1.3 cps/nA)
Beam Size: 0 ɬm

Dataset/Point	Na2O	MgO	Al2O3	SiO2	K2O	CaO	FeO
TBM 3	4,579	0,09951	29,23	53,4903	0,21	11,43	0,3055
TBM 3	4,4006	0,10264	29,33	54,0668	0,22	11,45	0,3541
TBM 3	4,4761	0,10459	29,17	53,8074	0,19	11,54	0,259
TBM 3	4,4961	0,12459	29,19	53,8274	0,21	11,56	0,279
TBM 3	4,5461	0,17459	29,24	53,8774	0,26	11,61	0,329
TBM 3	4,5861	0,21459	29,28	53,9174	0,3	11,65	0,369
TBM 3	4,6461	0,27459	29,34	53,9774	0,36	11,71	0,429
TBM 4	3,1463	0,12298	31,1	51,6552	0,17	13,6	0,2268
TBM 4	3,1963	0,17298	31,15	51,7052	0,22	13,65	0,2768
TBM 4	3,2013	0,17798	31,15	51,7102	0,23	13,66	0,2818
TBM 4	3,2033	0,17998	31,15	51,7122	0,23	13,66	0,2838
TBM 4	3,2633	0,23998	31,21	51,7722	0,29	13,72	0,3438

TBM 4	3,2693	0,24598	31,22	51,7782	0,3	13,72	0,3498
TBM 5	4,3158	0,07939	26,44	58,9659	1,52	8,634	0,3556
TBM 5	4,3208	0,08439	26,44	58,9709	1,52	8,639	0,3606
TBM 5	4,3248	0,08839	26,45	58,9749	1,53	8,643	0,3646
TBM 6	4,4477	0,09642	29,15	54,3374	0,39	10,96	0,2133
TBM 6	4,4977	0,14642	29,2	54,3374	0,44	11,01	0,2633
TBM 6	4,5027	0,15142	29,21	54,3374	0,44	11,02	0,2683
TBM 6	4,5047	0,15342	29,21	54,3374	0,44	11,02	0,2703

Standards Before TBM 7m, 7b-1, 7b-2, and 7b-3

Filename: Standard after TBM 3 4 5 6 and before TBM 7m 7b1 7b2 7b3.qtiDat
Signal(s) Used: Na Ka, Mg Ka, Al Ka, Si Ka, K Ka, Ca Ka, Fe Ka
Spectromers Conditions: Sp4 TAP, Sp4 TAP, Sp2 TAP, Sp1 TAP, Sp5 LPET, Sp5 LPET, Sp3 LLIF
Full Spectromers Conditions : Sp4 TAP(2d= 25.745,K= 0.00218), Sp4 TAP(2d= 25.745,K= 0.00218), Sp2 TAP(2d= 25.745,K 25.745,K= 0.00218), Sp5 LPET(2d= 8.75,K= 0.000144), Sp5 LPET(2d= 8.75,K= 0.000144), Sp3 LLIF(2d= 4.0267,K= 0.0000
Column Conditions: Cond 1: 15keV -0.001nA
Date:
Username: SX
Setup Name: Plagioclase quantification method 15. qtiSet
Dataset Comment:
Comment:
Analysis Date: 12/9/2019 12:16:02 PM

Project Name: Default Project

Sample Name: Default Sample

Analysis Parameters:

Sp	Elements	Xtal	Position	Bg+	Bg-	Slope	Bias	Gain	Dtime	Blin	Wind	M
Sp4	Na Ka		TAP	46357		-500	500		1278	2516	3	56
Sp4	Mg Ka		TAP	39181		-500	500		1278	2516	3	56
Sp2	Al Ka		TAP	32457		-500	500		1296	2927	3	56
Sp1	Si Ka		TAP	27745		-500	500		1330	4095	3	56
Sp5	K Ka		LPET	42777		-500	500		1820	617	3	56
Sp5	Ca Ka		LPET	38392		-500	500		1820	617	3	56
Sp3	Fe Ka		LLIF	48122		-500	500		1865	494	3	56

Peak Position : Sp4 46357 (-500, 500), Sp4 39181 (-500, 500), Sp2 32457 (-500, 500), Sp1 27745 (-500, 500), Sp5 4277

(-500, 500), Sp3 48122 (-500, 500)

Current Sample Position: X = 12783 Y = -28806 Z = 4

Standard Name:

Na, Mg, Al, Si, K, Ca, Fe On Plagioclase

Standard composition:

Plagioclase = O: 46.79%, Na: 3.24%, Mg: 0.06%, Al: 15.54%, Si: 24.83%, K: 0.2%, Ca: 8.53%, Fe: 0.27%

Calibration file name (Element intensity cps/nA):

Na, K: Plagioclase_NaSp4_K Sp5_001.calDat (Na: 21.2 cps/nA, K: 5.9 cps/nA)

Mg: Plagioclase_MgSp4_001.calDat (Mg: 3.8 cps/nA)

Al, Si: Plagioclase_AlSp2_SiSp1_001.calDat (Al: 322.1 cps/nA, Si: 377.5 cps/nA)

Ca, Fe: Plagioclase_CaSp5_FeSp3_001.calDat (Ca: 217.2 cps/nA, Fe: 1.3 cps/nA)							
Beam Size: 0 µm							
Dataset/Point	Na2O	MgO	Al2O3	SiO2	K2O	CaO	Fe
Standards after TBM 3 4 5 6	4,69974	0,1063	29,35	53,17	0,23	12,09	0,
Standards after TBM 3 4 5 6	4,01184	0,1081	29,35	53,768	0,24	11,93	0,
Standards after TBM 3 4 5 6	3,90081	0,1051	29,35	53,948	0,24	11,82	0,
Standards after TBM 3 4 5 6	4,00056	0,1002	29,35	53,896	0,24	11,94	0,
Standards after TBM 3 4 5 6	3,9668	0,1086	29,35	53,844	0,25	11,85	0,
Standards after TBM 3 4 5 6	4,17547	0,1076	29,35	54,578	0,26	11,78	0,
Standards after TBM 3 4 5 6	4,12281	0,1051	29,35	53,31	0,24	11,6	0,
True standard value	4,36	0,1	29,35	53,12	0,24	11,93	0,

Sample TBM 7m, 7b-1, 7b-2, and 7b-3

Filename: TBM 7M 7B1 7B2 7B3. 2 qtiDat. QtiDat
Signal(s) Used: Na Ka, Mg Ka, Al Ka, Si Ka, K Ka, Ca Ka, Fe Ka
Spectromers Conditions: Sp4 TAP, Sp4 TAP, Sp2 TAP, Sp1 TAP, Sp5 LPET, Sp5 LPET, Sp3 LLIF
Full Spectromers Conditions : Sp4 TAP(2d= 25.745,K= 0.00218), Sp4 TAP(2d= 25.745,K= 0.00218), Sp2 TAP(2d= 25 TAP(2d= 25.745,K= 0.00218), Sp5 LPET(2d= 8.75,K= 0.000144), Sp5 LPET(2d= 8.75,K= 0.000144), Sp3 LLIF(2d= 4.0267,K
Column Conditions: Cond 1: 15keV -0.001nA
Date: 9-Dec-2019
Username: SX

Setup Name: Plagioclase quantification method 15. qtiSet

Dataset Comment:

Comment:

Analysis Date: 12/9/2019 1:45:59 PM

Project Name: Default Project

Sample Name: Default Sample

Analysis Parameters:

Sp	Elements	Xtal	Position	Bg+	Bg-	Slope	Bias	Gain	Dtime	Blin	Wind	M
Sp4	Na Ka		TAP	46357		-500	500		1278	2516	3	5
Sp4	Mg Ka		TAP	39181		-500	500		1278	2516	3	5
Sp2	Al Ka		TAP	32457		-500	500		1296	2927	3	5
Sp1	Si Ka		TAP	27745		-500	500		1330	4095	3	5
Sp5	K Ka		LPET	42777		-500	500		1820	617	3	5
Sp5	Ca Ka		LPET	38392		-500	500		1820	617	3	5
Sp3	Fe Ka		LLIF	48122		-500	500		1865	494	3	5

Peak Position : Sp4 46357 (-500, 500), Sp4 39181 (-500, 500), Sp2 32457 (-500, 500), Sp1 27745 (-500, 500), Sp5 42777

(-500, 500), Sp3 48122 (-500, 500)

Current Sample Position: X = -18112 Y = 40227 Z = 91

Standard Name:

Na, Mg, Al, Si, K, Ca, Fe On Plagioclase

Standard composition:

Plagioclase = O: 46.79%, Na: 3.24%, Mg: 0.06%, Al: 15.54%, Si: 24.83%, K: 0.2%, Ca: 8.53%, Fe: 0.27%

Calibration file name (Element intensity cps/nA):
Na, K: Plagioclase_NaSp4_K Sp5_001.calDat (Na: 21.2 cps/nA, K: 5.9 cps/nA)
Mg: Plagioclase_MgSp4_001.calDat (Mg: 3.8 cps/nA)
Al, Si: Plagioclase_AlSp2_SiSp1_001.calDat (Al: 322.1 cps/nA, Si: 377.5 cps/nA)
Ca, Fe: Plagioclase_CaSp5_FeSp3_001.calDat (Ca: 217.2 cps/nA, Fe: 1.3 cps/nA)
Beam Size: 0 ǂm

Dataset/Point	Na2O	MgO	Al2O3	SiO2	K2O	C
TBM 7m	3,790294	0,116	30,7	51,1	0,137	1
TBM 7m	4,080375	0,119	30,17	52,4	0,33	1
TBM 7m	3,862586	0,115	30,61	52,2	0,321	1
TBM 7m	4,326615	0,104	29,4	53,4	0,357	1
TBM 7m	3,938332	0,101	30,64	52,1	0,414	1
TBM 7m	3,795694	0,11	30,71	51,1	0,332	1
TBM 7m	4,085775	0,113	30,18	52,4	0,341	1
TBM 7m	3,867986	0,11	30,61	52,2	0,332	1
TBM 7m	4,332015	0,098	29,4	53,4	0,367	1
TBM 7m	3,943732	0,096	30,64	52,1	0,424	1
TBM 7B1	3,633293	0,109	28,8	49,3	0,346	1
TBM 7B1	3,91423	0,126	30,49	51,8	0,306	1
TBM 7B1	5,171441	0,095	28,7	54,4	0,367	1
TBM 7B1	4,685223	0,1	28,24	50,5	0,368	1

TBM 7B1	3,978665	0,107	30,64	51,5	0,288	1
TBM 7B1	3,638693	0,104	28,81	49,3	0,294	1
TBM 7B1	3,91963	0,121	30,49	51,8	0,317	1
TBM 7B1	5,176841	0,09	28,71	54,4	0,378	1
TBM 7B1	4,690623	0,094	28,25	50,5	0,379	1
TBM 7B1	3,984065	0,101	30,64	51,5	0,299	1
TBM 7B2	2,849006	0,112	30,16	46,7	0,242	1
TBM 7B2	3,560535	0,1	29,89	49,4	0,294	1
TBM 7B2	3,835255	0,108	29,77	50,1	0,316	1
TBM 7B2	2,80995	0,102	28,89	43,1	0,257	1
TBM 7B2	3,821119	0,11	29,65	51	0,318	1
TBM 7B2	2,854406	0,106	30,17	46,7	0,292	1
TBM 7B2	3,565935	0,095	29,89	49,4	0,305	1
TBM 7B2	3,840655	0,102	29,78	50,1	0,327	1
TBM 7B2	2,81535	0,096	28,89	43,1	0,268	1
TBM 7B2	3,826519	0,104	29,66	51	0,329	1
TBM 7B3	3,980574	0,114	30,21	51,7	0,357	1
TBM 7B3	3,429615	0,107	30,97	50,8	0,586	1
TBM 7B3	3,073792	0,106	30,84	49,5	0,547	1
TBM 7B3	3,884	0,106	29,6	51,5	0,327	1
TBM 7B3	3,932673	0,1	29,12	51,4	0,359	1
TBM 7B3	3,985974	0,109	30,22	51,7	0,331	1
TBM 7B3	3,435015	0,102	30,98	50,8	0,597	1

TBM 7B3	3,079192	0,101	30,84	49,5	0,558	1
TBM 7B3	3,8894	0,101	29,61	51,6	0,338	1
TBM 7B3	3,938073	0,094	29,12	51,4	0,37	1

Standards Before TBM 8, 9, 10, 11

Filename: Standard after TBM 7M 7B1 7B2 7B3 and before TBM 8 9 10 11. qtiDat

Signal(s) Used: Na Ka, Mg Ka, Al Ka, Si Ka, K Ka, Ca Ka, Fe Ka

Spectromers Conditions: Sp4 TAP, Sp4 TAP, Sp2 TAP, Sp1 TAP, Sp5 LPET, Sp5 LPET, Sp3 LLIF

Full Spectromers Conditions : Sp4 TAP(2d= 25.745,K= 0.00218), Sp4 TAP(2d= 25.745,K= 0.00218), Sp2 TAP(2d= 25.74

25.745,K= 0.00218), Sp5 LPET(2d= 8.75,K= 0.000144), Sp5 LPET(2d= 8.75,K= 0.000144), Sp3 LLIF(2d= 4.0267,K= 0.0000

Column Conditions: Cond 1: 15keV -0.001nA

Date: 9-Dec-2019

Username: SX

Setup Name: Plagioclase quantification method 15. qtiSet

Dataset Comment:

Comment:

Analysis Date: 12/9/2019 1:45:59 PM

Project Name: Default Project

Sample Name: Default Sample

Analysis Parameters:

Sp	Elements	Xtal	Position	Bg+	Bg-	Slope	Bias	Gain	Dtime	Blin
Sp4	Na Ka		TAP	46357		-500	500		1278	2516

Sp4	Mg Ka		TAP	39181		-500	500		1278	2516
Sp2	Al Ka		TAP	32457		-500	500		1296	2927
Sp1	Si Ka		TAP	27745		-500	500		1330	4095
Sp5	K Ka		LPET	42777		-500	500		1820	617
Sp5	Ca Ka		LPET	38392		-500	500		1820	617
Sp3	Fe Ka		LLIF	48122		-500	500		1865	494

Peak Position : Sp4 46357 (-500, 500), Sp4 39181 (-500, 500), Sp2 32457 (-500, 500), Sp1 27745 (-500, 500), Sp5 427

500, 500), Sp3 48122 (-500, 500)

Current Sample Position: X = -18112 Y = 40227 Z = 91

Standard Name:

Na, Mg, Al, Si, K, Ca, Fe On Plagioclase

Standard composition:

Plagioclase = O: 46.79%, Na: 3.24%, Mg: 0.06%, Al: 15.54%, Si: 24.83%, K: 0.2%, Ca: 8.53%, Fe: 0.27%

Calibration file name (Element intensity cps/nA):

Na, K: Plagioclase_NaSp4_K Sp5_001.calDat (Na: 21.2 cps/nA, K: 5.9 cps/nA)

Mg: Plagioclase_MgSp4_001.calDat (Mg: 3.8 cps/nA)

Al, Si: Plagioclase_AlSp2_SiSp1_001.calDat (Al: 322.1 cps/nA, Si: 377.5 cps/nA)

Ca, Fe: Plagioclase_CaSp5_FeSp3_001.calDat (Ca: 217.2 cps/nA, Fe: 1.3 cps/nA)

Beam Size: 0 ȝm

Dataset/Point	Na2O	MgO	Al2O3	SiO2	K2O	CaO
Standards after TBM 7m, 7b-1, 7b-2, and 7b-3	4,397955	0,09885	29,19664	53,1245	0,243467	11,9
Standards after TBM 7m, 7b-1, 7b-2, and 7b-4	4,351528	0,098697	29,23026	52,89335	0,246595	11,9

Standards after TBM 7m, 7b-1, 7b-2, and	7b-5	4,330502	0,105544	29,00615	53,17074	0,255241	11,9
Standards after TBM 7m, 7b-1, 7b-2, and	7b-6	4,338891	0,096842	29,55054	53,47711	0,266474	11,9
Standards after TBM 7m, 7b-1, 7b-2, and	7b-7	4,381124	0,100067	29,76643	52,93428	0,267698	12
True standard value		4,36	0,1	29,35	53,12	0,24	11,9

Sample TBM 8, 9,10, 11

Filename: TBM 8 9 10 11. qtiDat
Signal(s) Used: Na Ka, Mg Ka, Al Ka, Si Ka, K Ka, Ca Ka, Fe Ka
Filename: Standard after TBM 7M 7B1 7B2 7B3 and before TBM 8 9 10 11. qtiDat
Signal(s) Used: Na Ka, Mg Ka, Al Ka, Si Ka, K Ka, Ca Ka, Fe Ka
Spectromers Conditions: Sp4 TAP, Sp4 TAP, Sp2 TAP, Sp1 TAP, Sp5 LPET, Sp5 LPET, Sp3 LLIF
Full Spectromers Conditions : Sp4 TAP(2d= 25.745,K= 0.00218), Sp4 TAP(2d= 25.745,K= 0.00218), Sp2 TAP(2d= 25.74 25.745,K= 0.00218), Sp5 LPET(2d= 8.75,K= 0.000144), Sp5 LPET(2d= 8.75,K= 0.000144), Sp3 LLIF(2d= 4.0267,K= 0.0000
Column Conditions: Cond 1: 15keV -0.001nA
Date: 9-Dec-2019
Username: SX
Setup Name: Plagioclase quantification method 15. qtiSet
Dataset Comment:
Comment:
Analysis Date: 12/9/2019 1:45:59 PM
Project Name: Default Project
Sample Name: Default Sample

Analysis Parameters:

Sp	Elements	Xtal	Position	Bg+	Bg-	Slope	Bias	Gain	Dtime	Blin
Sp4	Na Ka		TAP	46357		-500	500		1278	2516
Sp4	Mg Ka		TAP	39181		-500	500		1278	2516
Sp2	Al Ka		TAP	32457		-500	500		1296	2927
Sp1	Si Ka		TAP	27745		-500	500		1330	4095
Sp5	K Ka		LPET	42777		-500	500		1820	617
Sp5	Ca Ka		LPET	38392		-500	500		1820	617
Sp3	Fe Ka		LLIF	48122		-500	500		1865	494

Peak Position : Sp4 46357 (-500, 500), Sp4 39181 (-500, 500), Sp2 32457 (-500, 500), Sp1 27745 (-500, 500), Sp5 427

500, 500), Sp3 48122 (-500, 500)

Current Sample Position: X = -18112 Y = 40227 Z = 91

Standard Name:

Na, Mg, Al, Si, K, Ca, Fe On Plagioclase

Standard composition:

Plagioclase = O: 46.79%, Na: 3.24%, Mg: 0.06%, Al: 15.54%, Si: 24.83%, K: 0.2%, Ca: 8.53%, Fe: 0.27%

Calibration file name (Element intensity cps/nA):

Na, K: Plagioclase_NaSp4_K Sp5_001.calDat (Na: 21.2 cps/nA, K: 5.9 cps/nA)

Mg: Plagioclase_MgSp4_001.calDat (Mg: 3.8 cps/nA)

Al, Si: Plagioclase_AlSp2_SiSp1_001.calDat (Al: 322.1 cps/nA, Si: 377.5 cps/nA)

Ca, Fe: Plagioclase_CaSp5_FeSp3_001.calDat (Ca: 217.2 cps/nA, Fe: 1.3 cps/nA)

Beam Size: 0 ⅀m

Dataset/Point	Na2O	MgO	Al2O3	SiO2	K2O	CaO
TBM 8	3,329185	0,129371	31,35657	49,32837	0,095833	14
TBM 8	3,506023	0,102214	30,59653	49,08182	0,112078	14,1
TBM 8	3,507726	0,114985	32,0249	52,47443	0,186731	13,5
TBM 8	3,329185	0,124371	31,36157	49,32337	0,090833	14,1
TBM 8	3,511023	0,097214	30,60153	49,07682	0,107078	14,1
TBM 8	3,512726	0,109985	32,0299	52,46943	0,181731	13,5
TBM 8	3,334185	0,119371	31,36657	49,31837	0,085833	14,1
TBM 8	3,516023	0,112164	30,60653	49,07182	0,102078	14,1
TBM 9	4,322971	0,110224	29,66829	53,24104	0,184151	12,4
TBM 9	4,280618	0,104101	29,6708	53,14953	0,185942	12,4
TBM 9	3,979706	0,105224	29,82412	52,61187	0,204136	12,7
TBM 9	4,285618	0,099101	29,6758	53,14453	0,180942	12,4
TBM 9	3,984706	0,100224	29,82912	52,60687	0,199136	12,7
TBM 10	4,050757	0,131175	30,13562	52,78688	0,134467	12,8
TBM 10	2,596679	0,089933	30,13541	46,70902	0,674966	15,2
TBM 10	5,181228	0,098985	28,11789	55,63124	0,25712	10,6
TBM 10	3,769069	0,09968	28,79709	48,77091	0,200935	12,3
TBM 10	3,708321	0,126175	29,10684	49,91938	0,198449	12,4
TBM 10	2,601679	0,084933	30,14041	46,70402	0,669966	15,2
TBM 10	5,186228	0,093985	28,12289	55,62624	0,25212	10,6
TBM 10	3,774069	0,09468	28,80209	48,76591	0,195935	12,3
TBM 10	3,713321	0,121175	29,11184	49,91438	0,193449	12,4

TBM 10	2,606679	0,106132	30,14541	46,69902	0,664966	15,2
TBM 11	3,772873	0,09324	27,7094	46,87941	0,207195	11,6
TBM 11	3,353412	0,11019	28,27379	45,60344	0,171958	12,3
TBM 11	3,777873	0,08824	27,7144	46,87441	0,202195	11,6
TBM 11	3,358412	0,10519	28,27879	45,59844	0,166958	12,3
TBM 11	3,782873	-0,00871	27,7194	46,86941	0,197195	11,6

Standard before 19, 20m, 20b and 21

Filename: Standards before TBM 19, 20m, 20b, and 21. qtiDat

Signal(s) Used: Na Ka, Mg Ka, Al Ka, Si Ka, K Ka, Ca Ka, Fe Ka
Filename: Standard after TBM 7M 7B1 7B2 7B3 and before TBM 8 9 10 11. qtiDat
Signal(s) Used: Na Ka, Mg Ka, Al Ka, Si Ka, K Ka, Ca Ka, Fe Ka
Spectromers Conditions: Sp4 TAP, Sp4 TAP, Sp2 TAP, Sp1 TAP, Sp5 LPET, Sp5 LPET, Sp3 LLIF
Full Spectromers Conditions : Sp4 TAP(2d= 25.745,K= 0.00218), Sp4 TAP(2d= 25.745,K= 0.00218), Sp2 TAP(2d= 25.74 TAP(2d= 25.745,K= 0.00218), Sp5 LPET(2d= 8.75,K= 0.000144), Sp5 LPET(2d= 8.75,K= 0.000144), Sp3 LLIF(2d= 4.0267,K
Column Conditions: Cond 1: 15keV -0.001nA
Date: 9-Dec-2019
Username: SX
Setup Name: Plagioclase quantification method 15. qtiSet
Dataset Comment:
Comment:
Analysis Date: 12/9/2019 1:45:59 PM

Project Name: Default Project

Sample Name: Default Sample

Analysis Parameters:

Sp	Elements	Xtal	Position	Bg+	Bg-	Slope	Bias	Gain	Dtime	E
Sp4	Na Ka		TAP	46357		-500	500		1278	2
Sp4	Mg Ka		TAP	39181		-500	500		1278	2
Sp2	Al Ka		TAP	32457		-500	500		1296	2
Sp1	Si Ka		TAP	27745		-500	500		1330	4
Sp5	K Ka		LPET	42777		-500	500		1820	6
Sp5	Ca Ka		LPET	38392		-500	500		1820	6
Sp3	Fe Ka		LLIF	48122		-500	500		1865	4

Peak Position : Sp4 46357 (-500, 500), Sp4 39181 (-500, 500), Sp2 32457 (-500, 500), Sp1 27745 (-500, 500), Sp5 427

38392 (-500, 500), Sp3 48122 (-500, 500)

Current Sample Position: X = -18112 Y = 40227 Z = 91

Standard Name:

Na, Mg, Al, Si, K, Ca, Fe On Plagioclase

Standard composition:

Plagioclase = O: 46.79%, Na: 3.24%, Mg: 0.06%, Al: 15.54%, Si: 24.83%, K: 0.2%, Ca: 8.53%, Fe: 0.27%

Calibration file name (Element intensity cps/nA):

Na, K: Plagioclase_NaSp4_K Sp5_001.calDat (Na: 21.2 cps/nA, K: 5.9 cps/nA)

Mg: Plagioclase_MgSp4_001.calDat (Mg: 3.8 cps/nA)

Al, Si: Plagioclase_AlSp2_SiSp1_001.calDat (Al: 322.1 cps/nA, Si: 377.5 cps/nA)

Ca, Fe: Plagioclase_CaSp5_FeSp3_001.calDat (Ca: 217.2 cps/nA, Fe: 1.3 cps/nA)						
Beam Size: 0 µm						
Dataset/Point	Na2O	MgO	Al2O3	SiO2	K2O	C
Standard before TBM 12, 13, 17 and 18	4,585474	0,096245	28,94711	54,12638	0,257364	1
Standard before TBM 12, 13, 17 and 18	4,613428	0,100334	28,9888	54,59468	0,247135	1
Standard before TBM 12, 13, 17 and 18	4,422337	0,092467	28,75678	53,402	0,245958	1
Standard before TBM 12, 13, 17 and 18	4,633205	0,103763	29,15907	54,5079	0,270199	1
True standard value	4,36	0,1	29,35	53,12	0,24	1

Sample 19, 20m, 20b and 21

Filename: TBM 19 m 20m 20b 21
Signal(s) Used: Na Ka, Mg Ka, Al Ka, Si Ka, K Ka, Ca Ka, Fe Ka
Filename: Standard after TBM 7M 7B1 7B2 7B3 and before TBM 8 9 10 11. qtiDat
Signal(s) Used: Na Ka, Mg Ka, Al Ka, Si Ka, K Ka, Ca Ka, Fe Ka
Spectromers Conditions: Sp4 TAP, Sp4 TAP, Sp2 TAP, Sp1 TAP, Sp5 LPET, Sp5 LPET, Sp3 LLIF
Full Spectromers Conditions : Sp4 TAP(2d= 25.745,K= 0.00218), Sp4 TAP(2d= 25.745,K= 0.00218), Sp2 TAP(2d= 25.74 TAP(2d= 25.745,K= 0.00218), Sp5 LPET(2d= 8.75,K= 0.000144), Sp5 LPET(2d= 8.75,K= 0.000144), Sp3 LLIF(2d= 4.0267,K
Column Conditions: Cond 1: 15keV -0.001nA
Date: 9-Dec-2019
Username: SX
Setup Name: Plagioclase quantification method 15. qtiSet
Dataset Comment:

Comment:

Analysis Date: 12/9/2019 1:45:59 PM

Project Name: Default Project

Sample Name: Default Sample

Analysis Parameters:

Sp	Elements	Xtal	Position	Bg+	Bg-	Slope	Bias	Gain	Dtime	Blin	Wind
Sp4	Na Ka		TAP	46357		-500	500		1278	2516	3
Sp4	Mg Ka		TAP	39181		-500	500		1278	2516	3
Sp2	Al Ka		TAP	32457		-500	500		1296	2927	3
Sp1	Si Ka		TAP	27745		-500	500		1330	4095	3
Sp5	K Ka		LPET	42777		-500	500		1820	617	3
Sp5	Ca Ka		LPET	38392		-500	500		1820	617	3
Sp3	Fe Ka		LLIF	48122		-500	500		1865	494	3

Peak Position : Sp4 46357 (-500, 500), Sp4 39181 (-500, 500), Sp2 32457 (-500, 500), Sp1 27745 (-500, 500), Sp5 42

38392 (-500, 500), Sp3 48122 (-500, 500)

Current Sample Position: X = -18112 Y = 40227 Z = 91

Standard Name:

Na, Mg, Al, Si, K, Ca, Fe On Plagioclase

Standard composition:

Plagioclase = O: 46.79%, Na: 3.24%, Mg: 0.06%, Al: 15.54%, Si: 24.83%, K: 0.2%, Ca: 8.53%, Fe: 0.27%

Calibration file name (Element intensity cps/nA):

Na, K: Plagioclase_NaSp4_K Sp5_001.calDat (Na: 21.2 cps/nA, K: 5.9 cps/nA)

Mg: Plagioclase_MgSp4_001.calDat (Mg: 3.8 cps/nA)
Al, Si: Plagioclase_AlSp2_SiSp1_001.calDat (Al: 322.1 cps/nA, Si: 377.5 cps/nA)
Ca, Fe: Plagioclase_CaSp5_FeSp3_001.calDat (Ca: 217.2 cps/nA, Fe: 1.3 cps/nA)
Beam Size: 0 ǂm

Dataset/Point	Na2O	MgO	Al2O3	SiO2	K2O	CaO	FeO
TBM 19	3,918972	0,102013	29,10514	52,30252	0,211491	13	0,359
TBM 19	3,881135	0,108798	29,3471	52,37931	0,193421	12,9	0,388
TBM 19	3,851346	0,104816	29,20348	52,72946	0,193239	12,9	0,326
TBM 20 m	4,077568	0,10894	29,56602	53,19734	0,190863	12	0,21
TBM 20 m	3,126853	0,122962	31,19521	51,04724	0,153122	13,7	0,249
TBM 20 m	4,393485	0,105792	29,08059	54,1638	0,145939	11,5	0,246
TBM 20 m	3,805516	0,114495	30,10851	52,77713	0,171576	12,5	0,276
TBM 20 m	4,123974	0,102757	29,58826	53,49593	0,131951	12	0,246
TBM 20B	2,612507	0,115862	31,73064	51,28303	0,288912	13,4	0,242
TBM 20B	2,615708	0,105267	31,59278	51,79334	0,267348	13,3	0,232
TBM 20B	2,648459	0,113871	32,56979	50,51689	0,211377	14,3	0,243
TBM 20B	2,977889	0,122339	32,59392	50,07578	0,148794	13,5	0,229
TBM 20B	2,468431	0,118581	31,6237	51,27441	0,259943	13,7	0,275
TBM 20B	2,706166	0,102082	31,45743	52,36928	0,308934	13,1	0,238
TBM 20B	2,793236	0,115861	33,06756	49,4861	0,203723	14,8	0,309
TBM 20B	2,5852	0,10786	31,56271	51,74334	0,286188	13,4	0,221
TBM 21	3,593227	0,108201	28,87388	52,34657	0,149842	12,8	0,246

TBM 21	3,418853	0,123159	29,94673	49,59791	0,158925	12,9	0,312

Standard before 22, 23, 24m and 24b

Filename: Standards after TBM 19 20M 20B 21 and before TBM 22 23 24B 25M.qtiDat

Signal(s) Used: Na Ka, Mg Ka, Al Ka, Si Ka, K Ka, Ca Ka, Fe Ka

Spectromers Conditions: Sp4 TAP, Sp4 TAP, Sp2 TAP, Sp1 TAP, Sp5 LPET, Sp5 LPET, Sp3 LLIF

Full Spectromers Conditions : Sp4 TAP(2d= 25.745,K= 0.00218), Sp4 TAP(2d= 25.745,K= 0.00218), Sp2 TAP(2d= 25.745,K

TAP(2d= 25.745,K= 0.00218), Sp5 LPET(2d= 8.75,K= 0.000144), Sp5 LPET(2d= 8.75,K= 0.000144), Sp3 LLIF(2d= 4.0267,K

Column Conditions: Cond 1: 15keV -0.001nA

Date: 9-Dec-2019

Username: SX

Setup Name: Plagioclase quantification method 15. qtiSet

Dataset Comment:

Comment:

Analysis Date: 12/9/2019 10:22:26 AM

Project Name: Default Project

Sample Name: Default Sample

Analysis Parameters:

Sp	Elements	Xtal	Position	Bg+	Slope	Bias	Gain	Dtime	Blin	Wind	Mode
Sp4	Na Ka		TAP	46357	-500	500		1278	2516	3	560
Sp4	Mg Ka		TAP	39181	-500	500		1278	2516	3	560
Sp2	Al Ka		TAP	32457	-500	500		1296	2927	3	560

Sp1	Si Ka		TAP	27745	-500	500		1330	4095	3	560
Sp5	K Ka		LPET	42777	-500	500		1820	617	3	560
Sp5	Ca Ka		LPET	38392	-500	500		1820	617	3	560
Sp3	Fe Ka		LLIF	48122	-500	500		1865	494	3	560

Peak Position : Sp4 46357 (-500, 500), Sp4 39181 (-500, 500), Sp2 32457 (-500, 500), Sp1 27745 (-500, 500), Sp5 42

Sp5 38392 (-500, 500), Sp3 48122 (-500, 500)

Current Sample Position: X = -12780 Y = 38424 Z = 125

Standard Name:

Na, Mg, Al, Si, K, Ca, Fe On Plagioclase

Standard composition:

Plagioclase = O: 46.79%, Na: 3.24%, Mg: 0.06%, Al: 15.54%, Si: 24.83%, K: 0.2%, Ca: 8.53%, Fe: 0.27%

Calibration file name (Element intensity cps/nA):

Na, K: Plagioclase_NaSp4_K Sp5_001.calDat (Na: 21.2 cps/nA, K: 5.9 cps/nA)

Mg: Plagioclase_MgSp4_001.calDat (Mg: 3.8 cps/nA)

Al, Si: Plagioclase_AlSp2_SiSp1_001.calDat (Al: 322.1 cps/nA, Si: 377.5 cps/nA)

Ca, Fe: Plagioclase_CaSp5_FeSp3_001.calDat (Ca: 217.2 cps/nA, Fe: 1.3 cps/nA)

Beam Size: 0 ŧm

Dataset/Point	Na2O	MgO	Al2O3	SiO2	K2O	CaO	FeO
standards before 22 23 24m 24b	4,180015	0,109784	29,68543	54,61459	0,24	11,81	0,34
standards before 22 23 24m 24b	4,141086	0,114488	29,35165	54,40406	0,23	11,86	0,31
standards before 22 23 24m 24b	4,232267	0,106665	29,62895	54,3223	0,23	11,73	0,42
standards before 22 23 24m 24b	4,190546	0,108748	29,58258	54,60263	0,25	11,83	0,35

standards before 22 23 24m 24b	4,108761	0,10413	29,79876	54,60463	0,24	11,81	0,32
True standard value	4,36	0,1	29,35	53,12	0,24	11,93	0,34

Sample 22, 23, 24m and 24b

Filename: TBM 22 23 24M 24B.qtiDat
Signal(s) Used: Na Ka, Mg Ka, Al Ka, Si Ka, K Ka, Ca Ka, Fe Ka
Spectromers Conditions: Sp4 TAP, Sp4 TAP, Sp2 TAP, Sp1 TAP, Sp5 LPET, Sp5 LPET, Sp3 LLIF
Full Spectromers Conditions : Sp4 TAP(2d= 25.745,K= 0.00218), Sp4 TAP(2d= 25.745,K= 0.00218), Sp2 TAP(2d= 25.745, TAP(2d= 25.745,K= 0.00218), Sp5 LPET(2d= 8.75,K= 0.000144), Sp5 LPET(2d= 8.75,K= 0.000144), Sp3 LLIF(2d= 4.0267,K
Column Conditions: Cond 1: 15keV -0.001nA
Date: 9-Dec-2019
Username: SX
Setup Name: Plagioclase quantification method 15. qtiSet
Dataset Comment:
Comment:
Analysis Date: 12/9/2019 10:22:26 AM
Project Name: Default Project
Sample Name: Default Sample
Analysis Parameters:

Sp	Elements	Xtal	Position	Bg+	Bg-	Slope	Bias	Gain	Dtime	Blin	Wind	Mode
Sp4	Na Ka		TAP	###		-500	500		1278	2516	3	560
Sp4	Mg Ka		TAP	###		-500	500		1278	2516	3	560

Sp2	Al Ka		TAP	###		-500	500		1296	2927	3	560
Sp1	Si Ka		TAP	###		-500	500		1330	4095	3	560
Sp5	K Ka		LPET	###		-500	500		1820	617	3	560
Sp5	Ca Ka		LPET	###		-500	500		1820	617	3	560
Sp3	Fe Ka		LLIF	###		-500	500		1865	494	3	560

Peak Position : Sp4 46357 (-500, 500), Sp4 39181 (-500, 500), Sp2 32457 (-500, 500), Sp1 27745 (-500, 500), Sp5 42777

38392 (-500, 500), Sp3 48122 (-500, 500)

Current Sample Position: X = -12780 Y = 38424 Z = 125

Standard Name:

Na, Mg, Al, Si, K, Ca, Fe On Plagioclase

Standard composition:

Plagioclase = O: 46.79%, Na: 3.24%, Mg: 0.06%, Al: 15.54%, Si: 24.83%, K: 0.2%, Ca: 8.53%, Fe: 0.27%

Calibration file name (Element intensity cps/nA):

Na, K: Plagioclase_NaSp4_K Sp5_001.calDat (Na: 21.2 cps/nA, K: 5.9 cps/nA)

Mg: Plagioclase_MgSp4_001.calDat (Mg: 3.8 cps/nA)

Al, Si: Plagioclase_AlSp2_SiSp1_001.calDat (Al: 322.1 cps/nA, Si: 377.5 cps/nA)

Ca, Fe: Plagioclase_CaSp5_FeSp3_001.calDat (Ca: 217.2 cps/nA, Fe: 1.3 cps/nA)

Beam Size: 0 ȝm

Dataset/Point	Na2O	MgO	Al2O3	SiO2	K2O	CaO	FeO
TBM 22	4,803396	0,104948	29,27096	54,72386	0,18	9,755	0,34
TBM 22	4,73837	0,090612	29,69156	54,41618	0,34	9,249	0,27
TBM 22	4,944032	0,083367	29,43322	54,71597	0,3	9,776	0,21

TBM 22	4,87206	0,098706	29,2334	54,61193	0,22	9,97	0,25
TBM 23	3,70824	0,118907	30,90949	52,40685	0,11	13,16	0,3
TBM 23	3,80119	0,102557	29,19632	52,06171	0,55	10,86	1,33
TBM 23	3,806276	0,110281	30,43363	52,79079	0,14	12,85	0,29
TBM 23	4,050215	0,107677	29,99963	53,96135	0,17	12,29	0,27
TBM 23	4,00698	0,11435	30,4568	53,13569	0,15	12,81	0,35
TBM 23	4,238232	0,114591	30,25005	53,4151	0,1	12,36	0,16
TBM 23	3,901206	0,108739	30,26481	53,0029	0,18	12,7	0,27
TBM 24m	4,262619	0,10226	28,84636	54,20753	0,21	11,32	0,35
TBM 24m	3,987416	0,096047	29,86025	54,36671	0,16	11,92	0,23
TBM 24m	4,088338	0,105881	29,5271	53,77653	0,21	11,85	0,22
TBM 24m	4,261229	0,103687	28,99994	54,4525	0,24	11,45	0,28
TBM 24m	4,206707	0,103085	29,44917	54,10155	0,24	11,79	0,21
TBM 24m	4,012194	0,108351	29,40614	53,75466	0,22	11,99	0,29
TBM 24b	3,20164	0,095831	29,81726	54,00583	0,17	11,59	0,24
TBM 24b	3,026148	0,10676	29,80288	52,8159	0,14	12,08	0,21
TBM 24b	3,601701	0,093181	28,7889	54,61922	0,18	10,91	0,21
TBM 24b	3,101499	0,09463	29,45227	52,61041	0,15	11,82	0,23
TBM 24b	3,463314	0,102833	29,33479	54,50824	0,19	11	0,25
TBM 24b	3,636137	0,100099	28,55199	53,99509	0,16	10,8	0,19
TBM 24b	3,478062	0,096043	28,90387	54,2504	0,18	11,01	0,24
TBM 24b	2,665744	0,106491	30,5031	51,46549	0,12	12,42	0,3
TBM 24b	3,010107	0,108296	29,51855	52,202	0,16	11,77	0,21

TBM 24b	3,527522	0,093973	28,47734	53,46584	0,22	10,82	0,45

Standard before 26, 27, 28, 29

Filename: Standard after TBM 22 23 24m 24b and before TBM 26 27 28 29. qtiDat

Signal(s) Used: Na Ka, Mg Ka, Al Ka, Si Ka, K Ka, Ca Ka, Fe Ka
Spectromers Conditions: Sp4 TAP, Sp4 TAP, Sp2 TAP, Sp1 TAP, Sp5 LPET, Sp5 LPET, Sp3 LLIF
Full Spectromers Conditions : Sp4 TAP(2d= 25.745,K= 0.00218), Sp4 TAP(2d= 25.745,K= 0.00218), Sp2 TAP(2d= 25.74 Sp5 LPET(2d= 8.75,K= 0.000144), Sp5 LPET(2d= 8.75,K= 0.000144), Sp3 LLIF(2d= 4.0267,K= 0.000058)
Column Conditions: Cond 1: 15keV -0.001nA
Date: 9-Dec-2019
Username: SX
Setup Name: Plagioclase quantification method 15. qtiSet
Dataset Comment:
Comment:
Analysis Date: 12/9/2019 10:22:26 AM
Project Name: Default Project
Sample Name: Default Sample
Analysis Parameters:

Sp	Elements	Xtal	Position	Bg+	Bg-	Slope	Bias	Gain	Dtime	Blin
Sp4	Na Ka		TAP	46357		-500	500		1278	2516
Sp4	Mg Ka		TAP	39181		-500	500		1278	2516
Sp2	Al Ka		TAP	32457		-500	500		1296	2927

Sp1	Si Ka		TAP	27745		-500	500		1330	4095
Sp5	K Ka		LPET	42777		-500	500		1820	617
Sp5	Ca Ka		LPET	38392		-500	500		1820	617
Sp3	Fe Ka		LLIF	48122		-500	500		1865	494

Peak Position : Sp4 46357 (-500, 500), Sp4 39181 (-500, 500), Sp2 32457 (-500, 500), Sp1 27745 (-500, 500), Sp5 4277

(-500, 500)

Current Sample Position: X = -12780 Y = 38424 Z = 125

Standard Name:

Na, Mg, Al, Si, K, Ca, Fe On Plagioclase

Standard composition:

Plagioclase = O: 46.79%, Na: 3.24%, Mg: 0.06%, Al: 15.54%, Si: 24.83%, K: 0.2%, Ca: 8.53%, Fe: 0.27%

Calibration file name (Element intensity cps/nA):

Na, K: Plagioclase_NaSp4_K Sp5_001.calDat (Na: 21.2 cps/nA, K: 5.9 cps/nA)

Mg: Plagioclase_MgSp4_001.calDat (Mg: 3.8 cps/nA)

Al, Si: Plagioclase_AlSp2_SiSp1_001.calDat (Al: 322.1 cps/nA, Si: 377.5 cps/nA)

Ca, Fe: Plagioclase_CaSp5_FeSp3_001.calDat (Ca: 217.2 cps/nA, Fe: 1.3 cps/nA)

Beam Size: 0 µm

Dataset/Point	Na2O	MgO	Al2O3	SiO2	K2O
Standards before TBM 26 27 28 29	4,052981	0,106374	29,34214	52,7627	0,2419
Standards before TBM 26 27 28 29	4,036051	0,105659	29,82462	53,69442	0,2365
Standards before TBM 26 27 28 29	4,029712	0,106668	29,85426	53,75578	0,2422
Standards before TBM 26 27 28 29	4,037696	0,105283	29,74778	53,84859	0,2435

Standards before TBM 26 27 28 29	4,278669	0,100048	29,88731	53,81601	0,2606
Standards before TBM 26 27 28 29	4,183038	0,111406	29,52457	53,661	0,2425
Standards before TBM 26 27 28 29	4,076963	0,103054	29,9259	53,90326	0,2242
Standards before TBM 26 27 28 29	4,130062	0,10267	29,81542	54,29584	0,2457
Standards before TBM 26 27 28 29	4,070507	0,105011	29,49161	53,74133	0,2385
Standards before TBM 26 27 28 29	4,099537	0,099073	29,67175	54,03232	0,2338
True standard value	4,36	0,1	29,35	53,12	0,24

Sample TBM 26, 27, 28 and 29

Filename: TBM 26 27 28 29. qtiDat
Signal(s) Used: Na Ka, Mg Ka, Al Ka, Si Ka, K Ka, Ca Ka, Fe Ka
Spectromers Conditions: Sp4 TAP, Sp4 TAP, Sp2 TAP, Sp1 TAP, Sp5 LPET, Sp5 LPET, Sp3 LLIF
Full Spectromers Conditions : Sp4 TAP(2d= 25.745,K= 0.00218), Sp4 TAP(2d= 25.745,K= 0.00218), Sp2 TAP(2d= 25.74 Sp1 TAP(2d= 25.745,K= 0.00218), Sp5 LPET(2d= 8.75,K= 0.000144), Sp5 LPET(2d= 8.75,K= 0.000144), Sp3 LLIF(2d= 4.026
Column Conditions: Cond 1: 15keV -0.001nA
Date: 9-Dec-2019
Username: SX
Setup Name: Plagioclase quantification method 15. qtiSet
Dataset Comment:
Comment:
Analysis Date: 12/9/2019 10:22:26 AM
Project Name: Default Project

Sample Name: Default Sample

Analysis Parameters:

Sp	Elements	Xtal	Position	Bg+	Bg-	Slope	Bias	Gain	Dtime	Blin	Wind	Mode
Sp4	Na Ka		TAP	46357		-500	500		1278	2516	3	560
Sp4	Mg Ka		TAP	39181		-500	500		1278	2516	3	560
Sp2	Al Ka		TAP	32457		-500	500		1296	2927	3	560
Sp1	Si Ka		TAP	27745		-500	500		1330	4095	3	560
Sp5	K Ka		LPET	42777		-500	500		1820	617	3	560
Sp5	Ca Ka		LPET	38392		-500	500		1820	617	3	560
Sp3	Fe Ka		LLIF	48122		-500	500		1865	494	3	560

Peak Position : Sp4 46357 (-500, 500), Sp4 39181 (-500, 500), Sp2 32457 (-500, 500), Sp1 27745 (-500, 500), Sp5 427

Sp5 38392 (-500, 500), Sp3 48122 (-500, 500)

Current Sample Position: X = -12780 Y = 38424 Z = 125

Standard Name:

Na, Mg, Al, Si, K, Ca, Fe On Plagioclase

Standard composition:

Plagioclase = O: 46.79%, Na: 3.24%, Mg: 0.06%, Al: 15.54%, Si: 24.83%, K: 0.2%, Ca: 8.53%, Fe: 0.27%

Calibration file name (Element intensity cps/nA):

Na, K: Plagioclase_NaSp4_K Sp5_001.calDat (Na: 21.2 cps/nA, K: 5.9 cps/nA)

Mg: Plagioclase_MgSp4_001.calDat (Mg: 3.8 cps/nA)

Al, Si: Plagioclase_AlSp2_SiSp1_001.calDat (Al: 322.1 cps/nA, Si: 377.5 cps/nA)

Ca, Fe: Plagioclase_CaSp5_FeSp3_001.calDat (Ca: 217.2 cps/nA, Fe: 1.3 cps/nA)

Beam Size: 0 ǂm

Dataset/Point	Na2O	MgO	Al2O3	SiO2	K2O	CaO	FeO	T
TBM 26	4,516306	0,096357	28,72	54,42942	0,22	11,12	0,269	9
TBM 26	2,823236	0,138318	31,019	49,89057	0,11	15,03	0,306	9
TBM 26	4,322462	0,095965	29,277	54,08997	0,2	11,54	0,268	9
TBM 26	3,285939	0,124496	30,82	51,08895	0,14	13,58	0,302	9
TBM 26	4,429768	0,10017	28,934	54,30662	0,2	11,6	0,269	9
TBM 26	4,533111	0,091057	28,829	54,85141	0,22	11,14	0,283	9
TBM 26	3,737982	0,107898	29,667	53,33251	0,19	12,29	0,241	9
TBM 26	4,408849	0,099888	29,113	54,85013	0,21	11,29	0,261	1
TBM 26	4,360315	0,101443	29,067	54,57735	0,2	11,41	0,282	1
TBM 27	3,504765	0,120473	30,907	52,864	0,17	13,25	0,284	1
TBM 27	3,560734	0,121671	30,515	53,01427	0,18	13,19	0,306	1
TBM 27	3,64279	0,112733	30,645	53,08093	0,17	13,04	0,273	1
TBM 28	5,373143	0,082019	27,112	56,97053	0,3	9,391	0,227	9
TBM 28	5,119364	0,095122	27,777	56,5458	0,26	9,883	0,231	9
TBM 28	5,350926	0,081503	27,437	57,53195	0,21	9,544	0,212	1
TBM 29	4,596774	0,09299	28,243	55,13127	0,21	10,92	0,49	9
TBM 29	4,736546	0,090968	28,207	55,79374	0,21	10,79	0,233	1
TBM 29	4,937893	0,085534	28,274	56,27514	0,24	10,23	0,184	1

Sample TBM 30, 31m 31b 32

Filename: TBM 30 31m 31b 32. qtiDat

Signal(s) Used: Na Ka, Mg Ka, Al Ka, Si Ka, K Ka, Ca Ka, Fe Ka
Spectromers Conditions: Sp4 TAP, Sp4 TAP, Sp2 TAP, Sp1 TAP, Sp5 LPET, Sp5 LPET, Sp3 LLIF
Full Spectromers Conditions : Sp4 TAP(2d= 25.745,K= 0.00218), Sp4 TAP(2d= 25.745,K= 0.00218), Sp2 TAP(2d= 25.745 TAP(2d= 25.745,K= 0.00218), Sp5 LPET(2d= 8.75,K= 0.000144), Sp5 LPET(2d= 8.75,K= 0.000144), Sp3 LLIF(2d= 4.0267,K
Column Conditions: Cond 1: 15keV -0.001nA
Date: 9-Dec-2019
Username: SX
Setup Name: Plagioclase quantification method 15. qtiSet
Dataset Comment:
Comment:
Analysis Date: 12/9/2019 10:22:26 AM
Project Name: Default Project
Sample Name: Default Sample
Analysis Parameters:

Sp	Elements	Xtal	Position	Bg+	Bg-	Slope	Bias	Gain	Dtime	Blin	Wind	Mode
Sp4	Na Ka		TAP	####		-500	500		1278	2516	3	560
Sp4	Mg Ka		TAP	####		-500	500		1278	2516	3	560
Sp2	Al Ka		TAP	####		-500	500		1296	2927	3	560
Sp1	Si Ka		TAP	####		-500	500		1330	4095	3	560
Sp5	K Ka		LPET	####		-500	500		1820	617	3	560
Sp5	Ca Ka		LPET	####		-500	500		1820	617	3	560

Sp3	Fe Ka		LLIF	####		-500	500		1865	494	3	560

Peak Position : Sp4 46357 (-500, 500), Sp4 39181 (-500, 500), Sp2 32457 (-500, 500), Sp1 27745 (-500, 500), Sp5 4277

38392 (-500, 500), Sp3 48122 (-500, 500)

Current Sample Position: X = -12780 Y = 38424 Z = 125

Standard Name:

Na, Mg, Al, Si, K, Ca, Fe On Plagioclase

Standard composition:

Plagioclase = O: 46.79%, Na: 3.24%, Mg: 0.06%, Al: 15.54%, Si: 24.83%, K: 0.2%, Ca: 8.53%, Fe: 0.27%

Calibration file name (Element intensity cps/nA):

Na, K: Plagioclase_NaSp4_K Sp5_001.calDat (Na: 21.2 cps/nA, K: 5.9 cps/nA)

Mg: Plagioclase_MgSp4_001.calDat (Mg: 3.8 cps/nA)

Al, Si: Plagioclase_AlSp2_SiSp1_001.calDat (Al: 322.1 cps/nA, Si: 377.5 cps/nA)

Ca, Fe: Plagioclase_CaSp5_FeSp3_001.calDat (Ca: 217.2 cps/nA, Fe: 1.3 cps/nA)

Beam Size: 0 ŧm

Dataset/Point	Na2O	MgO	Al2O3	SiO2	K2O	CaO	FeO
TBM 30	2,988048	0,03873	28,58981	53,54801	0,11	6,437	1E-05
TBM 30	3,076067	0,009289	23,53139	55,54468	0,02	5,973	0,181
TBM 31m	5,683727	0,080169	27,22296	58,86355	0,28	9,025	0,248
TBM 31m	5,500988	0,08154	27,79146	57,73507	0,2	9,719	0,202
TBM 31m	5,318406	0,091177	27,7911	57,37616	0,28	9,866	0,221
TBM 31b	4,141168	0,112518	30,1789	53,77939	0,17	12,11	0,322
TBM 31b	3,780905	0,121146	30,38127	52,77782	0,18	13,09	0,234

TBM 31b	4,375265	0,104427	29,18405	52,92772	0,18	12,14	0,242
TBM 31b	5,099888	0,094394	28,47558	56,35055	0,35	10,23	0,225
TBM 31b	4,240367	0,102722	29,909	56,18976	0,22	11,86	0,236
TBM 31b	4,314283	0,112879	29,89374	53,57285	0,2	12,17	0,317
TBM 31b	3,843824	0,103689	29,82114	53,16392	0,21	12,62	0,263
TBM 31b	3,857502	0,127526	30,47168	53,55711	0,18	12,68	0,235
TBM 32	3,11981	0,105281	28,98231	45,67501	0,24	12,37	0,353
TBM 32	3,410656	0,103821	27,28983	52,22491	0,22	11,87	0,358
TBM 32	3,24337	0,109943	29,62857	49,53265	0,23	12,63	0,355
TBM 32	3,386527	0,105068	28,9121	49,04514	0,22	12,48	0,339
TBM 32	3,404089	0,100976	29,44646	47,82877	0,22	12,54	0,323
TBM 32	3,416786	0,109789	28,97417	50,85582	0,19	12,42	0,331
TBM 32	3,108853	0,111139	30,01183	49,45347	0,2	12,61	0,533

Standard After TBM 30, 21m, 31b and 32

Filename: Standards after TBM 30 31M 31B 32. qtiDat

Signal(s) Used: Na Ka, Mg Ka, Al Ka, Si Ka, K Ka, Ca Ka, Fe Ka
Spectromers Conditions: Sp4 TAP, Sp4 TAP, Sp2 TAP, Sp1 TAP, Sp5 LPET, Sp5 LPET, Sp3 LLIF
Full Spectromers Conditions : Sp4 TAP(2d= 25.745,K= 0.00218), Sp4 TAP(2d= 25.745,K= 0.00218), Sp2 TAP(2d= 25.74 25.745,K= 0.00218), Sp5 LPET(2d= 8.75,K= 0.000144), Sp5 LPET(2d= 8.75,K= 0.000144), Sp3 LLIF(2d= 4.0267,K= 0.0000
Column Conditions: Cond 1: 15keV -0.001nA
Date: 9-Dec-2019

Username: SX

Setup Name: Plagioclase quantification method 15. qtiSet

Dataset Comment:

Comment:

Analysis Date: 12/9/2019 10:22:26 AM

Project Name: Default Project

Sample Name: Default Sample

Analysis Parameters:

Sp	Elements	Xtal	Position	Bg+	Bg-	Slope	Bias	Gain	Dtime	Blin	Wind
Sp4	Na Ka		TAP	46357		-500	500		1278	2516	3
Sp4	Mg Ka		TAP	39181		-500	500		1278	2516	3
Sp2	Al Ka		TAP	32457		-500	500		1296	2927	3
Sp1	Si Ka		TAP	27745		-500	500		1330	4095	3
Sp5	K Ka		LPET	42777		-500	500		1820	617	3
Sp5	Ca Ka		LPET	38392		-500	500		1820	617	3
Sp3	Fe Ka		LLIF	48122		-500	500		1865	494	3

Peak Position : Sp4 46357 (-500, 500), Sp4 39181 (-500, 500), Sp2 32457 (-500, 500), Sp1 27745 (-500, 500), Sp5 42

500, 500), Sp3 48122 (-500, 500)

Current Sample Position: X = -12780 Y = 38424 Z = 125

Standard Name:

Na, Mg, Al, Si, K, Ca, Fe On Plagioclase

Standard composition:

Plagioclase = O: 46.79%, Na: 3.24%, Mg: 0.06%, Al: 15.54%, Si: 24.83%, K: 0.2%, Ca: 8.53%, Fe: 0.27%
Calibration file name (Element intensity cps/nA):
Na, K: Plagioclase_NaSp4_K Sp5_001.calDat (Na: 21.2 cps/nA, K: 5.9 cps/nA)
Mg: Plagioclase_MgSp4_001.calDat (Mg: 3.8 cps/nA)
Al, Si: Plagioclase_AlSp2_SiSp1_001.calDat (Al: 322.1 cps/nA, Si: 377.5 cps/nA)
Ca, Fe: Plagioclase_CaSp5_FeSp3_001.calDat (Ca: 217.2 cps/nA, Fe: 1.3 cps/nA)
Beam Size: 0 ŧm

Data Set/Point	Na2O	MgO	Al2O3	SiO2	K2O	CaO
Closing standards	3,939495	0,104765	29,11691	52,78081	0,23	11,71
Closing standards	4,059886	0,10237	29,00509	52,77001	0,24	11,8
Closing standards	4,000296	0,099293	29,32227	52,8065	0,24	11,68
Closing standards	3,988913	0,101698	29,09081	53,15758	0,25	11,63
Closing standards	3,950619	0,094765	28,99324	52,44457	0,26	11,66
Closing standards	3,801365	0,105437	29,48998	53,20424	0,27	11,65
Closing standards	4,09476	0,10025	29,17773	53,38353	0,25	11,54
Closing standards	3,913676	0,102736	29,41116	52,8681	0,24	11,77
Closing standards	4,09865	0,095889	29,33655	53,68934	0,23	11,76
Closing standards	3,92438	0,103922	29,61365	53,50169	0,26	11,73

Sample ID	Height	Na2O	Na	MgO	Mg Wt.	Al2O3	Al Wt.	K20	K Wt.	CaO	Ca Wt.	Fe
		0,742		0,6031		0,5293		0,83		0,7147		0,7
TBM 3	1634	4,579	3,397	0,0995	0,06	29,233	15,472	0,21	0,174	11,433	8,1711	0,3
TBM 3	1634	4,401	3,2646	0,1026	0,0619	29,328	15,522	0,22	0,182	11,453	8,1854	0,3
TBM 3	1634	4,476	3,3206	0,1046	0,0631	29,172	15,439	0,189	0,157	11,536	8,2451	0,2
TBM 3	1634	4,496	3,3354	0,1246	0,0751	29,192	15,45	0,209	0,173	11,556	8,2594	0,2
TBM 3	1634	4,546	3,3725	0,1746	0,1053	29,242	15,476	0,259	0,215	11,606	8,2951	0,3
TBM 3	1634	4,586	3,4022	0,2146	0,1294	29,282	15,497	0,299	0,248	11,646	8,3237	0,3
TBM 4	1635	3,146	2,3341	0,123	0,0742	31,096	16,458	0,173	0,144	13,602	9,721	0,2
TBM 4	1635	3,196	2,3712	0,173	0,1043	31,146	16,484	0,223	0,185	13,652	9,7568	0,2
TBM 4	1635	3,201	2,3749	0,178	0,1073	31,151	16,487	0,228	0,189	13,657	9,7603	0,2
TBM 4	1635	3,203	2,3764	0,18	0,1085	31,153	16,488	0,23	0,191	13,659	9,7618	0,2
TBM 5	1642	4,316	3,2017	0,0794	0,0479	26,44	13,993	1,518	1,26	8,6343	6,171	0,3
TBM 5	1642	4,321	3,2054	0,0844	0,0509	26,445	13,996	1,523	1,265	8,6393	6,1745	0,3
TBM 5	1642	4,325	3,2084	0,0884	0,0533	26,449	13,998	1,527	1,268	8,6433	6,1774	0,3
TBM 6	1644	4,448	3,2996	0,0964	0,0581	29,154	15,43	0,385	0,32	10,963	7,8349	0,2
TBM 6	1644	4,498	3,3367	0,1464	0,0883	29,204	15,456	0,435	0,361	11,013	7,8707	0,2
TBM 6	1644	4,503	3,3404	0,1514	0,0913	29,209	15,459	0,44	0,365	11,018	7,8743	0,2
TBM 6	1644	4,505	3,3418	0,1534	0,0925	29,211	15,46	0,442	0,367	11,02	7,8757	0,2
TBM 7m	1646	4,327	3,2097	0,1037	0,0625	29,399	15,559	0,357	0,296	12,103	8,6497	0,5
TBM 7m	1646	4,086	3,0311	0,1133	0,0683	30,177	15,971	0,341	0,283	12,685	9,0659	0,5
TBM 7m	1646	4,332	3,2137	0,0983	0,0593	29,404	15,562	0,367	0,305	12,097	8,6459	0,5
TBM 7B1	1646	3,633	2,6954	0,1092	0,0658	28,804	15,244	0,346	0,287	12,827	9,1674	0,5

TBM 7B1	1646	3,914	2,9038	0,1262	0,0761	30,488	16,136	0,306	0,254	13,31	9,5127	0,4
TBM 7B1	1646	3,639	2,6994	0,1038	0,0626	28,809	15,247	0,294	0,244	12,822	9,1636	0,4
TBM 7B1	1646	3,92	2,9078	0,1208	0,0728	30,494	16,139	0,317	0,263	13,305	9,5089	0,4
TBM 7B1	1646	3,984	2,9556	0,1013	0,0611	30,641	16,217	0,299	0,248	13,296	9,5023	0,3
TBM 7B2	1646	3,561	2,6414	0,1002	0,0604	29,886	15,817	0,294	0,244	12,899	9,2192	0,4
TBM 7B2	1646	3,835	2,8452	0,1078	0,065	29,774	15,758	0,316	0,262	12,933	9,2429	0,4
TBM 7B2	1646	3,566	2,6454	0,0948	0,0572	29,891	15,82	0,305	0,253	12,894	9,2153	0,4
TBM 7B3	1646	3,43	2,5443	0,1071	0,0646	30,974	16,393	0,586	0,487	13,195	9,4303	0,5
TBM 7B3	1646	3,435	2,5483	0,1017	0,0613	30,98	16,396	0,597	0,496	13,189	9,4264	0,5
TBM 8	1648	3,329	2,4698	0,1294	0,078	31,357	16,595	0,096	0,08	14,05	10,041	0,2
TBM 8	1648	3,506	2,601	0,1022	0,0616	30,597	16,193	0,112	0,093	14,125	10,095	0,3
TBM 8	1648	3,508	2,6022	0,115	0,0693	32,025	16,949	0,187	0,155	13,537	9,675	0,2
TBM 8	1648	3,511	2,6047	0,0972	0,0586	30,602	16,196	0,107	0,089	14,13	10,099	0,3
TBM 8	1648	3,513	2,606	0,11	0,0663	32,03	16,952	0,182	0,151	13,542	9,6785	0,2
TBM 8	1648	3,516	2,6084	0,1122	0,0676	30,607	16,199	0,102	0,085	14,135	10,102	0,3
TBM 9	1654	4,323	3,207	0,1102	0,0665	29,668	15,702	0,184	0,153	12,359	8,8331	0,3
TBM 9	1654	4,281	3,1756	0,1041	0,0628	29,671	15,703	0,186	0,154	12,363	8,836	0,2
TBM 9	1654	4,286	3,1793	0,0991	0,0598	29,676	15,706	0,181	0,15	12,368	8,8396	0,2
TBM 10	1665	4,051	3,0051	0,1312	0,0791	30,136	15,949	0,134	0,112	12,8	9,1482	0,2
TBM 10	1665	3,769	2,7961	0,0997	0,0601	28,797	15,241	0,201	0,167	12,265	8,7659	0,3
TBM 10	1665	3,774	2,7998	0,0947	0,0571	28,802	15,244	0,196	0,163	12,27	8,7695	0,2
TBM 11	1669	3,773	2,7989	0,0932	0,0562	27,709	14,665	0,207	0,172	11,567	8,2668	0,2

TBM 11	1669	3,778	2,8027	0,0882	0,0532	27,714	14,668	0,202	0,168	11,572	8,2704	0,2
TBM 11	1669	3,783	2,8064	-0,009	-0,005	27,719	14,67	0,197	0,164	11,572	8,2704	0,2
TBM 12	1678	3,777	2,8021	0,1208	0,0729	29,059	15,38	0,17	0,141	12,956	9,2599	0,2
TBM 12	1678	3,938	2,9217	0,1142	0,0689	29,059	15,38	0,203	0,168	12,616	9,0166	0,2
TBM 12	1678	3,801	2,8195	0,1111	0,067	29,059	15,38	0,205	0,171	12,682	9,0637	0,2
TBM 12	1678	3,827	2,8391	0,1214	0,0732	30,375	16,076	0,201	0,166	12,346	8,8234	0,2
TBM 19	1706	3,881	2,8793	0,1088	0,0656	29,347	15,532	0,193	0,161	12,942	9,2497	0,3
TBM 19	1706	3,851	2,8572	0,1048	0,0632	29,203	15,456	0,193	0,16	12,903	9,2219	0,3
TBM 20 m	1715	4,078	3,025	0,1089	0,0657	29,566	15,648	0,191	0,158	12,026	8,5948	0,2
TBM 20 m	1715	3,806	2,8232	0,1145	0,0691	30,109	15,935	0,172	0,142	12,529	8,9544	0,2
TBM 20 m	1715	4,124	3,0594	0,1028	0,062	29,588	15,66	0,132	0,11	11,989	8,5683	0,2
TBM 20B	1715	2,613	1,9381	0,1159	0,0699	31,731	16,793	0,289	0,24	13,384	9,5655	0,2
TBM 20B	1715	2,616	1,9405	0,1053	0,0635	31,593	16,72	0,267	0,222	13,291	9,499	0,2
TBM 20B	1715	2,648	1,9648	0,1139	0,0687	32,57	17,238	0,211	0,175	14,288	10,211	0,2
TBM 20B	1715	2,793	2,0722	0,1159	0,0699	33,068	17,501	0,204	0,169	14,831	10,599	0,3
TBM 20B	1715	2,585	1,9179	0,1079	0,0651	31,563	16,705	0,286	0,238	13,362	9,55	0,2
TBM 21	1718	3,593	2,6657	0,1082	0,0653	28,874	15,282	0,15	0,124	12,768	9,1252	0,2
TBM 21	1718	3,419	2,5363	0,1232	0,0743	29,947	15,849	0,159	0,132	12,934	9,244	0,3
TBM 22	1719	4,803	3,5634	0,1049	0,0633	29,271	15,492	0,179	0,148	9,7552	6,9721	0,3
TBM 22	1719	4,738	3,5152	0,0906	0,0546	29,692	15,714	0,337	0,279	9,2493	6,6105	0,2
TBM 22	1719	4,944	3,6678	0,0834	0,0503	29,433	15,578	0,298	0,247	9,776	6,9869	0,2
TBM 22	1719	4,872	3,6144	0,0987	0,0595	29,233	15,472	0,224	0,186	9,9703	7,1258	0,2

TBM 23	1719	4,05	3,0047	0,1077	0,0649	30	15,877	0,172	0,143	12,291	8,7846	0,2
TBM 23	1719	4,007	2,9726	0,1144	0,069	30,457	16,119	0,152	0,126	12,813	9,1574	0,3
TBM 23	1719	3,901	2,8941	0,1087	0,0656	30,265	16,018	0,176	0,146	12,698	9,0755	0,2
TBM 24m	1722	4,263	3,1623	0,1023	0,0617	28,846	15,267	0,214	0,177	11,325	8,0939	0,3
TBM 24m	1722	3,987	2,9581	0,096	0,0579	29,86	15,804	0,158	0,131	11,923	8,5215	0,2
TBM 24m	1722	4,088	3,033	0,1059	0,0639	29,527	15,627	0,21	0,174	11,849	8,4686	0,2
TBM 24m	1722	4,261	3,1612	0,1037	0,0625	29	15,348	0,237	0,197	11,453	8,1853	0,2
TBM 24m	1722	4,207	3,1208	0,1031	0,0622	29,449	15,586	0,242	0,201	11,79	8,4266	0,2
TBM 24m	1722	4,012	2,9765	0,1084	0,0653	29,406	15,563	0,218	0,181	11,989	8,5687	0,2
TBM 24b	1722	3,202	2,3752	0,0958	0,0578	29,817	15,781	0,173	0,143	11,59	8,283	0,2
TBM 24b	1722	3,101	2,3009	0,0946	0,0571	29,452	15,588	0,151	0,125	11,824	8,4508	0,2
TBM 26	1739	4,516	3,3505	0,0964	0,0581	28,72	15,2	0,222	0,184	11,121	7,9484	0,2
TBM 26	1739	4,533	3,3629	0,0911	0,0549	28,829	15,257	0,218	0,181	11,143	7,9636	0,2
TBM 26	1739	4,409	3,2707	0,0999	0,0602	29,113	15,408	0,214	0,178	11,287	8,0666	0,2
TBM 26	1739	4,36	3,2347	0,1014	0,0612	29,067	15,383	0,199	0,165	11,415	8,158	0,2
TBM 27	1740	5,373	3,9861	0,082	0,0495	30,907	16,357	0,175	0,145	13,25	9,4695	0,2
TBM 27	1740	5,119	3,7979	0,0951	0,0574	30,515	16,15	0,184	0,153	13,193	9,4292	0,2
TBM 27	1740	5,351	3,9696	0,0815	0,0492	30,645	16,219	0,172	0,143	13,042	9,3209	0,2
TBM 28	1740	5,373	3,9861	0,0981	0,0591	27,112	14,349	0,3	0,249	9,391	6,7117	0,2
TBM 28	1740	5,119	3,7979	0,0663	0,04	27,777	14,701	0,257	0,213	9,883	7,0633	0,2
TBM 28	1740	5,351	3,9696	0,0951	0,0574	27,437	14,521	0,21	0,174	9,5437	6,8209	0,2
TBM 29	1758	4,597	3,4102	0,093	0,0561	28,243	14,948	0,21	0,175	10,922	7,806	0,4

TBM 29	1758	4,737	3,5139	0,091	0,0549	28,207	14,929	0,214	0,178	10,787	7,7092	0,2
TBM 29	1758	4,938	3,6632	0,0855	0,0516	28,274	14,964	0,242	0,201	10,234	7,3143	0,1
TBM 30	1763	2,988	2,2167	0,0387	0,0234	28,59	15,131	0,106	0,088	6,4374	4,6008	1E-
TBM 30	1763	3,076	2,282	0,0093	0,0056	23,531	12,454	0,023	0,019	5,9728	4,2687	0,1
TBM 32	1790	3,411	2,5302	0,1038	0,0626	27,29	14,443	0,223	0,185	11,873	8,4856	0,3
TBM 32	1790	3,243	2,4061	0,1099	0,0663	29,629	15,681	0,228	0,189	12,625	9,0231	0,3
TBM 32	1790	3,387	2,5123	0,1051	0,0634	28,912	15,302	0,221	0,184	12,482	8,9206	0,3
TBM 32	1790	3,404	2,5254	0,101	0,0609	29,446	15,585	0,223	0,185	12,544	8,9651	0,3
TBM 32	1790	3,417	2,5348	0,1098	0,0662	28,974	15,335	0,194	0,161	12,421	8,8772	0,3
TBM 32	1790	3,109	2,3063	0,1111	0,067	30,012	15,884	0,202	0,167	12,614	9,0156	0,5